Mathematical Models of the Retina in Health and Disease

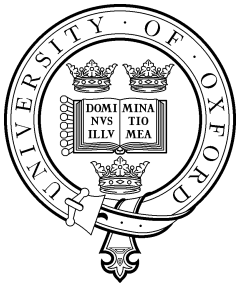

Paul Allen Roberts
University College
University of Oxford

A thesis submitted for the degree of
Doctor of Philosophy
Hilary 2015

For my parents:
Dennis A. Roberts and
Barbara D. Roberts.

Acknowledgements

This thesis could not have been written, were it not for the support of a number of people. Many have contributed in one way or another and, whilst it is not possible to mention them all, it seems appropriate to name a few here.

I would like to begin by thanking my supervisors, Helen Byrne and Eamonn Gaffney, for their wisdom, encouragement and generosity. It is through their mentorship that I have learnt to do research and to have fun in the process. Many thanks go also to my collaborators, Alex Foss and Phil Luthert, for their biological insight and enthusiasm.

I am grateful to Jon Whiteley for providing the finite element codes used to solve the 2D problem in Chapter 5 and to Joe Pitt-Francis for his assistance in writing the batch files for use with Jon's code.

My passion for mathematics was first kindled by my teacher, Ed Crocombe, at Ferndown Middle School. I have fond memories of his lessons spent playing 'carpet tiles' and 'random factor like a tractor'. Little did I know at the time, how important these lessons would be in my later life. This passion was further fanned into flame by another teacher, Keith Noble, at Poole Grammar School. I owe much to him, in helping me to gain the skill and confidence to pursue a career in mathematics.

Thanks go also to Philip Maini, for a letter of advice to a budding young mathematical biologist (he won't remember writing it, but I have followed every word) and to Ruth Baker, for giving me my first taste of research during a summer studentship.

Special thanks go to my family and friends, and in particular to my parents, Dennis and Barbara Roberts, for their unstinting love and support. It is to my parents that this thesis is dedicated.

I am grateful also to EPSRC, for funding my DPhil studentship through the Systems Biology Doctoral Training Centre.

Lastly, thanks be to God: Father, Son and Holy Spirit, who is my light in all things.

Soli Deo gloria!

Mathematical Models of the Retina in Health and Disease

Paul Allen Roberts
University College
University of Oxford
Hilary Term 2015

A thesis submitted for the degree of Doctor of Philosophy

Abstract

The retina is the ocular tissue responsible for the detection of light. Its extensive demand for oxygen, coupled with a concomitant elevated supply, renders this tissue prone to both hypoxia and hyperoxia. In this thesis, we construct mathematical models of the retina, formulated as systems of reaction-diffusion equations, investigating its oxygen-related dynamics in healthy and diseased states.

In the healthy state, we model the oxygen distribution across the human retina, examining the efficacy of the protein neuroglobin in the prevention of hypoxia. It has been suggested that neuroglobin could prevent hypoxia, either by transporting oxygen from regions where it is rich to those where it is poor, or by storing oxygen during periods of diminished supply or increased uptake. Numerical solutions demonstrate that neuroglobin may be effective in preventing or alleviating hypoxia via oxygen transport, but that its capacity for oxygen storage is essentially negligible, whilst asymptotic analysis reveals that, contrary to the prevailing assumption, neuroglobin's oxygen affinity is near optimal for oxygen transport. A further asymptotic analysis justifies the common approximation of a piecewise constant oxygen uptake across the retina, placing existing models upon a stronger theoretical foundation.

In the diseased state, we explore the effect of hyperoxia upon the progression of the inherited retinal diseases, known collectively as retinitis pigmentosa. Both numerical solutions and asymptotic analyses show that this mechanism may replicate many of the patterns of retinal degeneration seen *in vivo*, but that others are inaccessible to it, demonstrating both the strengths and weaknesses of the oxygen toxicity hypothesis. It is shown that the wave speed of hyperoxic degeneration is negatively correlated with the local photoreceptor density, high density regions acting as a barrier to the spread of photoreceptor loss. The effects of capillary degeneration and treatment with antioxidants or trophic factors are also investigated, demonstrating that each has the potential to delay, halt or partially reverse photoreceptor loss.

In addition to answering questions that are not accessible to experimental investigation, these models generate a number of experimentally testable predictions, forming the first loop in what has the potential to be a fruitful experimental/modelling cycle.

Contents

Glossary

A2E	A fluorophore which forms a major constituent of lipofuscin
AF	Autofluorescence
BDNF	Brain-Derived Neurotrophic Factor
bFGF	basic Fibroblast Growth Factor (same as FGF2)
BM	Bruch's Membrane
CC	Choriocapillaris
CNTF	Ciliary Neurotrophic Factor
CSA	Capillary Surface Area per unit volume
Cygb	Cytoglobin
DA	Dark Adaptation
DTT	Dithiothreitol
ELM	External Limiting Membrane (same as OLM)
ERG	Electroretinogram
FEM	Finite Element Method
FGF1	Fibroblast Growth Factor 1
FGF2	Fibroblast Growth Factor 2 (same as bFGF)
FMM	Fine Matrix Mapping
GCL	Ganglion Cell Layer
GDNF	Glial cell line-Derived Neurotrophic Factor
GFAP	Glial Fibrillary Acidic Protein

Hb	Haemoglobin
HBO	Hyperbaric Oxygen (therapy)
ILM	Inner Limiting Membrane
INL	Inner Nuclear Layer
IPL	Inner Plexiform Layer
IS	(Photoreceptor) Inner Segment
LA	Light Adaptation
LF	Lipofuscin
Mb	Myoglobin
mfERG	multi-focal Electroretinogram
MSS	Mutant Steady-State (hypothesis)
NFL	Nerve Fibre Layer
Ngb	Neuroglobin (refers to the pentacoordinate form when used in conjunction with Ngb-His and Ngb-O_2)
Ngb-His	Hexacoordinate Neuroglobin
Ngb-O_2	Oxygen-bound Neuroglobin
OCT	Optical Coherence Tomography
ODE	Ordinary Differential Equation
OGT	Ocular Gene Therapy
OLM	Outer Limiting Membrane (same as ELM)
ONL	Outer Nuclear Layer
OPL	Outer Plexiform Layer
OS	(Photoreceptor) Outer Segment
P_{50}	Partial pressure at which 50% of the relevant protein is bound to oxygen
PDE	Partial Differential Equation
PERG	Pattern Electroretinogram
RdCVF	Rod-derived Cone Viability Factor

RONS	Reactive Oxygen and Nitrogen Species
ROS	Reactive Oxygen Species
RP	Retinitis Pigmentosa
RPE	Retinal Pigment Epithelium
VEGF	Vascular Endothelial Growth Factor

Chapter 1

Introduction

In this thesis we use mathematical models to explore the behaviour of the retina in health and disease. In health, we explore the role of a protein known as neuroglobin in the prevention of oxygen deprivation, whilst in the disease state known as retinitis pigmentosa, we examine the effects of excess oxygen upon the progression of retinal degeneration. We begin by describing the basic physiology of the eye and retina.

1.1 The Human Eye and Retina: Structure and Function

1.1.1 The Human Eye

The eye is a fluid-filled chamber enclosed by three layers of tissue (Oyster, 1999, see Figure 1.1(a)). The outermost layer consists of the cornea, the limbus and the sclera; the middle layer, known as the uveal tract, contains the iris, the ciliary body and the choroid, while the innermost layer consists of the retina (Oyster, 1999). Our focus in this study is upon the retina and the choroid. The main chamber of the eye lying posterior to the lens is filled with a gel-like substance known as the vitreous humour, often referred to simply as the vitreous (Oyster, 1999). Light enters the eye through the cornea, passing through the aperture in the centre of the iris known as the pupil and then through the lens, where it is focused upon the retina on the inner surface of the eye.

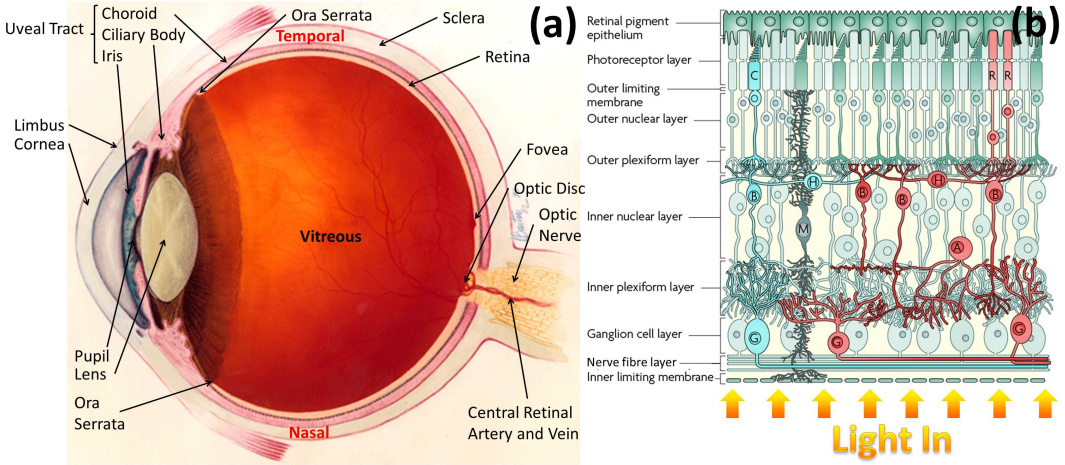

Figure 1.1: Diagrams of the human eye and retina. (a) Diagram of the (right) human eye, viewed in the transverse plane. Figure reproduced, with modifications, from `http://www.nei.nih.gov/health/coloboma/coloboma.asp`, courtesy: National Eye Institute, National Institutes of Health (NEI/NIH). (b) Diagram of the human retina, showing the retinal layers and cell types. The diagram is oriented such that the top lies outermost and the bottom innermost in the eye. R: rod photoreceptor. C: cone photoreceptor. H: horizontal cell. B: bipolar cell. M: Müller glial cell. A: amacrine cell. G: ganglion cell. Figure reproduced, with permission and modifications, from Swaroop et al. (2010).

1.1.2 The Human Retina

The retina is the layer of tissue at the back of the eye that is responsible for the detection of light. It extends from the optic disc, where the optic nerve, central retinal artery and vein puncture the eye, to the ora serrata and has a multilayered structure, consisting of numerous cell-types (see Figure 1.1(b)). The numerous acronyms below are summarised in the Glossary.

Structure and Cell Types

The structure of the retina is as follows, moving inward from the outermost layer: the retinal pigment epithelium (RPE), the photoreceptor layer, consisting of the photoreceptor outer segments (OSs) and inner segments (ISs), the outer limiting membrane (OLM, also known as the external limiting membrane or ELM), the outer nuclear layer (ONL), the outer plexiform

layer (OPL), the inner nuclear layer (INL), the inner plexiform layer (IPL), the ganglion cell layer (GCL), the nerve fibre layer (NFL) and the inner limiting membrane (ILM) (see Figure 1.1(b)). The retina can be divided into two halves: the outer retina lying outward from the boundary between the OPL and INL and the inner retina lying inward from this boundary.

The choroid, which is a vascular layer, lies outward from the RPE and is separated from it by Bruch's membrane (BM). Photoreceptor cells occupy not just the photoreceptor layer, but also the ONL, which contains their nuclei, and the OPL, which contains their axons and synaptic terminals. The INL contains the bipolar cells, together with the nuclei of the horizontal cells, the interplexiform cells and most of the amacrine cells, all of which are intermediate between the photoreceptors and ganglion cells (Oyster, 1999). It also contains the nuclei of the Müller's cells (Oyster, 1999). The IPL contains the synaptic terminals of the bipolar cells and the dendrites of the ganglion cells with which they synapse. The GCL contains the nuclei of the ganglion cells and some amacrine cells (Oyster, 1999), whilst the NFL contains the ganglion cell axons which lead to the brain via the optic nerve. The OLM is formed by a series of tight junctions between the photoreceptors and Müller's cells and the ILM is formed by the expansion and connection of the outermost tips of the Müller's cells (Oyster, 1999).

Photoreceptors are the retinal cells which detect and respond to incident light. They come in two varieties: rods and cones. Rod photoreceptors provide achromatic vision under scotopic (low light) conditions, whilst cone photoreceptors provide high-acuity colour vision under photopic (well-lit) conditions. Following light detection the visual signal is transmitted via the neurons of the inner retina, where some image processing occurs, to the optic nerve and then to the brain. Photoreceptors have four main structural elements: an outer segment (OS), which contains discs in which the photopigment molecules are embedded, an inner segment (IS), which contains the photoreceptor mitochondria and hence is the most metabolically active part of the cell, a nucleus, and an axon ending in a synaptic terminal (Oyster, 1999) (see Figure 1.2 for diagrams of rod and cone photoreceptors). The OS and IS are connected via a narrow cilium. Photoreceptors regularly shed disks from the tip of their OS and form replacement discs at the base of the OS, with an average OS turnover rate of approximately 9–13 days

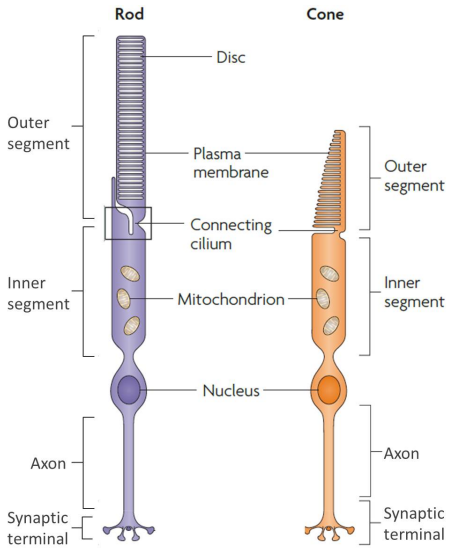

Figure 1.2: Diagram of rod and cone photoreceptors. Figure reproduced, with permission and modifications, from Wright et al. (2010).

(Young, 1971; Oyster, 1999). The shed discs are then phagocytosed by neighbouring RPE cells.

The RPE comprises a single layer of cuboidal cells which form the blood-retina barrier and are essential to the proper functioning and maintenance of the photoreceptors. In addition to removing shed OSs and acting as a mediator between the retina and the choroid of oxygen and other nutrients, the RPE is thought to play an important role in the maintenance of the choriocapillaris, via its production of vascular endothelial growth factor (VEGF, an angiogenic factor, Saint-Geniez et al., 2009).

Oxygen is supplied to the retina via two separate vascular systems: the choriocapillaris (CC), the fenestrated capillary bed which forms the innermost layer of the choroid next to BM, supplies the photoreceptors in the outer retina, whilst the retinal circulation supplies the inner retina (Oyster, 1999). The CC is supplied and drained by the blood vessels lying deeper in the choroid, which are themselves supplied and drained by the long and short posterior ciliary arteries, and the superior and inferior ophthalmic veins, whilst the retinal circulation is supplied and drained by the central retinal artery and vein (see Figure 1.3).

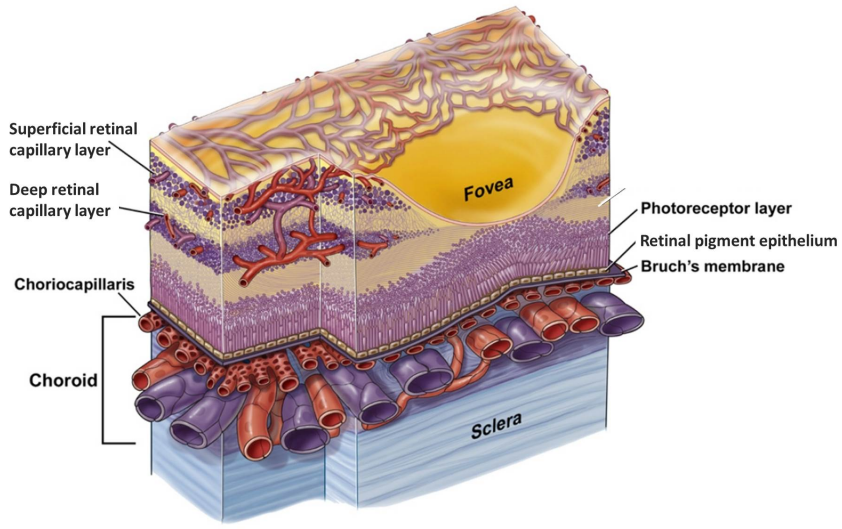

Figure 1.3: Diagram to show the retinal and choroidal vasculature. Figure reproduced, with permission and modifications, from Kur et al. (2012) and originates from Anand-Apte and Hollyfield (2009).

Regional Variations

The structure of the retina is not uniform across the inner surface of the eye, but rather contains many regional differences. Figure 1.4 shows the regions into which the retina is commonly decomposed. Here we have followed the convention of Iwasaki and Inomata (1986) in our labelling of the regions of the central retina. The fovea lies roughly at the centre of the retina, the other regions lying concentrically outward from this, with the exception of the foveola, which lies central to the fovea, and the optic disc, which occupies a position nasal to the fovea in the mid-periphery. The fovea is the region of the retina responsible for high acuity central vision and the optic disc gives rise to a blind spot which is compensated for by the other eye. The foveola is the region of the retina from which the GCL is absent (Iwasaki and Inomata, 1986) and the border between the fovea and the parafovea is formed by the thickest part of the retina, called the foveal rim. The borders between the parafovea and perifovea, and between the perifovea and mid-periphery are determined by retinal width (see Iwasaki and Inomata, 1986, for details). The equator is the circumference of the eye lying midway between the

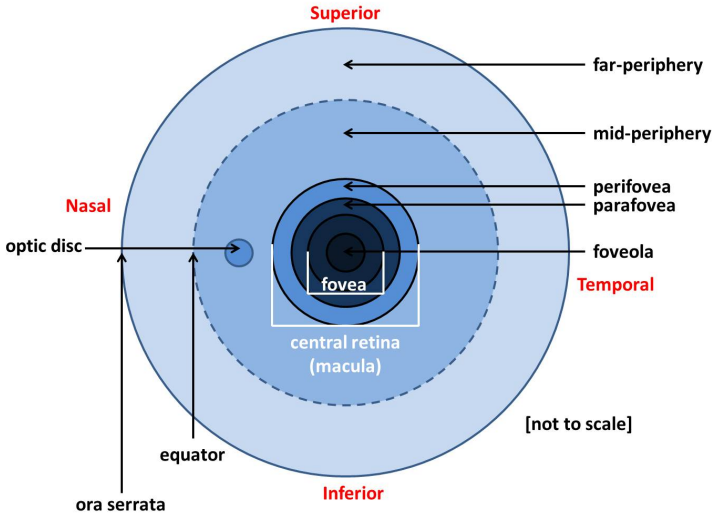

Figure 1.4: Diagram to show the various regions of the retina in the left eye (the optic disc would be on the right-hand side in the right eye). The equator lies half way between the front and the back of the eye. Nasal: the side of the eye nearest the nose. Temporal: the side of the eye furthest from the nose. Superior: the upper part of the eye. Inferior: the lower part of the eye.

front and the back of the eye and the retina comes to an end at the ora serrata.

Both the total retinal width and the width of most of the retinal layers vary across the retina. Only the RPE, photoreceptor layer, the ONL, some of the OPL and the ILM are present at the centre of the fovea (Oyster, 1999), whilst the remainder of the OPL and the inner neural layers are laterally displaced toward the foveal rim. As a result, the total retinal width is greatest at the foveal rim, decreasing sharply toward the centre of the foveal pit and decreasing gradually toward the periphery (see Figures 1.3 and 1.5(a)).

Photoreceptors are unevenly distributed across the retina. Cone density is highest at the centre of the fovea, falling off sharply toward the edge of the fovea and then more slowly toward the periphery of the retina, whilst rods are absent from the centre of the fovea, reach their maximum density in a ring about 20^{o} from the foveal centre and gradually reduce in density toward the periphery (see Figure 1.5(b)). Both rods and cones are absent from the optic disc.

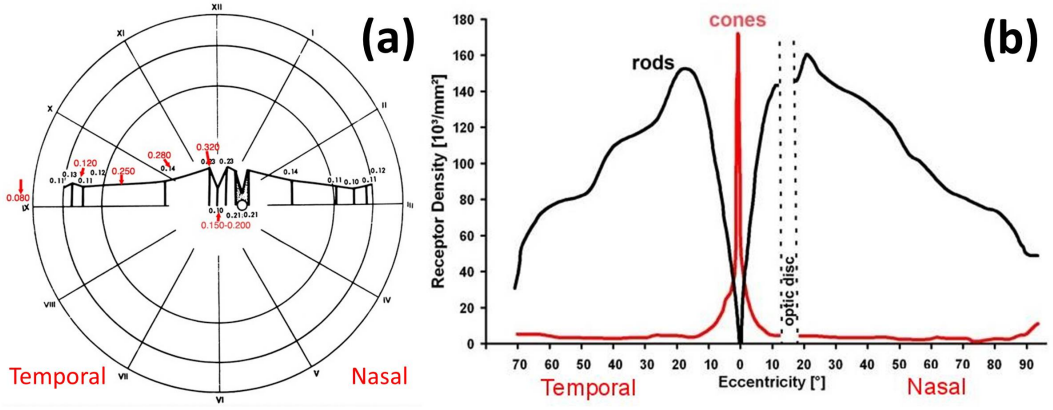

Figure 1.5: Regional variations across the retina. (a) Diagram to show the width of the retina across the horizontal meridian for a range of eccentricities (angles of displacement from the centre of the fovea). The retina is shown in profile. All widths are given in mm. The numbers in red are more accurate. (b) Graph to show rod and cone photoreceptor densities across the horizontal meridian of the human retina. Photoreceptors are absent from the region of the optic disc. Figures reproduced, with permission and modifications, from Webvision, `http://webvision.med.utah.edu/`, where (b) originates from Østerberg (1935).

The retinal vasculature consists of two capillary layers, one deep and the other superficial (Pournaras et al., 2008; Kur et al., 2012). The deep retinal capillary layer lies between the OPL and the INL, whilst the superficial retinal capillary layer lies in the GCL and NFL (Kur et al., 2012). The deep retinal capillaries disappear toward the periphery of the retina and there is a rim of approximately 1.5 mm at the furthest edge of the retina from which retinal capillaries are absent (Pournaras et al., 2008). There is also a capillary free region, of about 400–500 μm in diameter, spanning the central fovea (Oyster, 1999; Pournaras et al., 2008). A third capillary layer is present in a small rim around the optic disc, known as the peripapillary area (Pournaras et al., 2008; Kur et al., 2012). These radial peripapillary capillaries reside in the superficial portion of the NFL (Pournaras et al., 2008; Kur et al., 2012). Recent studies examining the human retina identified four retinal capillary layers in regions 3 mm superior to the optic disc and 2 mm nasal to the fovea (Chan et al., 2012; Tan et al., 2012), confirming similar findings in the central retina of the macaque monkey in which retinal capillary layers were found to border the inner and outer edges of both the INL and GCL (Snodderly et al.,

1992). The innermost and outermost of these layers have a laminar structure, whereas the middle two have a complex three-dimensional configuration (Chan et al., 2012; Tan et al., 2012). Similarly accurate measurements have yet to be performed in the mid- or far-peripheral retina, though at present it is thought that the number of capillary layers decreases toward the periphery of the retina, decreasing to two and then one layer (Oyster, 1999).

1.2 Retinal Oxygen Distribution and the Role of Neuroglobin

1.2.1 Retinal Oxygen Distribution

The retina has one of the highest rates of oxygen consumption of any tissue in the human body (Anderson and Saltzman, 1964; Anderson, 1968; Yu and Cringle, 2001) and, as such, is particularly vulnerable to hypoxia (oxygen deprivation). Indeed, hypoxia may contribute to photoreceptor death in the early stages of the retinal degenerative disease retinitis pigmentosa (Maslim et al., 1997; Valter et al., 1997; Stone et al., 1999; Choi et al., 2001; Mervin and Stone, 2002b) and there is some evidence that the rate of retinal oxygen uptake may be increased in patients in the early stages of this disease (see Section 1.3, Anderson, 1968; Haugh et al., 1990; Wangsa-Wirawan and Linsenmeier, 2003; Yu and Cringle, 2005).

Whilst the oxygen distribution across the human retina has not been measured, it has been measured for other mammals, including rats (Yu et al., 1994, 1999, 2000, 2004), rabbits (Stefánsson, 1988), cats (Alder et al., 1983; Linsenmeier, 1986; Linsenmeier and Yancey, 1989; Haugh et al., 1990; Linsenmeier and Braun, 1992; Braun et al., 1995; Linsenmeier and Padnick-Silver, 2000; Padnick-Silver and Linsenmeier, 2003) and monkeys (Birol et al. 2007, see also Yu and Cringle, 2001, 2005; Wangsa-Wirawan and Linsenmeier, 2003, for reviews). Under dark conditions (dark adaptation, DA) the photoreceptor ISs consume oxygen at twice the rate at which they consume oxygen under light conditions (light adaptation, LA). This is because under DA an ionic flow, known as the dark current, must be maintained by an

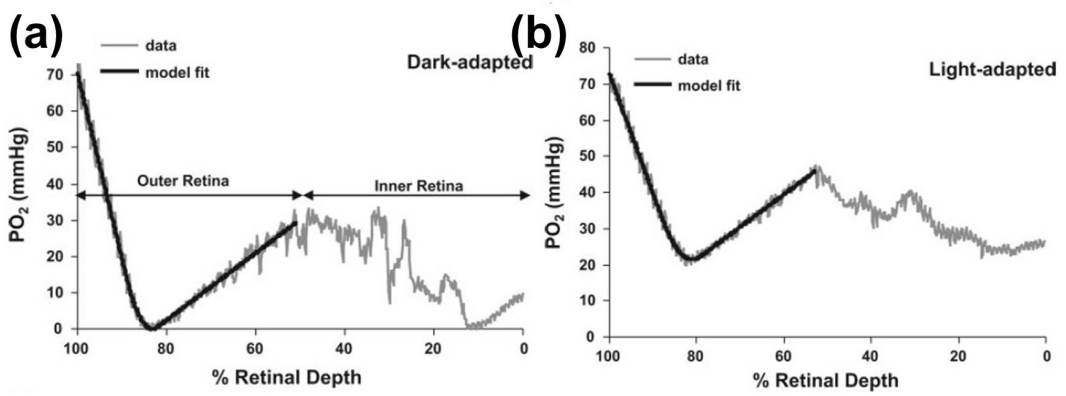

Figure 1.6: Retinal oxygen profiles. Graphs show the oxygen distribution across the perifoveal retina of a macaque monkey under DA (a) and LA (b). The retina is normoxic under LA, whilst hypoxic regions are present in both the inner and outer retina under DA. Grey lines show the profiles measured using an oxygen-sensitive microelectrode, whilst black lines show a piecewise linear and quadratic approximation fitted to the outer retinal profile. Figure reproduced, with permission, from Birol et al. (2007).

ATP dependent NA^+/K^+ pump, located in the IS membrane (Hart Jr., 1992). As a result, the retinal oxygen profile drops under DA, meaning that the retina is more likely to experience hypoxia under DA. Hypoxia is detrimental to cells, both in limiting oxidative metabolism and in increasing the production of reactive oxygen species, upsetting the redox potential and leading to oxidative stress and damage (Kohen and Nyska, 2002).

Birol et al. (2007) have measured oxygen profiles across the retina of the macaque monkey under DA and LA. The outer retina is normoxic under LA and hypoxic under DA, whilst the inner retina may be hypoxic under either LA or DA, depending upon local retinal capillary density (see Figure 1.6, where the inner retina is normoxic under LA and hypoxic under DA in this case). Since the macaque retina is physiologically similar to that of the human, it is likely that the human retina is also vulnerable to hypoxia, especially under DA. Thus any factor that promotes retinal oxygenation may be vital in preventing or minimising retinal hypoxia and hence cell death.

1.2.2 Neuroglobin

Globins are proteins that bind oxygen reversibly and regulate oxygen transport and storage (Burmester and Hankeln, 2004). The two best known vertebrate globins are haemoglobin (Hb) and myoglobin (Mb). Hb increases the oxygen carrying capacity of red blood cells, whilst Mb facilitates the diffusion of oxygen to mitochondria in striated and cardiac muscle cells (Burmester et al., 2000; Burmester and Hankeln, 2004, 2009). In 2000, Burmester et al. discovered a new vertebrate globin protein which they named neuroglobin (Ngb) because of its preferential expression in the cells of the nervous system, including the retina. Ngb has a similar structure and molecular mass to that of Mb (Burmester and Hankeln, 2009) and, as such, it has been proposed that Ngb may play a role in oxygen transport and storage (Burmester et al., 2000; Burmester and Hankeln, 2004, 2009). In Chapters 2 and 3 we use mathematical models to test this hypothesis.

By transport, we mean the process by which oxygen is moved from one region of the retina to another, resulting in a spatial redistribution of oxygen, whilst storage refers to the temporal retention of oxygen following a drop in oxygen levels within the retina. In the first case we seek to discover whether Ngb could increase the oxygen concentration in hypoxic regions under steady-state conditions, whilst in the second case we aim to discern whether Ngb could act as an oxygen buffer, maintaining an oxygen supply to the retina during a period of increased uptake, or decreased supply.

That Ngb has a role in oxygen transport and storage seems likely for the following reasons:

1. Ngb appears to be related to invertebrate nerve globins which are thought to be involved in oxygen supply (Burmester et al., 2000; Burmester and Hankeln, 2009);

2. this hypothesis is the most parsimonious from an evolutionary perspective (avoiding frequent switching of the role of globins during evolutionary history, Burmester and Hankeln, 2009);

3. Ngb is most highly concentrated in those areas of the retina with the highest density of mitochondria, that is, those regions with the highest oxidative metabolism (Bentmann

et al., 2005);

4. Ngb is likely to occur in high concentrations ($\geq 200\mu$M) in these regions and thus contribute significantly to the flux of oxygen across the retina (Bentmann et al., 2005);

5. Ngb's oxygen affinity is higher than that of Hb, but lower than that of the cytochrome oxidase of the mitochondria, suggesting a similar role to that suggested for Mb in transporting oxygen from the blood supply to mitochondria (Bentmann et al., 2005);

6. Ngb is up-regulated during hypoxia and ischemia, and has been shown to improve neuronal survival after hypoxia (Sun et al., 2001, 2003).

Despite these arguments, it is far from certain that Ngb plays a significant role in oxygen transport and storage, and opinion as to the main function of Ngb remains divided. To quote a recent review, 'the current evidence neither convincingly supports nor excludes an involvement of Ngb in O_2 supply' (Burmester and Hankeln, 2009). The following observations argue against a role in oxygen transport and storage:

1. As mentioned above, Ngb is thought to play an analogous role to that suggested for Mb in oxygen transport. However, Ngb's P_{50} value (the partial pressure of oxygen at which half of all Ngb molecules are bound to oxygen, lower values corresponding to a higher oxygen affinity) may be higher than the value of 2 mmHg originally estimated (Burmester et al., 2000), with estimates reaching as high as 8.4 mmHg (Hamdane et al., 2003). This compares with a P_{50} of 1–5 mmHg for Mb. Indeed, Mb's role in oxygen transport is itself a matter of controversy (Jürgens et al., 1994);

2. Dewilde et al. (2001) found that Ngb undergoes a fast autoxidation from a ferrous (Fe^{2+}) to a ferric (Fe^{3+}) form *in vitro*, an event which reduces the binding efficiency of O_2 to Ngb;

3. Although Ngb concentrations within certain cells or sub-cellular compartments in the retina may exceed the average retinal concentration, it is unclear whether they are high enough for Ngb to significantly affect oxygen transport;

4. The only previous mathematical model to examine the role of Ngb upon retinal oxygen distribution suggested that the effect of Ngb is insignificant (Fago et al., 2004b).

In Chapter 2 we show that Ngb's P_{50} value, far from arguing against a role in oxygen transport, is in fact near optimal for this process, whilst in Chapter 3 we show that Ngb can play a significant role in oxygen transport for biologically realistic concentrations.

A number of alternative roles have been suggested for Ngb. For example, Ngb may act as a scavenger of reactive oxygen or nitrogen species, it may detoxify excess nitric oxide, it may play a role in the control of blood pressure, it may be involved in a signal transduction pathway, it may be involved in a redox process preventing apoptosis or act as a sensor of the cellular oxygen concentration (Burmester and Hankeln, 2004, 2009). However, for the reasons outlined above, we consider the oxygen transport and storage hypothesis the most promising.

A fourth vertebrate globin, cytoglobin (Cygb), which is also expressed in the retina, was discovered in 2002 (Burmester et al., 2002; Trent and Hargrove, 2002). Whilst it may also play a role in oxygen transport and storage, we ignore its presence in this study, noting that since its distribution in the vertebrate retina is not correlated with mitochondrial distribution or oxygen consumption, it is unlikely to play a major role in these processes (Schmidt et al., 2005).

1.2.3 Previous Mathematical Models

A number of mathematical models for retinal oxygen distribution have been constructed (see for instance, Dollery et al., 1969; Linsenmeier, 1986; Stefánsson, 1988; Haugh et al., 1990; Linsenmeier and Braun, 1992; Braun et al., 1995; Linsenmeier and Padnick-Silver, 2000; Cringle and Yu, 2002; Yu and Cringle, 2002). The majority of these models fit piecewise linear and quadratic polynomials to oxygen profiles measured using oxygen sensitive micro-electrodes. They assume that the oxygen concentration is at steady-state and are posed on one-dimensional domains, oriented in a radial direction, across the width of the retina. They assume that the rate of oxygen uptake is constant in each model layer (where model layers incorporate various cellular layers) and so reduce to solving $\frac{\mathrm{d}^2 c}{\mathrm{d}x^2} = Q$ in each layer, where c is

the oxygen concentration, x is the distance across the retina and Q is the rate of oxygen uptake. In layers for which $Q > 0$, the profile is quadratic and in those for which $Q = 0$, the profile is linear. In Chapters 2 and 3 we employ the more realistic Michaelis-Menten term for oxygen uptake ($Qc/(\gamma + c)$), whilst using an asymptotic analysis to place these piecewise linear and quadratic models on a stronger theoretical foundation.

To the best of our knowledge, only one mathematical model of retinal oxygen distribution incorporating Ngb has been developed (Fago et al., 2004b). This model contains three layers spanning the outer retina, between the CC and the deep retinal capillaries. Unlike the models mentioned above, a Michaelis-Menten term is used for the rate of oxygen uptake. The proportion of Ngb molecules in their oxygen bound and unbound states are assumed to be at quasi-steady-state at all times. The model predicts that Ngb concentrations would have to exceed 100 μM to be effective in oxygen storage and to be greater than 300 μM to be effective in oxygen transport. Since they assume that Ngb levels do not exceed 100 μM, Fago et al. conclude that Ngb does not play a significant role in either the transport or storage of oxygen. However, based upon the reasoning outlined in Appendix A, we argue that Ngb concentrations could reach, and, perhaps, significantly exceed, these concentrations in some locations. In Chapter 3 we expand Fago et al.'s model to account for both the inner and outer retina, dropping the quasi-steady-state assumption and exploring the full range of biologically realistic Ngb concentrations. Our results suggest that Ngb's oxygen storage properties are negligible, in agreement with Fago et al., whilst challenging their conclusion that this holds true for oxygen transport.

Two models for retinal oxygen supply have been developed using a modified version of the Krogh tissue cylinder model; however, neither of these models account for the layered structure of the retina, or the action of Ngb (Friedland, 1978; Seth, 2012).

Oxygen transport in other biological tissues has received a great deal of attention from the applied mathematics community (see Goldman, 2008, for a review), as has the role of Mb in the facilitated diffusion of oxygen (see, for instance, Wyman, 1966; Keener and Sneyd, 1998; McGuire and Secomb, 2001; Whiteley et al., 2002).

1.3 Retinitis Pigmentosa

1.3.1 Overview

The term retinitis pigmentosa (RP) refers to a range of genetically mediated retinal diseases that cause the degeneration and subsequent loss of photoreceptors. RP most commonly occurs as a rod-cone dystrophy, with an initial degeneration of rod photoreceptors, followed by the degeneration of cone photoreceptors (Hamel, 2006). However, less common forms exist, in which rod and cone loss occurs on the same time scale, or in which cone loss precedes rod loss (termed a cone-rod dystrophy, Hartong et al., 2006). Whilst both the mode and rate of RP progression vary greatly between patients, a general pattern can be discerned. Typically, patients first exhibit symptoms during adolescence, when they develop difficulties with dark adaptation and night blindness. This is followed by loss of far- or mid-peripheral vision in early adulthood, which over time leads to tunnel vision. Central vision is generally the best preserved, but is usually lost by age 60 (Hartong et al., 2006). Examination of the fundus (the interior surface of the eye, opposite the lens) of RP patients typically reveals pigmentary deposits in the periphery of the retina, known as bone-spicules; attenuation of the retinal vasculature and a waxy pallor to the optic disc (see Figure 1.7).

RP is the most common inherited retinal degeneration (Shintani et al., 2009). Nonsyndromic RP (that is, occurring without any other symptoms) has a prevalence of about 1 in 4000 with about 1.5 million affected individuals worldwide (Hamel, 2006; Hartong et al., 2006; Shintani et al., 2009). As noted by Hartong et al. (2006), studies in Japan, Kuwait and Denmark have shown that RP is a major or leading cause of visual disability within certain age ranges. A number of treatment strategies are being developed (see Section 1.3.7), but as yet none of these are available in a clinical setting (Musarella and MacDonald, 2011).

In Chapters 4 and 5 we examine the role of oxygen toxicity upon the progression of RP. In what follows, we describe the genetic basis, pathophysiology and clinical manifestations of RP, before discussing oxygen toxicity in more detail.

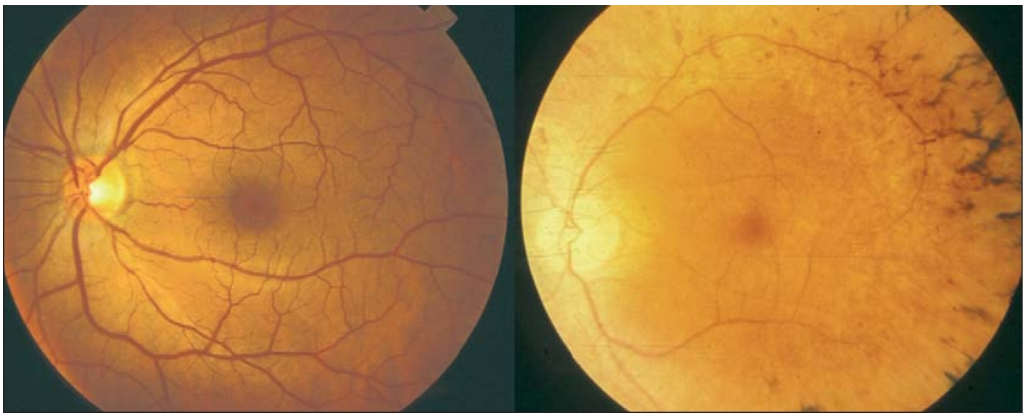

Figure 1.7: Fundi of a healthy patient (left) and a patient with RP (right). Note the presence of peripheral pigment deposits, attenuation of the retinal vessels and waxy pallor to the optic disc in the image of the diseased eye. Figure reproduced, with permission, from Hartong et al. (2006).

1.3.2 Genetic Basis

RP is genotypically heterogeneous, with mutations in at least 53 genes having been associated with RP to date (Al-Rashed et al., 2012). Most of these genes are expressed in rod photoreceptors and some by RPE cells, but most are not expressed in cone photoreceptors (Hamel, 2006; Hartong et al., 2006; Daiger et al., 2007). The question of why degeneration spreads to cone photoreceptors is addressed in Sections 1.3.5 and 1.3.6.

Mutant genes expressed in rods typically code for proteins involved in photoreceptor structure (for instance cytoskeleton proteins), the renewal and shedding of the rod OSs (for instance rhodopsin), phototransduction cascades (for instance cGMP phosphodiesterase), or the visual cycle (Van Soest et al., 1999; Hamel, 2006; Shintani et al., 2009), whilst mutation of the RPE may disrupt disc phagocytosis or retinol (a molecule in the visual cycle) metabolism (Hamel, 2006).

RP may also occur as part of a syndrome, in which other organ systems are affected. Examples include Usher's syndrome, Refsum disease, Bassen-Kornzweig syndrome, Bardet-Biedl syndrome, and Batten disease (Shintani et al., 2009).

1.3.3 Animal and Human Models

There is a distinct difference between the progression of RP in animals and humans. In animals (rats, mice, cats and pigs), degeneration occurs much more rapidly, over a period of weeks to a couple of years, with two temporally distinct phases of degeneration. The first phase involves rapid rod loss, whilst the second consists of a more gradual cone loss. During this second phase, cones exist in a virtually rod-free environment. There is generally no clear spatial pattern to photoreceptors loss, with photoreceptors being lost in all regions of the retina simultaneously (see in particular, Petters et al., 1997; Tso et al., 1997; Li et al., 1998, see also, Carter-Dawson et al. 1978; García-Fernández et al. 1995; Clarke et al. 2000; Yu et al. 2000, 2004; Yu and Cringle 2001, 2005; Campbell et al. 2006; Padnick-Silver et al. 2006; Chrysostomou et al. 2008; Huang et al. 2012; Li et al. 2012; Pennesi et al. 2012; Ross et al. 2012; Samardzija et al. 2012; Wang et al. 2012). The morphological features of degenerating cones are different from those of rods, suggesting that a different mechanism is responsible for their demise (Petters et al., 1997; Tso et al., 1997).

The RPE is usually well preserved, but may degenerate or migrate toward the inner neural layers in the later stages of the disease (Tso et al., 1997; Li et al., 1998; Samardzija et al., 2012). The CC is generally maintained and choroidal blood flow remains unaffected; however, retinal blood flow decreases with retinal degeneration and retinal vessel attenuation is common, whilst retinal vessels may also degenerate, particularly at the periphery (Li et al., 1998; Yu et al., 2000, 2004; Yu and Cringle, 2005; Padnick-Silver et al., 2006; Li et al., 2012; Samardzija et al., 2012)

In humans, photoreceptor degeneration is more gradual, there is no clear separation between phases of rod and cone loss, and a spatial pattern of degeneration is evident. Rod dysfunction typically occurs in adolescence, leading to night blindness and poor dark adaptation; however, the rods themselves remain intact (Milam et al., 1998). Significant photoreceptor loss does not usually begin until early adulthood, typically initiating in the mid- or far-peripheral retina and progressing outwards from there (Milam et al., 1998; Hartong et al., 2006). This corresponds to the loss of mid- or far-peripheral vision and the development of

tunnel vision (Grover et al., 1998). Central vision is generally best preserved and is usually lost by age 60 (Grover et al., 1998; Hartong et al., 2006). Prior to the degeneration of photoreceptors, their OSs shrink and vanish, most likely because the rate of production of discs has decreased, failing to keep pace with disc shedding. This explains the loss in rod function prior to their degeneration (Milam et al., 1998).

Studies using transgenic rats and *Xenopus laevis* tadpoles have shown that both rod and cone photoreceptors may regain OS length and function following light damage (Chrysostomou et al., 2008; Lee et al., 2012), suggesting that photoreceptor recovery may be possible in RP, following OS loss.

Following photoreceptor degeneration in humans, RPE cells migrate away from Bruch's membrane, towards the retinal capillary layers, producing black melanin granules, resulting in the distinctive bone spicule pattern (Li et al., 1995; Milam et al., 1998, see Figure 1.7). This is often followed by degeneration of the CC (Li et al., 1995; Milam et al., 1998; Mullins et al., 2012).

Fundus examination of many RP patients reveals abnormal autofluorescence (AF) patterns (von Rückmann et al., 1995, 1999). Fundus AF is due to the presence of a substance known as lipofuscin (LF) which is contained within RPE cells (Sparrow and Boulton, 2005; Ach et al., 2012). LF is derived from the material within phagocytosed photoreceptor OS tips. The fluorophore A2E is a major constituent of LF (Sparrow and Boulton, 2005; Zhou et al., 2006). A2E is not removed from RPE cells, but rather accumulates over time (Sparrow and Boulton, 2005). It is thought that increases in the levels of A2E may result in RPE dysfunction and damage (Kennedy et al., 1995; Sparrow and Boulton, 2005), together with photoreceptor death (Dorey et al., 1989).

The majority of abnormal AF patterns may be characterised as either a single or a double hyperfluorescent ring. In single ring AF, the ring may remain stable over time, or constrict, moving towards the fovea (Robson et al., 2006, 2011; Lima et al., 2012). In double ring AF, the inner ring is seen to constrict to a perifoveal location and the outer ring to expand from the vascular arcades (branches of the central retinal artery) toward the periphery, eventually

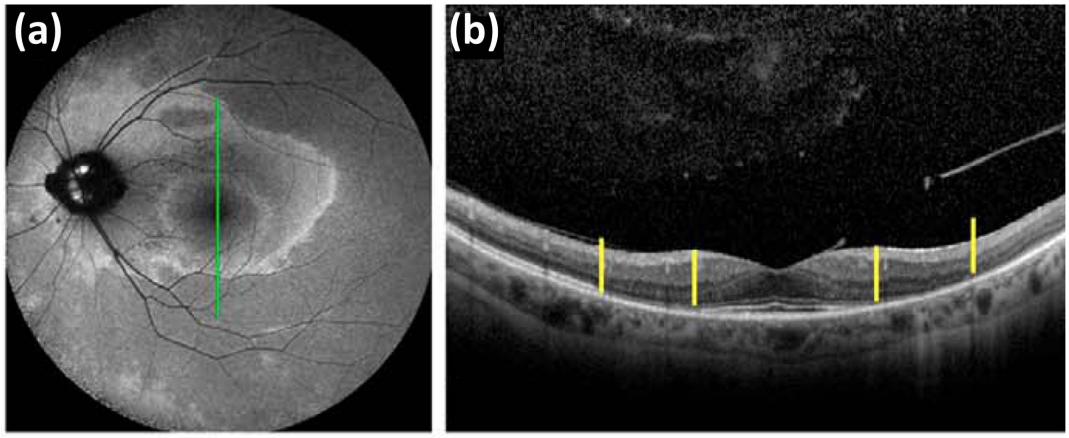

Figure 1.8: (a) Fundus autofluorescence image of the left eye of a patient with RP, showing a double ring pattern. (b) OCT scan through a section oriented along the green line in (a); the photoreceptor IS/OS band is undetectable in the area between the two AF rings (indicated by the yellow bars). Figure reproduced, with permission and modifications, from Escher et al. (2012).

becoming hypofluorescent (Escher et al., 2012, see Figure 1.8(a)). The accumulation of LF which results in AF rings may be caused by alterations in either the rod OSs or the RPE (Kennedy et al., 1995).

AF imaging has been compared against other measurements of the retina such as optical coherence tomography (OCT, Murakami et al., 2008; Lima et al., 2009, 2012; Robson et al., 2011; Escher et al., 2012), electroretinograms (ERGs) – including pattern ERGs (PERGs, Robson et al., 2003, 2004, 2006, 2008, 2011; Popović et al., 2005) and multi-focal ERGs (mfERGs, Popović et al., 2005; Robson et al., 2006, 2008) – and visual field tests (perimetry, Popović et al., 2005; Robson et al., 2006; Murakami et al., 2008; Escher et al., 2012) – including fine matrix mapping (FMM, Robson et al., 2004, 2006, 2008) – in order to relate the observed fluorescence patterns to retinal morphology and function. OCT measures the depth of various retinal layers, in particular the inner segment/outer segment (IS/OS) boundary and the outer nuclear layer (ONL). Absence of the IS/OS boundary indicates photoreceptor degeneration and perhaps apoptosis, whilst absence of the ONL indicates photoreceptor apoptosis. ERGs measure the electrophysiological responses of rods and cones and are a good indicator

of rod and cone function and hence scotopic (rod) and photopic (cone) sensitivity. Visual field tests measure the visual acuity at a range of points in a patient's visual field.

In the case of single ring AF, OCT reveals normal retinal morphology central to the ring, with disorganisation of the IS/OS junction and centrifugal thinning of the ONL across the width of the ring, the IS/OS junction and ONL vanishing at the outer boundary of the ring (Murakami et al., 2008; Lima et al., 2009, 2012; Robson et al., 2011). ERG shows preservation of scotopic and photopic vision central to the ring, with sensitivity loss increasing centrifugally across the ring and absence of both peripheral to the ring, with reduced scotopic vision encroaching past the inner boundary of the ring into the central retina (Robson et al., 2004, 2006, 2008; Popović et al., 2005). This is consistent with the characterisation of RP as a rod-cone dystrophy, with rod degeneration preceding cone degeneration and suggests that rod dysfunction precedes the accumulation of LF and visual field loss (Robson et al., 2008). The visual field is found to be preserved central to the ring and absent peripheral to the ring (Robson et al., 2003, 2006, 2008; Popović et al., 2005; Murakami et al., 2008), with a gradient of sensitivity change across the ring (Robson et al., 2004, 2008).

The fact that the IS/OS boundary and ONL are preserved across the AF ring and the fact that visual sensitivity is diminished, but not absent, across the ring, suggest that rescue of photoreceptors and, hence, visual function, may be possible in this region. The absence of the IS/OS boundary and ONL peripheral to the ring, together with the absence of visual sensitivity suggest that functional rescue in this region is not possible.

For double ring AF, OCT shows the absence of the IS/OS junction in the region between the rings (Figure 1.8(b)) and visual field tests reveal either a mid-peripheral annular scotoma (island of visual field loss) or tunnel vision in advanced cases (Escher et al., 2012). Fundus photography also shows RPE atrophy in the mid-periphery and pigmentary deposits along the vascular arcades (Escher et al., 2012). Escher et al. (2012) also measured the melanin-related near-infrared AF. It was found to colocalise with the outer and inner rims of the outer and inner rings respectively suggesting an early stage of photoreceptor degeneration as concentrations of the antioxidant melanin may increase due to increased rates of RPE phagocytosis.

It is still unclear whether the photoreceptors or the RPE initiate retinal degeneration. Mullins et al. (2012) found regions of preserved RPE underlying a completely atrophic ONL, suggesting that photoreceptors degenerate first. This would also appear to be the case in geographic atrophy, a late stage of macular degeneration (Panorgias et al., 2013). Alternatively, the RPE may degenerate first as a result of increased metabolic demand and LF accumulation due to increased rod OS turnover and photoreceptor apoptosis (Dorey et al., 1989; Popović et al., 2005; Murakami et al., 2008; Lima et al., 2012).

It is unclear how, on the basis of LF accumulation alone, the typical pattern of disease progression of RP could be generated. LF accumulation does not explain why degeneration begins at the mid- or far-periphery and nor does it explain why degeneration would spread. As such, LF accumulation does not present a promising mechanism for RP progression.

Some recent studies in transgenic rats have demonstrated that rods may die in circular 'hot spots' rather than uniformly across the retina (see Lee et al., 2011; Ji et al., 2012; García-Ayuso et al., 2013; Zhu et al., 2013). In the P23H-1 rat, hot spots are more common in the equatorial (far- and mid-peripheral) retina (García-Ayuso et al., 2013). These hot spots expand over time, initially maintaining their circular shape (Ji et al., 2012), with widths measured to lie in the range 60-295 μm, depending upon age and mutation type (Ji et al., 2012; García-Ayuso et al., 2013; Zhu et al., 2013). The cones which formerly inhabited the spots are initially displaced to the circumference, before degenerating at a later stage (Lee et al., 2011; Ji et al., 2012; García-Ayuso et al., 2013; Zhu et al., 2013). Very little histological data is available for the early stages of human RP, so these studies provide a key insight into the likely patterns of early photoreceptor loss. Cideciyan et al. (1998) studied the microscopic pattern of degeneration in humans. They found that some, but not all, forms of rhodopsin mutations (expressed in rods) may lead to an initial patchy loss of photoreceptors, with patches appearing to coalesce over time. In other cases rod dysfunction occurs more evenly across the retina.

Much remains to be understood concerning the aetiology of RP. It is not known why degeneration initiates in the far- or mid-periphery or why it spreads. Many of the RP-causing mutations have yet to be identified. Amongst those mutations that have been identified the ma-

jority are expressed solely by rods (Hamel, 2006; Hartong et al., 2006), though it is often not clear why these mutations should lead to rod death. Since cones do not generally express the mutant gene and their death proceeds secondarily to rod death, either cones must depend upon rods in some direct or indirect fashion, or the death of rods must set in motion other events which lead to cone death. Since cone loss (and secondary rod loss in humans) is largely independent of the disease-causing mutation and since it is the loss of cones that causes the most serious visual impairment, we will focus our attention upon secondary cone (and rod) loss. As a consequence, our models will be applicable to most forms of RP and not only to forms caused by particular mutations.

The reasons for the differences in disease progression between animal and human models have yet to be determined. The differences may be due in part to differences in eye size, the distribution and density of rods and cones, the ratio of rods to cones or the retinal architecture. Indeed, most animal retinas have a lower cone density and lack a cone-rich macula region (Tso et al., 1997). Wright et al. (2004) found that rates of neurodegeneration amongst mammals 'are strongly correlated with maximum lifespan potential and rates of formation of mitochondrial reactive oxygen and nitrogen species (RONS)'. Noting that cellular stresses are integrated by mitochondria to determine the time of cell death, they have made the intriguing suggestion that the greater production of RONS in the mitochondria of shorter lived species increases the probability of cell death and is thus chiefly responsible for the higher rate of neurodegeneration in these species.

1.3.4 Visual Fields

Grover et al. (1998) measured the visual fields of 162 patients using Goldman perimetry over a period of at least 3 years each. They identified three characteristic patterns of visual field progression.

Pattern 1 A concentric loss of visual field (vision loss starts at the periphery and progresses inward, see Figure 1.9(1A)). This is sometimes accompanied by a perifoveal or parafoveal ring scotoma (see Figure 1.9(1B)).

Pattern 2 Either an initial nasal or superior nasal restriction from which an arcuate (bow shaped) scotoma winds inferiorly through the mid-periphery from the nasal side (Figure 1.9(2A)), or a superior temporal (Figure 1.9(2C)) or complete temporal (Figure 1.9(2B)) restriction, from which an arcuate scotoma winds inferiorly through the mid-periphery from the temporal side. In each case both the central and inferior peripheral visual fields are preserved. Peripheral vision is then lost, leaving only a central island of vision.

Pattern 3 A complete or partial mid-peripheral ring scotoma develops. This then expands into the superior (more often) or inferior periphery leaving a central island of vision, together with a U- or n-shaped peripheral visual field. Lastly the arms of the 'U' or 'n' retract from both sides until the peripheral field is lost leaving only a central visual field (Figure 1.9(3)).

It was found that the pattern of visual field loss was the same within families and that some genetic subtypes tended to result in a particular pattern of visual field loss. It was also noted that, in most cases, visual field loss occurs at the margins of the remaining visual field. In Chapter 5 we compare the patterns of degeneration predicted by our model with these *in vivo* patterns of visual field loss, to test the explanatory power of the oxygen toxicity hypothesis (see below).

1.3.5 Hypothetical Mechanisms for Secondary Cone Loss

Thus far, four main hypotheses have been proposed to explain cone loss:

1. the oxygen toxicity hypothesis;
2. the rod trophic factor hypothesis;
3. the rod toxic substance hypothesis;
4. the microglia hypothesis.

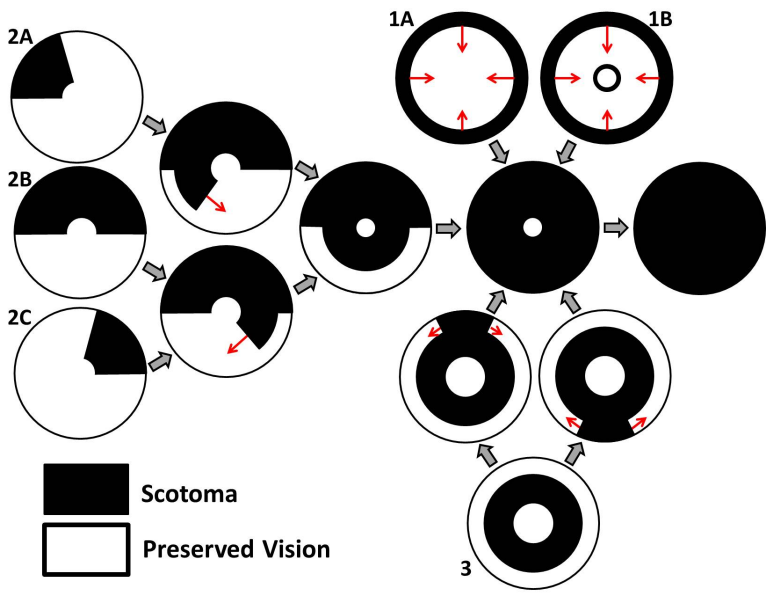

Figure 1.9: Diagram to show the patterns of visual field loss described by Grover et al. (1998). Black regions represent scotomas and white regions areas of preserved vision. See text for details.

In addition to explaining secondary cone loss, these hypotheses may also help to explain the loss of both rods and cones during the expansion of degenerate patches in human RP. We describe the latter three hypotheses below, delaying description of the first to the next section.

Rod photoreceptors are known to release trophic factors that are essential for cone viability (Mohand-Saïd et al., 1997, 1998, 2000; Fintz et al., 2003). Rod loss removes the source of these factors, leading to cone degeneration. One such factor, rod-derived cone viability factor (RdCVF), identified by Léveillard et al. (2004), was shown to slow cone degeneration in both chick and mouse models. Further support for this hypothesis has been provided by Camacho et al. (2010)'s mathematical model of photoreceptor interactions, which suggests that the interaction of rods and cones via rod trophic factor is vital to the survival of both (see Section 1.3.8). The chief weaknesses of this hypothesis are its inability to explain the survival of cones, in animal models, long after all rods have been lost and the preservation of the cone-rich fovea in humans.

Another mechanism by which rod cell death may lead to cone cell death is via the release of toxic substances by dying rods. These toxic substances are usually assumed to be released into the interphotoreceptor matrix; however, Ripps (2002) has suggested that they may be transmitted to healthy cones via gap junctions. This hypothesis could account for the relative sparing of cone photoreceptors in the foveal area, as cones in this area are likely to be less extensively coupled to rods (Ripps, 2002). If gap junctions between rods and cones express a directional selectivity (favouring the rod to cone direction) this may also explain why rod function is lost at a slower rate in cone-rod dystrophies than cone function is lost in rod-cone dystrophies (Ripps, 2002). Despite its potential, Ripps' hypothesis is now in doubt, following Kranz et al. (2013)'s study, in which the apparent disruption of gap junctions had no effect on disease progression in transgenic mice. Also, as with the trophic factor hypothesis, the toxic substance hypothesis fails to account for the preservation of cones long after complete rod loss in animal models.

Lastly, it has been suggested by Gupta et al. (2003) that cone degeneration could be caused by activated microglia cells. Under normal conditions microglia exist in a quiescent state in the inner layers of the retina. However, following activation by rod degeneration, they migrate to the outer retina where they phagocytose rod cell debris. By analogy with microglia in the central nervous system, it is hypothesised that activated microglia may release cytotoxic factors, such as nitric oxide, that kill nearby photoreceptors, including cones. Whilst this hypothesis might account for the sparing of cones in the fovea, it shares the weakness of the previous two hypotheses, in not explaining why cones remain in rod-free retinas in animal models.

Each of these four hypotheses can explain certain aspects of RP progression; however, it is unclear which, if any of them, is sufficient to explain all aspects. These hypotheses are not mutually exclusive and are probably best thought of as complimentary. It may be that all, or a combination of them, regulate RP progression, or that other mechanisms, as yet unknown, play a part.

A logical first step is to test these hypotheses in isolation from one another, to determine whether any one of them is sufficient to explain the spatio-temporal pattern of RP progression. To date, only the trophic factor and toxic substance hypotheses have received attention from the mathematical community (see Section 1.3.8). Of the remaining two hypotheses, the oxygen toxicity hypothesis is by far the most promising, both in terms of experimental evidence and explanatory power. It is upon this hypothesis that we shall now focus.

1.3.6 The Oxygen Toxicity Hypothesis

The oxygen toxicity hypothesis was first suggested by Travis et al. (1991) and later developed by Valter et al. (1998) and Stone et al. (1999). Following the loss of photoreceptors, the oxygen demand in the outer retina is significantly decreased, resulting in an increase in outer retinal oxygen concentrations (Stone et al., 1999; Yu et al., 2000, 2004; Padnick-Silver et al., 2006). This, combined with the shortening of the photoreceptor OSs, brings the remaining rod and cone ISs into a toxic environment (Travis et al., 1991; Stone et al., 1999). This results in a positive feedback loop, as high oxygen levels cause photoreceptor death, which in turn leads to an increase in oxygen levels (see Figure 4.2). Thus, the second stage of photoreceptor death is 'self-reinforcing' and continues until all photoreceptors are lost (Stone et al., 1999). The most severe oxidative damage probably occurs under LA, since oxygen levels are higher under LA (Wellard et al., 2005).

A powerful case can be constructed to support the oxygen toxicity hypothesis. Yu et al. (2000, 2004) and Padnick-Silver et al. (2006) have shown that oxygen levels rise in the outer retina in RP following photoreceptor degeneration, but that the inner retina maintains roughly normal oxygen levels and oxygen uptake (see also Yu and Cringle, 2001, 2005, for reviews). The choroid autoregulates poorly in response to changes in oxygen concentration, explaining the rise in outer retinal oxygen levels, whilst the maintenance of inner retinal oxygen levels is explained by the constriction and degeneration of the retinal capillaries (Yamada et al., 1999; Yu et al., 2000; Padnick-Silver et al., 2006; Ma et al., 2012; Mullins et al., 2012), their behaviour providing further evidence for hyperoxia. A number of studies have suggested that

RP protects against diabetic retinopathy, a disease thought to be driven by hypoxia (Arden, 2001). This again suggests that RP causes hyperoxia.

Valter et al. (1998) and Stone et al. (1999) have shown, using transgenic mouse and rat models, that hypoxia (a reduced oxygen supply) slows and hyperoxia (an increased oxygen supply) accelerates retinal degeneration when applied after an early critical developmental period, whilst Yamada et al. (2001); Okoye et al. (2003); Wellard et al. (2005) have shown, using mouse and rat models, that hyperoxia results in photoreceptor cell death, with the mid-periphery being the most vulnerable region.

The case that hyperoxia plays a role in the progression of RP is further strengthened by consideration of the mechanisms via which it causes damage to retinal cells. It is vital to the health of a cell that the balance between oxidizing agents and reducing agents, termed the redox potential, be maintained at a particular level (Kohen and Nyska, 2002). Hyperoxia results in an increase in oxidizing agents, often called reactive oxygen species (ROS), upsetting this balance, and resulting in oxidative stress and damage to cells (Kohen and Nyska, 2002). Mitochondria are the chief producers of oxidants, which play an important role in both ageing and degenerative diseases (Ames et al., 1995).

Shen et al. (2005) have shown that cones suffer oxidative damage to lipids, proteins and DNA in an RP (Pro347Leu) model in the pig. It was found that damage was greatest in the ISs and OSs and in particular within, and in the neighbourhood of, the mitochondria, which are located in the apical region of the ISs (Shen et al., 2005). This is consistent with the observation (noted above) that outer retinal oxygen levels rise, but inner retinal oxygen levels and uptake remain constant, following photoreceptor degeneration. Further evidence that oxidative damage leads to photoreceptor death was provided by Cingolani et al. (2006) by injecting the ROS producing chemical paraquat into the mouse vitreous. In this case, since ROS were no longer localised to the outer retina, inner retinal degeneration was also observed (Cingolani et al., 2006).

Oxidative damage may be increased in patients with RP mutations that disrupt the phagocytosis of shed OSs by the RPE, removing or decreasing the ability of photoreceptors to re-

move photo-oxidative products via this process (Tsuruma et al., 2012). Light irradiation may also increase oxidative stress and cause the rate of phagocytosis to decrease (Tsuruma et al., 2012).

Though it has been shown that hyperoxia can cause damage to and loss of photoreceptors, it is important to note that the ranges of oxygen concentrations under which different retinal cell types can remain healthy is still unknown (Yu and Cringle, 2005).

Antioxidants (reducing agents), both endogenous and exogenous, protect retinal cells from oxidative damage by neutralising ROS (Kohen and Nyska, 2002). Antioxidants have proven to be effective in reducing retinal damage in mouse models carrying RP genes (Komeima et al., 2006, 2007; Sanz et al., 2007). This both strengthens the case that the second stage of photoreceptor degeneration is due to oxygen toxicity and suggests a potential treatment strategy (Dong et al., 2006; Komeima et al., 2006, 2007; Sanz et al., 2007).

In order to be effective, it is important that antioxidants be present in the right locations, at the right times and in sufficiently high concentrations to prevent damage by ROS (Kohen and Nyska, 2002; Dong et al., 2006; Komeima et al., 2007). If this is not the case then oxidative damage will accumulate and cannot be undone by subsequent treatment with antioxidants (Ames et al., 1993, 1995; Kohen and Nyska, 2002). Shen et al. (2005) suggest that differences in the rate of disease progression could be explained by differences in the action of antioxidant enzymes (due to polymorphisms) or differences in the dietary intake of antioxidants.

In addition to antioxidants, the retina also produces trophic factors to protect against oxidative stress. The trophic factors produced in the retina include basic fibroblast growth factor (bFGF/FGF2), glial fibrillary acidic protein (GFAP), fibroblast growth factor 1 (FGF1), ciliary neurotrophic factor (CNTF) and brain-derived neurotrophic factor (BDNF) (Okoye et al., 2003; Yu et al., 2004). It has been shown that various combinations of these trophic factors are upregulated, and may improve photoreceptor survival and preserve photoreceptor function in rat and mouse models either expressing RP genes or in which hyperoxia has been induced (Yamada et al., 2001; Okoye et al., 2003; Yu et al., 2004).

A promising treatment strategy might be to use antioxidant and trophic factor treatments

together, the antioxidants neutralising the ROS and the trophic factors increasing photoreceptor resistance to apoptosis (Komeima et al., 2006, 2007), by activating antiapoptotic pathways for instance (Yu et al., 2004). Trophic factors may be delivered either via an intravitreal or subretinal injection, or using an implantable device for long term delivery (e.g. encapsulated cell therapy, Musarella and MacDonald, 2011), whilst antioxidants could be upregulated using ocular gene therapy (OGT, Orosz et al., 2004; Dong et al., 2006).

If oxidative stress causes cumulative damage, then one might expect the kinetics of cell death to be cumulative, with the risk of cell death increasing over time. Contrary to this expectation, Clarke and Lumsden (2005b) have shown that animal models of RP (including cats, dogs, mice and rats) have stretched exponential kinetics[1], indicating a constant (in time) risk of degeneration, where this risk may vary between cells (see also, Clarke et al., 2000; Clarke and Lumsden, 2005a). However, this does not rule out the oxygen toxicity hypothesis, as the stress induced upregulation of antioxidants and trophic factors may slow the disease progression, thus maintaining a constant risk of cell death (Yu et al., 2004). Additionally, photoreceptor kinetics are unlikely to fit a stretched exponential model in humans, since the pattern of degeneration is more spatio-temporally heterogeneous, progressing via the expansion of existing patches of loss. In this case, the risk of cell death at a particular location will increase over time when the death of neighbouring photoreceptors causes the local environment to become hyperoxic. Here hyperoxia caused cell death is local and rapid, rather than global and gradual as in animals.

Studies using human epithelial cells (Wang et al., 2003) and rd1 mouse photoreceptors (Sahaboglu et al., 2013) show that cells take about 72 hours to die from hyperoxia. A rough calculation shows that this corresponds to a timescale of decades for degeneration to spread across the retina, which is consistent with the timescale for degeneration in humans (Hartong et al., 2006).

Only one result appears to directly conflict with the oxygen toxicity hypothesis. It was

[1]These are given by the stretched exponential, or Kohlrausch-Williams-Watts (KWW) function: $N(t) = N_0 \exp[-(t/\tau_{KWW})^{\beta}]$, where $N(t)$ is the number of neurons at time t, N_0 is the initial neuron population, τ_{KWW} is the characteristic timescale of the decay process and β is a shape parameter (Clarke and Lumsden, 2005b).

found by Vingolo et al. (1999, 2008) that humans treated with hyperbaric oxygen (HBO) therapy (which results in a period of increased oxygen delivery to the retina) preserves visual fields and results in a mean improvement in ERG responses. On the oxygen toxicity hypothesis we would have expected vision to deteriorate more rapidly. It may be that the transient challenge to the system posed by HBO results in a prolonged upregulation of trophic factors or endogenous antioxidants, leading to a net preservation of vision. Further experimental work is required to test this hypothesis.

1.3.7 Treatment Strategies

Whilst RP is currently incurable, a number of treatment strategies are being developed either to restore or prevent the loss of visual function. These strategies include light protection, vitamin therapy, trophic factors, antioxidants, OGT, retinal transplantation, stem cells, drug delivery and retinal implants (Shintani et al., 2009; Musarella and MacDonald, 2011; Barry et al., 2012; Kaplan and Fernandez de Castro, 2012; Kusnyerik et al., 2012; Yin and Li, 2012).

1.3.8 Previous Mathematical Models

To date, there has been relatively little modelling work concerning either retinal degeneration in general or RP in particular. Camacho et al. (2010) produced a dynamical systems model, formulated as a system of ordinary differential equations (ODEs) for rods, cones and trophic pool, in which photoreceptors convert nutrients from the trophic pool into new OS discs, which are continuously shed, whilst rods contribute to cone health via a direct supply of RdCVF, at no cost to themselves. The model exhibits stable oscillations, corresponding to the rhythmic shedding and renewal of photoreceptor OSs and provides support for the claim that RdCVF is necessary for the survival of both rods and cones. Camacho and Wirkus (2013) extend this model to describe RP, including a fourth compartment for mutant rods. Using bifurcation theory, they determine the different paths that may be traced through various physiological states on the way to total blindness (see also Colón Vélez et al., 2003). This RP model was further

extended by Camacho et al. (2014), by applying optimal control theory, enabling optimal treatment strategies to be determined. Whilst these models have proven effective in capturing the local interaction between rods and cones, they do not include any form of spatial dependence and are thus unable to explain or predict the spatio-temporal pattern of RP progression.

Clarke et al. (2000, 2001) and Clarke and Lumsden (2005a,b) have suggested a one-hit model of neuronal cell death for a variety of conditions including RP. According to this model the time point at which any neuron dies is random (Clarke et al., 2000). This is based upon the observation that the kinetics of cell death are most consistent with models in which the risk of cell death is either constant or decreases exponentially with age (Clarke et al., 2000). This is explained at the biochemical level by the mutant steady-state (MSS) hypothesis, which suggests that mutations result in elevated levels of a pre-apoptotic compound, placing it closer to a critical threshold, above which apoptosis is induced (Clarke et al., 2001). Random fluctuations in the concentration of this compound may cause it to exceed this threshold, resulting in cell death (Clarke et al., 2001).

The MSS hypothesis was incorporated into a spatially explicit 1D model, consisting of a pair of partial differential equations (PDEs), in which a diffusible toxic factor, produced by dying photoreceptors, upregulates the production of pre-apoptotic factors in the surrounding photoreceptors (Burns et al., 2002). This model was able to replicate the patchy photoreceptor loss observed in the early stages of RP and predicted an exponential decline in photoreceptor number over the lifetime of the disease, in agreement with Clarke et al. (2000), provided cell death times were exponentially distributed. Whilst this model accounts for the spatial spread of photoreceptor degeneration, it does not take into account the distribution of photoreceptors, nor does it distinguish between rods and cones. It also fails to replicate, and hence explain, the spatio-temporal pattern of photoreceptor degeneration in humans.

More recently, Lomasko et al. (2007a,b) and Lomasko and Lumsden (2009) have constructed stochastic models of cytoskeleton-induced neuron death, extending the work of Burns et al. (2002). These papers do not have the retina specifically in mind and so are less relevant to the present work; however, it is worth noting that they also replicate the exponential and

sigmoidal patterns of cell loss measured by Clarke et al. (2000).

Till et al. (2003) developed a model to describe laser-induced thermal damage in the retina. The model is initially formulated as a system of ODEs, describing the formation of free radicals and the accumulation of damage, from which expressions are derived to determine the width of the degenerate patch that will result from a given laser pulse. The model's dependence on the artificial nature of the initial cause of degeneration limits its applicability to this study; however, free radical dynamics of the type described in this model could be incorporated into a more biochemically detailed model of hyperoxia induced photoreceptor degeneration.

Lastly, Tayyab et al. (2009) conducted a brief study of RP in which they propose combining image processing and neural networks modelling, in an effort to understand the differences between the ways in which rod and cone function are affected by the disease. To the best of our knowledge, this work has not been continued.

In Chapters 4 and 5 we construct spatially explicit PDE models in 1D and 2D, on domains spanning the region between the foveal centre and the ora serrata. These models are the first to account for the heterogeneous distribution of rods and cones within the retina, to model RP in 2D and to consider the oxygen toxicity hypothesis and its associated treatment strategies. Our models also distinguish between rods and cones where necessary.

1.4 Additional Mathematical Models of the Retina

In addition to the mathematical models described in Sections 1.2.3 and 1.3.8, there have been several other modelling studies of the retina. Some representative highlights are included below.

Pearlman (1979) used linear regression analyses to compare the rate of visual loss between genetic variants of RP. No statistically significant differences were found.

Maggelakis and Savakis (1996, 1999) used 1D PDE models to describe abnormal capillary growth due to hypoxia in proliferative retinopathy.

Recently, two models have been developed by Aubert et al. (2011) and McDougall et al.

(2012); Watson et al. (2012) to describe the development of murine superficial retinal vasculature. The first is a PDE model in 1D (Aubert et al., 2011) and the second, which builds on the first, is a more comprehensive hybrid discrete-continuum model in 2D (McDougall et al., 2012; Watson et al., 2012). Both models show excellent quantitative agreement with experimental data and the second may be used to model disease states involving aberrant angiogenesis, such as macular degeneration.

Liu et al. (2009) have constructed a model of the flow distribution and oxygen transport within a 2D retinal arterial network. Whilst this model considers the oxygen concentration internal to the arterioles it does not describe the oxygen concentration in the surrounding retinal tissue.

Ganesan et al. (2010a,b) created a network model of the murine (mouse/rat) retinal vasculature. It was found that the blood hematocrit (the ratio of red blood cell volume to total blood volume) is smaller close to the optic disc and greater toward the periphery. This is of relevance in considering the site of initiation of RP under the oxygen toxicity hypothesis.

Camacho et al. (2004) developed a dynamical systems model to describe the circadian rhythms in the quantity of melatonin in the eyes (melatonin has been shown to protect against oxidative stress, Beyer et al., 1998). The model consists of two van der Pol oscillators (the left and right eyes) coupled via a bath (the bloodstream).

There have also been a number of computational models of retinal mosaic formation (see Eglen, 2006, for a review).

Lastly, Keener and Sneyd (1998) summarise a number of simple mathematical models of the retina describing such features as retinal light adaptation, photoreceptor physiology (specifically the biochemical events involved in phototransduction, see also, Sneyd and Tranchina, 1989; Tranchina et al., 1991), photoreceptor and horizontal cell interactions, and receptive fields. The reader is referred to the aforementioned text for further details.

1.5 Thesis Aims and Outline

In this thesis we use mathematical models to investigate the behaviour of the retina in health and disease. In the healthy case we aim to assess the effectiveness of Ngb in oxygen transport and storage, whilst in the diseased case we isolate hyperoxia as a prospective causative mechanism behind the spread of photoreceptor degeneration in RP, exploring the extent to which this mechanism alone can explain the *in vivo* dynamics and assessing possible treatment strategies.

The remainder of this thesis is structured as follows.

In Chapter 2, we develop a single layer model in 1D, investigating the capacity of Ngb to transport and store oxygen and hence to prevent hypoxia. The model is formulated as a system of four reaction-diffusion PDEs (for oxygen and the various states of Ngb) and is solved using the method of lines and the finite element method. It is found that Ngb may play a significant role in transport, but not in storage. We also perform an analysis of a simplified version of this model, challenging the prevailing assumption that Ngb's low oxygen affinity decreases its ability to transport oxygen and showing that it is in fact near optimal for this process.

In Chapter 3, we extend the model from Chapter 2, decomposing the domain into eight layers, spanning the full width of the retina between the RPE and the ILM. We use this model to explore Ngb's role in oxygen transport and storage in a physiologically human retina, solving the equations using the method of lines and the finite element method. As with the single layer model, we find that Ngb may be effective in transport, but not in storage. We also perform an asymptotic analysis of a Ngb-free model to determine the conditions under which the common assumption of piecewise constant oxygen uptake is valid. It is found that the assumption is valid, provided oxygen levels do not become near hypoxic. When this is the case, a quadratic may still be used for the oxygen profile; however, the coefficients must be modified in ways that we describe.

In Chapter 4, we use a 1D model to investigate the effect of hyperoxia on the progression of retinal degeneration in RP. In the first instance, the model is formulated as a system of two PDEs, for oxygen concentration and photoreceptor density. This is later extended to

three PDEs, the equation for photoreceptor density being replaced by separate equations for rod and cone density. The equations are defined on a domain spanning the region between the foveal centre and the ora serrata, and are solved using the method of lines. We also use asymptotic analyses to elucidate the behaviour of the system. We determine conditions under which degeneration will spread or remain stable, the qualitative dependence of the wave speed of degeneration upon local photoreceptor density and the effects of antioxidants and trophic factors in the treatment of RP.

It is found that the retina may be divided into a series of stable and unstable regions. Our model predicts that patches of photoreceptor loss will spread when one of their margins lies in an unstable region, but will remain stationary when both margins lie in stable regions. The wave speed of degeneration is faster in regions with a lower local photoreceptor density, whilst treatment with antioxidants and trophic factors may delay, halt, or partially reverse photoreceptor degeneration according to modelling predictions.

In Chapter 5, we extend the model from Chapter 4 in two ways. In the first case we include degeneration of the CC, exploring how this modifies the progression of hyperoxia driven degeneration. This involves the addition of a PDE for capillary surface area per unit volume, enlarging the system to three or four PDEs, depending upon whether rods and cones are taken together or separately (see above). We solve these equations using the method of lines and perform an asymptotic analysis to determine the conditions under which degeneration will spread. In the second case we expand the original 1D model into 2D, investigating the range of spatio-temporal patterns of degeneration that can be generated and comparing these with *in vivo* observations. The 2D system is solved using the finite element method, on a spherical surface, spanning the region between the foveal centre and the ora serrata.

Our results show that a region of capillary loss must be essentially coincident with a patch of photoreceptor loss in order to prevent the spread of degeneration, in those cases where degeneration would spread in the absence of capillary loss. Also, the dynamic loss of capillaries in response to photoreceptor loss may result in the delay, halt or partial reversal of photoreceptor degeneration. The 2D model replicates a number of the *in vivo* patterns of de-

generation, though some patterns are inaccessible to it, indicating that additional mechanisms are involved.

Lastly, in Chapter 6, we summarise our findings and suggest directions for future research.

Chapter 2

Retinal Oxygen Distribution and the Role of Neuroglobin: Single Layer Model

In this chapter, and that which follows, we construct reaction-diffusion models for retinal oxygen distribution and use them to examine the role of the protein neuroglobin (Ngb) in the prevention of hypoxia. Here we consider a (toy) model consisting of a single cellular layer, supplied at one end by a capillary bed, whilst in the following chapter we examine a more detailed and realistic eight layer model, spanning the region between the choriocapillaris (CC) and the inner limiting membrane (ILM), capturing the physiology of the human retina.

2.1 Introduction

The retina is the ocular tissue which detects visual information. It has a high oxygen demand (Anderson and Saltzman, 1964; Anderson, 1968; Yu and Cringle, 2001; Wangsa-Wirawan and Linsenmeier, 2003) placing it in danger of hypoxia (oxygen deprivation), despite being well vascularised.

The retina is the innermost layer of tissue in the eye, occupying the region between the optic disc and the ora serrata (see Figure 1.1(a)). It contains four layers of cells, which extend between the CC and the ILM, where it meets the vitreous (see Figure 1.1(b) and Figure 1.3).

The CC is the capillary bed which supplies the outer retina with oxygen, whilst the inner retina is supplied by the retinal capillaries, which form part of a separate vascular system.

Measurements of the oxygen distribution across the macaque retina (which is physiologically similar to that of humans) show that both the inner and outer retina are in danger of hypoxia under dark conditions (dark adaptation, DA), during which the rate of oxygen uptake by the photoreceptor inner segments is twice that under light conditions (light adaptation, LA, Birol et al., 2007). Hypoxia is detrimental to cells, both in limiting oxidative metabolism and in increasing the production of reactive oxygen species (ROS), upsetting the redox potential and leading to oxidative stress and damage (Kohen and Nyska, 2002). Thus any factor with the potential to promote retinal oxygenation may be vital in preventing retinal hypoxia and hence cell death.

In 2000, Burmester et al. discovered a new vertebrate globin protein which they named neuroglobin because of its preferential expression in the cells of the nervous system, including the retina. Ngb has a similar structure and molecular mass to that of myoglobin (Mb) (Burmester and Hankeln, 2009) and, as such, it has been proposed that Ngb, like Mb, may play a role in oxygen transport and storage (Burmester et al., 2000; Burmester and Hankeln, 2004, 2009).

Despite its oxygen binding properties, it is unclear whether Ngb plays a significant role in oxygen transport and storage, and opinion as to the main function of Ngb remains divided (Burmester and Hankeln, 2009, see Section 1.2.2 for more details and Section 1.2.3 for a review of previous mathematical modelling work in this area). In particular, it has been thought that Ngb's oxygen affinity is too low to allow for effective transport, a conclusion which we challenge in Section 2.4. The analysis in Section 2.4 is similar to that of the problem involving the facilitated diffusion of oxygen by Mb in a slab reactor considered in Chapter 2 of Keener and Sneyd (1998), the main difference being that Keener and Sneyd's equations lack an oxygen uptake term.

In this chapter, and that which follows, we investigate the possible role of Ngb in oxygen transport and storage in the human retina. The questions we wish to address are as follows:

could Ngb prevent tissue hypoxia by transporting oxygen from regions of high oxygen tension to regions of low oxygen tension, or by providing a temporary store of oxygen during a period when oxygen is scarce?

We derive two models for the concentration of oxygen and Ngb across the retina. The first model, described in the present chapter, treats the retina as a single cell layer, whilst the second model, treated in the next chapter, captures details of its structure and geometry by decomposing it into four cell layers, spread across eight model layers. The first model is used to ascertain, for a general case, whether Ngb could play a significant role in oxygen transport and storage. Its simplicity renders it analytically tractable and enables us to generate important insights into the affect of Ngb's oxygen affinity upon its transport properties. The second model is used to investigate Ngb's role in a geometry that more accurately approximates that of the human retina.

We develop time-dependent and time-independent (steady-state) versions of each of these models. The time-dependent versions are used to investigate the oxygen storage properties of Ngb, whilst the steady-state versions are used to investigate the oxygen transport properties of Ngb.

The remainder of this chapter is structured as follows. In Section 2.2 we derive time-dependent and steady-state models on a single layer geometry for the dynamics of oxygen and Ngb within the retina. In Section 2.3 we present some numerical results for the time-dependent and steady-state models. In Section 2.4 we perform a mathematical analysis of a simplified version of the steady-state model. Lastly, in Section 2.5, we summarise our findings and discuss their implications.

2.2 Model Formulation

In this section we derive a model to describe oxygen and Ngb dynamics on a single layer geometry. Before doing this, it is necessary to understand the kinetics of Ngb.

2.2.1 Neuroglobin Kinetics

Ngb is a 'hexacoordinate' globin, with the sixth coordination position of the heme group occupied by an internal histidine molecule in the absence of an external ligand (Burmester and Hankeln, 2004, 2009; Fago et al., 2004b). This means that in order for oxygen to bind to Ngb, the histidine molecule must first unbind from the heme group.

Writing C, N, N_H and N_O for oxygen, Ngb (pentacoordinate Ngb), Ngb-His (hexacoordinate Ngb) and Ngb-O_2 (oxygen-bound Ngb) respectively, the reaction scheme may be written as

$$\mathrm{N} \underset{\mathrm{k_h}^-}{\overset{\mathrm{k_h}^+}{\rightleftharpoons}} \mathrm{N_H}, \tag{2.1}$$

$$\mathrm{N} + \mathrm{C} \underset{\mathrm{k_o}^-}{\overset{\mathrm{k_o}^+}{\rightleftharpoons}} \mathrm{N_O}, \tag{2.2}$$

where $\mathrm{k_h^+}$, $\mathrm{k_h^-}$, $\mathrm{k_o^+}$ and $\mathrm{k_o^-}$ are the forward and reverse rate constants for the different reactions (see Table 2.1 for values).

2.2.2 Time-Dependent Model

We begin by formulating a system of four partial differential equations (PDEs) for the concentrations of O_2, $c(x,t)$, Ngb, $n(x,t)$, Ngb-His, $n_h(x,t)$ and Ngb-O_2, $n_o(x,t)$, on a one-dimensional domain $x \in (0,L)$ and for time $t \in (0,\infty)$. We choose a domain orientation perpendicular to the wall of the eye, which cuts across the retinal layers, starting at $x = 0$, where the retinal pigment epithelium (RPE) meets the CC and ending at $x = L$, at the ILM, where the retina meets the vitreous humour (see Figure 2.1).

Using the principle of mass balance and applying the law of mass action to the reaction scheme (2.1)–(2.2), we derive the following PDE for oxygen,

$$\frac{\partial c}{\partial t} = \underbrace{D_o \frac{\partial^2 c}{\partial x^2}}_{\text{diffusion}} - \underbrace{\frac{Qc}{\gamma + c}}_{\substack{\text{uptake by} \\ \text{retinal tissue}}} + \underbrace{k_o^- n_o - k_o^+ nc}_{\substack{\text{unbinding from and} \\ \text{binding to Ngb}}}, \tag{2.3}$$

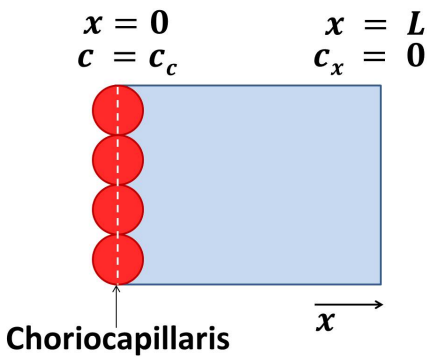

Figure 2.1: Single layer model diagram. Oxygen is supplied to the tissue via the choriocapillaris at $x = 0$ and the net-flux of oxygen at $x = L$ is zero.

where D_o is the oxygen diffusion coefficient, which is assumed to be constant (Roh et al., 1990). The rate of oxygen uptake is known to be near constant above hypoxic levels, but falls rapidly to zero as oxygen levels fall below a critical oxygen concentration (Goldman, 2008). Since we are interested in the role of Ngb in preventing tissue hypoxia, it is important that our oxygen uptake term captures this concentration dependence (Goldman, 2008). Thus we use a Michaelis-Menten term for the oxygen uptake (see Wilson et al., 1988; Costa et al., 1997), where Q is the maximum rate of oxygen uptake by the retinal tissue (achieved in the limit as $c \to \infty$) and γ is the Michaelis constant, the concentration of oxygen at which the rate of oxygen uptake is $Q/2$. The inclusion of oxygen dependence in the uptake term represents an important difference between this model of retinal oxygen distribution and most existing ones (see, for example, Dollery et al., 1969; Stefánsson, 1988; Haugh et al., 1990; Linsenmeier and Braun, 1992; Braun et al., 1995; Cringle and Yu, 2002; Yu and Cringle, 2002, an exception being Fago et al. 2004b). We also interpret γ as being the *hypoxic threshold*: regions in which oxygen concentrations drop below this value are considered to be hypoxic (Richmond et al., 1999; McGuire and Secomb, 2001, see also Appendix A.10 for further details).

Proceeding similarly, we derive PDEs for Ngb (n), Ngb-His (n_h), and Ngb-O_2 (n_o),

$$\frac{\partial n}{\partial t} = D_n \frac{\partial^2 n}{\partial x^2} + k_h^- n_h + k_o^- n_o - k_h^+ n - k_o^+ nc, \tag{2.4}$$

$$\frac{\partial n_h}{\partial t} = D_n \frac{\partial^2 n_h}{\partial x^2} + k_h^+ n - k_h^- n_h, \tag{2.5}$$

$$\frac{\partial n_o}{\partial t} = D_n \frac{\partial^2 n_o}{\partial x^2} + k_o^+ nc - k_o^- n_o. \tag{2.6}$$

In (2.4)–(2.6) we assume that the diffusion coefficients for Ngb, Ngb-His and Ngb-O_2 are identical, since they are almost identical in molecular weight and structure (see Keener and Sneyd, 1998, where a similar assumption is made about Mb).

We close equations (2.3)–(2.6) by imposing the following initial and boundary conditions:

$$c(x,0) = c_{init}(x),\ n(x,0) = n_{init}(x),\ n_h(x,0) = n_{h_{init}}(x),\ n_o(x,0) = n_{o_{init}}(x), \tag{2.7}$$

$$\begin{aligned} c(0,t) = c_c,\ \frac{\partial n}{\partial x}(0,t) = \frac{\partial n_h}{\partial x}(0,t) = \frac{\partial n_o}{\partial x}(0,t) = 0, \\ \frac{\partial c}{\partial x}(L,t) = \frac{\partial n}{\partial x}(L,t) = \frac{\partial n_h}{\partial x}(L,t) = \frac{\partial n_o}{\partial x}(L,t) = 0. \end{aligned} \tag{2.8}$$

In (2.8), c_c is the oxygen concentration in that part of the retina which abuts the CC. We use a Dirichlet boundary condition at $x = 0$, rather than a Robin boundary condition, since the fenestrated capillaries of the CC are highly permeable to low molecular weight substances such as oxygen (Törnquist et al., 1990). For simplicity, the flux of oxygen at the ILM ($x = L$) is assumed to be zero. This is reasonable since the rate of oxygen consumption by the vitreous is negligible (Stefánsson, 1988; Cringle and Yu, 2002). We could alternatively have used Robin or Dirichlet boundary conditions; however, in the absence of better data, this added complexity is unjustified. Due to their size, Ngb, Ngb-His and Ngb-O_2 are unable to leave the cells of the retina and, hence, we impose zero-flux boundary conditions for these species at $x = 0, L$. See Table 2.1 for parameter values.

Table 2.1: Dimensional parameters associated with the single layer model (see equations (2.3)–(2.8)). Where two sets of units are stated, the first set was specified in the reference and the second, in brackets, uses units consistent with the dimensional model.

Parameter	Description	Value	Source
$\tilde{L}$	Minimum retinal width	80 μm	Webvision, `http://webvision.med.utah.edu/`
k	Oxygen solubility in retinal tissue	2.4×10^{-5} LO_2(L tissue·mmHg)$^{-1}$	(Linsenmeier and Braun, 1992)
$\tilde{c}$	Typical oxygen concentration at the choriocapillaris	60 mmHg (5.8×10^{-5} M)	(Wangsa-Wirawan and Linsenmeier, 2003) (Birol et al., 2007)
$\tilde{n}$	Average Ngb concentration across the retina	100 μM	(Schmidt et al., 2003)
D_o	Oxygen diffusion coefficient	1.97×10^{-9} m^{2}s^{-1}	(Roh et al., 1990)
D_n	Ngb diffusion coefficient	1.73×10^{-11} m^{2}s^{-1}	(Jürgens et al., 1994) (McGuire and Secomb, 2001)
L	Retinal width	80 to 320 μm	Webvision, `http://webvision.med.utah.edu/`
c_c	Oxygen concentration at the choriocapillaris	60 mmHg (typically) (5.8×10^{-5} M)	(Wangsa-Wirawan and Linsenmeier, 2003) (Birol et al., 2007)
n_T	Ngb concentration	0 to 4000 μM	(Schmidt et al., 2003, 2005) (Bentmann et al., 2005) (Ostojić et al., 2006, 2008) (Rajendram and Rao, 2007)
Q	Maximum rate of oxygen uptake	0 to 20 mlO_2(100g tissue·min)$^{-1}$ (0 to 1.33×10^{-4} Ms^{-1})	(Haugh et al., 1990; Cringle and Yu, 2002) (Wangsa-Wirawan and Linsenmeier, 2003) (Birol et al., 2007)
γ	Michaelis constant	1 mmHg (9.6×10^{-7} M)	(Costa et al., 1997; Richmond et al., 1999) (McGuire and Secomb, 2001) (Goldman, 2008)
k_o^+	Rate constant of oxygen binding to Ngb	1.7×10^8 M^{-1}s^{-1}	(Kiger et al., 2004)
k_o^-	Rate constant of oxygen dissociation from Ngb	0.7 s^{-1}	(Kiger et al., 2004)
k_h^+	Rate constant of histidine binding to Ngb	1800 s^{-1}	(Kiger et al., 2004)
k_h^-	Rate constant of histidine dissociation from Ngb	0.6 s^{-1}	(Kiger et al., 2004)

2.2.3 Non-dimensionalisation

To simplify the subsequent analysis, we recast the system in non-dimensional form, scaling the independent variables, dependent variables and initial conditions as:

$$x^* = \frac{x}{\tilde{L}}, \quad t^* = \frac{D_o}{\tilde{L}^2}t, \qquad c^* = \frac{c}{\tilde{c}}, \qquad n^* = \frac{n}{\tilde{n}}, \qquad n_h^* = \frac{n_h}{\tilde{n}}, \qquad n_o^* = \frac{n_o}{\tilde{n}},$$
$$c_{init}^* = \frac{c_{init}}{\tilde{c}}, \quad n_{init}^* = \frac{n_{init}}{\tilde{n}}, \quad n_{h_{init}}^* = \frac{n_{h_{init}}}{\tilde{n}}, \quad n_{o_{init}}^* = \frac{n_{o_{init}}}{\tilde{n}},$$

where $\tilde{L}$ is the minimum retinal width, $\tilde{c}$ is a typical oxygen concentration at the CC and $\tilde{n}$ is the average Ngb concentration across the retina (see Table 2.1). (We scale c and c_{init} with $\tilde{c}$, rather than c_c, and x and t with $\tilde{L}$, rather than L, so that results using different values of c_c and L can be compared more easily.) We define the following non-dimensional parameters:

$$L^* = \frac{L}{\tilde{L}}, \qquad c_c^* = \frac{c_c}{\tilde{c}}, \qquad D = \frac{D_n}{D_o}, \qquad Q^* = \frac{\tilde{L}^2}{D_o\tilde{c}}Q, \qquad \gamma^* = \frac{\gamma}{\tilde{c}},$$
$$\alpha = \frac{\tilde{c}}{\tilde{n}}, \quad k_1 = \frac{\tilde{L}^2\tilde{n}}{D_o}k_o^+, \quad k_2 = \frac{\tilde{L}^2\tilde{n}}{D_o\tilde{c}}k_o^-, \quad k_3 = \frac{\tilde{L}^2}{D_o}k_h^+, \quad k_4 = \frac{\tilde{L}^2}{D_o}k_h^-.$$

Dropping the stars, the system (2.3)–(2.6) becomes

$$\frac{\partial c}{\partial t} = \frac{\partial^2 c}{\partial x^2} - \frac{Qc}{\gamma + c} + k_2 n_o - k_1 nc, \tag{2.9}$$
$$\frac{\partial n}{\partial t} = D\frac{\partial^2 n}{\partial x^2} + k_4 n_h + \alpha k_2 n_o - k_3 n - \alpha k_1 nc, \tag{2.10}$$
$$\frac{\partial n_h}{\partial t} = D\frac{\partial^2 n_h}{\partial x^2} + k_3 n - k_4 n_h, \tag{2.11}$$
$$\frac{\partial n_o}{\partial t} = D\frac{\partial^2 n_o}{\partial x^2} + \alpha k_1 nc - \alpha k_2 n_o, \tag{2.12}$$

with initial and boundary conditions as in (2.7) and (2.8). See Table 2.2 for non-dimensional parameter values.

2.2.4 Steady-State Model

At steady-state, summation and integration of (2.10)–(2.12) subject to the zero-flux boundary conditions yields $n + n_h + n_o = \text{constant} = n_T$, where n_T, the total Ngb concentration, is given.

Table 2.2: Non-dimensional parameters associated with the single layer model (see equations (2.7)–(2.12)). (Values given to an accuracy of at most three significant figures.)

Parameter	Value
L	1 to 4
c_c	1
n_T	0 to 40
D	8.78×10^{-3}
Q	0 to 7.52
γ	0.017
α	0.58
k_1	55,200
k_2	3.95
k_3	5,850
k_4	1.95

Thus the total quantity of Ngb in its three forms is locally conserved across the domain. We use this identity to eliminate equation (2.10), writing $n = n_T - n_h - n_o$ in equations (2.9), (2.11) and (2.12), to obtain the steady-state boundary value problem:

$$0 = \frac{\mathrm{d}^2 c}{\mathrm{d}x^2} - \frac{Qc}{\gamma + c} + k_2 n_o - k_1 (n_T - n_h - n_o) c, \tag{2.13}$$

$$0 = D\frac{\mathrm{d}^2 n_h}{\mathrm{d}x^2} + k_3 (n_T - n_h - n_o) - k_4 n_h, \tag{2.14}$$

$$0 = D\frac{\mathrm{d}^2 n_o}{\mathrm{d}x^2} + \alpha k_1 (n_T - n_h - n_o) c - \alpha k_2 n_o, \tag{2.15}$$

for $c = c(x)$, $n_h = n_h(x)$ and $n_o = n_o(x)$, with boundary conditions as in (2.8).

2.3 Numerical Results

2.3.1 Steady-State Problem – Oxygen Transport

We begin by presenting results for the steady-state single layer problem, where we investigate the role of Ngb in oxygen transport. The equations for the steady-state model, (2.8) and (2.13)–(2.15), were solved using the finite element method (FEM), using piecewise linear

basis functions. We solved the resulting system of nonlinear algebraic equations using the Matlab routine fsolve, employing the Trust-Region-Dogleg algorithm. We use a finite element discretisation, rather than a finite difference discretisation, to facilitate future extensions to a 2D geometry. We validated our FEM solutions to the steady-state problem by checking that they matched the steady-state solutions to the time-dependent problem, (2.7)–(2.12), solved using the method of lines. In what follows, all variable and parameter values are given in their non-dimensional form, unless stated otherwise.

Figure 2.2 shows how increasing the total concentration of Ngb in the retina, n_T, affects the steady-state oxygen distribution. Increased Ngb levels result in a minor decrease in the oxygen concentration in the well oxygenated region of the tissue near $x = 0$, but a significant increase in the oxygen concentration near $x = L$. The decrease in oxygen concentration near the CC is insignificant since oxygen is rich here; however, the increase in oxygen concentration near $x = L$ represents a significant alleviation of hypoxia. Indeed, the oxygen concentration does not pass beneath the hypoxic threshold, γ, for $n_T \geq 12$, where $n_T = 16$ is the maximum biologically realistic value for a domain of this length.

Figure 2.3(b) shows the results for a sensitivity analysis of the single layer model. The parameters n_T, L, Q and c_c were varied over a range of biologically realistic values and the minimum oxygen concentration, $c_{min} = c(x = L)$, was plotted for each point in parameter space. Figure 2.3(a) demonstrates the structure of the plots in Figure 2.3(b). The plots are divided by a coarse grid over which n_T and Q vary in the x and y directions respectively. This coarse grid is then further sub-divided by a finer grid over which L and c_c vary in the x and y directions respectively. Thus, within each square of the coarse grid, that is for each point in (n_T, Q)-space, (L, c_c)-space is explored. In the left-hand plot of Figure 2.3(b) the effect of Ngb appears insignificant. The right-hand plot is a thresholded version of that on the left, with oxygen concentrations greater than or equal to γ set equal to γ. By looking along the rows of the coarse grid of this plot, it can be seen that an increase in Ngb concentration may prevent or significantly reduce tissue hypoxia in many regions of parameter space.

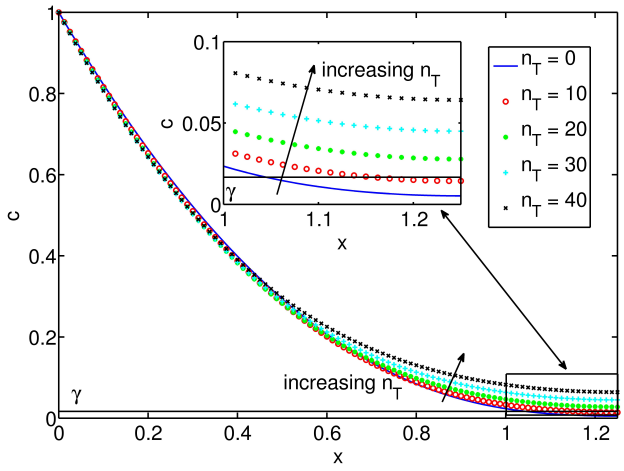

Figure 2.2: Simulation results from the steady-state single layer model. As the total concentration of Ngb, n_T, is increased, the steady-state oxygen concentration at $x = L$ increases above the hypoxic threshold, γ. Equations (2.8) and (2.13)–(2.15) were solved using the FEM with 101 mesh points. Parameter values: $L = 1.25$, $c_c = 1$ and $Q = 1.88$. Remaining parameter values as in Table 2.2.

2.3.2 Time-Dependent Problem – Oxygen Storage

In this section we investigate the effect of Ngb upon oxygen storage. We do this by making a step-change in a system parameter so that the steady-state concentration of oxygen decreases or increases, and observe the delay due to Ngb in the time taken to move between steady-states. We are interested to see whether this effect can prevent or reduce periods of hypoxia. The parameters we shall vary are the oxygen concentration at the CC, c_c, and the rate of oxygen uptake, Q, both of which may fluctuate over an average day. For instance, Q will increase at night under DA and c_c might decrease as a result of blinking, eye movement or eye rubbing.

In the results that follow, the FEM is used to solve the steady-state problem (2.8) and (2.13)–(2.15), as in Section 2.3.1, and the resulting oxygen profiles are then used as initial conditions for the time-dependent problem (2.7)–(2.12). The time-dependent problem is solved using the Matlab routine pdepe, which employs the method of lines.

Figures 2.4(a) and (c) show the effect of a change in the oxygen concentration at the CC,

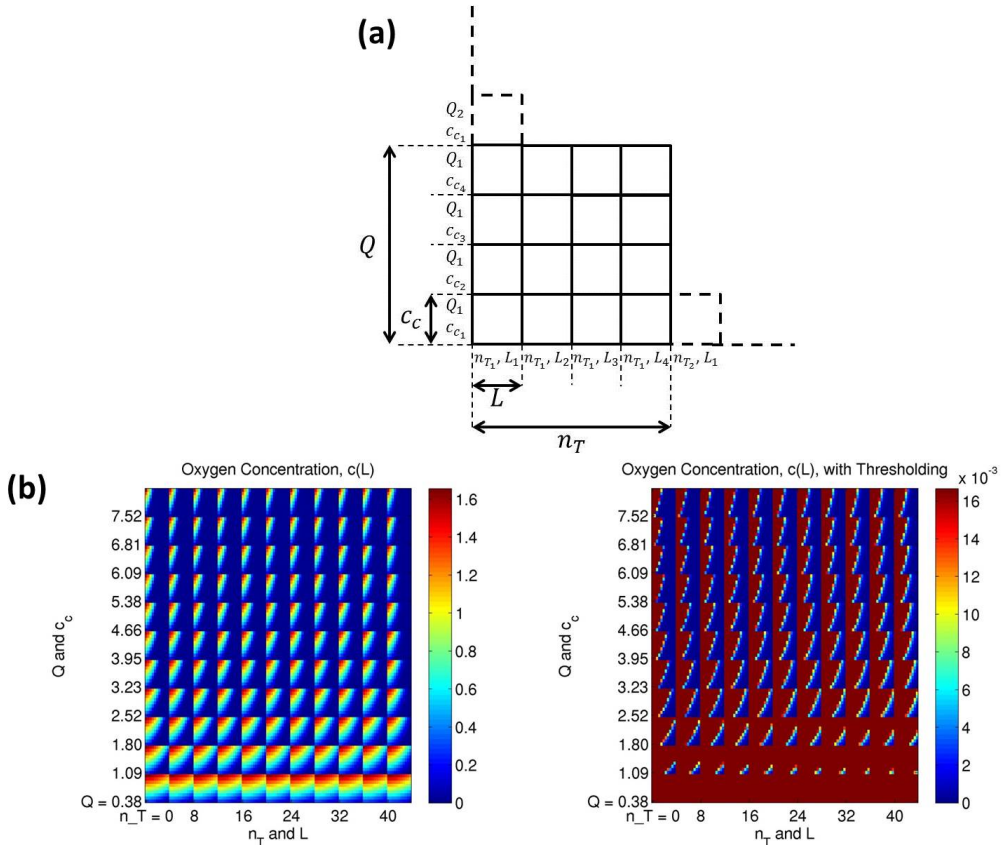

Figure 2.3: Sensitivity analysis of the steady-state single layer model. (a) Diagram to show the arrangement of the sensitivity analysis grid. Parameters n_T (large scale) and L (small scale) are varied along the x-axis, increasing left-to-right and parameters Q (large scale) and c_c (small scale) are varied along the y-axis, increasing bottom-to-top. (b) Left: the oxygen concentration at $x = L$ (i.e. the minimum value) is plotted for a range of parameter values. Right: the same as on the left, but thresholded such that values greater than or equal to the hypoxic threshold, γ, are set to γ. Left: the effect of Ngb is barely discernible. Right: as n_T is increased, tissue hypoxia is reduced. Equations (2.8) and (2.13)–(2.15) were solved using the FEM with 101 mesh points. Parameter values: $L = 0.25, 0.50, \ldots, 1.50$, $c_c = 0.33, 0.50, \ldots, 1.66$, $n_T = 0, 4, \ldots, 40$ and $Q = 0.38, 1.09, \ldots, 7.52$. Remaining parameter values as in Table 2.2.

$c_c(t)$, upon the minimum oxygen concentration, $c(L,t)$, for a range of concentrations of Ngb, n_T. In Figure 2.4(a), $c_c(t)$ is decreased from 1 to 0.33 at $t = 10$, that is $c_c(t) = 1 - \frac{2}{3}H(t-10)$ where H is a Heaviside step function, such that $H(s) = 0$ for $s < 0$ and $H(s) = 1$ for $s \geq 0$. The values of $c_c(t)$ are chosen such that for $c_c(t) = 1$, $c(L,t) > \gamma$ for all $n_T \in [0,40]$ and for $c_c(t) = 0.33$, $c(L,t) < \gamma$ for all $n_T \in [0,40]$. It can be seen that as n_T is increased, the time taken for $c(L,t)$ to reach its new steady-state following the drop in $c_c(t)$ increases, as does the time for it to cross the hypoxic threshold, γ. The reasons for this are twofold: firstly, the oxygen concentration drops less rapidly and secondly, it begins at a higher steady-state value. The time, Δt, for $c(L,t)$ to fall below γ, is a monotone increasing function of n_T (see Figure 2.4(b)). In Figure 2.4(c), $c_c(t)$ is increased from 0.33 to 1 at $t = 10$, that is $c_c(t) = \frac{1}{3} + \frac{2}{3}H(t-10)$, where H is a step function. As in Figure 2.4(a), the time taken for $c(L,t)$ to reach its new steady-state increases as n_T increases, since it rises less rapidly and because it must rise to a higher concentration. However, the relationship between n_T and the time, Δt, to reach γ, is no longer monotonic, reaching a maximum somewhere between $n_T = 30$ and $n_T = 35$ (see Figure 2.4(d)). From this point onwards further increases in n_T reduce the time taken to reach γ. This is because, as n_T increases, the steady-state value of $c(L,t)$ at $c_c(t) = 0.33$ increases, meaning that $c(L,t)$ has less far to rise before reaching γ. The same qualitative behaviour can be obtained by changing Q instead of c_c (results not shown).

Figure 2.5(a) shows the net increase in the time spent in normoxia (healthy oxygen levels), Δt_{norm}, when Ngb is present and $c_c(t)$ is decreased from 1 to 0.33 and then increased back to 1, the system having been allowed to settle to steady-state before each change in $c_c(t)$. In other words, it is the curve that results from subtracting the curve in Figure 2.4(d) from that in Figure 2.4(b). It can be seen that for $n_T < 11$, the presence of Ngb results in a net decrease in the time spent in normoxia, whereas for $n_T > 11$, the presence of Ngb results in a net increase in the time spent in normoxia. For $n_T = 20$ (the maximum biologically realistic concentration for a domain of this length), the net increase in time spent in normoxia is 4.2 non-dimensional time units, which corresponds to approximately 1.29 seconds. Figure 2.5(b) shows the equivalent results for a change in $Q(t)$ from 2.26 to 4.51 and then back again. In this case we require

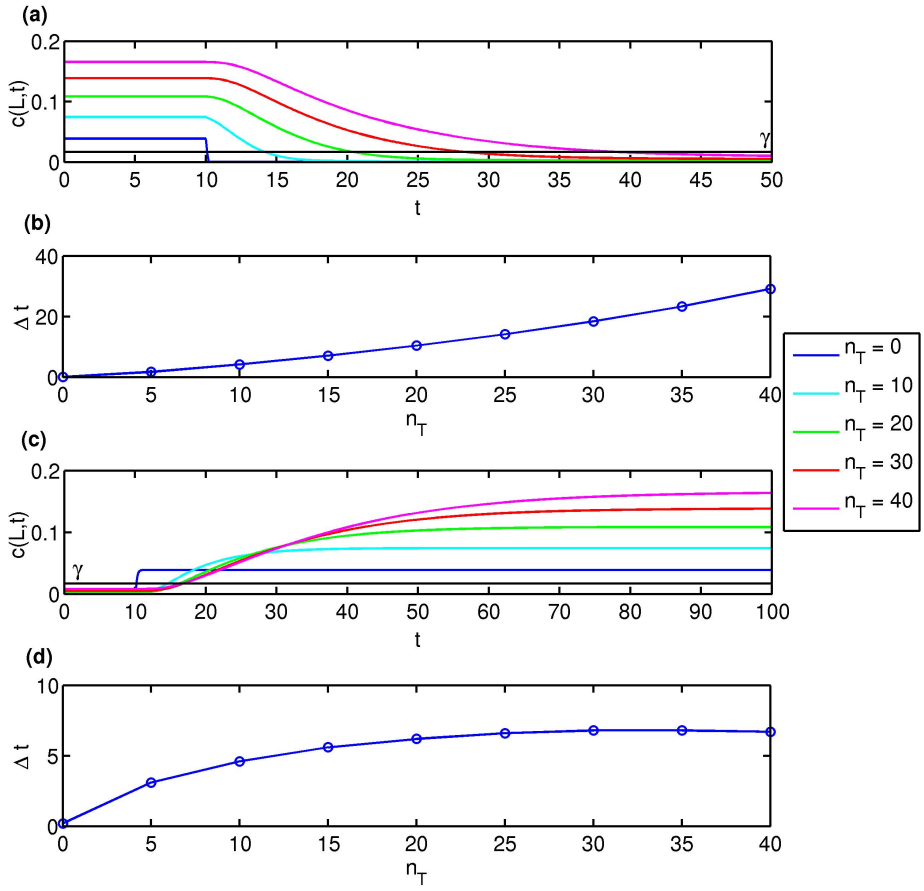

Figure 2.4: Simulation results from the time-dependent single layer model. Panels (a) and (c) show the dynamics of the minimum oxygen concentration, $c(x = L,t)$, following a change in the oxygen concentration at the CC, c_c, for a range of Ngb concentrations, n_T. In panel (a), $c_c(t) = 1$ for $t \in [0,10)$ and $c_c(t) = 0.33$ for $t \in [10,50]$. In panel (c), $c_c(t) = 0.33$ for $t \in [0,10)$ and $c_c(t) = 1$ for $t \in [10,100]$. Panels (b) and (d) show the time taken, Δt, for the minimum oxygen concentration to fall and rise to the hypoxic threshold, γ, respectively. In (b) the time taken to reach $c(L,t) = \gamma$ increases as n_T increases. In (d) the time taken to reach $c(L,t) = \gamma$ increases initially as n_T increases, but then decreases as n_T increases beyond 35. The steady-state problem (2.8) and (2.13)–(2.15) was solved using the FEM to give the initial oxygen profiles and then the time-dependent problem (2.7)–(2.12) was solved using pdepe. In both cases 101 spatial mesh points were used. Parameter values: $L = 1$ and $Q = 2.26$. Remaining parameter values as in Table 2.2.

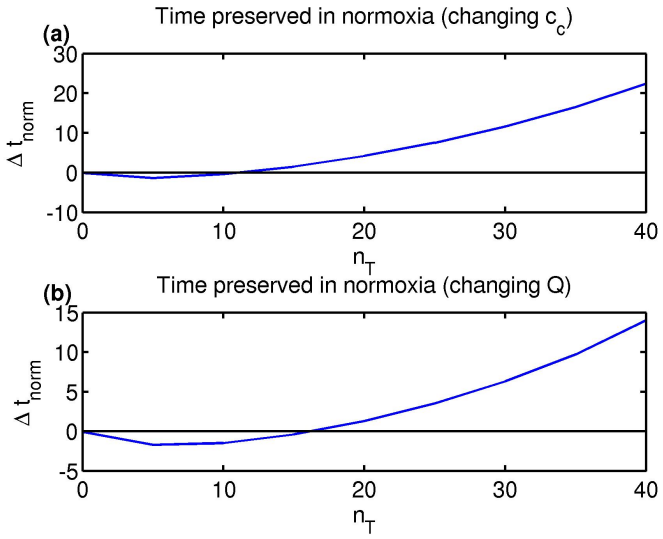

Figure 2.5: Simulation results from the time-dependent single layer model. Graphs show the net time gained in normoxia due to the presence of Ngb, Δt_{norm}, when the oxygen concentration at the CC, c_c, (panel (a)) and the oxygen consumption rate, Q, (panel (b)) are varied. These results assume that the oxygen concentration is allowed to reach its steady-state before a parameter switch is made. (a) The oxygen concentration at the CC is switched between $c_c = 1$ and $c_c = 0.33$, for consistency with the results in Figure 2.4. (b) The rate of oxygen uptake is switched between $Q = 2.26$ and $Q = 4.51$. The addition of Ngb in low concentrations results in a net decrease in the time spent in normoxia, whereas high concentrations result in a net increase. The steady-state problem (2.8) and (2.13)–(2.15) was solved using the FEM to give the initial oxygen profiles and then the time-dependent problem (2.7)–(2.12) was solved using pdepe. In both cases 101 spatial mesh points were used. Parameter values: $L = 1$. Remaining parameter values as in Table 2.2.

$n_T > 16$ in order for the presence of Ngb to be beneficial in oxygen storage and the net increase in time spent in normoxia for $n_T = 20$ is 1.3 non-dimensional time units, which corresponds to approximately 0.40 seconds. These results suggest that, even in high concentrations, the role of Ngb in oxygen storage is minimal if the fluctuation in system parameters occurs on a timescale slow enough to allow the system to settle to steady-state, that is anything more than about 5-10 seconds (see Figure 2.4).

However, what if the fluctuation in system parameters were to occur on a faster timescale? In Figure 2.6 we explore the utility of Ngb in preventing or minimising hypoxia for a range of durations of low $c_c(t)$. Simulations begin with $c_c(0) = 1$, then $c_c(t)$ is decreased to 0.33 for

Table 2.3: Non-dimensional parameters associated with the simplified single layer model (see equations (2.16)–(2.18)). Only those parameter values that change have been listed, all other parameter values remain as in Table 2.2. (Values given to an accuracy of at most three significant figures).

Parameter	Value
n_T	0 to 69.4
α	1
k_1	31,800
k_2	2.27

a period of time, after which it is set back to 1 and the simulation continued until $c(x = L,t)$ increases above γ in those cases where it has dropped below γ. The time for which $c(x = L,t) < \gamma$ is then plotted for a range of values of n_T. It can be seen that for $n_T \leq 10$, Ngb prolongs the duration of hypoxia for all but very short durations of low $c_c(t)$. For $n_T \geq 15$, however, hypoxia is either eliminated or reduced in all cases. Similar results are obtained when the tissue is transiently exposed to elevated levels of $Q(t)$ (results not presented). In this case $Q(t)$ is varied between 2.26 and 4.51 and we require $n_T \geq 20$ for Ngb to be beneficial for oxygen storage for all durations of high $Q(t)$. Thus, if the fluctuation in system parameters were sufficiently rapid and the Ngb concentration sufficiently high, then Ngb could have an important cumulative effect, were these fluctuations a regular occurrence.

2.4 Analysis of a Simplified Steady-State Single Layer Model

In this section we develop and analyse a simplified version of the single layer model at steady-state. We use the simplified model to investigate Ngb's effect upon the domain length that can be supported under normoxic conditions and upon the minimum oxygen concentration when oxygen levels do not become hypoxic. (Keener and Sneyd, 1998, Chapter 2, perform a similar analysis for a problem involving the facilitated diffusion of oxygen by Mb in a slab reactor, the main difference being that their equations lack an oxygen uptake term.)

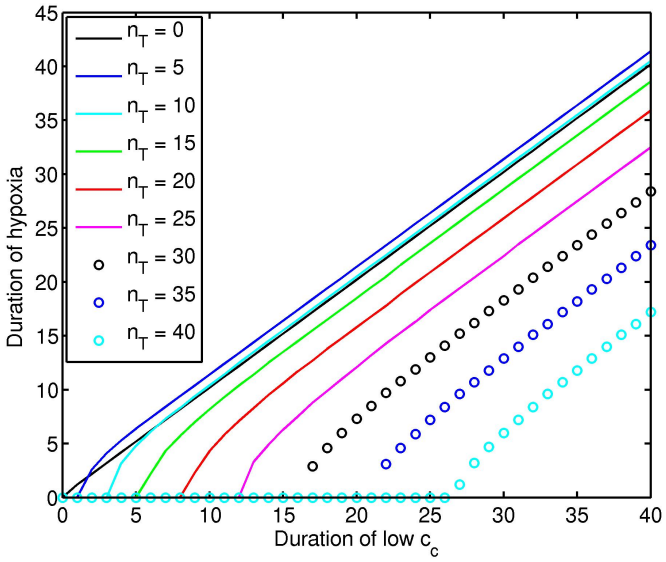

Figure 2.6: Simulation results from the time-dependent single layer model. The graph shows how the presence of different levels of Ngb affect the period of time for which the system is hypoxic as the duration of the period of time for which c_c is reduced varies. The oxygen concentration at the CC is switched from $c_c = 1$ to $c_c = 0.33$ and then returned to $c_c = 1$ after a given time, plotted on the x-axis, whilst the corresponding time for which $c(x = L,t) < \gamma$ is plotted on the y-axis (this time spans a period that starts during the period for which $c_c = 0.33$ and ends some time after c_c has increased back to 1). For $n_T \leq 10$ the presence of Ngb is only advantageous for short durations of low c_c, whereas for $n_T \geq 15$ Ngb reduces the duration of hypoxia for all durations of low c_c. The steady-state problem (2.8) and (2.13)–(2.15) was solved using the FEM to give the initial oxygen profiles and then the time-dependent problem (2.7)–(2.12) was solved using pdepe. In both cases 101 spatial mesh points were used. Parameter values: $L = 1$ and $Q = 2.26$. Remaining parameter values as in Table 2.2.

To simplify our analysis we make two changes: we replace the Michaelis-Menten term, $Qc/(\gamma+c)$, with a step function $Q(1-H(\gamma-c))$, so that the rate of oxygen uptake is equal to zero when $c \leq \gamma$ and Q when $c > \gamma$. Secondly, we set $\tilde{n} = 58\mu$M, so that $\alpha = 1$. This alternative choice for the non-dimensionalisation does not affect the behaviour of the system, it merely simplifies the analysis presented below (allowing cancellation of the kinetic terms). The non-dimensional parameters n_T, k_1 and k_2 also change, attaining the values stated in Table 2.3, whereas all other parameter values remain as in Table 2.2.

Following these simplifications, equations (2.13)–(2.15) take the form

$$0 = \frac{\mathrm{d}^2 c}{\mathrm{d}x^2} - Q(1-H(\gamma-c)) + k_2 n_o - k_1 n c, \tag{2.16}$$

$$0 = D\frac{\mathrm{d}^2 n_h}{\mathrm{d}x^2} + k_3 n - k_4 n_h, \tag{2.17}$$

$$0 = D\frac{\mathrm{d}^2 n_o}{\mathrm{d}x^2} + k_1 n c - k_2 n_o, \tag{2.18}$$

where $n = n_T - n_o - n_h$. We impose the boundary conditions (2.8) to close the system.

We begin by considering the case where the retina becomes hypoxic, such that $c(x) \leq \gamma$ for $x_c \leq x \leq L$. Adding equations (2.16) and (2.18), applying the zero-flux boundary condition for n_o at $x = 0$ and integrating between 0 and x supplies

$$0 = \frac{\mathrm{d}c}{\mathrm{d}x}(x) - \frac{\mathrm{d}c}{\mathrm{d}x}(0) + D\frac{\mathrm{d}n_o}{\mathrm{d}x}(x) - Q\underbrace{\int_0^x (1-H(\gamma-c))\mathrm{d}\tilde{x}}_{=min(x,x_c)}, \tag{2.19}$$

where x_c is the maximum domain length that can be supported under normoxic conditions, such that $c(x_c) = \gamma$. Applying the zero-flux boundary conditions for c and n_o at $x = L$, we find that $\frac{\mathrm{d}c}{\mathrm{d}x}(0) = -Qx_c$. Rearranging equation (2.19), we obtain the following expression for $J(x)$, the flux of oxygen (in its bound and unbound forms):

$$J(x) = -\left(\frac{\mathrm{d}c}{\mathrm{d}x} + D\frac{\mathrm{d}n_o}{\mathrm{d}x}\right) = Q(x_c - \min(x, x_c)). \tag{2.20}$$

Integrating equation (2.20) between 0 and x_c, we obtain the following expression:

$$J_A = \int_0^{x_c} J(x)\mathrm{d}x = (c_c - \gamma) + D(n_o(0) - n_o(x_c)) = \frac{Qx_c^2}{2}, \tag{2.21}$$

where J_A is a conserved quantity equal to the area under the curve $J(x)$. We seek an expression for x_c, in order to determine the contribution of Ngb to the domain length that can be supported under normoxia. We proceed by deriving leading order approximations for $n_o(0)$ and $n_o(x_c)$ in terms of $c(0) = c_c$ and $c(x_c) = \gamma$ respectively.

We begin by re-scaling the variables and parameters, fixing $\varepsilon = 0.1$ to separate the various scales. We scale $c = \varepsilon c^*$, since c is of this order across most of the retina (see, for instance, Figure 2.2), $D = \varepsilon^2 D^*$, $\gamma = \varepsilon^2 \gamma^*$, $k_1 = \varepsilon^{-4} k_1^*$ and $k_3 = \varepsilon^{-3} k_3^*$. The parameter scalings are chosen to ensure that D^*, γ^*, k_1^* and k_3^* are all of $O(1)$ (see Tables 2.2 and 2.3 for unscaled parameter values).

In Appendix B we show that n is bounded above by $\alpha k_2 n_T / k_3$. Using the alternative non-dimensionalisation adopted in this section, this becomes $k_2 n_T / k_3 \approx \varepsilon^3 n_T$ (where the changes in α and k_2 cancel). Whilst n_o and n_h vary across the domain, they are of the same order of magnitude, and so, at leading order, they satisfy the conservation relation $n_o + n_h = n_T$. Assuming that $2 \leq n_T \leq 69.4$, the Ngb terms can be scaled in one of two ways, depending upon the size of n_T:

- Scaling 1: for $2 \leq n_T < 7$ we scale $n = \varepsilon^3 n^*$, where $n_h = O(1)$, $n_o = O(1)$ and $n_T = O(1)$.
- Scaling 2: for $7 \leq n_T \leq 69.4$ we scale $n = \varepsilon^2 n^*$, $n_h = \varepsilon^{-1} n_h^*$, $n_o = \varepsilon^{-1} n_o^*$ and $n_T = \varepsilon^{-1} n_T^*$.

In both cases $n/n_T = O(\varepsilon^3)$, $n_h/n_T = O(1)$ and $n_o/n_T = O(1)$. In what follows we work with the first scaling, noting that the leading order solution under the second scaling is the same.

Applying Scaling 1 to equations (2.16)–(2.18) we obtain:

$$0 = \varepsilon \frac{\mathrm{d}^2 c^*}{\mathrm{d}x^2} - Q(1 - H(\varepsilon^2 \gamma^* - \varepsilon c^*)) + k_2 n_o - k_1^* n^* c^*, \tag{2.22}$$

$$0 = \varepsilon^2 D^* \frac{\mathrm{d}^2 n_h}{\mathrm{d}x^2} + k_3^* n^* - k_4 n_h, \tag{2.23}$$

$$0 = \varepsilon^2 D^* \frac{\mathrm{d}^2 n_o}{\mathrm{d}x^2} + k_1^* n^* c^* - k_2 n_o, \tag{2.24}$$

Upon dropping the stars, equations (2.23) and (2.24) provide

$$k_3 n - k_4 n_h = 0, \qquad k_1 n c - k_2 n_o = 0, \tag{2.25}$$

at leading order, using the same notation to denote the dependent variables at leading order in equation (2.25) as is used for their exact form in equations (2.22)–(2.24) (upon dropping the stars). Whilst c satisfies equation (2.25) at leading order, we also consider it to include a first order term, to allow us to capture the dominant behaviour of the system where $c = c^* = O(\varepsilon)$. Substituting the second of these equations into (2.22), the dominant balance involves the diffusion and uptake terms. For $x \geq x_c$, $Q(1 - H(\varepsilon^2 \gamma - \varepsilon c)) = 0$, so that, after applying $c(x_c) = \varepsilon\gamma$, together with the zero-flux boundary condition at $x = L$, we find that $c(x) = \varepsilon\gamma$ for $x \in [x_c, L]$. For $x \in [0, x_c)$, $c > \varepsilon\gamma$, so that $Q(1 - H(\varepsilon^2 \gamma - \varepsilon c)) > 0$, and we must scale $x = \varepsilon^{\frac{1}{2}} x^*$ to attain a dominant balance between the diffusion and uptake terms, resulting in a quadratic oxygen profile in this region. Applying this scaling to equations (2.23) and (2.24) retrospectively, we see that the leading order equations in (2.25) are preserved. Formally, there is also a passive boundary layer at $x = 0$, to allow us to satisfy the boundary conditions there (though there is no sharp change in the solution in this region).

We use (2.25), together with the leading order conservation relation $n_h + n_o = n_T$, to derive an expression for n_o in terms of c as follows

$$n_o = \frac{n_T c}{P_{50} + c}, \text{ where } P_{50} := \frac{k_2 k_3}{k_1 k_4}. \tag{2.26}$$

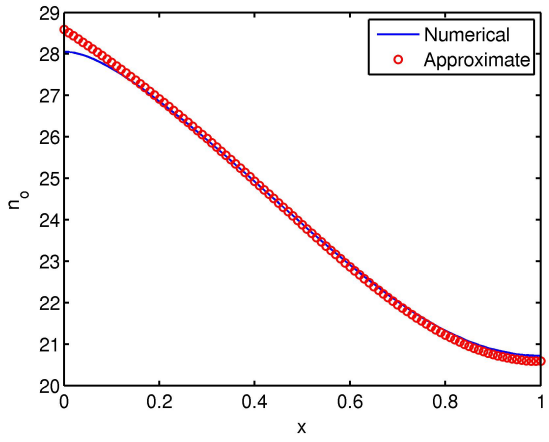

Figure 2.7: Graph showing that the approximate solution for n_o matches closely with the numerical solution. The numerical solution was obtained by solving equations (2.8) and (2.16)–(2.18) using the FEM, with 101 mesh points. The approximate solution was obtained using the numerical solution for c in equation (2.26). Parameter values: $L = 1$, $c_c = 1$, $n_T = 34.7$ and $Q = 1.50$. Remaining parameter values as in Tables 2.2 and 2.3. Parameters and variables are in their unscaled form.

P_{50} is the oxygen concentration at which exactly half of the Ngb molecules are in their oxygen bound form, that is at which $n_o = n_T/2$ ($= n_h$ at leading order). This expression for P_{50} differs from that used by Kiger et al. (2004), where $P_{50} = k_2(k_3 + k_4)/(k_1 k_4)$. Kiger et al.'s expression can be obtained by considering the unscaled, spatially homogeneous versions of equations (2.16)–(2.18) with $Q = 0$. However, since $k_4 \ll k_3$ (in their unscaled form), the difference between these two expressions is small. As Figure 2.7 reveals, the approximate solution for n_o in equation (2.26) matches closely with the numerical solution.

Substituting for n_o from (2.26) into (2.21) we obtain

$$J_A = (c_c - \gamma)\left(1 + \underbrace{\frac{P_{50} D n_T}{(P_{50} + c_c)(P_{50} + \gamma)}}_{\text{Ngb contribution}}\right) = \frac{Q x_c^2}{2}. \tag{2.27}$$

Rearranging equation (2.27), we may derive an expression for x_c, the maximum domain

length that can be supported under normoxic conditions, as follows

$$x_c = \sqrt{\frac{2(c_c-\gamma)}{Q}\left(1+\frac{P_{50}Dn_T}{(P_{50}+c_c)(P_{50}+\gamma)}\right)}. \tag{2.28}$$

If $n_T = \gamma = 0$ then (2.28) reduces to the expression derived by Dollery et al. (1969) for the maximum tissue length that can be supported by a single vascular bed. It can be seen both from equation (2.28) and from Figure 2.8(a) that Ngb increases the size of x_c. For $c_c = 1$ and $n_T = 34.7$ (our predicted maximum Ngb concentration for domains of this length, assuming a maximal retinal width of 320μm, and that Ngb is absent from all other retinal layers), x_c is 11% longer than it would be in the absence of Ngb. Further, Ngb makes a proportionally larger contribution to x_c as c_c decreases (see Figure 2.8(a)), for instance, when $n_T = 34.7$ and $c_c = 0.33$, x_c is 23% larger than it would be in the absence of Ngb.

Differentiating equation (2.28) with respect to P_{50}, we find that x_c achieves a global maximum at $P_{50,max} = \sqrt{\gamma c_c}$. Figure 2.8(b) shows the dependence of x_c upon P_{50}, with the maximum value of x_c, at which $P_{50} = P_{50,max}$, marked with a circle. It can be seen that the curve is fairly flat in the vicinity of $P_{50,max}$ such that x_c remains near maximal for a small decrease, or even quite a large increase, in P_{50} away from $P_{50,max}$. Further, x_c decreases sharply as P_{50} approaches zero for $P_{50} < 0.05$. This result is surprising since it is usually assumed that Ngb would be a more effective oxygen transporter if it had a lower P_{50} value: our analysis reveals that as P_{50} decreases below $P_{50,max}$, Ngb will become less effective in oxygen transport. For $c_c = 1$, $P_{50,max} = 0.129$ = 7.44 μM = 7.75 mmHg, which is within the range of measured values in the literature (see Table A.3 in Appendix A.11).

So far we have assumed that the retina becomes hypoxic at some location, $x = x_c < L$. If instead, oxygen levels are normoxic throughout the domain, that is $x_c > L$, then we may derive an expression for $c(x = L)$, the minimum oxygen concentration. Equation (2.20) becomes

$$J(x) = -\left(\frac{\mathrm{d}c}{\mathrm{d}x} + D\frac{\mathrm{d}n_o}{\mathrm{d}x}\right) = Q(L-x). \tag{2.29}$$

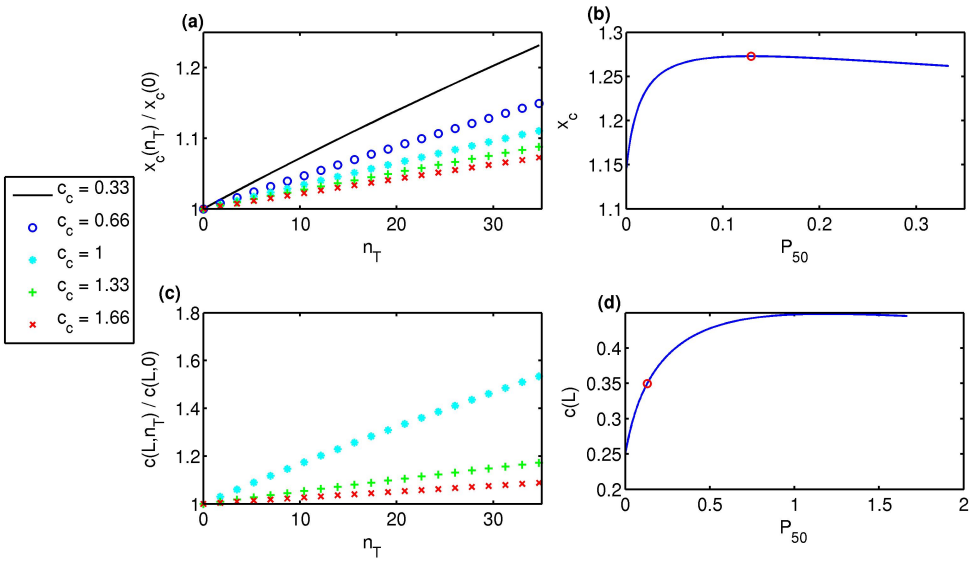

Figure 2.8: Graphs showing results for the simplified model. Graphs (a) and (c) show the proportional increase in x_c and $c(L)$ respectively, due to the action of Ngb, the effect being more pronounced for lower values of c_c. Graphs (b) and (d) show the effect of P_{50} upon x_c and $c(L)$ respectively. The value of the dependent variable at $P_{50} = \sqrt{\gamma c_c}$ is marked with a circle in each case. The value of x_c is maximal at $P_{50} = \sqrt{\gamma c_c}$; however, $c(L)$ takes its maximum value for some $P_{50} > \sqrt{\gamma c_c}$. Graphs (a) and (b) were obtained using solutions to (2.28) and graphs (c) and (d) were obtained using solutions to (2.31). Parameter values: $Q = 1.50$, (c)–(d) $L = 1$, (b) and (d) $c_c = 1$ and $n_T = 34.7$. Remaining parameter values as in Tables 2.2 and 2.3. The key on the left applies to graphs (a) and (c) only.

Integrating (2.29) between 0 and L and substituting for n_o from (2.26) we obtain

$$J_A = (c_c - c(L))\left(1 + \frac{P_{50}Dn_T}{(P_{50}+c_c)(P_{50}+c(L))}\right) = \frac{QL^2}{2}. \tag{2.30}$$

This equation can be rearranged to give the following expression for $c(L)$:

$$c(L) = \frac{-A + \sqrt{A^2 - 4B}}{2}, \tag{2.31}$$

where we have chosen the positive root to satisfy the condition that $c(L) = c_c$ when $Q = n_T = 0$ (see equation (2.30)), and

$$A = P_{50} + \frac{QL^2}{2} + \frac{P_{50}Dn_T}{P_{50}+c_c} - c_c, \qquad B = P_{50}\left(\frac{QL^2}{2} - \frac{Dn_T c_c}{P_{50}+c_c} - c_c\right). \tag{2.32}$$

Figure 2.8(c) shows that Ngb acts to increase $c(L)$, making a proportionally larger contribution for lower c_c. Indeed, for $L = 1$, $c_c = 1$, $n_T = 34.7$ (our predicted maximum Ngb concentration for domains of length $L = 1$) and $Q = 1.50$, $c(L)$ is 53% higher than what it would be in the absence of Ngb.

Plotting $c(L)$ against P_{50} shows that the maximum value of $c(L)$ does not correspond with $P_{50} = \sqrt{\gamma c_c}$, but instead lies at a P_{50} significantly above this value (this relationship was found to hold for all combinations of parameter values tested, see Figure 2.8(d)). It may be that the optimum P_{50} lies somewhere above $\sqrt{\gamma c_c}$, since x_c decreases slowly as P_{50} increases beyond $\sqrt{\gamma c_c}$, but $c(L)$ increases more rapidly. In both cases a decrease in P_{50} below $\sqrt{\gamma c_c}$ is disadvantageous, counter to the prevailing assumption that lower P_{50} values improve Ngb's effectiveness in oxygen transport.

2.4.1 Comparing Numerical and Approximate Solutions

In deriving an analytical solution for x_c we have made two simplifying assumptions: (i) that the Michaelis-Menten term for oxygen uptake may be approximated by a step function and (ii) that n_o can be approximated as a function of c (equation (2.26)). In this section we compare

the approximate analytical solutions with the FEM solutions to the full (equations (2.8) and (2.13)–(2.15)) and simplified (equations (2.8) and (2.16)–(2.18)) problems. As in Section 2.3, we use piecewise linear basis functions for the FEM, solving the resulting system of nonlinear algebraic equations using the Matlab routine fsolve, employing the Trust-Region-Dogleg algorithm. When solving the simplified problem numerically, we replace the step function in (2.16), $1-H(\gamma-c)$, with the modified hyperbolic function, $\frac{1}{2}(\tanh((c-\gamma)/\delta)+1)$, where $\delta = 0.001$, to avoid the numerical difficulties resulting from a discontinuity in the governing equations.

Figure 2.9 (a) compares the approximate solution to the numerical solution to the full problem, for the proportional increase in x_c due to Ngb (the numerical solution to the simplified problem provides a closer match to the approximate solution, but is omitted for clarity), whilst Figure 2.9 (b) compares the results for the approximate solution and the numerical solutions to the simplified and full models, for the dependence of x_c upon P_{50}. The difference between results is at most $O(\varepsilon)$ (where $\varepsilon = 0.1$) in all cases, as expected for a leading order approximation. The numerical solution to the simplified problem achieves its maximum for P_{50} slightly above $\sqrt{\gamma c_c}$, whilst the numerical solution to the full problem achieves its maximum for $P_{50} \approx 0.28 = 16.7$ mmHg. This is approximately twice $\sqrt{\gamma c_c} = 0.13 = 7.7$ mmHg, and lies at the upper end of the range of measured values in the literature (see Table A.3 in Appendix A.11, where the bracketed P_{50} values are the ones consistent with the parameters used in our model). Unlike the approximate and simplified numerical solutions, the prediction of x_c from the full numerical solution initially decreases as P_{50} increases from 0 (this result was verified using the Matlab routine pdepe to solve the time-dependent problem (2.7)–(2.12), allowing it to settle to steady-state). Whilst this results in a local maximum at $P_{50} = 0$, the global maximum remains at $P_{50,max,numeric} > 0$.

Figure 2.10 (a) compares the approximate solution and the numerical solution to the full problem for the proportional increase in $c(L)$ due to Ngb (the numerical solution to the simplified solution provides a closer match to the approximate solution, but is omitted for clarity), whilst Figure 2.10 (b) compares the approximate solution with the numerical solutions to the

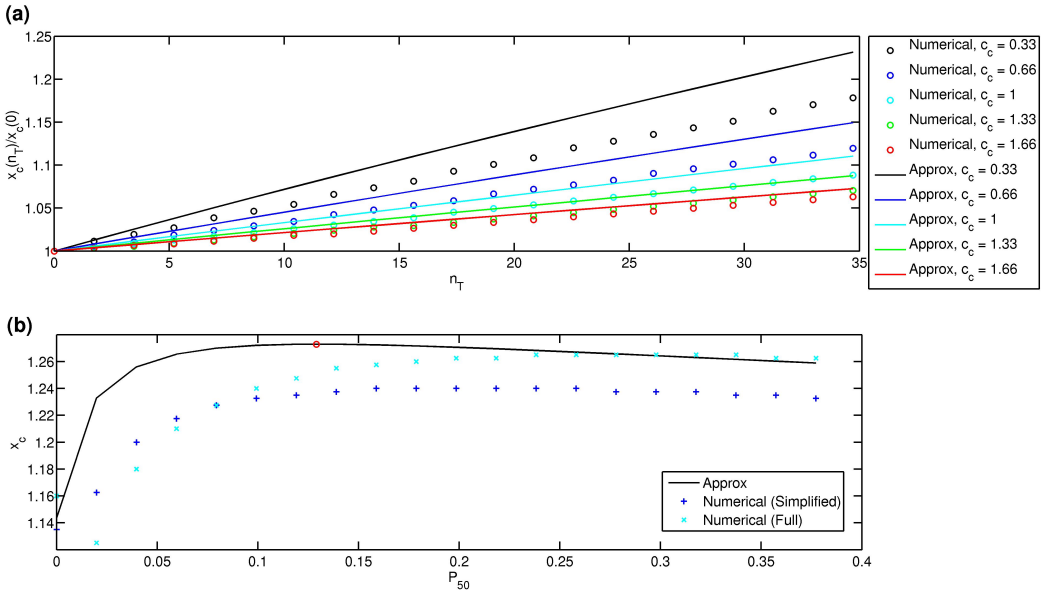

Figure 2.9: Graphs comparing numerical and approximate solutions to the single layer model. Graph (a) compares the results for the proportional increase in x_c, due to the action of Ngb, from the approximation (2.28) and the solution to the full problem (2.8) and (2.13)–(2.15). In general the approximate solution overestimates the numerical solution, particularly for small values of c_c. Graph (b) compares the results for the effect of P_{50} upon x_c from the approximation (2.28), the solution to the simplified problem (2.8) and (2.16)–(2.18) and the solution to the full problem (2.8) and (2.13)–(2.15); the value of x_c at $P_{50} = \sqrt{\gamma c_c}$ is marked with a circle. The numerical solutions to the simplified and full problems lie mostly beneath the approximate solution. The numerical solutions to the full and simplified problems were obtained using the FEM with 801 mesh points. Parameter values: $L = 2$ and $Q = 1.50$; (b) $c_c = 1$ and $n_T = 34.7$. Remaining parameter values as in Tables 2.2 and 2.3.

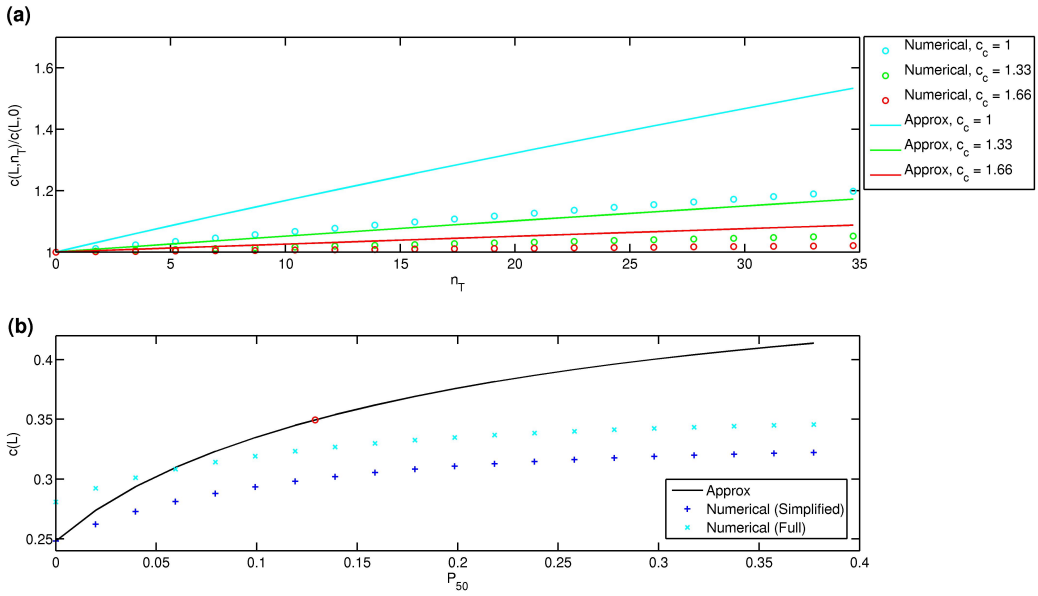

Figure 2.10: Graphs comparing numerical and approximate solutions to the single layer model. Graph (a) compares the results for the proportional increase in $c(L)$, due to the action of Ngb, from the approximation (2.31) and the solution to the full problem (2.8) and (2.13)–(2.15). In general the approximate solution overestimates the numerical solution, particularly for small values of c_c. Graph (b) compares the results for the effect of P_{50} upon $c(L)$ from the approximation (2.31), the solution to the simplified problem (2.8) and (2.16)–(2.18) and the solution to the full problem (2.8) and (2.13)–(2.15); the value of $c(L)$ at $P_{50} = \sqrt{\gamma c_c}$ is marked with a circle. The numerical solutions to the simplified and full problems mostly lie beneath the approximate solution. The numerical solutions to the full and simplified problems were obtained using the FEM with 801 mesh points. Parameter values: $L = 1$ and $Q = 1.50$; (b) $c_c = 1$ and $n_T = 34.7$. Remaining parameter values as in Tables 2.2 and 2.3.

simplified and full problems for the dependence of $c(L)$ upon P_{50}. In this case the error is greater than that observed in Figure 2.9, though it is still of $O(\varepsilon)$. Also, as we decrease ε, the error scales with ε, indicating that the approximation is valid (results not shown).

Therefore, we have a reasonable agreement between the numerical solutions to the full and simplified problems and our approximations.

2.5 Discussion

In this chapter we have investigated, through the use of a single layer model, the possible role of the protein Ngb in preventing hypoxia. Both steady-state and time-dependent models were used to explore Ngb's role in oxygen transport and storage respectively.

Whilst the single layer model does not capture the complex physiology and cellular compartmentalisation of the retina, it provides a useful starting point for investigating the role of Ngb in oxygen transport and storage. Examination of the steady-state single layer model (Section 2.3.1) demonstrated that Ngb acts by removing oxygen from oxygen rich regions and redistributing it to oxygen poor regions, with the potential to eliminate or alleviate hypoxia. Sensitivity analysis of the steady-state single layer model revealed that there exist regions in parameter space in which Ngb may play an important role in preventing or minimising hypoxia.

Ngb must be present in high concentrations and the duration of unfavourable parameter fluctuations brief in order for Ngb to be of significant benefit in oxygen storage (Section 2.3.2). If there was a scenario in which c_c or Q oscillated on the time scale of a few seconds, and particularly if the periods of recovery were longer than the periods of challenge, then Ngb could prevent or reduce hypoxia to a significant degree (results not shown); however, as far as we are aware, no such scenario exists.

Analysis of the simplified single layer model (Section 2.4) demonstrated that Ngb increases the maximum domain length that can be supported under normoxia, x_c, and the minimum oxygen concentration in a normoxic domain, $c(L)$. It was found that the proportional contribution of Ngb to these quantities is larger for lower values of c_c, the oxygen concentration at the CC. This is consistent with the idea that Ngb has an important role in oxygen transport, particularly when the oxygen supply is limited.

The analysis also indicated that x_c is maximised for an oxygen affinity of $P_{50,max} = \sqrt{\gamma c_c}$, decreasing sharply as $P_{50} \to 0$ and decreasing gradually initially as P_{50} increases past its optimum value. This trend was confirmed by the numerical solution to the full problem; however,

the P_{50} value for which x_c is maximised was shown to be approximately twice that predicted by the analysis. It is surprising that the optimum P_{50} value should be so high, since it is assumed in the literature that a lower P_{50} value will result in more efficient oxygen transport. For c_c in the range 20–100 mmHg (the maximum expected range in humans and other mammals), the numerical solution to the full problem predicts that $P_{50,max,numeric} = 9.5\text{-}17.9\ (\pm\ 2)$ mmHg, whereas a P_{50} corresponding to that of Mb (0.9-2.2 mmHg) is generally thought to be preferable in the literature (see for instance Burmester and Hankeln, 2004, 2009). Four of the eight measured values of Ngb P_{50} presented in Table A.3 in Appendix A.11 (relevant P_{50} values in brackets) fall within our predicted range, meaning that the oxygen affinity has the value one would expect if Ngb plays a role in oxygen transport. Therefore, the fact that Ngb has a higher P_{50} value than Mb is advantageous, rather than problematic, for oxygen transport (suggesting that natural selection may have tuned this parameter to its present value). Indeed, given the shallow gradient of the curve in Figure 2.9(b) for $P_{50} > P_{50,max,numeric}$, oxygen transport would remain near-optimal even for P_{50} values significantly higher than $P_{50,max,numeric}$. We note also that these results suggest that the P_{50} value of Ngb may differ between species, varying according to the square root of the average oxygen concentration at the capillaries. Further experimental work is required to test this prediction.

A tractable analytical expression for the P_{50} value which maximises $c(L)$ in a normoxic domain could not be obtained; however, numerical solution with a range of parameter values suggests that the optimal P_{50} value lies consistently above that which optimises x_c, that is above $P_{50,max,numeric}$. This suggests that the overall optimal P_{50} value may lie a little above $P_{50,max,numeric}$.

In conclusion, Ngb may play an important role in oxygen transport, but is unlikely to be important for oxygen storage. Contrary to the prevailing assumption, the fact that Ngb has a higher P_{50} value than Mb is not evidence against its role in oxygen transport, indeed many of the P_{50} values measured thus far are near optimal for oxygen transport.

In the next chapter we move from a single layer geometry to an eight layer geometry, in order to investigate the role of Ngb in a physiologically human retina.

Chapter 3

Retinal Oxygen Distribution and the Role of Neuroglobin: Eight Layer Model

In the previous chapter we explored the role of Ngb in oxygen transport and storage using a single layer model. In this chapter we extend this investigation by considering the role of Ngb in the human retina, using an eight layer model to capture its physiology.

3.1 Introduction

The human retina extends from the optic disc to the ora serrata and has a multilayered structure, consisting of numerous cell-types (see Figure 3.1(a)). It can be divided into inner and outer regions. The outer retina extends from the RPE to the middle of the outer plexiform layer (OPL), where the photoreceptors synapse with bipolar and horizontal cells, whilst the inner retina spans the region between the inner OPL and the ILM.

Oxygen is supplied to the retina via two separate vascular systems: the CC and the retinal capillaries. The CC is a capillary layer which lies directly outward from the RPE and which supplies the outer retina with oxygen. It forms the innermost layer of the choroid. The retinal capillaries supply the inner retina with oxygen. Throughout most of the mid-peripheral retina, the retinal capillaries are divided between two layers, one deep and the other superfi-

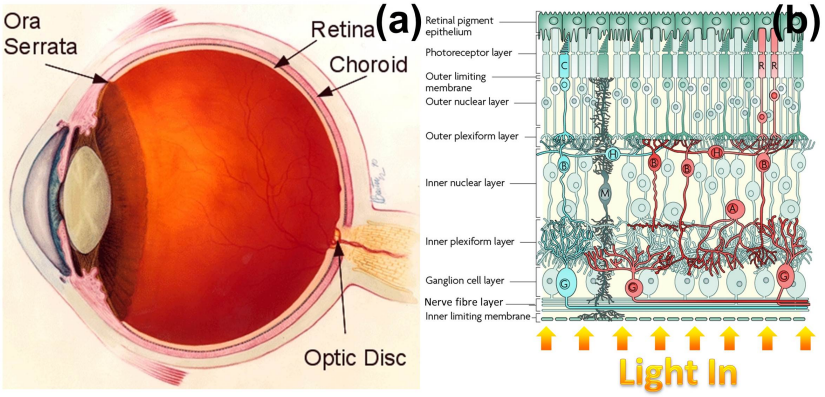

Figure 3.1: Diagrams of the human eye and retina. (a) Diagram of the (right) human eye, viewed in the transverse plane. Figure reproduced, with modifications, from `http://www.nei.nih.gov/health/coloboma/coloboma.asp`, courtesy: National Eye Institute, National Institutes of Health (NEI/NIH). (b) Diagram of the human retina, showing the retinal layers and cell types. The diagram is oriented such that the top lies outermost and the bottom innermost in the eye. R: rod photoreceptor. C: cone photoreceptor. H: horizontal cell. B: bipolar cell. M: Müller glial cell. A: amacrine cell. G: ganglion cell. Figure reproduced, with permission and modifications, from Swaroop et al. (2010).

cial (see Section 1.1.2 for more details Oyster, 1999; Pournaras et al., 2008; Kur et al., 2012). Therefore, in this chapter, we shall consider only the two retinal capillary layer scenario.

Whilst the oxygen distribution across the human retina has not been measured, it has been measured for other mammals, including monkeys (Birol et al. 2007, see also Yu and Cringle, 2001; Wangsa-Wirawan and Linsenmeier, 2003; Yu and Cringle, 2005, for reviews). Under DA the photoreceptor inner segments consume oxygen at twice the rate at which they consume oxygen under LA. As a result, the outer retinal oxygen profile drops under DA.

Birol et al. (2007) have measured oxygen profiles across the retina of the macaque monkey under DA and LA. The outer retina is normoxic under LA and hypoxic under DA, whilst the inner retina may be hypoxic under either LA or DA, depending upon local retinal capillary density (see Figure 3.2, where the inner retina is normoxic under LA and hypoxic under DA in this case). Since the macaque retina is physiologically similar to that of the human, it is likely that the human retina is also vulnerable to hypoxia, especially under DA. Thus any factor that

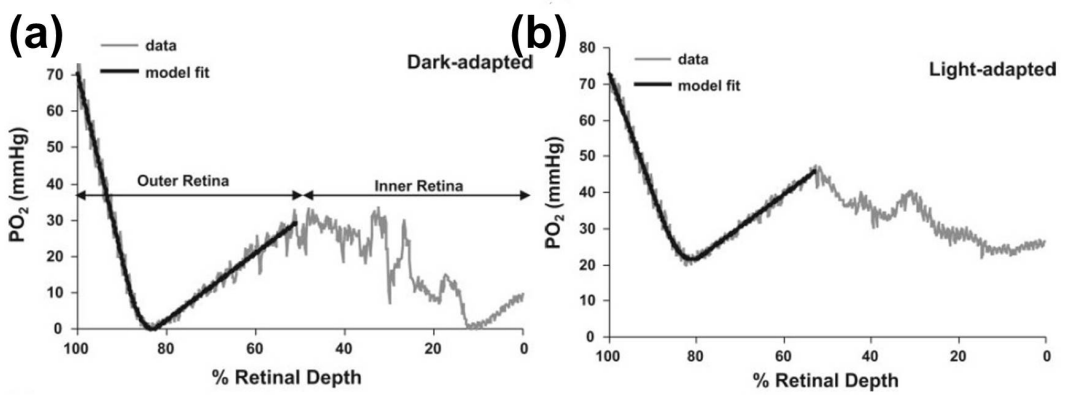

Figure 3.2: Retinal oxygen profiles. Graphs show the oxygen distribution across the perifoveal retina of a macaque monkey under DA (a) and LA (b). The retina is normoxic under LA, whilst hypoxic regions are present in both the inner and outer retina under DA. Grey lines show the profiles measured using an oxygen-sensitive microelectrode, whilst black lines show a piecewise linear and quadratic approximation fitted to the outer retinal profile. Figure reproduced, with permission, from Birol et al. (2007).

promotes retinal oxygenation may be vital in preventing or minimising retinal hypoxia and hence cell death.

A number of mathematical models for retinal oxygen distribution have been constructed (see for instance, Dollery et al., 1969; Linsenmeier, 1986; Stefánsson, 1988; Haugh et al., 1990; Linsenmeier and Braun, 1992; Braun et al., 1995; Linsenmeier and Padnick-Silver, 2000; Cringle and Yu, 2002; Yu and Cringle, 2002). They assume that the oxygen concentration is at steady-state and are posed on one-dimensional domains, oriented in a radial direction, across the width of the retina (the orientation is the same as the model in this chapter, see Figure 3.3). They assume that the rate of oxygen uptake is constant in each model layer (where model layers incorporate various cellular layers) and so reduce to solving $\frac{\mathrm{d}^2 c}{\mathrm{d}x^2} = Q$ in each layer, where c is the oxygen concentration, x is the distance across the retina and Q is the rate of oxygen uptake. In Section 3.4 we perform an asymptotic analysis to determine conditions under which the assumption of a constant rate of oxygen uptake is valid, and, in so doing, aim to place existing models on a stronger theoretical foundation.

To the best of our knowledge, only one mathematical model of retinal oxygen distribu-

tion incorporating Ngb has been developed (Fago et al., 2004b). This model contains three layers spanning the outer retina, between the CC and the deep retinal capillaries. Unlike the models mentioned above, a Michaelis-Menten term is used for the rate of oxygen uptake. The proportion of Ngb molecules in their oxygen bound and unbound states are assumed to be at quasi-steady-state at all times. In what follows, we extend the model of Fago et al. to describe the whole retina, neglecting the assumption that Ngb maintains an instantaneous equilibrium between its oxygen bound and unbound states.

As in the previous chapter, we address the following questions: could Ngb prevent tissue hypoxia by transporting oxygen from regions of high oxygen tension to regions of low oxygen tension, or by providing a temporary store of oxygen for use during periods when oxygen is scarce?

A fourth vertebrate globin, cytoglobin (Cygb), which is also expressed in the retina, was discovered in 2002 (Burmester et al., 2002; Trent and Hargrove, 2002). Whilst it may also play a role in oxygen transport and storage, we ignore its presence in this study, noting that since its distribution in the vertebrate retina is not correlated with mitochondrial distribution or oxygen consumption it is unlikely to play a major role in these processes (Schmidt *et al.*, 2005; however, see Section 3.5 where we challenge this conclusion).

The remainder of this chapter is structured as follows. In Section 3.2 we derive time-dependent and steady-state models on an eight layer geometry for the dynamics of oxygen and Ngb within the retina. In Section 3.3 we present some numerical results for the time-dependent and steady-state models. In Section 3.4 we perform an asymptotic analysis of the Ngb-free steady-state problem. Lastly, in Section 3.5, we summarise our findings and discuss possible directions for future research.

3.2 Model Formulation

3.2.1 Time-Dependent Model

In this section we develop a detailed model that accounts for the multilayered structure of the human retina. We decompose our model retina into eight layers:

- Layer 1: RPE;
- Layer 2: photoreceptor OSs (outer segments);
- Layer 3: photoreceptor ISs (inner segments);
- Layer 4: ONL;
- Layer 5: the outer half of the OPL;
- Layer 6: the inner half of the OPL, the INL and the outer half of the IPL;
- Layer 7: the inner half of the IPL, and the outer half of the GCL and NFL;
- Layer 8: the inner half of the GCL and NFL (see Figure 3.3).

We note that whilst Cringle and Yu (2002) also divide the model retina into 8 layers, their layers are arranged differently, incorporating different tissue layers. We label the ends of each model layer by L_i, where $i \in \{1,2,\ldots,8\}$ and $0 < L_1 < L_2 < \ldots < L_8$.

The number and arrangement of layers have been chosen to account for the differing oxygen demands of the various retinal layers, to allow the incorporation of vasculature along the boundaries between layers and to allow for the containment of Ngb within certain layers. The model includes all three vascular layers: the CC (on the left-hand boundary of layer 1), the deep retinal capillaries (on the boundary between layers 5 and 6), and the superficial retinal capillaries (on the boundary between layers 7 and 8, see Figure 3.3).

In placing the retinal capillaries along the boundaries between layers we are making the biologically justified assumption that they lie in a plane (due, in part, to the fact that the width

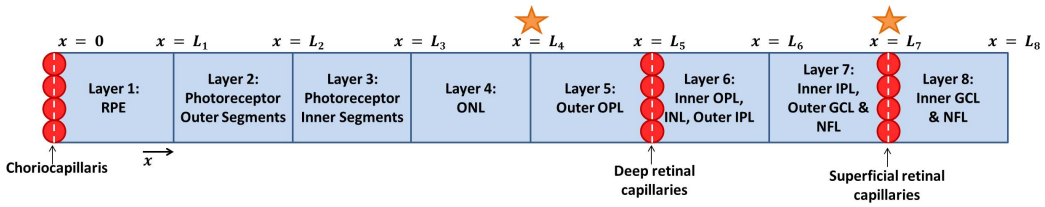

Figure 3.3: Eight layer model diagram. Oxygen is supplied to the tissue via the choriocapillaris and retinal capillaries, and the net-flux of oxygen at $x = L_8$ is zero. The flux of Ngb between layers is zero, except at those boundaries marked with stars, across which the concentration and flux of Ngb is continuous. RPE: retinal pigment epithelium. ONL: outer nuclear layer. OPL: outer plexiform layer. INL: inner nuclear layer. IPL: inner plexiform layer. GCL: ganglion cell layer. NFL: nerve fibre layer.

of the retina is much smaller than the radius of curvature of the eye) and that their width (about 5 μm, Pournaras *et al.*, 2008) is small relative to the other model layers. (The exception is the RPE which is of a similar width to the capillary layers. We treat the RPE as a layer in its own right so that we can use our knowledge of the oxygen concentration at the CC, thus avoiding the problem of determining the drop in oxygen concentration across the RPE.) Placing retinal capillaries along the boundaries between layers, rather than assigning them their own separate layers, also allows us to account for the fact at many locations, a vertical section through the retina is free from deep or superficial capillaries, though still supplied by neighbouring capillaries.

As with the single layer model, the following non-dimensional equations hold in each retinal layer:

$$\frac{\partial c}{\partial t} = \frac{\partial^2 c}{\partial x^2} - \frac{Q_i c}{\gamma + c} + k_2 n_o - k_1 n c, \tag{3.1}$$

$$\frac{\partial n}{\partial t} = D\frac{\partial^2 n}{\partial x^2} + k_4 n_h + \alpha k_2 n_o - k_3 n - \alpha k_1 n c, \tag{3.2}$$

$$\frac{\partial n_h}{\partial t} = D\frac{\partial^2 n_h}{\partial x^2} + k_3 n - k_4 n_h, \tag{3.3}$$

$$\frac{\partial n_o}{\partial t} = D\frac{\partial^2 n_o}{\partial x^2} + \alpha k_1 n c - \alpha k_2 n_o, \tag{3.4}$$

where Q_i (1,...,8) denotes the maximum rate of oxygen uptake in each layer. Guided by Roh

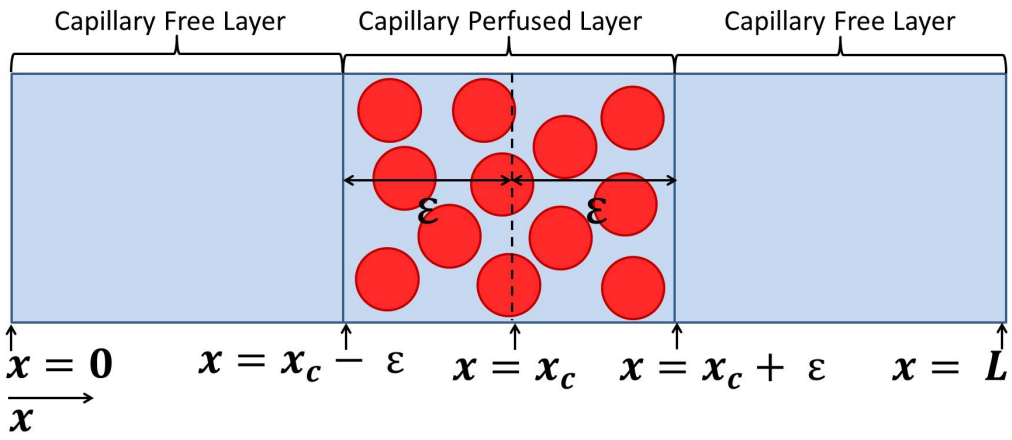

Figure 3.4: Diagram of the simple model system used to derive the oxygen boundary conditions along the boundaries containing capillaries. Capillaries are present in the central layer and absent from the surrounding layers. The boundary condition is obtained in the limit as $\varepsilon \to 0$.

et al. (1990), we suppose that the oxygen diffusion coefficient is constant across the retina and we make the same assumption for the diffusivity of Ngb.

We impose the following initial conditions:

$$c(x,0) = c_{init}(x),\ n(x,0) = n_{init}(x),\ n_h(x,0) = n_{h_{init}}(x),\ n_o(x,0) = n_{o_{init}}(x). \tag{3.5}$$

Boundary Conditions

To determine the oxygen boundary conditions across the boundaries containing capillaries ($x = L_5$ and $x = L_7$), we consider the case of a layer of tissue perfused by capillaries, surrounded on either side by tissue free of capillaries, on the domain $x \in [0,L]$ (see Figure 3.4). The perfused layer is of width 2ε and centred at $x = x_c$, where $\varepsilon < x_c < L - \varepsilon$ and $0 < \varepsilon \ll 1$. Shrinking the width of the perfused layer to zero, we obtain the desired boundary condition between the two capillary-free layers in the limit as $\varepsilon \to 0$. We describe the derivation of this condition in detail below.

Equations (3.1)–(3.4) hold in the capillary-free layers as do equations (3.2)–(3.4) in the perfused layer. Equation (3.1) is modified in the perfused layer, to include a term for the

exchange of oxygen with the capillaries:

$$\frac{\partial c}{\partial t} = \frac{\partial^2 c}{\partial x^2} - \frac{\bar{Q}c}{\gamma + c} + \underbrace{\bar{h}(c_v - c)}_{\substack{\text{exchange with} \\ \text{capillaries}}} + k_2 n_o - k_1 n c, \tag{3.6}$$

where $\bar{h}$ represents the permeability of the retinal capillaries and also accounts for their density, whilst c_v is the concentration of oxygen in the retinal capillaries (see Appendix A.4 and Appendix A.5 for more details). We define $\bar{Q} := Q_L H(x_c - x) + Q_R H(x - x_c)$, where H is a Heaviside step function, to account for the fact that the rate of oxygen uptake may differ either side of $x = x_c$.

We impose the initial conditions (3.5), with zero-flux boundary conditions for all species at $x = 0$ and $x = L$, and continuity of concentration and flux of all species across the boundaries at $x = x_c - \varepsilon$ and $x = x_c + \varepsilon$.

Integrating (3.6) with respect to x we obtain

$$\begin{aligned}\int_{x_c-\varepsilon}^{x_c+\varepsilon} \frac{\partial c}{\partial t} \mathrm{d}x = \left[\frac{\partial c}{\partial x}\right]_{x_c-\varepsilon}^{x_c+\varepsilon} - \int_{x_c-\varepsilon}^{x_c+\varepsilon} \frac{\bar{Q}c}{\gamma + c} \mathrm{d}x + \int_{x_c-\varepsilon}^{x_c+\varepsilon} \bar{h}(c_v - c) \mathrm{d}x \\ + \int_{x_c-\varepsilon}^{x_c+\varepsilon} (k_2 n_o - k_1 n c)\, \mathrm{d}x.\end{aligned} \tag{3.7}$$

As the width of the capillary perfused layer shrinks to zero, supply increases to compensate, such that, in the limit as $\varepsilon \to 0$, $\bar{h} = \hat{h}\delta(x - x_c)$, where $\delta(x - x_c)$ is the Dirac delta function, which is defined such that $\int_{x_c-\varepsilon}^{x_c+\varepsilon} f(x)\delta(x - x_c)\mathrm{d}x = f(x_c)$ for any real constant $\varepsilon > 0$ (see Ockendon *et al.*, 2003, pg. 97). Therefore,

$$\int_{x_c-\varepsilon}^{x_c+\varepsilon} \bar{h}(c_v - c)\mathrm{d}x = \hat{h}(c_v - c(x_c)),$$

as $\varepsilon \to 0$.

The oxygen concentration is piecewise smooth on the interval $x \in [x_c - \varepsilon, x_c + \varepsilon]$, with a discontinuity in its flux at $x = x_c$, due to the point source at this location. Splitting the range

of integration as follows,

$$\int_{x_c-\varepsilon}^{x_c+\varepsilon} \frac{\partial c}{\partial t}\mathrm{d}x = \int_{x_c-\varepsilon}^{x_c} \frac{\partial c}{\partial t}\mathrm{d}x + \int_{x_c}^{x_c+\varepsilon} \frac{\partial c}{\partial t}\mathrm{d}x, \tag{3.8}$$

we note that c is smooth on each of the subintervals $x \in [x_c-\varepsilon, x_c]$ and $x \in [x_c, x_c+\varepsilon]$, implying that $\frac{\partial c}{\partial t}$ is continuous and hence bounded in both intervals. Therefore, as $\varepsilon \to 0$, the integral on each subinterval tends to zero and, by equation (3.8), so does the integral over the interval $x \in [x_c-\varepsilon, x_c+\varepsilon]$.

Since $0 \leq c/(\gamma+c) < 1$, we may deduce that

$$0 \leq \int_{x_c-\varepsilon}^{x_c+\varepsilon} \frac{\bar{Q}c}{\gamma+c}\mathrm{d}x < \varepsilon(Q_L+Q_R).$$

We derive an upper bound on c by considering equation (3.6) in its steady-state, spatially homogeneous form, with the uptake terms ($\bar{Q}c/(\gamma+c)$ and k_1nc) removed, this being the scenario for which c is maximised (assuming that the initial value for c is less than or equal to this upper bound). Since $n+n_h+n_o = n_T$, n and n_o are bounded above by n_T. Setting $n_o = n_T$ in equation (3.6), to maximise the oxygen supply, and solving for c, we find that c is bounded above by $\hat{c} = c_v + \frac{k_2 n_T}{\hat{h}}$. Therefore we have that

$$\begin{aligned}
&\left| \int_{x_c-\varepsilon}^{x_c+\varepsilon} (k_2 n_o - k_1 nc)\,\mathrm{d}x \right| \\
\leq &\int_{x_c-\varepsilon}^{x_c+\varepsilon} |k_2 n_o - k_1 nc|\,\mathrm{d}x \\
\leq &\int_{x_c-\varepsilon}^{x_c+\varepsilon} |k_2 n_T + k_1 n_T \hat{c}|\,\mathrm{d}x \\
= &2\varepsilon(k_2 n_T + k_1 n_T \hat{c}).
\end{aligned}$$

Therefore, taking the limit as $\varepsilon \to 0$ in (3.7), we obtain the boundary condition:

$$\left(\frac{\partial c}{\partial x}^{+}(x_c) - \frac{\partial c}{\partial x}^{-}(x_c) \right) + \hat{h}(c_v - c(x_c)) = 0, \tag{3.9}$$

where the '$-$' and '$+$' superscripts indicate that the quantity is evaluated on the left- and right-hand sides of the boundary respectively.

Returning to the eight layer model, the oxygen boundary conditions are as follows:

$$\begin{aligned} &c(0,t) = c_c, \ \frac{\partial c}{\partial x}(L_8,t) = 0, \ [c(L_i,t)]^+_- = 0, \text{ for } i = 1,\ldots,7, \\ &\left[\frac{\partial c}{\partial x}(L_i,t)\right]^+_- = \begin{cases} 0, & \text{for } i = 1,\ldots,4 \text{ and } 6, \\ \hat{h}_i(c(L_i,t) - c_v), & \text{for } i = 5 \text{ and } 7. \end{cases} \end{aligned} \tag{3.10}$$

Thus we impose Dirichlet and zero-flux boundary conditions at the left- and right-hand ends of the domain respectively, as for the single layer model, with continuity of concentration and flux at all internal boundaries except those at which the capillaries lie, where the flux is discontinuous (see equation (3.10)). We use a Dirichlet boundary condition at $x = 0$, rather than a Robin boundary condition, since the fenestrated capillaries of the CC are highly permeable to low molecular weight substances such as oxygen (Törnquist et al., 1990).

We impose zero-flux boundary conditions upon Ngb, Ngb-His and Ngb-O_2 at $x = 0$, L_1, L_5, L_6 and L_8 since these represent boundaries between cell layers and Ngb molecules are too large to pass through cell membranes (Ngb only existing intracellularly). We also impose zero-flux boundary conditions upon Ngb, Ngb-His and Ngb-O_2 at $x = L_2$ and L_3 since we wish to maintain the high concentration of Ngb found in the photoreceptor ISs of human retinas. It may be that Ngb is unable to diffuse from the IS to the OS as it is unable to pass through the narrow connecting cilium; however, it is unclear what prevents Ngb from diffusing into the ONL. The concentration and flux of Ngb, Ngb-His and Ngb-O_2 are continuous across $x = L_4$ and L_7 since these *model* boundaries occur within cell layers, there being nothing to physically prevent these species from diffusing across these boundaries.

3.2.2 Steady-State Model

As with the single layer model, the following non-dimensional equations define the steady-state distributions for $c = c(x)$, $n_h = n_h(x)$ and $n_o = n_o(x)$ in each retinal layer:

$$0 = \frac{\mathrm{d}^2 c}{\mathrm{d}x^2} - \frac{Q_i c}{\gamma + c} + k_2 n_o - k_1 (n_{T_i} - n_h - n_o) c, \tag{3.11}$$

$$0 = D \frac{\mathrm{d}^2 n_h}{\mathrm{d}x^2} + k_3 (n_{T_i} - n_h - n_o) - k_4 n_h, \tag{3.12}$$

$$0 = D \frac{\mathrm{d}^2 n_o}{\mathrm{d}x^2} + \alpha k_1 (n_{T_i} - n_h - n_o) c - \alpha k_2 n_o, \tag{3.13}$$

where Q_i and n_{T_i} (1,...,8) denote the maximum rate of oxygen uptake in each layer and the total Ngb concentration in each layer respectively. The boundary conditions are the same as for the time-dependent eight layer model (see (3.10) above).

The dimensional and non-dimensional parameters associated with the eight layer model are presented in Tables 3.1 and 3.2 respectively (where the upper and lower values for Q_3 correspond to DA and LA respectively). Those parameters used in the eight layer model which are the same as in the single layer model are stated in Tables 2.1 and 2.2.

3.3 Numerical Results

3.3.1 Steady-State Problem – Oxygen Transport

As with the single layer model, we solved the steady-state eight layer model, (3.10)–(3.13), using the FEM. As in Chapter 2, we use piecewise linear basis functions for the FEM, solving the resulting system of nonlinear algebraic equations using the Matlab routine fsolve, employing the Trust-Region-Dogleg algorithm. We validated our FEM solutions to the steady-state problem by checking that they matched the steady-state solution to the time-dependent problem, (3.1)–(3.5) and (3.10), solved using the method of lines. We now return to the non-dimensionalisation described in Section 2.2 (as opposed to that adopted in Section 2.4).

Figure 3.5 shows the oxygen profile across a healthy human retina under LA (dotted curve)

Table 3.1: Dimensional parameters associated with the eight layer model (see equations (3.1)–(3.5) and (3.10)–(3.13)). Where two sets of units are stated, the first set was specified in the reference and the second, in brackets, uses units consistent with the dimensional model.

Parameter	Description	Value	Source
L_1		5 μm	
L_2		27.5 μm	
L_3	Positions of the	50 μm	(Yu et al., 1994)
L_4	boundaries between	100 μm	Webvision,
L_5	retinal layers	106.5 μm	`http://webvision.med.utah.edu/`
L_6		193.5 μm	
L_7		237.5 μm	
L_8		250 μm	
n_{T_i} ($i = 1,4,\ldots,8$)	Typical Ngb	2 μM	(Schmidt et al., 2003, 2005)
n_{T_2}	concentrations	0 μM	(Bentmann et al., 2005)
n_{T_3}	in each retinal layer	200 to 4000 μM	(Ostojić et al., 2006, 2008)
			(Rajendram and Rao, 2007)
Q_1		4.5 mlO_2 (100g tissue·min)$^{-1}$	
		(3×10^{-5} Ms^{-1})	
Q_i ($i = 2,4$)		0 mlO_2 (100g tissue·min)$^{-1}$	(Haugh et al., 1990)
Q_3	Maximum rate of	10 to 20	(Cringle and Yu, 2002)
	oxygen uptake by	mlO_2 (100g tissue·min)$^{-1}$	(Wangsa-Wirawan and Linsenmeier
	each retinal layer	(6.67×10^{-5} to	2003)
		1.33×10^{-4} Ms^{-1})	(Birol et al., 2007)
Q_i ($i = 5,\ldots,8$)		4 mlO_2 (100g tissue·min)$^{-1}$	
		(2.67×10^{-5} Ms^{-1})	
$\hat{h}_5$	Permeability of the	6.5×10^{-5} ms^{-1} (typically)	
	deep retinal capillaries		(Gillies et al., 1995)
$\hat{h}_7$	Permeability of the	1.3×10^{-4} ms^{-1} (typically)	(Tan et al., 2012)
	superficial retinal capillaries		
	Oxygen concentration	40 mmHg (typically)	(Hardarson et al., 2009)
c_v	in the retinal	(3.84×10^{-5} M)	(Hardarson and Stefánsson, 2010)
	capillaries		

Table 3.2: Non-dimensional parameters associated with the eight layer model (see equations (3.1)–(3.5) and (3.10)–(3.13)). (Values given to an accuracy of at most three significant figures.)

Parameter	Value
L_1	0.063
L_2	0.34
L_3	0.63
L_4	1.25
L_5	1.33
L_6	2.42
L_7	2.97
L_8	3.13
n_{T_i} ($i = 1,4,\ldots,8$)	0.02
n_{T_2}	0
n_{T_3}	2 to 40
Q_1	1.69
Q_i ($i = 2,4$)	0
Q_3	3.76 to 7.52
Q_i ($i = 5,\ldots,8$)	1.50
$\hat{h}_5$	2.64
$\hat{h}_7$	5.28
c_v	0.67

and DA (solid curve) in the absence of Ngb. The boundaries between model layers are shown by vertical lines and the layers are labelled 1–8, whilst a horizontal line marks the hypoxic threshold, γ. The only difference between LA and DA in our model is that the rate of oxygen uptake by the photoreceptor ISs, Q_3, under DA is double that under LA. As a result, the oxygen concentration in the outer retina (layers 1–5) and in layer 6, is significantly lower under DA than under LA, whereas the oxygen concentration in layers 7 and 8 remains relatively unaffected. The parameters used to generate this plot are either taken directly from the literature, or estimated from the literature, except for the permeabilities of the deep and superficial retinal capillaries, $\hat{h}_5$ and $\hat{h}_7$. These are chosen to yield profiles similar to those measured in the rat retina (which is physiologically similar to that of the human, see Yu et al., 1994, Figure 2(a)), whilst satisfying the relationship $\hat{h}_7 = 2\hat{h}_5$, since the superficial retinal capillary bed has twice the density of the deep retinal capillary bed (Gillies et al., 1995; Tan et al., 2012, see Appendix A.5 for more details). Therefore, our simulations of the retinal oxygen profile in humans constitute testable predictions. Further, as we vary $\hat{h}_5$ and $\hat{h}_7$ between 0–5 and 0–10 respectively (results not shown) we find that the outer retina will remain normoxic provided c_c is not significantly reduced, but that the inner retina (layers 6–8) may be in danger of hypoxia in layer 6, as is the case in Figure 3.5.

In Figure 3.6 we show that Ngb may prevent inner retinal hypoxia. The parameters chosen are the same as those for Figure 3.5 under DA (for which the inner retina is hypoxic in the absence of Ngb). The solid curve shows the oxygen profile in the absence of Ngb (this is the same as the solid curve in Figure 3.5) and the dotted curve shows the oxygen profile in the presence of Ngb, when Ngb is most heavily concentrated in layers 3, 6, 7 and 8. This Ngb distribution corresponds with that found in the retina of the rat by Bentmann et al. (2005) (see Appendix A.6 and Figure A.3(b)). The average Ngb concentration across the retina in this simulation is approximately 432 μM, which is larger than the average of 100-200 μM measured in the mouse retina by Schmidt et al. (2003). However, since Ngb is confined to the cytosol (the fluid compartment of cells excluding the nucleus and organelles) of retinal cells, it may be that Ngb could reach an average concentration in the cytosol much greater than 200

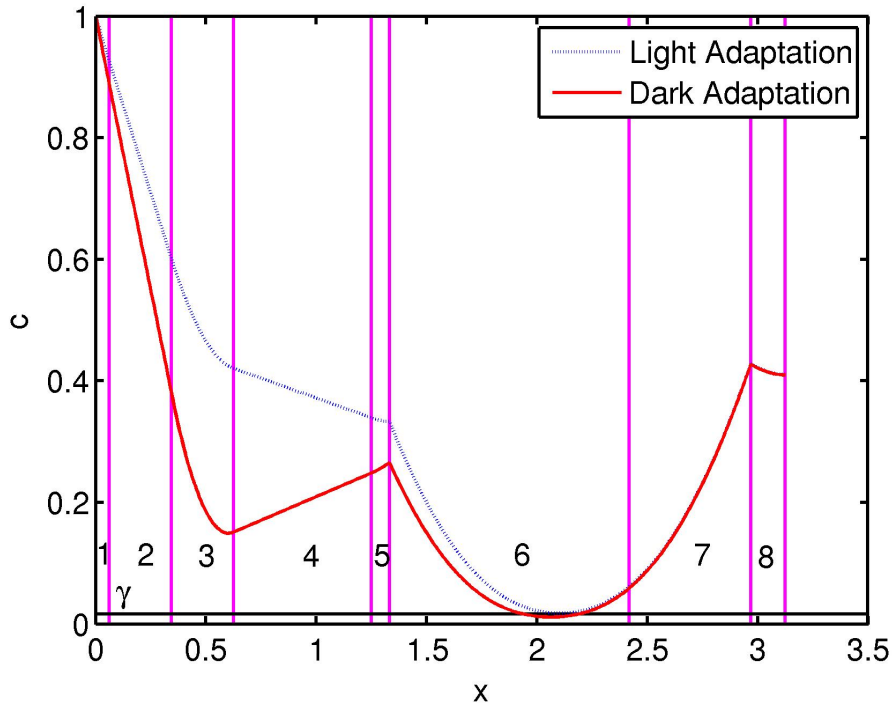

Figure 3.5: Simulation results from the eight layer model showing the oxygen distribution in the healthy human retina under LA and DA in the absence of Ngb. The spatial extent of the different layers is depicted by the vertical lines, whilst the hypoxic threshold, $c = \gamma$, is denoted by a horizontal line. The oxygen concentration in the outer retina (layers 1-5) and layer 6 is significantly lower under DA due to the increased rate of oxygen uptake by the photoreceptor ISs. Equations (3.10)–(3.13) were solved using the FEM with 501 mesh points. Under LA $Q_3 = 3.76$, whereas under DA $Q_3 = 7.52$. In both cases $n_{T_i} = 0$ ($i = 1,\ldots, 8$). Remaining parameter values as in Tables 2.2 and 3.2.

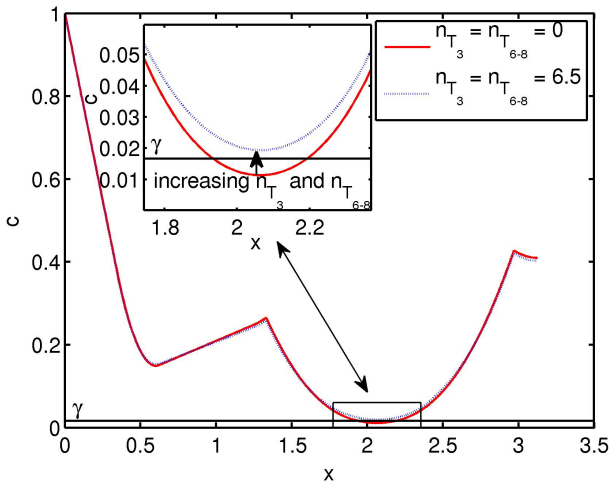

Figure 3.6: Simulation results from the eight layer model showing how the presence of Ngb in the inner retinal layers may prevent inner retinal hypoxia under DA. Key: Ngb absent (solid curve: $n_{T_i} = 0$, $i = 1,\ldots, 8$); Ngb present (dotted curve: $n_{T_1} = n_{T_4} = n_{T_5} = 0.02$, $n_{T_2} = 0$ and $n_{T_3} = n_{T_6} = n_{T_7} = n_{T_8} = 6.50$). Equations (3.10)–(3.13) were solved using the FEM with 501 mesh points. Parameter values: $Q_3 = 7.52$. Remaining parameter values as in Tables 2.2 and 3.2.

μM, without the average concentration of Ngb across the whole retina exceeding this value. As such, the Ngb concentration in our model should be interpreted as the concentration in the cytosol. It can be seen that the addition of Ngb raises the oxygen profile in the inner retina, increasing the minimum in layer 6 so that it no longer passes beneath the hypoxic threshold, $c = \gamma$. This corresponds to an increase in the minimum rate of oxygen uptake in the inner retina from 40.1% to 53.3% of Q_6, the maximum rate of oxygen uptake in this region (see equation (3.11)).

In Figure 3.7 we decrease c_c, c_v, $\hat{h}_5$ and $\hat{h}_7$ (the oxygen concentration at the CC and in the retinal capillaries, and the permeabilities of the deep and superficial retinal capillaries respectively) so that the outer retina is hypoxic in the absence of Ngb, more closely representing the macaque retina under DA (Birol et al., 2007). It is found that if Ngb is concentrated primarily in the photoreceptor ISs ($L_2 < x < L_3$), then it may prevent outer retinal hypoxia. This corresponds to an increase in the minimum rate of oxygen uptake in the outer retina from 36.8%

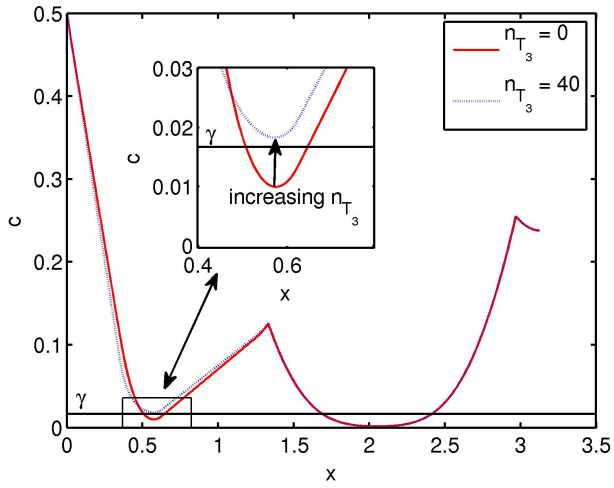

Figure 3.7: Simulation results from the eight layer model showing how the presence of Ngb in the photoreceptor ISs may prevent outer retinal hypoxia under DA. Key: Ngb absent (solid curve: $n_{T_i} = 0$, $i = 1,\ldots, 8$); Ngb present (dotted curve: $n_{T_1} = n_{T_i} = 0.02$, $n_{T_2} = 0$, $n_{T_3} = 40$, $i = 4,\ldots, 8$). Equations (3.10)–(3.13) were solved using the FEM with 501 mesh points. Parameter values: $c_c = 0.5$, $Q_3 = 7.52$, $\hat{h}_5 = 2.03$, $\hat{h}_7 = 4.06$ and $c_v = 0.5$. Remaining parameter values as in Tables 2.2 and 3.2.

to 51.8% of Q_3, the maximum rate of oxygen uptake in this region (see equation (3.11)). We remark that the inner retina is hypoxic in both cases since there is insufficient Ngb in this region. In this case, the average concentration of Ngb across the retina is approximately 362 μM.

3.3.2 Time-Dependent Problem – Oxygen Storage

Two sets of simulations were conducted for the eight layer model to explore the oxygen storage capacity of Ngb on a more realistic geometry. In both sets of simulations the FEM was used to solve the steady-state problem, (3.10)–(3.13), as in Section 3.3.1, to provide the initial conditions for the time-dependent problem, (3.1)–(3.5) and (3.10), which was solved using the method of lines.

We proceed as with the single layer model, making a step-change in a system parameter so that the steady-state concentration of oxygen decreases or increases, and observe the delay

due to Ngb in the time taken to move between steady-states. We are interested in whether this effect can prevent or reduce periods of hypoxia. The parameters we shall vary are the oxygen concentration in the retinal capillaries, c_v, and the rate of oxygen uptake in the photoreceptor ISs, Q_3, both of which may fluctuate over an average day. For instance, Q_3 will increase at night under DA and c_v might decrease as a result of blinking, eye movement or eye rubbing.

In the first set of simulations, the parameter values employed in Figure 3.6 were used for the Ngb and Ngb-free problems, the only difference being that either $c_v(t = 0) = 0.58$ and is then switched to $c_v(t = t_0) = 0.75$, for some $t_0 > 0$, or vice-versa. For $c_v = 0.58$, the inner retina is hypoxic at steady-state, in a region within layer 6, both in the presence and absence of Ngb, whereas for $c_v = 0.75$, the inner retina is normoxic at steady-state, both in the presence and absence of Ngb. Thus, following an instantaneous decrease in c_v, from $c_v = 0.75$ to $c_v = 0.58$, the inner retinal oxygen profile drops beneath the hypoxic threshold, γ, and following an instantaneous increase in c_v, from $c_v = 0.58$ to $c_v = 0.75$, the inner retinal oxygen profile rises above γ, the presence of Ngb causing a delay in each case. It was found that Ngb created a time delay of $\Delta t = 1.6$ seconds for the minimum of the inner retinal oxygen profile to drop to γ and a delay of $\Delta t = 0.8$ seconds for the minimum of the inner retinal oxygen profile to rise to γ. Thus, assuming that the system is given time to reach steady-state after each change in c_v, the net decrease in time spent in hypoxia is $\Delta t = 0.8$ seconds.

In the second set of simulations, the parameter values employed in Figure 3.7 were used for the Ngb and Ngb-free problems, the only difference being that $c_c = 0.4$ throughout and $Q_3(t)$ is switched between $Q_3 = 10$ (LA), for which the outer retina is normoxic in both the presence and absence of Ngb, and $Q_3 = 20$ (DA), for which the outer retina has an area of hypoxia in both the presence and absence of Ngb. Thus, following an instantaneous increase in Q_3, from $Q_3 = 10$ to $Q_3 = 20$, the outer retinal oxygen profile drops beneath γ, and following an instantaneous decrease in Q_3, from $Q_3 = 20$ to $Q_3 = 10$, the outer retinal oxygen profile rises above γ, the presence of Ngb causing a delay in each case. It was found that Ngb created a time delay of $\Delta t = 2.2$ seconds for the minimum of the outer retinal oxygen profile to drop to γ and a delay of $\Delta t = 0.2$ seconds for the minimum of the outer retinal oxygen profile to

rise to γ. Thus, assuming that the system is given time to reach steady-state after each change in Q_3, the net decrease in time spent in hypoxia is $\Delta t = 2.0$ seconds.

These results suggest that Ngb will preserve the human retina in normoxia for at most a few seconds.

3.4 Asymptotic Analysis of the Neuroglobin-free Problem

In this section we perform an asymptotic analysis of the Ngb-free, steady-state problem, in order to validate the piecewise linear and quadratic approximations to the oxygen profile used by Braun et al. (1995); Cringle and Yu (2002) and others.

In the absence of Ngb there is no reason to distinguish between layers 6 and 7, since the purpose of the boundary between these layers was to ensure that Ngb could not pass between them. Therefore, we now group layers 6 and 7 together, labelling this new merged layer, 'layer 6*', and relabel 'layer 8' as 'layer 7*'. In addition, equations (3.11)–(3.13) reduce to a single equation for oxygen:

$$0 = \frac{\mathrm{d}^2 c}{\mathrm{d}x^2} - \frac{Q_i c}{\gamma + c}, \tag{3.14}$$

for Q_i (1,...,7*), where we consider the parameter values to be of the same order of magnitude as those used in Figure 3.5, as these represent standard conditions for the human retina.

In layers 2 and 4, $Q_2 = Q_4 = 0$, so that an exact analytical solution to equation (3.14) may be obtained. In all other layers, Q_i is strictly positive, so that an exact analytical solution cannot be derived. In these layers we look instead for a leading order solution. Since the value of Q_i is not, in general, continuous between layers, we cannot use standard matching techniques to construct a solution which is valid across all layers. Instead we use patching, ensuring that the solution in each layer satisfies the boundary conditions between it and the adjoining layers (see Bender and Orszag, 1999, pgs. 335–336 for a discussion of patching).

We construct an asymptotic expansion for $c(x)$:

$$c(x) \sim c_0(x) + \varepsilon c_1(x) + O(\varepsilon^2), \tag{3.15}$$

choosing $\varepsilon = 0.1$, so as to provide a clear separation between the various scales, and introduce $\gamma^* = \varepsilon^{-2}\gamma$ so that $\gamma^* = O(1)$. We also note that $Q_i = O(1)$ for $i \in \{1,3,5,6^*,7^*\}$ and that $Q_2 = Q_4 = 0$. Applying the scaling on γ, equation (3.14) becomes

$$0 = \frac{\mathrm{d}^2 c}{\mathrm{d}x^2} - \frac{Q_i c}{\varepsilon^2 \gamma^* + c}. \tag{3.16}$$

We now consider the leading order solution to equation (3.16) within each layer, grouping layers that have the same scaling.

Layer 1

In layer 1, $c = O(1)$, as can be seen in Figure 3.5, and equation (3.16) supplies, at leading order,

$$c(x) \sim c_0(x) = \frac{Q_1 x^2}{2} + A_1 x + B_1, \tag{3.17}$$

where A_1 and B_1 are constants.

Layers 2 and 4

In layers 2 and 4, $Q_2 = Q_4 = 0$, so that equation (3.16) can be solved exactly to yield

$$c(x) = A_i x + B_i, \tag{3.18}$$

for $i = 2$, 4, where A_i and B_i are constants.

Layers 3, 5 and 7^*

In layers 3, 5 and 7^*, $c = O(\varepsilon)$, as can be seen in Figure 3.5. Rescaling oxygen as $c = \varepsilon c^*$, we then rescale x as $x = \varepsilon^{1/2} x_i^* + L_{i-1}$ in order to achieve a dominant balance, so that, after returning to our original scaling on c and x we have, at leading order,

$$c(x) \sim \frac{Q_i x^2}{2} + A_i x + B_i, \tag{3.19}$$

for $i \in \{3,5,7^*\}$, where A_i and B_i are constants.

Layer 6^*

The situation in layer 6^* is less straightforward. On the left- and right-hand sides of layer 6^*, $c = O(\varepsilon)$, whereas, toward the centre of the layer, in a neighbourhood around the local minimum, $c = O(\varepsilon^2)$. Where $c = O(\varepsilon)$, we could scale c and x as in layers 3, 5 and 7^*; however, in the central region, where $c = O(\varepsilon^2)$, we would regain equation (3.14) in the dominant balance after dropping the stars. Since seeking leading order solutions does not allow us to avoid dealing with equation (3.14), we instead retain equation (3.14) across the whole of layer 6^* and use quadrature methods to derive approximate analytical solutions for the oxygen profile in this layer.

We will derive separate approximations to the oxygen profile for the left-hand side, centre and right-hand side of layer 6^*, in order to account for the variation in c between $O(\varepsilon)$ and $O(\varepsilon^2)$. We will also derive approximations to the minimum oxygen concentration in layer 6^*, c_{min}, and its position, x_{min}.

Multiplying equation (3.14) by $\mathrm{d}c/\mathrm{d}x$ and integrating between x_{min} and x, we find that

$$\frac{\mathrm{d}c}{\mathrm{d}x} = \pm\sqrt{2Q_{6^*}}\sqrt{c - c_{min} - \gamma\log\left(\frac{\gamma + c}{\gamma + c_{min}}\right)}, \tag{3.20}$$

where we take the positive (negative) root to the right (left) of x_{min}, since the gradient of the oxygen profile is positive (negative) there. We note that the values of c_{min} and x_{min} are unknown at this stage.

We begin by seeking the left-hand and right-hand approximations near L_5 and L_{6^*} respectively. For the left-hand approximation, we integrate equation (3.20) between x and L_5 to obtain

$$\int_{c(x)}^{c_L}\left(s - c_{min} - \gamma\log\left(\frac{\gamma + s}{\gamma + c_{min}}\right)\right)^{-\frac{1}{2}}\mathrm{d}s = \sqrt{2Q_{6^*}}(x - L_5), \tag{3.21}$$

where $c_L = c(x = L_5)$ is unknown at this stage. Since $c \approx c_L$ in the left-hand region, where $c_L = O(\varepsilon)$, and since $c_{min} = O(\varepsilon^2)$ and $\gamma = O(\varepsilon^2)$ (see Figure 3.5 for values of c_L and c_{min}),

we may approximate the integrand by $s^{-\frac{1}{2}}$ to obtain the left-hand approximation as

$$c(x) \approx \frac{Q_{6^*}}{2}(L_5 - x)^2 + \sqrt{2Q_{6^*}c_L}(L_5 - x) + c_L. \tag{3.22}$$

In a similar way, we obtain the right-hand approximation:

$$c(x) \approx \frac{Q_{6^*}}{2}(x - L_{6^*})^2 + \sqrt{2Q_{6^*}c_R}(x - L_{6^*}) + c_R, \tag{3.23}$$

where $c_R = c(x = L_{6^*})$ is unknown at this stage. Both c_L and c_R may be found by applying the boundary conditions as described at the end of this section.

To derive the central approximation, valid in the neighbourhood of x_{min}, we integrate equation (3.20) between x_{min} and x. Writing $\log((\gamma+s)/(\gamma+c_{min})) = \log(1+(s-c_{min})/(\gamma+c_{min}))$, we expand the integrand (which is the same as in equation (3.21)) about $s = c_{min}$, in powers of $(s-c_{min})/(\gamma+c_{min})$, where s is the variable of integration and $|(s-c_{min})/(\gamma+c_{min})| \ll 1$. Retaining only the first term and neglecting higher order terms, we obtain the central solution:

$$c(x) \approx \left(1 + \frac{Q_{6^*}(x_{min} - x)^2}{2(\gamma + c_{min})}\right) c_{min}, \tag{3.24}$$

in which x_{min} and c_{min} are presently unknown.

To determine x_{min}, we integrate equation (3.20) between the limits x_{min} and L_5, and x_{min} and L_{6^*}, to obtain the following pair of equations:

$$\int_{c_{min}}^{c_L} \left(s - c_{min} - \gamma \log\left(\frac{\gamma+s}{\gamma+c_{min}}\right)\right)^{-\frac{1}{2}} \mathrm{d}s = \sqrt{2Q_{6^*}}(x_{min} - L_5), \tag{3.25}$$

$$\int_{c_{min}}^{c_R} \left(s - c_{min} - \gamma \log\left(\frac{\gamma+s}{\gamma+c_{min}}\right)\right)^{-\frac{1}{2}} \mathrm{d}s = \sqrt{2Q_{6^*}}(L_{6^*} - x_{min}). \tag{3.26}$$

Subtracting equation (3.25) from equation (3.26), and noting that $\min(c_L, c_R) \leq s \leq \max(c_L, c_R)$ in the integrand, where $c_L = O(\varepsilon)$, $c_R = O(\varepsilon)$, $c_{min} = O(\varepsilon^2)$ and $\gamma = O(\varepsilon^2)$ (see Figure 3.5

for values of c_L, c_R and c_{min}), we may approximate the integrand by $s^{-\frac{1}{2}}$ to obtain

$$x_{min} \approx \frac{L_5 + L_{6^*}}{2} - \left(\frac{\sqrt{c_R} - \sqrt{c_L}}{\sqrt{2Q_{6^*}}} \right). \tag{3.27}$$

We obtain an implicit expression for c_{min}, by substituting for x_{min} from equation (3.27) into equation (3.25):

$$\int_{c_{min}}^{c_L} \left(s - c_{min} - \gamma \log \left(\frac{\gamma + s}{\gamma + c_{min}} \right) \right)^{-\frac{1}{2}} \mathrm{d}s \approx \sqrt{\frac{Q_{6^*}}{2}} (L_{6^*} - L_5) - (\sqrt{c_R} - \sqrt{c_L}), \tag{3.28}$$

where the integral must be calculated numerically. With x_{min} and c_{min} specified by (3.27) and (3.28) respectively, we can use equation (3.24) to calculate the central solution.

Summary

To summarise, we have found that $c(x)$ is quadratic in layers 1, 3, 5 and 7^* at leading order, that it is linear in layers 2 and 4, and may be approximated by quadratics in layer 6^*. That is,

$$c(x) = \begin{cases} \frac{Q_i x^2}{2} + A_i x + B_i, & \text{for } i \in \{1,3,5,7^*\}, \\ A_i x + B_i, & \text{for } i \in \{2,4\}, \\ \frac{Q_{6^*}}{2}(L_5 - x)^2 + \sqrt{2Q_{6^*}c_L}(L_5 - x) + c_L, & \text{left-hand, layer } 6^*, \\ \left(1 + \frac{Q_{6^*}(x_{min} - x)^2}{2(\gamma + c_{min})}\right) c_{min}, & \text{central, layer } 6^*, \\ \frac{Q_{6^*}}{2}(x - L_{6^*})^2 + \sqrt{2Q_{6^*}c_R}(x - L_{6^*}) + c_R, & \text{right-hand, layer } 6^*, \end{cases} \tag{3.29}$$

where x_{min} and c_{min}, the position and size respectively, of the local minimum in layer 6^*, are given by equations (3.27) and (3.28) respectively, $c_L = c(L_5)$, $c_R = c(L_{6^*})$ and the A_is and B_is are constants of integration. The equations contain 14 unknowns ($A_1 \ldots A_5$, A_{7^*}, $B_1 \ldots B_5$, B_{7^*}, c_L and c_R), which can be found by imposing the 14 boundary conditions upon the external and internal boundaries ($c(0) = c_c$, $c_x(L_{7^*}) = 0$ and the concentration and flux conditions across the internal boundaries at $x = L_i$, for $i = 1,\ldots,6^*$). The approximation is continuous, except within layer 6^*, where it is not possible to obtain continuity between the left-hand, central and

right-hand approximations.

We can iteratively improve the accuracy of our approximation using the exact derivative, given by equation (3.20), in the oxygen-flux boundary conditions at $x = L_{6^*}$ and $x = L_{7^*}$, given by equation (3.10), to yield:

$$0 = \sqrt{2Q_{6^*}}\sqrt{c_L - c_{min} - \gamma \log\left(\frac{\gamma + c_L}{\gamma + c_{min}}\right)} + (Q_5 L_5 + A_5(c_L)) - \hat{h}_5(c_v - c_L), \tag{3.30}$$

$$0 = \sqrt{2Q_{6^*}}\sqrt{c_R - c_{min} - \gamma \log\left(\frac{\gamma + c_R}{\gamma + c_{min}}\right)} + Q_{7^*}(L_{7^*} - L_{6^*}) - \hat{h}_{6^*}(c_v - c_R). \tag{3.31}$$

The constant c_{min} takes the value calculated by solving (3.28), using the original values of c_L and c_R, whilst the constant A_5 is a function of c_L, given by:

$$A_5(c_L) = \frac{1}{L_5}\left[c_L - c_c - \frac{1}{2}\left(Q_5(L_5^2 + L_4^2) + Q_3(L_2^2 - L_3^2) - Q_1 L_1^2\right)\right]. \tag{3.32}$$

Equations (3.30)–(3.31) can be solved numerically, using the Matlab routine fsolve (employing the Trust-Region-Dogleg algorithm), to find updated values for c_L and c_R. The updated c_L and c_R can then be used to calculate an updated value for c_{min}, using equation (3.28). We may then repeat the iteration, using the updated value of c_{min} in equations (3.30)– (3.32), to find new values for c_L and c_R. Once the solution has converged, the final values of c_L and c_R can then be used to calculate improved values for $A_1, \ldots, A_5$, B_{7^*}, x_{min} and c_{min}, by applying the boundary conditions to equation (3.29) as described above and using equations (3.27) and (3.28).

It was found that iteration results in a small improvement in the accuracy of the approximation and that the solution does not change significantly (by $O(10^{-4})$ or greater) after the third iteration. Therefore, we use the parameters generated by the third iteration for the approximate solution below.

Figure 3.8 compares the approximate solution with the finite element solution to the full problem using the same parameter values as in Figure 3.5 for the dark adapted case (the FEM solution being the same as that plotted in Figure 3.5). The approximate solution agrees reasonably well with the FEM solution, though it underestimates it, particularly in layers 3

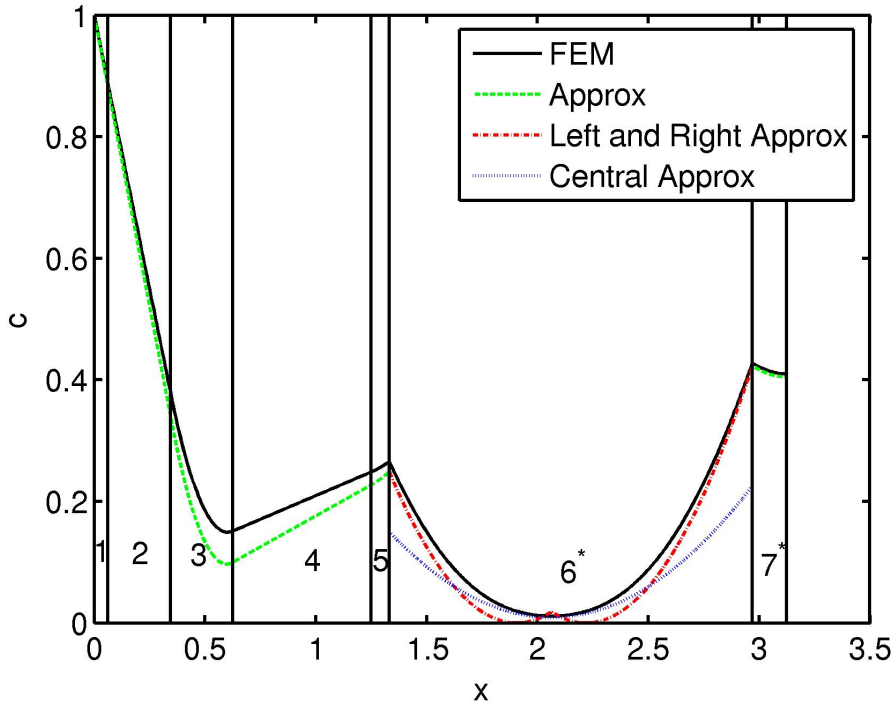

Figure 3.8: Comparison of the approximate solution with the FEM solution to the full problem. The approximate solution matches well with the FEM solution, though it is less accurate in layers 3 and 4. The left-hand solution in layer 6^* is plotted from $x = L_5$ to $x = x_{min}$, the right-hand solution is plotted from $x = x_{min}$ to $x = L_{6^*}$ and the central solution is plotted throughout layer 6^*. The spatial extent of the different layers is depicted by the vertical lines. Parameter values are the same as those used in Figure 3.5 for the dark adapted case.

and 4. The approximate value of x_{min}, $x_{min}^{app} = 2.0625$ (4 d.p.), is very close to the FEM value, $x_{min}^{FEM} = 2.0625$ (4 d.p.), with an error of $O(10^{-5})$, whilst the approximate value of c_{min}, $c_{min}^{app} = 0.0091$ (4 d.p.), is less close to the FEM value, $c_{min}^{FEM} = 0.0114$ (4 d.p.), though it is of the same order of magnitude, with an error of $O(10^{-3})$.

This analysis shows that the piecewise linear and quadratic profiles used by Braun et al. (1995); Cringle and Yu (2002) and others are valid, provided the oxygen concentration is $O(1)$ or $O(\varepsilon)$. If the oxygen concentration drops to $O(\varepsilon^2)$, that is, if it becomes hypoxic or near hypoxic, a quadratic approximation is valid; however, the coefficients of the quadratic are not the same as those based on the assumption of constant oxygen uptake used in the literature.

In this case the coefficients must be modified, as outlined above. We also note that when fitting curves to measured oxygen profiles, the value of Q in those layers where $c = O(\varepsilon^2)$ will be underestimated when using a constant oxygen uptake assumption since $c/(\gamma + c)$ is significantly less than unity in these regions.

3.5 Discussion

The retina is one of the most oxygen hungry tissues in the human body, such that, despite being well vascularised, it is frequently at risk of hypoxia. In this chapter we have investigated, via an eight layer model, the role that may be played by the protein Ngb in preventing hypoxia in the human retina. Both steady-state and time-dependent models were studied to explore Ngb's role in oxygen transport and storage respectively.

Steady-state solutions of the eight layer model revealed that Ngb may play an important role in oxygen transport in the human retina (Section 3.3.1). Whilst the effect of Ngb on the oxygen profile is subtle, an increase in the oxygen concentration through the hypoxic threshold, γ, may result in a significant increase in the rate of oxygen uptake (as much as 30–40%) since the Michaelis-Menten curve is steepest in a neighbourhood of $c = \gamma$. It was found that Ngb may prevent inner retinal hypoxia, provided it is sufficiently concentrated in this region. Similarly, if the outer retina is vulnerable to hypoxia, then outer retinal hypoxia may be avoided, provided Ngb is present in sufficient quantities in the photoreceptor ISs. Detailed measurements of the cytosolic Ngb concentration in different cellular layers of the retina are needed in order to determine whether Ngb is present in the quantities that we suggest are necessary for Ngb to play a significant role in oxygen transport.

We expect Ngb to be most highly concentrated in those layers of the retina that are most vulnerable to hypoxia. This would mean that Ngb distribution would differ between species, as retinal oxygen distribution differs between species, and perhaps within individual eyes, as oxygen supply and demand vary with eccentricity. The most closely related species in which retinal oxygen and Ngb distributions have been measured are the mouse and rat, where it was

found that Ngb is indeed most highly concentrated in those regions where oxygen is most scarce (Yu et al., 1994; Schmidt et al., 2003, 2005). Further studies are needed to confirm whether this holds true in other species. The only study to date to examine the relationship between Ngb distribution and eccentricity in the human retina found no differences in the patterns of immunoreactivity for Ngb between the central and peripheral retina (Ostojić et al., 2008); however, this does not exclude the possibility that, whilst Ngb may be present within the same retinal layers across the retina, it may be distributed differently between those layers for different eccentricities. Further experimental work is required to test this prediction.

We also note that Ngb in one region of the retina can play a protective role in preventing hypoxia in another region, even if Ngb cannot pass between these two regions. This is evident in Figure 3.6, where Ngb in layer 7 ($x \in [2.42, 2.97]$) raises the oxygen concentration on the left-hand side of the layer, so that it is at a higher concentration as it enters layer 6, a region vulnerable to hypoxia. Furthermore, whilst Bentmann et al. (2005) observe that Cygb distribution is unrelated to mitochondria distribution and oxygen consumption, this does not imply that Cygb cannot play a role in oxygen transport and storage, since it does not need to be colocalised with mitochondria containing regions in order to increase the oxygen supply to these regions. Having said this, the compartmentalisation of Ngb within the retina does reduce its capacity to transport oxygen across the retina, since oxygen-bound Ngb will often meet a barrier before reaching an oxygen poor region where it can deposit its oxygen. In other words, if Ngb is confined within a narrow region across which the drop in oxygen concentration is small, then Ngb will have a less pronounced effect than if allowed to move across a larger region where the drop in oxygen concentration is large and hence across which the drop in Ngb oxygen saturation is large.

Our simulations suggest that Ngb could protect the retina from hypoxia for at most a few seconds, by acting as an oxygen buffer, following a fluctuation in system parameters. Therefore, it is unlikely to play an important role in oxygen storage (Section 3.3.2).

Lastly, asymptotic analysis of the steady-state Ngb-free problem (Section 3.4) demonstrated that the assumption of a constant rate of oxygen uptake is valid, provided the oxygen

concentration is $O(\varepsilon)$ (where $\varepsilon = 0.1$, corresponding to ≈ 6 mmHg), or larger. This places existing models for retinal oxygen distribution on a stronger theoretical foundation. If the oxygen concentration drops to hypoxic or near-hypoxic levels, at $O(\varepsilon^2)$, then the oxygen profile can still be approximated using a quadratic, but the coefficients will be different from those that result from the constant rate of oxygen uptake assumption.

This work could be extended in several ways. The magnitude of the histidine dissociation rate, k_h^-, could be made to vary according to the oxygen concentration, so that Ngb's oxygen affinity decreases in hypoxia and increases in normoxia, to examine the extent to which this enhances the oxygen transport and storage properties of Ngb (see Appendix A.11 and Hamdane et al., 2003, for details). Models could be developed to examine the potential role of Ngb at other eccentricities within the human retina, or in other species, by adjusting the parameters relating to geometry, oxygen supply and oxygen demand. Also, Cygb could be included in the models, to determine whether it significantly augments the oxygen transport and storage properties of Ngb. The model could also be extended to 2D or 3D, and more detailed descriptions of cell metabolism and blood flow incorporated.

In conclusion, although Ngb's transport function results in only a minor shift in the oxygen profile, this can result in a significant rise in oxygen uptake and may be enough to prevent hypoxia if supply and demand are finely balanced. Ngb is unlikely to be important for oxygen storage. Finally, the assumption of a piecewise constant rate of oxygen uptake, used in previous studies, is valid, provided oxygen levels do not drop to $O(\varepsilon^2)$.

Having explored Ngb's role in the prevention of retinal hypoxia, we now consider the role of hyperoxia in the progression of the retinal degenerative diseases known as retinitis pigmentosa.

Chapter 4

Retinitis Pigmentosa: The Oxygen Toxicity Hypothesis (1D)

In the previous two chapters we considered the case in which the retina is in danger of oxygen deprivation (hypoxia). In this chapter, and that which follows, we use mathematical models, formulated as systems of PDEs and ODEs, to explore the potential role of excess oxygen (hyperoxia) in the progression of the retinal degenerative diseases, known collectively as retinitis pigmentosa. In this chapter we investigate oxygen and photoreceptor dynamics in 1D, whilst in Chapter 5 we include capillary degeneration and extend the model to 2D.

4.1 Introduction

The term retinitis pigmentosa (RP) refers to a group of genetically mediated retinal degenerative diseases that cause a progressive loss of visual function. RP is the most common inherited retinal degeneration, with a prevalence (in its nonsyndromic form) of 1 in 4000, corresponding to a total of 1.5 million affected individuals worldwide (Hamel, 2006; Hartong et al., 2006; Shintani et al., 2009). At present no treatments are clinically available either to slow its progression or reverse its effects (Musarella and MacDonald, 2011). In this chapter we investigate the prospective role of oxygen toxicity (or hyperoxia) in the progression of RP.

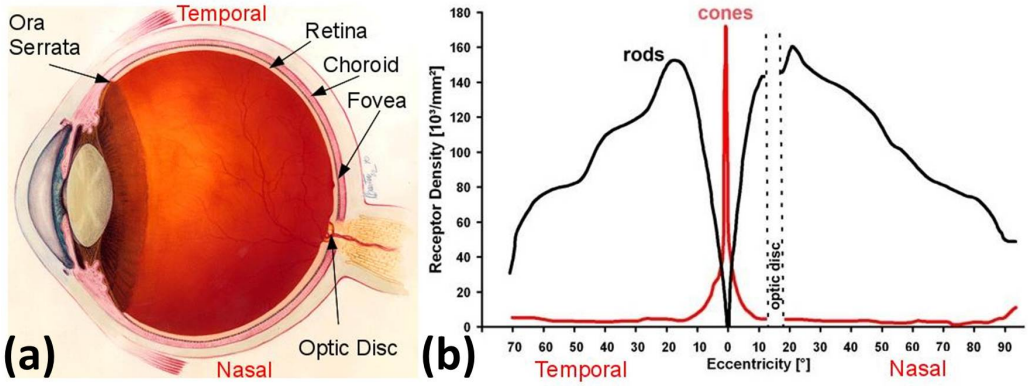

Figure 4.1: Diagrams of the human eye and retinal photoreceptor distribution. (a) Diagram of the (right) human eye, viewed in the transverse plane. Figure reproduced, with modifications, from `http://www.nei.nih.gov/health/coloboma/coloboma.asp`, courtesy: National Eye Institute, National Institutes of Health (NEI/NIH). (b) Graph to show the distribution of rods and cones, along the horizontal meridian, in the human retina. Figure reproduced, with permission and modifications, from Webvision, `http://webvision.med.utah.edu/` and originates from Østerberg (1935).

We begin by briefly describing the physiology of the retina, the pathophysiology of RP and previous mathematical models relevant to RP (see Chapter 1 for more details).

As can be seen in Figure 4.1(a), the retina is the innermost tissue layer in the eye, extending from the optic disc, where the optic nerve, central retinal artery and vein puncture the retina, to the ora serrata. Oxygen is delivered to the retina via two blood supplies: the choriocapillaris (CC, the capillary bed forming the innermost layer of the choroid), which mainly supplies the outer retina, and the retinal capillaries, which mainly supply the inner retina (Yu and Cringle, 2001; Wangsa-Wirawan and Linsenmeier, 2003). In both this and the following chapter we are concerned with the outer retina and choroid only.

The outer layer of the retina is mainly populated by two types of cell: photoreceptors and RPE cells. The light detecting photoreceptors come in two varieties: rods and cones. Rods confer achromatic vision under scotopic (low light) conditions, whilst cones provide high-acuity colour vision under photopic (well-lit) conditions. The outer parts of the photoreceptors are composed of ISs and OSs. The ISs contain most of a photoreceptor's mitochondria,

constituting their primary site of oxygen consumption, whilst the OSs are composed of discs in which light sensitive photopigments are embedded. Discs are periodically shed from the tips of OSs (where they are phagocytosed by the overlying RPE cells) and are regenerated at the OS base, with a turnover rate of 9–13 days (Young, 1971, see also Young, 1967; Young and Bok, 1969; Young, 1978; Oyster, 1999).

The average human retina contains 92 million rods and 4.6 million cones, where rod diameters lie in the range 1.5–3.0μm and cone diameters in the range 1–10μm (Curcio et al., 1990). Figure 4.1(b) shows the distribution of rods and cones in a typical human retina. Cones attain their highest density in a sharp peak centred at zero degrees eccentricity, in a region known as the fovea (see Figure 4.1(a)), their density falling off rapidly with increasing eccentricity, whilst rods are absent from the centre of the fovea, their density increasing sharply with increasing eccentricity, reaching a maximum at around 20 degrees, before falling off more gradually toward the periphery. Thus the fovea is cone dominated, whilst the rest of the retina is rod dominated. Both rods and cones are absent from the optic disc.

RP is (usually) a rod-cone dystrophy, meaning that rods are affected earlier and more severely than cones (Hamel, 2006). However, less common forms exist, in which rod and cone loss occurs on the same time scale, or in which cone loss precedes rod loss (termed a cone-rod dystrophy, Hartong et al., 2006). Histological data from humans and rats suggest that the initial loss of photoreceptors occurs in roughly circular patches which expand and coalesce over time (Cideciyan et al., 1998; Lee et al., 2011; Ji et al., 2012; García-Ayuso et al., 2013; Zhu et al., 2013).

The oxygen toxicity hypothesis was first suggested by Travis et al. (1991) and later developed by Valter et al. (1998) and Stone et al. (1999). Following the loss of photoreceptors, the oxygen demand in the outer retina is significantly decreased, resulting in an increase in outer retinal oxygen concentrations (Stone et al., 1999; Yu et al., 2000, 2004; Padnick-Silver et al., 2006). This, combined with the shortening of the photoreceptor OSs (due to mutation- or hyperoxia-induced damage), brings the remaining rod and cone ISs into a toxic oxygen environment (Travis et al., 1991; Stone et al., 1999). This results in a positive feedback loop,

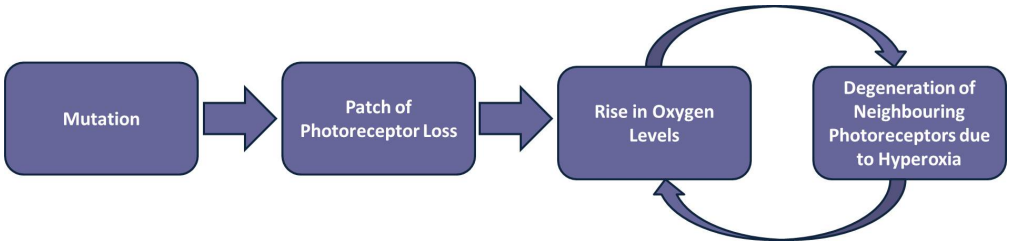

Figure 4.2: Flow chart for hyperoxia driven photoreceptor degeneration. Mutant rods degenerate, leading to patches of photoreceptor loss. This results in a rise in oxygen levels causing the degeneration of neighbouring photoreceptors, which leads to a further rise in oxygen levels, resulting in a positive feedback loop.

as high oxygen levels cause photoreceptor death, which in turn leads to an increase in oxygen levels (see Figure 4.2). Thus, the second stage of photoreceptor death is 'self-reinforcing' (Stone et al., 1999).

Both antioxidants and trophic factors may be used to treat RP: antioxidants neutralise the excess of reactive oxygen species produced under hyperoxia, while trophic factors increase photoreceptor resistance to apoptosis (Yamada et al., 2001; Kohen and Nyska, 2002; Okoye et al., 2003; Yu et al., 2004; Dong et al., 2006; Komeima et al., 2006, 2007; Sanz et al., 2007).

To date, there has been relatively little modelling work concerning either retinal degeneration in general or RP in particular.

Colón Vélez et al. (2003); Camacho et al. (2010); Camacho and Wirkus (2013) and Camacho et al. (2014) have produced a series of spatially-averaged ODE models examining the rod trophic factor hypothesis (see Section 1.3.5). Their work suggests the importance of rod trophic factor to the survival of both rods and cones. They were also able to trace the progression of the disease through distinct physiological stages and to suggest optimal treatment strategies for RP under this hypothesis.

Building on the work of Clarke et al. (2000, 2001), Burns et al. (2002) constructed a spatially explicit 1D PDE model, to examine the rod toxic substance release hypothesis (see Section 1.3.5). The model captures the initial patchy loss of photoreceptors as well as the

exponential decline in photoreceptor number measured by Clarke et al. (2000, 2001) (see also, Clarke and Lumsden, 2005a,b; Lomasko et al., 2007a,b; Lomasko and Lumsden, 2009).

The rod trophic factor models have no spatial dependence, whilst the rod toxic substance model does not distinguish between rods and cones. None of these models account for the heterogeneous distribution of rods and cones, and, as yet, no model has investigated the oxygen toxicity hypothesis (see Section 1.3.8 for more details of relevant models).

In this chapter we construct mathematical models to answer the following questions: could photoreceptor degeneration spread due to hyperoxia? If so, what spatio-temporal patterns of progression are possible or most likely via this mode of degeneration? Given that photoreceptor loss occurs in patches, is there a critical patch width, below which patches are stable and above which degeneration will spread? If so, what is this width and how does it depend upon eccentricity, if at all? Does the speed of degeneration vary with eccentricity and if so how? What effect might treatment with antioxidants and trophic factors have?

The remainder of the chapter is structured as follows: in Section 4.2 we develop our model, in Section 4.3 we perform an asymptotic analysis to determine conditions under which degeneration will spread, in Section 4.4 we solve the model numerically and in Section 4.5 we discuss our results and suggest directions for future research.

4.2 Model Formulation

Modelling the posterior of the eye as a spherical cap, we describe the geometry of the retina using spherical polar coordinates, (r, θ, ϕ), where θ is the polar angle and ϕ is the azimuthal angle. Since the part of the eye containing the retina is almost spherical (Oyster, 1999) this is a reasonable approximation. The fovea lies almost exactly at the centre of the retina, opposite the lens, and so, ignoring the optic disc, we assume that the retina is axisymmetric about the z-axis (oriented to pass outwards through the centre of the fovea, perpendicular to the wall of the eye) and neglect variation in the azimuthal angle, ϕ. We also neglect variation in the radial displacement, r, in order to form the simplest possible non-trivial model and to ensure that it

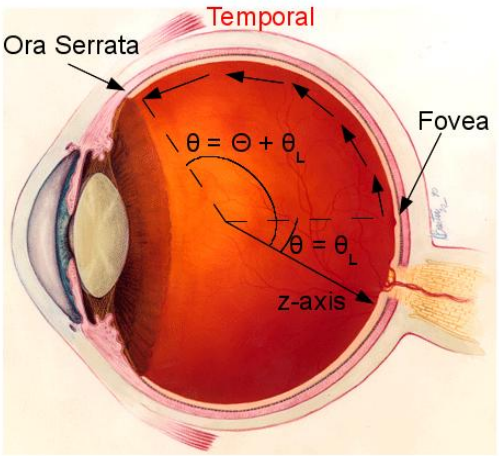

Figure 4.3: Model geometry. The domain is located between the foveal centre, at $\theta = \theta_L$, and the ora serrata, at $\theta = \Theta + \theta_L$, along the temporal horizontal meridian. The eye is pictured in the transverse plane. Figure reproduced, with modifications, from `http://www.nei.nih.gov/health/coloboma/coloboma.asp`, courtesy: National Eye Institute, National Institutes of Health (NEI/NIH).

is analytically tractable. This approximation is justified since the retina is extremely thin in comparison with its displacement from the origin and we are concerned only with its outer portion, between the photoreceptor ISs and the CC. We rotate the coordinate system such that $\theta = \theta_L$ at the foveal centre and $\theta = \Theta + \theta_L$ at the ora serrata, displacing the coordinate system from $\theta = 0$ by a positive constant θ_L, in order to avoid the coordinate singularity there. Figure 4.3 shows the model geometry.

Having defined the geometry, we construct equations for the retinal oxygen concentration, $c(\theta,t)$ and photoreceptor density, $p(\theta,t)$. The oxygen equation is as follows

$$\frac{\partial c}{\partial t} = \underbrace{\frac{D}{R^2\sin(\theta)}\frac{\partial}{\partial\theta}\left(\sin(\theta)\frac{\partial c}{\partial\theta}\right)}_{\text{diffusion}} - \underbrace{\frac{\alpha Q p c}{\gamma + c}}_{\text{uptake}} + \underbrace{\beta h(c_{ch} - c)}_{\substack{\text{exchange with}\\ \text{choroid}}}, \tag{4.1}$$

where D is the diffusion coefficient and R is the radius of the retina. We use a Michaelis-Menten term for the rate of oxygen uptake, where γ, the Michaelis constant, is the oxygen concentration at which the rate of uptake is half maximal. The rate of oxygen uptake is di-

rectly proportional to the local photoreceptor density, p.[1] The parameter Q is defined as the maximum rate of oxygen uptake per photoreceptor containing tissue unit, achieved as $c \to \infty$. It is defined in terms of photoreceptor containing tissue units, rather than simply photoreceptors, since the whole of the outer retina, from the ISs outward, is included in the model, including the OSs, which do not consume oxygen, and the RPE, which does. The parameter α is the ratio of unit surface area (per photoreceptor containing tissue unit) to unit volume (per photoreceptor containing tissue unit) and is required for dimensional consistency. We define c_{ch} as the oxygen concentration in the CC and β as the permeability of the CC vessels to oxygen. Lastly, h is the capillary surface area per unit volume, which is required for dimensional consistency.

The photoreceptor dynamics are given by the following equation

$$\frac{\partial p}{\partial t} = \underbrace{\mu p \left(1 - \frac{p}{\tilde{p}(\theta)}\right) \lambda_1(c)}_{\text{regrowth (normoxia)}} - \underbrace{\delta p \lambda_2(c)}_{\substack{\text{degeneration} \\ \text{(hyperoxia)}}}, \tag{4.2}$$

where μ is the intrinsic growth rate and δ is the rate of hyperoxia driven degeneration. The functions $\lambda_1(c)$ and $\lambda_2(c)$ are defined as follows:

$$\begin{aligned} &\lambda_1(c) = 1 - H(c - c_{crit}), \\ &\lambda_2(c) = 1 - \lambda_1(c) = H(c - c_{crit}) = \begin{cases} 0 & \text{if } c < c_{crit}, \\ 1 & \text{if } c \geq c_{crit}, \end{cases} \end{aligned} \tag{4.3}$$

[1] Here we assume that the rate of oxygen uptake by a rod is equal to that of a cone. Hoang et al. (2002) have measured the mitochondrial densities of rods and cones at a range of eccentricities in macaque and human retinas. It was found that, on average, cones contain 9-10 times more mitochondria than rods. This might lead one to expect that the rate of metabolism is greater in cones than in rods. However, the energy requirements of rods and cones are similar and the additional cone mitochondria most likely serve to enhance the cone light-gathering properties. Another possibility is that cone mitochondria are less efficient than those in rods (Hoang et al., 2002). In either case, and in the absence of further information, it is reasonable to assume that the rate of oxygen uptake of a rod is the same as that of a cone. In addition, cone diameter is at its minimum in the fovea (Hoang et al., 2002), where cone density is highest, so that the disparity in the width of the ellipsoidal mitochondria containing region (and hence the number of mitochondria) between rods and cones is minimal there.

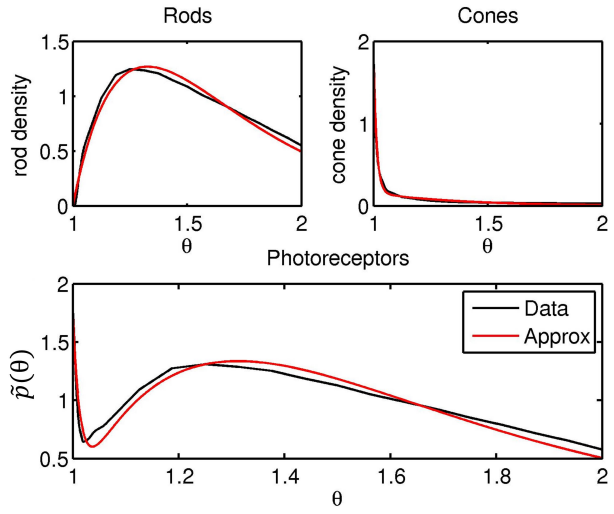

Figure 4.4: Measured and fitted photoreceptor profiles. Profiles correspond to the temporal horizontal meridian. Cone profile: $B_1 e^{-b_1(\theta-\theta_L)} + B_2 e^{-b_2(\theta-\theta_L)}$, and rod profile: $B_3(\theta - \theta_L)e^{-b_3(\theta-\theta_L)}$. The photoreceptor profile is the sum of the rod and cone profiles. Graphs are plotted in dimensionless form, using parameter values as in Table 4.3. Experimental data provided by Curcio and published in Curcio et al. (1990).

where $H(c - c_{crit})$ is a Heaviside step function and c_{crit} is the hyperoxic threshold, below which oxygen levels are considered normoxic and above which they are considered hyperoxic. We assume that rods and cones have the same hyperoxic threshold. Therefore, under normoxia, $\lambda_1 = 1$, $\lambda_2 = 0$ and regrowth is active, whereas, under hyperoxia, $\lambda_1 = 0$, $\lambda_2 = 1$ and degeneration is active. The carrying capacity, $\tilde{p}(\theta)$, is the healthy photoreceptor profile, and is given by

$$\tilde{p}(\theta) = \underbrace{B_1 e^{-b_1(\theta-\theta_L)} + B_2 e^{-b_2(\theta-\theta_L)}}_{\text{Cones}} + \underbrace{B_3(\theta - \theta_L)e^{-b_3(\theta-\theta_L)}}_{\text{Rods}}, \tag{4.4}$$

where B_1, B_2, B_3, b_1, b_2 and b_3 are positive constants. This is the simplest expression we could find that gives a good fit with the experimental profiles (see Figure 4.4 for a comparison between the fitted and experimental profiles).

Before continuing we remark that, whilst the interpretation of $p(\theta,t)$ as photoreceptor density is consistent with the work presented throughout most of this chapter, in which regrowth

does not occur, it is inconsistent with the scenario, considered in Section 4.4.5, in which regrowth does occur, since no new photoreceptors are generated following development. In this case, $p(\theta,t)$ should be interpreted as the OS biomass density (multiplied by an appropriate scaling factor to ensure dimensional consistency), since the photoreceptor OSs shrink to near zero length prior to the point at which irreversible photoreceptor damage is reached and can regrow once normoxia is restored. In this case photoreceptor oxygen demand is assumed to scale linearly with OS length, this being a measure of the health of the photoreceptor and hence its oxygen requirement.

We impose initial and boundary conditions to close equations (4.1) and (4.2). The initial conditions are as follows:

$$c(\theta,0) = c_{init}(\theta), \qquad p(\theta,0) = p_{init}(\theta) = (H(\theta-\theta_2)+H(\theta_1-\theta))\tilde{p}(\theta), \tag{4.5}$$

where the initial photoreceptor density consists of the healthy photoreceptor distribution, $\tilde{p}(\theta)$, with a single patch of photoreceptors removed from the interval $\theta \in [\theta_1,\theta_2]$, where $\theta_L \leq \theta_1 < \theta_2 \leq \Theta+\theta_L$. The initial oxygen distribution, $c_{init}(\theta)$, is the steady-state oxygen concentration corresponding to the initial photoreceptor profile (that is, the steady-state solution to (4.1) with $p = p_{init}(\theta)$). Figure 4.5 shows an example of the initial oxygen and photoreceptor profiles.

Lastly, we impose zero-flux boundary conditions at either end of the domain:

$$\frac{\partial c}{\partial \theta}(\theta_L,t) = 0 = \frac{\partial c}{\partial \theta}(\Theta+\theta_L,t). \tag{4.6}$$

Zero-flux boundary conditions are justified by symmetry at the centre of the fovea ($\theta = \theta_L$), whilst the retina terminates at the ora serrata ($\theta = \Theta+\theta_L$) indicating that zero-flux boundary conditions are appropriate here also. See Tables 4.1 and 4.2 for dimensional model parameter values.

Table 4.1: Parameters associated with the dimensional model (see equations (4.1)–(4.6)). Where two sets of units are stated, the first set is consistent with the dimensional model and the second, in brackets, is that specified in the reference.

Parameter	Description	Value	Source
Θ	Eccentricity of the ora serrata	1.33 rad	Curcio et al. (1990)
θ_L	Angle of displacement	1.33 rad	—
θ_1	Central extremum of degenerate patch	1.33 to 2.65 rad	—
θ_2	Peripheral extremum of degenerate patch	1.33 to 2.65 rad	—
D	Oxygen diffusion coefficient	1.97×10^{-9} m^{2}s^{-1}	Roh et al. (1990)
R	Retinal radius	1.2×10^{-2} m	Oyster (1999)
α	Ratio of unit surface area to unit volume	2.01×10^{4} m^{-1}	Estimate
Q	Maximum rate of oxygen uptake per photoreceptor containing tissue unit	1.26×10^{-17} mol s^{-1} (tissue unit)$^{-1}$	Estimated using data from Wangsa-Wirawan and Linsenmeier (2003) Birol et al. (2007)
γ	Michaelis constant	9.60×10^{-7} M (1 mmHg)	Costa et al. (1997) Richmond et al. (1999) McGuire and Secomb (2001) Goldman (2008)
β	Capillary permeability	3.6×10^{-5} m s^{-1}	Estimated using data from Törnquist et al. (1990)
h	Capillary surface area per unit volume	2.01×10^{4} m^{-1}	Estimate
c_{ch}	Oxygen concentration in the CC	5.76×10^{-5} M (60 mmHg)	Wangsa-Wirawan and Linsenmeier (2003) Birol et al. (2007)
c_{crit}	Hyperoxic threshold	3.86×10^{-5} M	Estimate
μ	Photoreceptor intrinsic growth rate	10^{-7} s^{-1}	Estimate
δ	Rate of photoreceptor degeneration	10^{-7} s^{-1}	Estimate

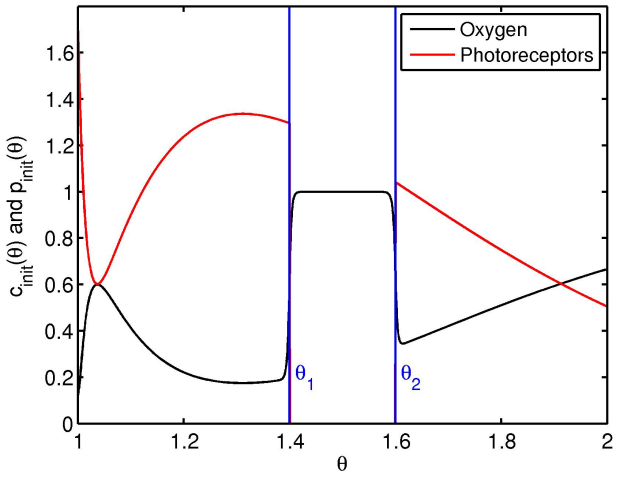

Figure 4.5: An example of the initial photoreceptor profile and associated oxygen profile used in the (non-dimensionalised) model. The vertical lines demarcate the boundaries of the degenerate patch. To obtain $c_{init}(\theta)$, equation (4.7) was solved using the finite difference method (see Section 4.4 for details), with $p(\theta)$ defined by (4.9). Parameter values: $\theta_1 = 1.4$ and $\theta_2 = 1.6$. Remaining parameter values as in Table 4.3.

Table 4.2: Dimensional photoreceptor parameters (see equation (4.4)).

Parameter	Description	Value	Source
B_1	Cone profile parameter	1.73×10^{11} photoreceptors m^{-2}	Fitted using data from Curcio et al. (1990)
B_2	Cone profile parameter	1.76×10^{10} photoreceptors m^{-2}	Fitted using data from Curcio et al. (1990)
B_3	Rod profile parameter	8.84×10^{11} photoreceptors $\mathrm{m}^{-2}\mathrm{rad}^{-1}$	Fitted using data from Curcio et al. (1990)
b_1	Cone profile parameter	54.1 rad^{-1}	Fitted using data from Curcio et al. (1990)
b_2	Cone profile parameter	2.01 rad^{-1}	Fitted using data from Curcio et al. (1990)
b_3	Rod profile parameter	2.31 rad^{-1}	Fitted using data from Curcio et al. (1990)
$\tilde{p}_A$	Mean photoreceptor density	1.11×10^{11} photoreceptors m^{-2}	Calculated using data from Curcio et al. (1990)

4.2.1 Estimation of Parameters

Before non-dimensionalising the model, we explain how the parameter values were estimated.

The photoreceptor profile parameters B_1, B_2, B_3, b_1, b_2 and b_3 were fitted to the mean photoreceptor profile across the temporal horizontal meridian of a sample of eight human retinas from seven individuals between 27 and 44 years in age. Data was provided by Curcio and is published in Curcio et al. (1990). Fitting was performed using Matlab's curve fitting toolbox, with the Trust-Region Reflective algorithm. This same data was used to calculate the mean healthy photoreceptor density, $\tilde{p}_A$.

We fixed Θ, to the most eccentric point reached by both the rods and cones along the temporal horizontal meridian (data provided by Curcio and published in Curcio et al., 1990).

The angle of displacement, θ_L, used to avoid the singularity at $\theta = 0$, was fixed such that $\theta_L = \Theta$ for three reasons: (i) to be small enough to ensure that $\Theta + \theta_L < \pi$, so as to avoid the singularity at the other pole, (ii) to be of $O(1)$ to simplify the asymptotics in Section 4.3 and (iii) so as to rescale to unity when we scale θ with Θ below.

The ratio of unit surface area to unit volume, α, was calculated by taking the ratio of the surface area of the outer surface of the RPE with the volume of the retina between the outer surface of the RPE and the inner boundary of the photoreceptor ISs (a depth of 50μm, see Table A.1). Since the CC is densely packed, we assume that its surface area is equal to the surface area of the outer surface of the RPE, therefore we fix the capillary surface area per unit volume such that $h = \alpha$, which corresponds to a fully vascularised CC.

The maximum rate of oxygen uptake, Q, is a combination of the oxygen uptake of an average photoreceptor (rod or cone) IS and OS, combined with the portion of the RPE lying directly outward from it. We assume that the photoreceptors are under LA, since it is under these conditions, when the rate of oxygen uptake of the ISs is half that under DA, that the retina will be most in danger of hyperoxia. We take the height of the RPE to be 5 μm and that of the ISs and OSs to be 22.5 μm each (see Table A.1), whilst the area of a tissue unit is assumed to be $1/\tilde{p}_A$, where $\tilde{p}_A$ is the mean photoreceptor density. The rate of oxygen uptake by the RPE is 3.00×10^{-5} Ms^{-1}, whilst that of the ISs under LA is 6.67×10^{-5} Ms^{-1} and the

OSs do not consume oxygen (see Appendix A.9 and Haugh et al., 1990; Cringle and Yu, 2002; Wangsa-Wirawan and Linsenmeier, 2003; Birol et al., 2007). Multiplying the rate of oxygen uptake of the RPE, OSs and ISs by their respective volumes and taking their sum, we obtain the maximum rate of oxygen uptake per photoreceptor containing tissue unit. When multiplied by the photoreceptor density, p, this gives the maximum rate of oxygen uptake per unit area (mol s^{-1} m^{-2}), so that upon multiplying by α, we obtain the maximum rate of oxygen uptake per unit volume (mol s^{-1} m^{-3}). We note that, by incorporating the oxygen uptake of the RPE into Q, we are assuming that the oxygen demand of the RPE is proportional to the photoreceptor density. This is reasonable given that the RPE uses oxygen to phagocytose shed OS tips and given that it degenerates around the same time as photoreceptors are lost.

Based upon the atomic weight, charge and size of an oxygen (O_2) molecule, the capillary permeability to oxygen, β, is assumed to be of the same order of magnitude as that of sodium, which is 1.8×10^{-5} ms^{-1} (Törnquist et al., 1990).

Given that neither Q nor β are known exactly, there is a degree of freedom in the choice of these values. Indeed, provided that the ratio between them is preserved, the qualitative behaviour of the system remains unaffected for a wide range of values. We have chosen Q and β so that the oxygen concentration across the retina, under healthy conditions, is similar in value to that found in the ISs under LA (see, for instance, Birol et al., 2007), whilst maintaining the correct order of magnitude for both parameters.

We choose the hyperoxic threshold, c_{crit}, to be slightly larger than the maximum steady-state oxygen concentration under healthy conditions.

The rate of photoreceptor degeneration, δ, is chosen so that degeneration occurs on a biologically realistic timescale of decades (Hartong et al., 2006). This is consistent with *in vivo* and *in vitro* measurements of the time taken for individual photoreceptors and epithelial cells to die due to hyperoxia (Wang et al., 2003; Sahaboglu et al., 2013). The intrinsic growth rate of the photoreceptors, μ, is assumed to be equal to δ, which is consistent with the timescale of photoreceptor OS regrowth (Young, 1971; Oyster, 1999).

Justification for the parameter estimates used for D and γ is given in Appendices A.7 and

A.10 respectively.

4.2.2 Non-dimensionalisation

To simplify the subsequent analysis, we non-dimensionalise the system, scaling the independent and dependent variables, together with the initial condition for oxygen, as follows

$$\theta = \Theta\theta^*, \quad t = \frac{t^*}{\delta}, \quad c = c_{ch}c^*, \quad p = \tilde{p}_A p^*, \quad c_{init} = c_{ch}c^*_{init}.$$

We define the following non-dimensional parameters:

$$\begin{aligned}
&\theta_L^* = \frac{\theta_L}{\Theta}, \quad \theta_1^* = \frac{\theta_1}{\Theta}, \quad \theta_2^* = \frac{\theta_2}{\Theta}, \quad D^* = \frac{D}{R^2\Theta^2\delta}, \quad Q^* = \frac{\alpha\tilde{p}_A}{c_{ch}\delta}Q, \\
&\gamma^* = \frac{\gamma}{c_{ch}}, \quad \beta^* = \frac{h\beta}{\delta}, \quad c^*_{crit} = \frac{c_{crit}}{c_{ch}}, \quad \mu^* = \frac{\mu}{\delta}, \quad B_1^* = \frac{B_1}{\tilde{p}_A}, \\
&B_2^* = \frac{B_2}{\tilde{p}_A}, \quad B_3^* = \frac{\Theta B_3}{\tilde{p}_A}, \quad b_1^* = \Theta b_1, \quad b_2^* = \Theta b_2, \quad b_3^* = \Theta b_3,
\end{aligned}$$

noting that $\lambda_1^*(c^*) = \lambda_1(c)$ and $\lambda_2^*(c^*) = \lambda_2(c)$.

Since oxygen diffusion, uptake and production occur on much faster timescales (seconds) than photoreceptor degeneration and regrowth (days–decades, see the dimensionless values of D, Q, β and μ in Table 4.3), we assume that the oxygen concentration is at quasi-steady-state. Therefore, dropping the stars, the system (4.1)–(4.2) reduces to

$$0 = \frac{D}{\sin(\Theta\theta)}\frac{\partial}{\partial\theta}\left(\sin(\Theta\theta)\frac{\partial c}{\partial\theta}\right) - \frac{Qpc}{\gamma + c} + \beta(1-c), \tag{4.7}$$

$$\frac{\partial p}{\partial t} = \mu p\left(1 - \frac{p}{\tilde{p}(\theta)}\right)\lambda_1(c) - p\lambda_2(c), \tag{4.8}$$

on the domain $\theta \in [\theta_L, 1+\theta_L]$, with initial conditions:

$$p(\theta, 0) = p_{init}(\theta) = (H(\theta - \theta_2) + H(\theta_1 - \theta))\tilde{p}(\theta), \tag{4.9}$$

Table 4.3: Parameters associated with the non-dimensional model (see equations (4.7)–(4.10)). (Values given to an accuracy of at most three significant figures).

Parameter	Value
θ_L	1
θ_1	1 to 2
θ_2	1 to 2
D	77.7
Q	4.89×10^6
γ	1.67×10^{-2}
β	7.23×10^6
c_{crit}	0.67
μ	1
B_1	1.56
B_2	0.158
B_3	10.6
b_1	71.8
b_2	2.67
b_3	3.06

and zero-flux boundary conditions:

$$\frac{\partial c}{\partial \theta}(\theta_L, t) = 0 = \frac{\partial c}{\partial \theta}(1 + \theta_L, t). \tag{4.10}$$

Table 4.3 shows the non-dimensional parameter values. The parameters span eight orders of magnitude, from $\gamma = O(10^{-2})$ to $Q, \beta = O(10^6)$. We exploit this in the next section, where we perform an asymptotic analysis to determine the leading order behaviour of the steady-state system.

4.3 Mathematical Analysis: Conditions for the Spread of Degeneration

In this section we perform asymptotic analyses to determine the conditions under which a patch of photoreceptor loss will enlarge over time. In particular, we seek to understand how

the stability of a degenerate patch depends upon its width and the eccentricity of its end points and how this relates to the (non-uniform) photoreceptor density profile. We consider three scenarios: in the first (Section 4.3.1), we assume that the width of the degenerate patch is significantly larger than the width of the diffusive boundary layers; in the second (Section 4.3.2), we assume that the width of the degenerate patch is less than or equal to the width of the diffusive boundary layers. In both cases we assume that the patch is separated from either edge of the domain by a distance significantly larger than the width of the diffusive boundary layers. In the third scenario (Section 4.3.3), we assume that all photoreceptors have been lost except in a narrow region (with a width of the same order of magnitude as the diffusive boundary layers) at the centre of the retina. In this way our analysis covers each stage of the disease progression, as narrow degenerate patches progress to become wide patches, eventually leading to the loss of all photoreceptors, except in the central retina.

We make the assumption, justified by the subsequent analysis and simulations, that the effect of a degenerate patch on the oxygen concentration is local. That is, the change in the oxygen profile resulting from the degenerate patch will not extend far beyond the boundaries of the patch. By making this assumption we rule out the possibility that a degenerate patch in one region of the retina could cause hyperoxia driven photoreceptor loss in a separate region, outside the neighbourhood of the initial degenerate patch. Therefore, the only way in which a degenerate patch could lead to further photoreceptor loss is by causing oxygen levels to rise above the hyperoxic threshold in the region that borders it. Thus a patch of photoreceptor loss, $\theta \in [\theta_1, \theta_2]$, can only cause further photoreceptor loss by spreading and will do so if and only if the oxygen concentration on one or both of the borders of the patch, $c(\theta_1)$ and $c(\theta_2)$, exceeds the hyperoxic threshold, c_{crit}.

In order to determine whether a degenerate patch will spread, we need only consider the quasi-steady-state oxygen concentration corresponding to the photoreceptor profile which includes this patch of loss. By deriving a leading order solution to equation (4.7), we may derive expressions for the oxygen concentrations at the boundaries of the degenerate patch and hence determine which degenerate patches will spread and which will remain stable.

We begin by scaling the model parameters so that they are all of $O(1)$. Choosing $\varepsilon = O(10^{-2})$, we scale: $D = \varepsilon^{-1}D^*$, $Q = \varepsilon^{-3}Q^*$, $\gamma = \varepsilon\gamma^*$, $\beta = \varepsilon^{-3}\beta^*$ and $b_1 = \varepsilon^{-1}b_1^*$. We have chosen ε to provide a clear separation between the magnitudes of the parameters. Dropping the stars, equation (4.7) yields the following singular ODE for $c = c(\theta)$:

$$0 = \varepsilon^2 D\frac{\mathrm{d}^2c}{\mathrm{d}\theta^2} + \varepsilon^2 D\Theta\cot(\Theta\theta)\frac{\mathrm{d}c}{\mathrm{d}\theta} - \frac{Qp(\theta)c}{\varepsilon\gamma + c} + \beta(1-c), \tag{4.11}$$

where $p(\theta) = (H(\theta-\theta_2) + H(\theta_1-\theta))\tilde{p}$ is the instantaneous photoreceptor distribution, and

$$\tilde{p}(\theta) = B_1 e^{-\varepsilon^{-1}b_1(\theta-\theta_L)} + B_2 e^{-b_2(\theta-\theta_L)} + B_3(\theta-\theta_L)e^{-b_3(\theta-\theta_L)}. \tag{4.12}$$

As before, we impose zero-flux boundary conditions so that

$$\frac{\mathrm{d}c}{\mathrm{d}\theta}(\theta_L) = 0 = \frac{\mathrm{d}c}{\mathrm{d}\theta}(1+\theta_L). \tag{4.13}$$

We form the regular perturbation expansions:

$$c(\theta) = c_0(\theta) + \varepsilon c_1(\theta) + O(\varepsilon^2), \qquad p(\theta) = p_0(\theta) + \varepsilon p_1(\theta) + O(\varepsilon^2), \tag{4.14}$$

noting that

$$(\varepsilon\gamma + c)^{-1} = \frac{1}{c_0} - \varepsilon\frac{c_1+\gamma}{c_0^2} + O(\varepsilon^2), \tag{4.15}$$

and $\cot(\Theta\theta) \leq O(1)$ for $\theta \in [\theta_L, 1+\theta_L]$.

In each of the following three cases, the analysis proceeds as follows. We decompose the domain into outer and inner regions. In the outer regions, photoreceptor and oxygen profiles vary gradually with eccentricity, whilst, in the inner regions, photoreceptor and oxygen profiles vary rapidly with eccentricity. We construct the leading order solution in each interval, using the boundary conditions and asymptotic matching to determine the constants of integration (Bender and Orszag, 1999). This enables us to determine the oxygen concentrations on the borders of a degenerate patch and hence to determine which patches will spread and which

will remain stationary.

4.3.1 Case 1: Wide Degenerate Patch

We begin by considering the case where the degenerate patch is significantly wider than the diffusive boundary layers. This scenario emerges as a special case of the analysis presented in Section 4.3.2. We present this case first as it is the simpler of the two, allowing the key features of the analysis to be demonstrated more clearly.

It can be seen from equations (4.11) and (4.15) that $c_0(\theta) = 1 - Qp_0(\theta)/\beta$ in the outer regions. Therefore, there are three outer regions — 'left-outer' and 'right-outer' regions, in which the photoreceptors maintain a healthy distribution ($p(\theta) = \tilde{p}(\theta)$) and a 'centre-outer' region, from which photoreceptors are absent ($p(\theta) = 0$) — surrounded by boundary layers, in which the oxygen concentration varies rapidly in order to match between the outer regions and to satisfy the boundary conditions at $\theta = \theta_L$ and $\theta = \theta_L + 1$. As a result, the domain must be partitioned as shown in Figure 4.6.

At $\theta = \theta_L$ and $\theta = \theta_L + 1$, boundary layers of width $O(\varepsilon)$ are introduced in order to satisfy the zero-flux boundary conditions and, in the former case, to account for the peak in cone density (see the first term in equation (4.12)). We label these boundary layers the 'far-left-inner' and the 'far-right-inner' respectively.

The boundary layers (of width $O(\varepsilon)$) surrounding the centre-outer region must each be divided in two, at the points $\theta = \theta_1$ and $\theta = \theta_2$, since $p(\theta) = 0$ for $\theta \in [\theta_1, \theta_2]$ and $p(\theta) = \tilde{p}(\theta)$ for $\theta < \theta_1$ and $\theta > \theta_2$. These discontinuities in $p(\theta)$ produce discontinuities in equation (4.11). As a result, we cannot use standard matching techniques to construct a solution which is valid across the whole domain. Instead, we use patching at these points, imposing continuity of the concentration and flux of oxygen (Bender and Orszag, 1999). We label the boundary layers surrounding $\theta = \theta_1$ ($\theta = \theta_2$) the 'left-inner' ('right-inner') boundary layers, the boundary layer to the left of this point being the 'left-left-inner' ('left-right-inner') and the boundary layer to the right being the 'right-left-inner' ('right-right-inner', see Figure 4.6).

Since the leading order solutions to the left of the centre-outer region are not coupled

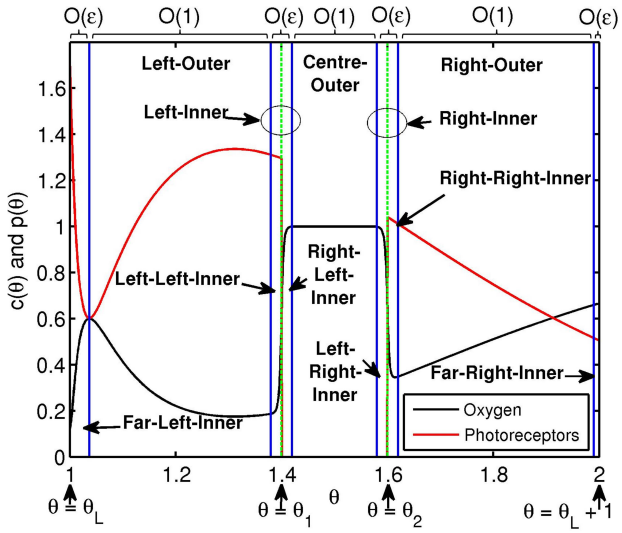

Figure 4.6: Diagram to show the locations of the outer and inner regions for the case of a wide degenerate patch. The solid vertical lines demarcate the approximate limits of the boundary layers, whilst the dashed vertical lines mark the positions of θ_1 and θ_2. Equation (4.7) was solved using the finite difference method, with $p(\theta)$ defined by (4.9). Parameter values: $\theta_1 = 1.4$ and $\theta_2 = 1.6$. Remaining parameter values as in Table 4.3.

to those from the right of this region, and since they are obtained in a similar way, we will describe only the calculation concerning the left-hand region in detail, sketching the derivation of the solutions for the right-hand region.

In the left-outer (and right-outer) region, equation (4.12) supplies $p_0(\theta) = F(\theta)$, where $F(\theta) := B_2 e^{-b_2(\theta-\theta_L)} + B_3(\theta-\theta_L)e^{-b_3(\theta-\theta_L)}$, while equation (4.11) yields

$$c_0(\theta) = 1 - \frac{Q}{\beta}F(\theta). \tag{4.16}$$

In the centre-outer region, $p_0(\theta) = 0$, and equation (4.11) yields

$$c_0(\theta) = 1. \tag{4.17}$$

In the far-left-inner region we rescale $\theta^* = \varepsilon^{-1}(\theta - \theta_L)$, in order to achieve a dominant

balance between the diffusion term and the kinetic terms in equation (4.11), yielding

$$0 = D\frac{\mathrm{d}^2 c}{\mathrm{d}\theta^{*2}} + \varepsilon D\Theta\cot(\Theta(\theta_L + \varepsilon\theta^*))\frac{\mathrm{d}c}{\mathrm{d}\theta^*} - \frac{Qp(\theta^*)c}{\varepsilon\gamma + c} + \beta(1-c), \tag{4.18}$$

where equation (4.12) supplies $p_0(\theta^*) = B_1 e^{-b_1\theta^*} + B_2$. At leading order, equation (4.18) yields

$$c_0(\theta^*) = A_1 e^{\sqrt{\frac{\beta}{D}}\theta^*} + A_2 e^{-\sqrt{\frac{\beta}{D}}\theta^*} + 1 - \frac{QB_2}{\beta} - \frac{QB_1}{\beta - b_1^2 D}e^{-b_1\theta^*}, \tag{4.19}$$

where the A_is in this equation, and all the equations that follow, are constants.

In the left-inner region we rescale $\hat{\theta} = \varepsilon^{-1}(\theta - \theta_1)$, in order to achieve a dominant balance between the diffusion term and the kinetic terms in equation (4.11), yielding an equation equivalent to equation (4.18), where $\theta^* \mapsto \hat{\theta}$ and $\theta_L \mapsto \theta_1$.

In the left-left-inner region, equation (4.12) supplies $p_0(\hat{\theta}) = F(\theta_1)$, which is constant, so that we obtain

$$c_0(\hat{\theta}) = A_3 e^{\sqrt{\frac{\beta}{D}}\hat{\theta}} + A_4 e^{-\sqrt{\frac{\beta}{D}}\hat{\theta}} + 1 - \frac{Q}{\beta}F(\theta_1), \tag{4.20}$$

whereas, in the right-left-inner region, $p_0(\hat{\theta}) = 0$, yielding

$$c_0(\hat{\theta}) = A_5 e^{\sqrt{\frac{\beta}{D}}\hat{\theta}} + A_6 e^{-\sqrt{\frac{\beta}{D}}\hat{\theta}} + 1. \tag{4.21}$$

It now remains to determine the constants $A_1, \ldots, A_6$ using matching and imposing the relevant boundary conditions.

We begin by matching the far-left-inner and left-outer solutions using Van Dyke's matching rule, which states that the m term inner expansion of the n term outer solution, should equal the n term outer expansion of the m term inner solution. In this case we take both $m = 1$ and $n = 1$, since we are dealing with leading order solutions only. The 1 term (far-left-) inner expansion of the 1 term (left-) outer solution, (4.16), is

$$c(\theta^*) \sim 1 - \frac{Q}{\beta}B_2.$$

Expanding the 1 term (far-left-) inner solution, (4.19), in (left-) outer variables we obtain

$$c(\theta) \sim A_1 e^{\varepsilon^{-1}\sqrt{\frac{\beta}{D}}(\theta-\theta_L)} + A_2 e^{-\varepsilon^{-1}\sqrt{\frac{\beta}{D}}(\theta-\theta_L)} + 1 - \frac{QB_2}{\beta} - \frac{QB_1}{\beta - b_1^2 D} e^{-\varepsilon^{-1} b_1 (\theta-\theta_L)}.$$

Since $(\theta - \theta_L) > 0$, the second and last terms are exponentially small, and so we may neglect them. However, the first term is exponentially large. Therefore, in order for the far-left-inner and left-outer solutions to match, we must have $A_1 = 0$.

Matching the left-outer and left-left-inner regions, and the right-left-inner and centre-outer regions in the same way, we find that $A_4 = A_5 = 0$.

Imposing the zero-flux boundary condition to the far-left-inner solution at $\theta = \theta_L$, and patching the left-left-inner and right-left-inner solutions together at $\theta = \theta_1$ by imposing continuity of concentration and flux at this point, we obtain three expressions for the remaining three unknowns, A_2, A_3 and A_6 in terms of the model parameters.

Substituting for $A_1, \ldots, A_6$ into equations (4.19), (4.20) and (4.21), yields the far-left-inner solution,

$$c_0(\theta^*) = 1 - \frac{QB_2}{\beta} - \frac{QB_1}{\beta - b_1^2 D}\left(e^{-b_1\theta^*} - b_1\sqrt{\frac{D}{\beta}}e^{-\sqrt{\frac{\beta}{D}}\theta^*}\right), \tag{4.22}$$

the left-left-inner solution

$$c_0(\hat{\theta}) = 1 - \frac{Q}{2\beta}(2 - e^{\sqrt{\frac{\beta}{D}}\hat{\theta}})F(\theta_1), \tag{4.23}$$

and the right-left-inner solution

$$c_0(\hat{\theta}) = 1 - \frac{Q}{2\beta}e^{-\sqrt{\frac{\beta}{D}}\hat{\theta}}F(\theta_1), \tag{4.24}$$

respectively.

We now proceed to sketch out the derivation of the leading order solutions to the right of the centre outer region, passing over the matching and patching steps, which are equivalent to those taken above, and stating the solutions with the integration constants evaluated.

In the right-inner region we rescale $\theta' = \varepsilon^{-1}(\theta - \theta_2)$, in order to achieve a dominant bal-

ance between the diffusion term and the kinetic terms in equation (4.11), yielding an equation equivalent to equation (4.18), where $\theta^* \mapsto \theta'$ and $\theta_L \mapsto \theta_2$.

In the left-right-inner region, $p_0(\theta') = 0$, so that we obtain

$$c_0(\theta') = 1 - \frac{Q}{2\beta} e^{\sqrt{\frac{\beta}{D}}\theta'} F(\theta_2), \tag{4.25}$$

whereas, in the right-right-inner region, equation (4.12) supplies $p_0(\theta') = F(\theta_2)$, which is constant, yielding

$$c_0(\theta') = 1 - \frac{Q}{2\beta}(2 - e^{-\sqrt{\frac{\beta}{D}}\theta'})F(\theta_2). \tag{4.26}$$

Lastly, in the far-right-inner region we rescale $\bar{\theta} = \varepsilon^{-1}(\theta - (\theta_L + 1))$, in order to achieve a dominant balance between the diffusion term and the kinetic terms in equation (4.11), yielding an equation equivalent to equation (4.18), where $\theta^* \mapsto \bar{\theta}$ and $\theta_L \mapsto \theta_L + 1$. Equation (4.12) supplies $p_0(\bar{\theta}) = F(\theta_L + 1)$, which is constant, so that, at leading order, we obtain

$$c_0(\bar{\theta}) = 1 - \frac{Q}{\beta} F(\theta_L + 1). \tag{4.27}$$

Having found the leading order solution in each of the inner and outer regions, we construct composite solutions for the left-hand $\theta \in [\theta_L, \theta_1]$, centre $\theta \in [\theta_1, \theta_2]$ and right-hand $\theta \in [\theta_2, 1 + \theta_L]$ regions, where we have three composite solutions due to the discontinuities in $p(\theta)$ at $\theta = \theta_1$ and $\theta = \theta_2$. Each of these regions is similar, consisting of an outer region, with an inner region on either side. In each case we expand the outer solution in terms of inner variables, and the inner solutions in terms of outer variables, to find the common terms between the inner and outer solutions. We then take the sum of the inner and outer solutions, subtracting the common terms, which would otherwise be counted twice. This yields:

the left ($\theta \in [\theta_L, \theta_1]$) composite solution:

$$c_0(\theta) = 1 - \frac{Q}{2\beta}\left(2F(\theta) - F(\theta_1)e^{-\varepsilon^{-1}\sqrt{\frac{\beta}{D}}(\theta_1-\theta)}\right) - \frac{QB_1}{\beta - b_1^2 D}\left(e^{-\varepsilon^{-1}b_1(\theta-\theta_L)} - b_1\sqrt{\frac{D}{\beta}}e^{-\varepsilon^{-1}\sqrt{\frac{\beta}{D}}(\theta-\theta_L)}\right), \tag{4.28}$$

which spans the far-left-inner, left-outer and left-left-inner regions; the centre ($\theta \in [\theta_1, \theta_2]$) composite solution:

$$c_0(\theta) = 1 - \frac{Q}{2\beta}\left(F(\theta_1)e^{-\varepsilon^{-1}\sqrt{\frac{\beta}{D}}(\theta-\theta_1)} + F(\theta_2)e^{-\varepsilon^{-1}\sqrt{\frac{\beta}{D}}(\theta_2-\theta)}\right), \tag{4.29}$$

which spans the right-left-inner, centre-outer and left-right-inner regions; and the right ($\theta \in [\theta_2, 1+\theta_L]$) composite solution:

$$c_0(\theta) = 1 - \frac{Q}{2\beta}\left(2F(\theta) - F(\theta_2)e^{-\varepsilon^{-1}\sqrt{\frac{\beta}{D}}(\theta-\theta_2)}\right), \tag{4.30}$$

which spans the right-right-inner, right-outer and far-right-outer regions.

Figure 4.7 compares the composite solution against the numerical solution to equation (4.7), with $p(\theta)$ defined by (4.9), where $\theta_1 = 1.4$ and $\theta_2 = 1.6$ (see Section 4.4 for details of the numerical solution). Numerical solutions are plotted with both Michaelis-Menten ($Qpc/(\gamma + c)$) and constant (Qp) oxygen uptake terms. The composite solution matches the numerical solution with constant uptake almost exactly, whilst the match with Michaelis-Menten uptake is still good for a leading order solution. It can be seen that the centre composite solution matches closely, whilst the left and right composite solutions slightly underestimate the numerical solution, the accuracy being lower where the photoreceptor density is greater. In particular, the oxygen concentrations at $\theta = \theta_1$ and $\theta = \theta_2$ are a close fit to the numerical solution, which is important in determining whether or not degeneration will spread. The composite solution remains accurate provided the width of the patch is of $O(1)$. If the patch width is decreased to $O(\varepsilon)$ then the composite solution breaks down in the neighbour-

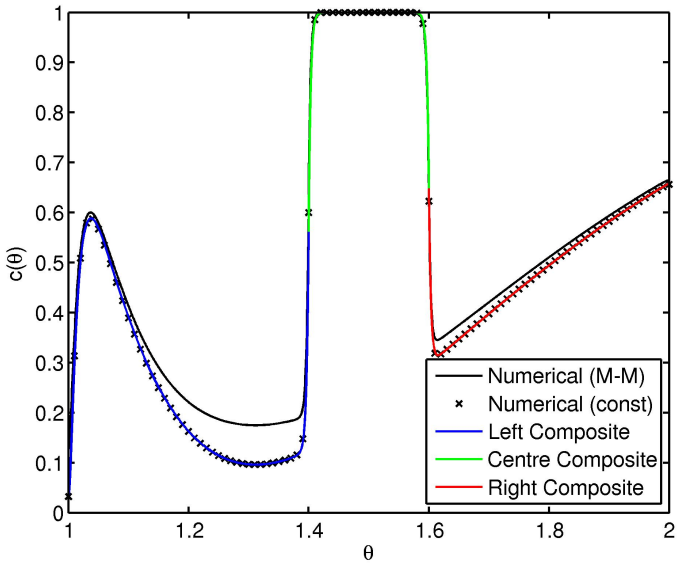

Figure 4.7: Comparison of numerical and composite solutions for the case of a wide degenerate patch. Numerical solutions are plotted with both Michaelis-Menten ($Qpc/(\gamma+c)$) and constant (Qp) oxygen uptake terms. The numerical solutions were obtained by solving equation (4.7) (subject to modification of the uptake term) using the finite difference method, with $p(\theta)$ defined by (4.9), whilst the composite solution is given by equations (4.28)–(4.30). Parameter values: $\theta_1 = 1.4$ and $\theta_2 = 1.6$. Remaining parameter values as in Table 4.3, where the parameters are scaled as described in Section 4.3 for the composite solution.

hood of the degenerate patch, as expected, given our initial assumptions.

By setting $\theta = \theta_1$ in either of equations (4.23) or (4.24) and by setting $\theta = \theta_2$ in either of equations (4.25) or (4.26), we may derive the following expression for the oxygen concentration on the left- and right-hand boundaries of the degenerate patch respectively[2]:

$$c_0(\theta_i) = 1 - \frac{Q}{2\beta} F(\theta_i) \qquad (i = 1,2). \tag{4.31}$$

Using this equation, we may determine whether degeneration will spread. We note that, because the degenerate patch is much wider than the diffusive boundary layers, necessitating a central outer region, $c_0(\theta_1)$ is independent of $c_0(\theta_2)$ and vice versa.

[2]We do not use the composite solutions to derive this expression, since they are not continuous (in concentration or flux) across $\theta = \theta_1$ and $\theta = \theta_2$, the boundary conditions having been imposed prior to their formation. In any case, the extra terms introduced in the composite solutions are negligible at these points.

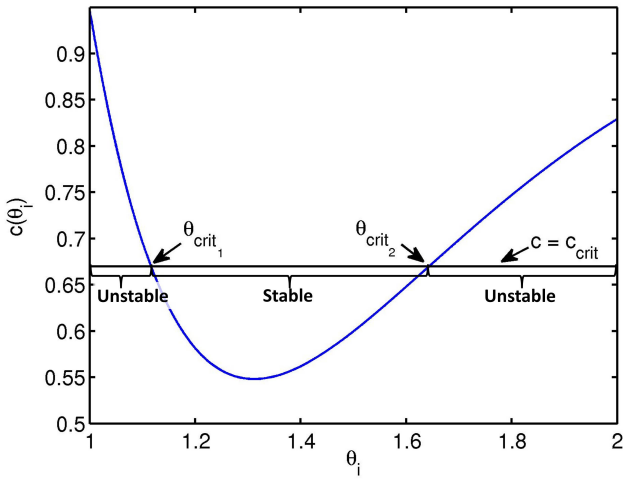

Figure 4.8: Variation of the oxygen concentration on the edge of a degenerate patch with eccentricity of the edge. Equation (4.31) is plotted with parameter values as in Table 4.3, following the application of the scalings described in Section 4.3. The horizontal line marks the hyperoxic threshold. The positions of the endpoints of the stable region, θ_{crit_1} and θ_{crit_2}, are given by equation (4.32).

Figure 4.8 shows a plot of $c_0(\theta_i)$, from equation (4.31), for $\theta_i \in [\theta_L, \theta_L + 1]$. It can be seen that for $\theta_i \in (\theta_{crit_1}, \theta_{crit_2})$, $c < c_{crit}$ and that for $\theta_i \leq \theta_{crit_1}$ and $\theta_i \geq \theta_{crit_2}$, $c \geq c_{crit}$. Therefore, the degenerate patch will remain stationary provided both ends lie in the interval $(\theta_{crit_1}, \theta_{crit_2})$, henceforth known as the 'mid-peripheral stable region'. However, if one of its ends lies outside of this interval, in one of the 'unstable regions', then it will move outwards, enlarging the patch. We label the left unstable region, the 'para/perifoveal unstable region' and the right unstable region the 'peripheral unstable region'.

Since we have assumed in our analysis that the degenerate patch is separated from the left- and right-hand boundaries by outer regions, equation (4.31) is inaccurate in a neighbourhood of $\theta_i = \theta_L$ and $\theta_i = \theta_L + 1$. Indeed, inspection of equation (4.31) reveals that only the rod profile and the second term in the cone profile affect this equation, the first term in the cone profile, which is largely responsible for the central peak in cone density, being absent (see equation (4.4)). Examination of the steady-state oxygen and photoreceptor profiles at the boundaries suggests that the approximation will break down for $\theta_i < \theta_L + 0.04$ (due to the

peak in cone density) and $\theta_i > \theta_L + 0.99$ (due to the diffusive boundary layer). The peak in cone density at $\theta = \theta_L$ introduces a second, near-central stable region. This is explored in Section 4.3.3. The effect of the zero-flux condition at $\theta = \theta_L + 1$ on the steady-state oxygen profile is subtle, causing it to flatten out for $\theta \in [1.99, 2]$ and so does not have a significant effect on the accuracy of our approximation at this boundary.

Inspection of equation (4.31) and Figure 4.8 reveals that the width of the mid-peripheral stable region will increase as Q, B_2, B_3 or c_{crit} are increased and that its width will decrease as β, b_2 or b_3 are increased. It has been shown that rod density decreases with age in healthy individuals (Curcio et al., 1993), an effect which is exacerbated by RP. Therefore, as rods are lost, B_3 will decrease, leading to a decrease in the width of the mid-peripheral stable region, which may cause previously stable degenerate patches to become unstable and so to spread. We explore this possibility in Section 4.4.3.

We can find an implicit equation for the boundaries of the mid-peripheral stable region, θ_{crit_1} and θ_{crit_2}, by setting $c = c_{crit}$ in equation (4.31) to yield

$$0 = (1 - c_{crit}) - \frac{Q}{2\beta} F(\theta_{crit_i}) \qquad (i = 1, 2). \tag{4.32}$$

As can be seen from Figure 4.8, this equation has two roots in the interval $\theta_i \in [\theta_L, \theta_L + 1]$, the lower of which corresponds to θ_{crit_1} and the higher of which corresponds to θ_{crit_2}. Using the parameter values in Table 4.3 and applying the scalings described above, we find $\theta_{crit_1} = 1.116$ and $\theta_{crit_2} = 1.643$ (to four significant figures).

As we vary θ_1 and θ_2 for $\theta_L \leq \theta_1 < \theta_2 \leq \theta_L + 1$, four types of region arise. These are displayed diagrammatically in Figure 4.9. In region A, both boundaries lie within the mid-peripheral stable region and so the patch remains stationary. In region B, θ_1 lies in the para/perifoveal unstable region whilst θ_2 lies in the mid-peripheral stable region, therefore the patch degenerates to the left, until θ_1 reaches the near-central stable region, but remains stationary on the right. In region C, θ_2 lies in the peripheral unstable region whilst θ_1 lies in the mid-peripheral stable region, therefore the patch degenerates to the right, until θ_2 reaches

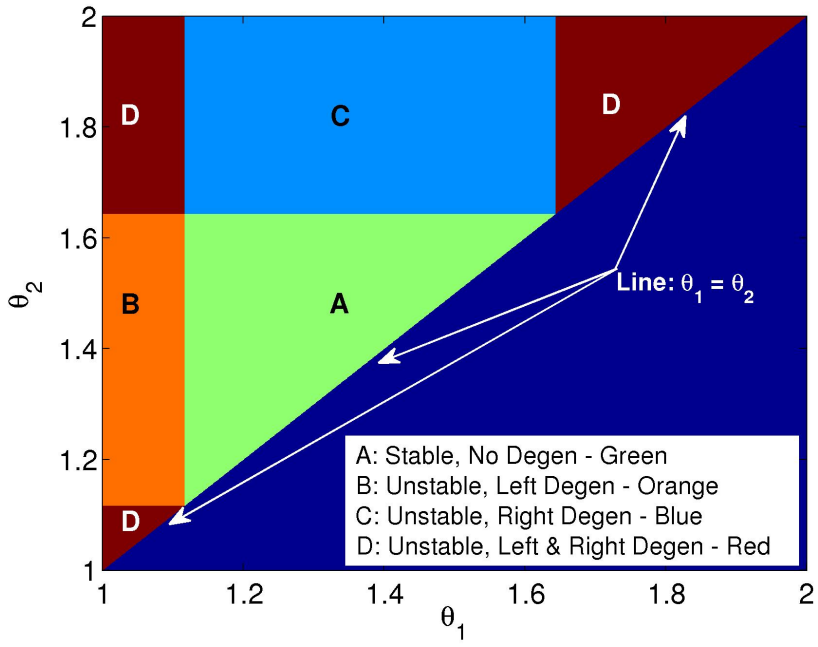

Figure 4.9: Diagram to show stable and unstable regions in (θ_1, θ_2) parameter space, under the wide degenerate patch assumption. Equation (4.31) was evaluated for a range of values of θ_1 and θ_2 ($> \theta_1$). If $c(\theta_i) < c_{crit}$, then the boundary at θ_i is stable, and if $c(\theta_i) \geq c_{crit}$, then the boundary is unstable. Parameter values as in Table 4.3, following the application of the scalings described in Section 4.3.

$\theta_L + 1$, but remains stationary on the left. Lastly, in region D (upper-left, upper-right and lower-left), both boundaries lie within one of the unstable regions, such that one of three scenarios pertain. In the first scenario (lower-left), both θ_1 and θ_2 lie in the para/perifoveal unstable region, so that the patch degenerates to the left and right until θ_1 reaches the near-central stable region and $\theta_2 = \theta_{crit_1}$. In the second scenario (upper-right), both θ_1 and θ_2 lie in the peripheral unstable region, so that the patch degenerates to the left and right until $\theta_1 = \theta_{crit_2}$ and $\theta_2 = \theta_L + 1$. Finally, in the third scenario (upper-left), θ_1 lies in the para/perifoveal unstable region and θ_2 lies in the peripheral unstable region, so that the patch degenerates to the left and right until θ_1 reaches the near-central stable region and $\theta_2 = \theta_L + 1$.

In summary, through the analysis in this section, applicable to wide degenerate patches, we have identified the existence and location of a mid-peripheral stable region, within which

degenerate patch boundaries remain stationary and outside of which they move, enlarging the patch.

4.3.2 Case 2: Narrow Degenerate Patch

In this section we consider the more general case, where the degenerate patch may be of width $O(\varepsilon)$ or less, that is, narrow enough to be contained within a diffusive boundary layer. This matches well with the patch widths measured in the rat by Ji et al. (2012); García-Ayuso et al. (2013); Zhu et al. (2013), which lie in the (non-dimensional) range 3.8×10^{-3}–1.9×10^{-2}.

We partition the domain as shown in Figure 4.10. This partitioning differs from that in Section 4.3.1 in that, since the degenerate patch is of width $O(\varepsilon)$, there is now no centre-outer region, and the right-left-inner and left-right-inner regions merge into one. For clarity, we relabel the remaining three left- and right-inner regions as the left-, centre- and right-centre-inner regions. The centre-centre-inner region extends from $\theta = \theta_1$ to $\theta = \theta_2$, whilst the left- and right-centre-inner regions lie directly to the left and right of these boundaries respectively. As before, we must patch the solutions at $\theta = \theta_1$ and $\theta = \theta_2$, due to the discontinuity in $p(\theta)$ at these points.

The leading order solutions in each region are found in a similar way to those in Section 4.3.1, the main difference being that, in the absence of a centre outer region, the solutions in the regions to either side of the degenerate patch are now coupled. We match the far-left-inner and left-outer solutions, the left-outer and left-centre-inner solutions, the right-centre-inner and right-outer solutions, and the right-outer and far-right-inner solutions, and apply the boundary conditions at $\theta = \theta_L$, $\theta = \theta_1$, $\theta = \theta_2$ and $\theta = \theta_L + 1$, noting that $\theta_2 - \theta_1 = O(\varepsilon)$.

The solutions in the far-left-inner, left-outer, right-outer and far-right-inner regions are all the same as for a wide degenerate patch (see equations (4.16), (4.22) and (4.27)), as are the scalings in those regions. It remains to calculate the solutions in the centre-inner regions.

In the left- and centre-centre-inner regions we rescale $\hat{\theta} = \varepsilon^{-1}(\theta - \theta_1)$, as with the left-inner region in Section 4.3.1.

In the left-centre-inner region, equation (4.12) supplies $p_0(\hat{\theta}) = F(\theta_1)$, which is constant,

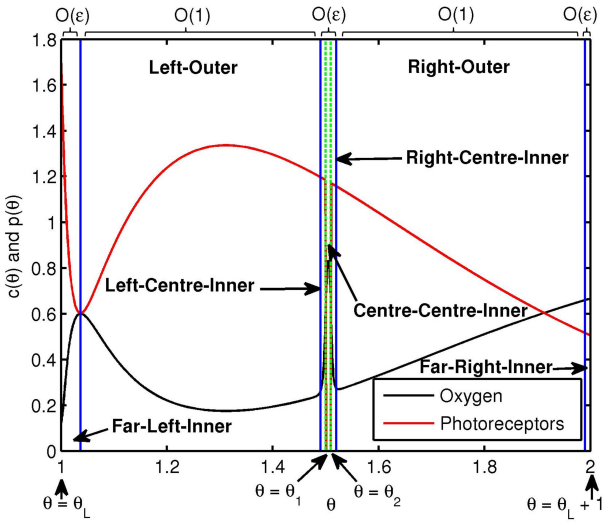

Figure 4.10: Diagram to show the locations of the outer and inner regions for the case of a narrow degenerate patch. The solid vertical lines demarcate the approximate limits of the boundary layers, whilst the dashed vertical lines mark the positions of θ_1 and θ_2. Equation (4.7) was solved using the finite difference method, with $p(\theta)$ defined by (4.9). Parameter values: $\theta_1 = 1.5$ and $\theta_2 = 1.51$. Remaining parameter values as in Table 4.3.

and we obtain

$$c_0(\hat{\theta}) = 1 - \frac{Q}{2\beta}\left(F(\theta_1)\left(2 - e^{\sqrt{\frac{\beta}{D}}\hat{\theta}}\right) + F(\theta_2)e^{-\varepsilon^{-1}\sqrt{\frac{\beta}{D}}(\theta_2-\theta_1)}e^{\sqrt{\frac{\beta}{D}}\hat{\theta}}\right). \tag{4.33}$$

The terms containing $(\theta_2 - \theta_1)$, where they occur in this and all following equations, arise through patching at $\theta = \theta_1$ and $\theta = \theta_2$. Since $\theta_2 - \theta_1 = O(\varepsilon)$, $\varepsilon^{-1}(\theta_2 - \theta_1) = O(1)$ and so $e^{\varepsilon^{-1}\sqrt{\frac{\beta}{D}}(\theta_2-\theta_1)} = O(1)$; therefore, these terms should not be neglected as exponentially small, as would be the case were $\theta_2 - \theta_1 = O(1)$. The $F(\theta_2)$ term arises from patching the centre-centre-inner and right-centre-inner solutions at $\theta = \theta_2$, the three centre-inner solutions being solved simultaneously within the boundary layer.

In the centre-centre-inner region, $p_0(\hat{\theta}) = 0$. Since the solution in this region is also (trivially) the central composite solution, we list it below with the other composite solutions.

In the right-centre-inner region we rescale $\theta' = \varepsilon^{-1}(\theta - \theta_2)$, as with the right-inner region

in Section 4.3.1. Equation (4.12) supplies $p_0(\theta') = F(\theta_2)$, which is constant, and we obtain

$$c_0(\theta') = 1 - \frac{Q}{2\beta}\left(F(\theta_2)\left(2 - e^{-\sqrt{\frac{\beta}{D}}\theta'}\right) + F(\theta_1)e^{-\varepsilon^{-1}\sqrt{\frac{\beta}{D}}(\theta_2-\theta_1)}e^{-\sqrt{\frac{\beta}{D}}\theta'}\right). \tag{4.34}$$

Proceeding as in Section 4.3.1, we may derive the following composite solutions:
the left ($\theta \in [\theta_L, \theta_1]$) composite solution:

$$\begin{aligned} c_0(\theta) = 1 &- \frac{Q}{2\beta}\left(2F(\theta) + F(\theta_2)e^{-\varepsilon^{-1}\sqrt{\frac{\beta}{D}}(\theta_2-\theta)} - F(\theta_1)e^{-\varepsilon^{-1}\sqrt{\frac{\beta}{D}}(\theta_1-\theta)}\right) \\ &- \frac{QB_1}{\beta - b_1^2 D}\left(e^{-\varepsilon^{-1}b_1(\theta-\theta_L)} - b_1\sqrt{\frac{D}{\beta}}e^{-\varepsilon^{-1}\sqrt{\frac{\beta}{D}}(\theta-\theta_L)}\right), \end{aligned} \tag{4.35}$$

which spans the far-left-inner, left-outer and left-centre-inner regions; the centre ($\theta \in [\theta_1, \theta_2]$) (trivially) composite solution:

$$c_0(\theta) = 1 - \frac{Q}{2\beta}\left(F(\theta_1)e^{-\varepsilon^{-1}\sqrt{\frac{\beta}{D}}(\theta-\theta_1)} + F(\theta_2)e^{-\varepsilon^{-1}\sqrt{\frac{\beta}{D}}(\theta_2-\theta)}\right), \tag{4.36}$$

which spans the centre-centre-inner region; and the right ($\theta \in [\theta_2, 1+\theta_L]$) composite solution:

$$c_0(\theta) = 1 - \frac{Q}{2\beta}\left(2F(\theta) + F(\theta_1)e^{-\varepsilon^{-1}\sqrt{\frac{\beta}{D}}(\theta-\theta_1)} - F(\theta_2)e^{-\varepsilon^{-1}\sqrt{\frac{\beta}{D}}(\theta-\theta_2)}\right), \tag{4.37}$$

which spans the right-centre-inner, right-outer and far-right-inner regions. We have three composite solutions due to the discontinuities in $p(\theta)$ at $\theta = \theta_1$ and $\theta = \theta_2$.

Figure 4.11 compares the composite solution against the numerical solution to equation (4.7) with $p(\theta)$ defined by (4.9), where $\theta_1 = 1.5$ and $\theta_2 = 1.51$ (see Section 4.4 for details of the numerical solution). Numerical solutions are plotted with both Michaelis-Menten ($Qpc/(\gamma+c)$) and constant (Qp) oxygen uptake terms. As with the wide degenerate patch, the composite solution is an almost exact match to the numerical solution with constant oxygen uptake, whilst the match with Michaelis-Menten uptake is also good, becoming less accurate where the photoreceptor density is greater. The composite solution also accurately approximates the numerical result for patches of width $O(1)$ (see discussion below).

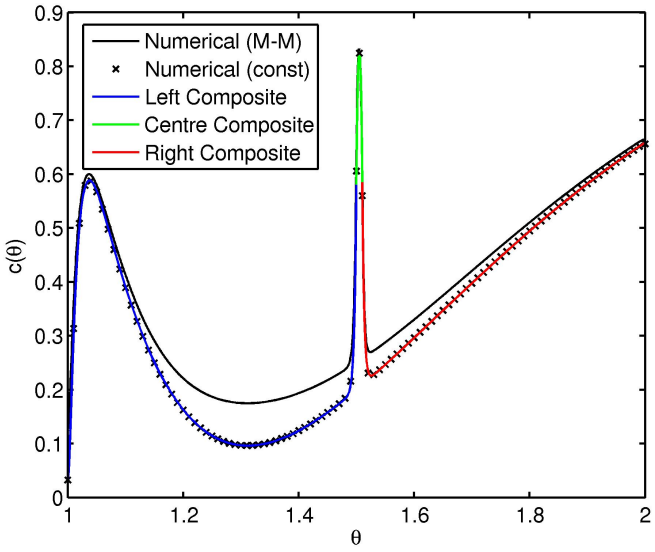

Figure 4.11: Comparison of numerical and composite solutions for the case of a narrow degenerate patch. Numerical solutions are plotted with both Michaelis-Menten ($Qpc/(\gamma+c)$) and constant (Qp) oxygen uptake terms. The numerical solutions were obtained by solving equation (4.7) (subject to modification of the uptake term) using the finite difference method, with $p(\theta)$ defined by (4.9), whilst the composite solution is given by equations (4.35)–(4.37). Parameter values: $\theta_1 = 1.5$ and $\theta_2 = 1.51$. Remaining parameter values as in Table 4.3, where the parameters are scaled as described in Section 4.3 for the composite solution.

By substituting $\theta = \theta_1$ into either of equations (4.33) or (4.36), and by substituting $\theta = \theta_2$ into either of equations (4.34) or (4.36), we may derive the following expressions for the oxygen concentration at the left- and right-hand ends of the degenerate patch respectively:

$$c_0(\theta_1) = 1 - \frac{Q}{2\beta}\left(F(\theta_1) + F(\theta_2)e^{-\varepsilon^{-1}\sqrt{\frac{\beta}{D}}(\theta_2-\theta_1)}\right), \tag{4.38}$$

$$c_0(\theta_2) = 1 - \frac{Q}{2\beta}\left(F(\theta_1)e^{-\varepsilon^{-1}\sqrt{\frac{\beta}{D}}(\theta_2-\theta_1)} + F(\theta_2)\right). \tag{4.39}$$

In can be seen that as $(\theta_2 - \theta_1)$ increases in magnitude to $O(1)$, the $e^{-\varepsilon^{-1}\sqrt{\frac{\beta}{D}}(\theta_2-\theta_1)}$ terms become exponentially small, so that equations (4.38) and (4.39) reduce to equation (4.31) at leading order. Thus the results of the wide patch analysis emerge as a special case of the narrow patch analysis, equations (4.38) and (4.39) being valid for $(\theta_2 - \theta_1) \leq O(1)$.

Unlike in the case of the wide degenerate patch, the oxygen concentration at the left-hand boundary depends upon the position of the right-hand boundary and vice-versa in equations (4.38) and (4.39). As a result, the expressions that could be derived for the boundaries of the mid-peripheral stable region (by setting $c = c_{crit}$ in equations (4.38) and (4.39), to yield expressions equivalent to (4.32)) are not particularly instructive. Instead, we may use equations (4.38) and (4.39) to determine the regions in (θ_1, θ_2) parameter space in which the patch is stable and unstable (see Figure 4.12). The same four types of region (A, B, C and D) arise as for the wide patch case and the graph is identical to that in Figure 4.9, except where $(\theta_2 - \theta_1) \leq O(\varepsilon)$. Regions A, C and D (upper-right), and A, B and D (lower-left) no longer intersect at $\theta_2 = \theta_1$ and region A extends along the line $\theta_2 = \theta_1$ to the right of the upper-right and lower-left D regions. This shows that patches can remain stable outside of the mid-peripheral stable region described by the wide patch analysis, provided they are sufficiently narrow.

4.3.3 Case 3: Preservation of the Central Retina

Lastly, we consider the case in which all photoreceptors have degenerated, except in a narrow region at the centre of the retina, where there is a peak in cone density. This corresponds to

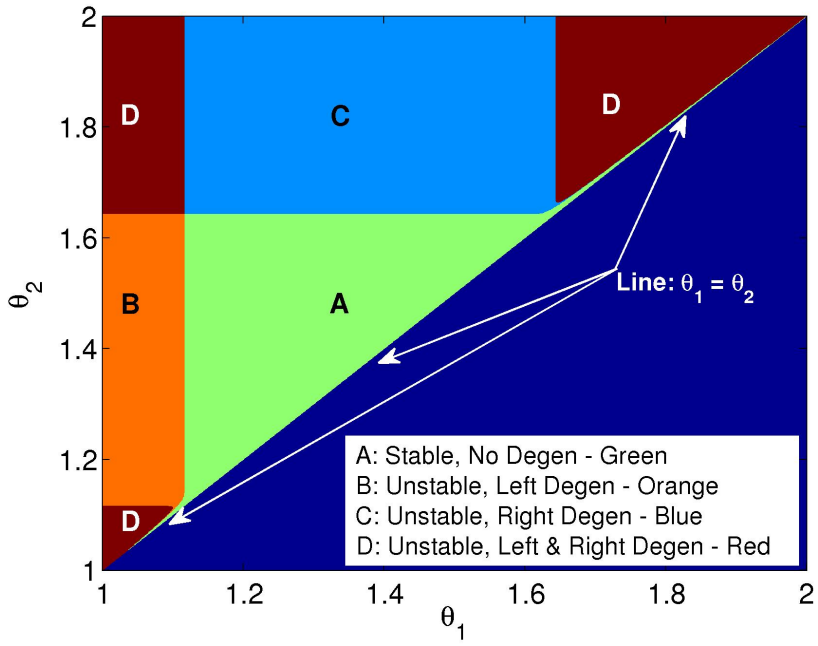

Figure 4.12: Diagram to show stable and unstable regions in (θ_1, θ_2) parameter space, under the narrow degenerate patch assumption. This figure modifies the picture presented in Figure 4.9, in the region where $\theta_1 \approx \theta_2$, demonstrating the extension of the stable region along the line $\theta_1 = \theta_2$. Equations (4.38) and (4.39) were evaluated for a range of values of both θ_1 and θ_2, where $\theta_1 < \theta_2$. If $c(\theta_i) < c_{crit}$, then the boundary at θ_i is stable, and if $c(\theta_i) \geq c_{crit}$, then the boundary is unstable. Parameter values as in Table 4.3, following the application of the scalings described in Section 4.3.

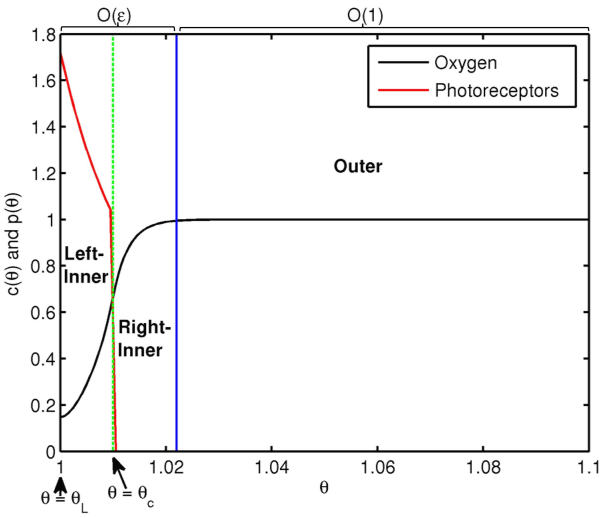

Figure 4.13: Diagram to show the locations of the outer and inner regions for the case of a preserved central retina. The solid vertical line demarcates the approximate limit of the right-inner boundary layer, whilst the dashed vertical line marks the position of θ_c. Equation (4.7) was solved using the finite difference method, with $p(\theta) = H(\theta_c - \theta)\tilde{p}(\theta)$. Parameter values: $\theta_c = 1.01$. Remaining parameter values as in Table 4.3.

the end stage of the disease in which only central vision is preserved (Hartong et al., 2006). The previous analyses are not applicable here, since they both assumed that the patch of loss was separated from $\theta = \theta_L$ by a wide outer region.

We set $p(\theta) = H(\theta_c - \theta)\tilde{p}(\theta)$, where $\theta_c - \theta_L = O(\varepsilon)$. In this case we must partition the domain into three regions: a left-inner region ($\theta \in [\theta_L, \theta_c]$), where $p(\theta) = \tilde{p}(\theta)$, and right-inner and outer regions, where $p(\theta) = 0$, as shown in Figure 4.13. We patch the left-inner and right-inner solutions together at $\theta = \theta_c$, imposing continuity of the concentration and flux of oxygen, and we match between the right-inner and outer regions.

In the outer region, $p_0(\theta) = 0$ and equation (4.11) yields

$$c_0(\theta) = 1. \tag{4.40}$$

Since the outer solution satisfies the zero-flux boundary condition at $\theta = 1 + \theta_L$, there is no boundary layer at this boundary in this case.

In the left- and right-inner regions we rescale $\theta^* = \varepsilon^{-1}(\theta - \theta_L)$, yielding equation (4.18).

In the left-inner region equation (4.12) supplies $p_0(\theta^*) = B_1 e^{-b_1\theta^*} + B_2$, while equation (4.18) yields

$$c_0(\theta) = A_1 e^{\sqrt{\frac{\beta}{D}}\theta^*} + A_2 e^{-\sqrt{\frac{\beta}{D}}\theta^*} + 1 - \frac{QB_2}{\beta} - \frac{QB_1}{\beta - b_1^2 D} e^{-b_1\theta^*}. \tag{4.41}$$

In the right-inner region, $p_0(\theta^*) = 0$, while equation (4.18) yields

$$c_0(\theta) = A_3 e^{\sqrt{\frac{\beta}{D}}\theta^*} + A_4 e^{-\sqrt{\frac{\beta}{D}}\theta^*} + 1. \tag{4.42}$$

We use the boundary conditions at $\theta = \theta_L$ and $\theta = \theta_c$, together with matching, to determine the constants $A_1, \ldots, A_4$.

We begin by matching the right-inner and outer solutions using Van Dyke's matching rule, in the same way as in Section 4.3.1. The 1 term inner expansion of the 1 term outer solution is

$$c(\theta^*) \sim 1. \tag{4.43}$$

Expanding the 1 term inner solution in outer variables we obtain

$$c(\theta) \sim A_3 e^{\varepsilon^{-1}\sqrt{\frac{\beta}{D}}(\theta - \theta_L)} + A_4 e^{-\varepsilon^{-1}\sqrt{\frac{\beta}{D}}(\theta - \theta_L)} + 1. \tag{4.44}$$

Since $(\theta - \theta_L) > 0$, the second term is exponentially small, while the first is exponentially large. Therefore, in order for the inner and outer solutions to match, we must have $A_3 = 0$. Imposing the zero-flux boundary condition at $\theta = \theta_L$ and patching at $\theta = \theta_c$, we obtain expressions for A_1, A_2 and A_4 in terms of the model parameters.

Substituting for $A_1, \ldots, A_4$ into equations (4.41) and (4.42), and converting to outer vari-

ables, yields the left-inner solution

$$c_0(\theta) = 1 - \frac{QB_2}{\beta} - \frac{QB_1}{\beta - b_1^2 D}\left(e^{-\varepsilon^{-1}b_1(\theta-\theta_L)} - b_1\sqrt{\frac{D}{\beta}}e^{-\varepsilon^{-1}\sqrt{\frac{\beta}{D}}(\theta-\theta_L)}\right) + Q\left(\frac{B_2}{\beta} + \frac{B_1}{\beta - b_1^2 D}\left[1 - b_1\sqrt{\frac{D}{\beta}}\right]e^{-\varepsilon^{-1}b_1(\theta_c-\theta_L)}\right) \times e^{-\varepsilon^{-1}\sqrt{\frac{\beta}{D}}(\theta_c-\theta_L)}\cosh\left(\varepsilon^{-1}\sqrt{\frac{\beta}{D}}(\theta-\theta_L)\right), \tag{4.45}$$

and the right-inner solution

$$c_0(\theta) = 1 - Q\left(\frac{b_1 B_1}{\beta - b_1^2 D}\sqrt{\frac{D}{\beta}}\left[e^{\varepsilon^{-1}\left(\sqrt{\frac{\beta}{D}}-b_1\right)(\theta_c-\theta_L)} - 1\right] + \left[\frac{B_2}{\beta} + \frac{B_1}{\beta - b_1^2 D}\left(1 - b_1\sqrt{\frac{D}{\beta}}\right)e^{-\varepsilon^{-1}b_1(\theta_c-\theta_L)}\right] \times \sinh\left(\varepsilon^{-1}\sqrt{\frac{\beta}{D}}(\theta_c-\theta_L)\right)\right)e^{-\varepsilon^{-1}\sqrt{\frac{\beta}{D}}(\theta-\theta_L)}, \tag{4.46}$$

respectively. We note that, since $\theta_c - \theta_L = O(\varepsilon)$, $\varepsilon^{-1}(\theta_c - \theta_L) = O(1)$ and so $e^{\varepsilon^{-1}b_1(\theta_c-\theta_L)} = O(1)$ and $e^{\varepsilon^{-1}\sqrt{\frac{\beta}{D}}(\theta_c-\theta_L)} = O(1)$; therefore, these terms should not be neglected as exponentially small, as would be the case were $\theta_c - \theta_L = O(1)$.

Equation (4.45) is trivially the left-composite solution, whilst (4.46) is the right-composite solution, where we have two composite solutions due to the discontinuity in $p(\theta)$ at $\theta = \theta_c$.

Figure 4.14 compares the composite solution against the numerical solution, with both Michaelis-Menten ($Qpc/(\gamma + c)$) and constant (Qp) oxygen uptake terms, to equation (4.7) with $p(\theta) = H(\theta_c - \theta)\tilde{p}(\theta)$, where $\theta_c = 1.01$ (see Section 4.4 for details of the numerical solution). As in the previous two sections, the composite solution matches the numerical solution with constant uptake very closely, and matches well, though less closely, when Michaelis-Menten uptake is included.

By substituting $\theta = \theta_c$ into either of equations (4.45) or (4.46), we may obtain the following expression for the oxygen concentration at the right-hand edge of the intact patch of

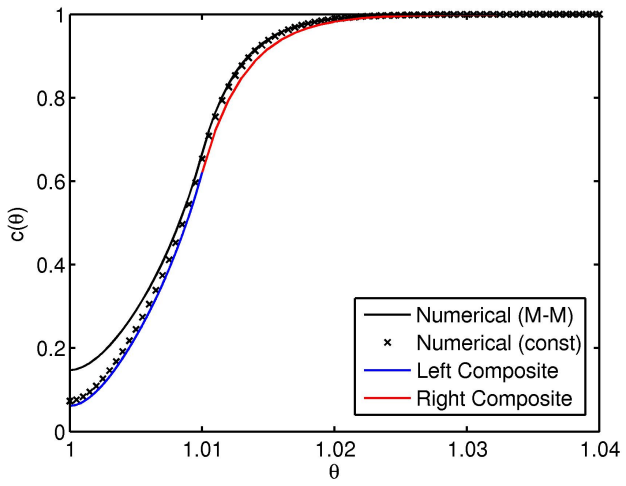

Figure 4.14: Comparison of numerical and composite solutions for the case of a preserved central retina. Numerical solutions are plotted with both Michaelis-Menten ($Qpc/(\gamma+c)$) and constant (Qp) oxygen uptake terms. The numerical solutions were obtained by solving equation (4.7) (subject to modification of the uptake term) using the finite difference method, with $p(\theta) = H(\theta_c - \theta)\tilde{p}(\theta)$, whilst the composite solution is given by equations (4.45) and (4.46). Parameter values: $\theta_c = 1.01$. Remaining parameter values as in Table 4.3, where the parameters are scaled as described in Section 4.3 for the composite solution.

photoreceptors:

$$c_0(\theta_c) = 1 - \frac{b_1 Q B_1}{\beta - b_1^2 D}\sqrt{\frac{D}{\beta}}\left(e^{-\varepsilon^{-1}b_1(\theta_c-\theta_L)} - e^{-\varepsilon^{-1}\sqrt{\frac{\beta}{D}}(\theta_c-\theta_L)}\right) - \frac{Q}{2}\left[\frac{B_2}{\beta} + \frac{B_1}{\beta - b_1^2 D}\left(1 - b_1\sqrt{\frac{D}{\beta}}\right)e^{-\varepsilon^{-1}b_1(\theta_c-\theta_L)}\right] \times \left(1 - e^{-2\varepsilon^{-1}\sqrt{\frac{\beta}{D}}(\theta_c-\theta_L)}\right), \tag{4.47}$$

allowing us to determine, for a given value of θ_c, whether the intact patch will remain stable or shrink. Figure 4.15 shows a plot of $c(\theta_c)$ for $\theta_c \in [1, 1.1]$. It can be seen that for $\theta_c \in (\theta_{crit_3}, \theta_{crit_4})$, $c < c_{crit}$, making this a stable region, whilst for $\theta_c \leq \theta_{crit_3}$ and $\theta_c \geq \theta_{crit_4}$, $c \geq c_{crit}$, making these unstable regions. Therefore, if the preserved central region extends to the right of θ_{crit_4}, it will shrink until θ_c reaches θ_{crit_4}, at which point it will halt. Similarly, if the intact patch lies to the left of θ_{crit_3}, it will degenerate until all photoreceptors are lost. Provided $\theta_c \in (\theta_{crit_3}, \theta_{crit_4})$, the patch will remain stable.

This analysis modifies the picture presented in Section 4.3.1 by introducing a second stable region, $(\theta_{crit_3}, \theta_{crit_4})$, within the para/perifoveal unstable region $[\theta_L, \theta_{crit_1}]$. We label this new stable region the 'near-central stable region', whilst we label the unstable region in which $\theta_c \leq \theta_{crit_3}$, the 'central unstable region'.

Therefore, the retina may be divided into 5 stability regions, as described in Figure 4.16. Starting from the centre of the fovea, at $\theta = \theta_L$, and proceeding peripherally, these are: the central unstable region, the near-central stable region, the para/perifoveal unstable region, the mid-peripheral stable region and the peripheral unstable region.

The transition between Figure 4.15 and Figure 4.8 is seen in the numerical solution in Figure 4.15. The numerical solution matches quite well with the approximate solution within the boundary layer, where the assumption that $\theta_c = O(\varepsilon)$ holds, but diverges as θ_c increases past 1.02. As θ_c exceeds 1.04, the numerical solution starts to descend due to the effect of increasing rod density. This effect is not captured by the approximate solution since the terms corresponding to rod density disappear from the leading order solution within the boundary

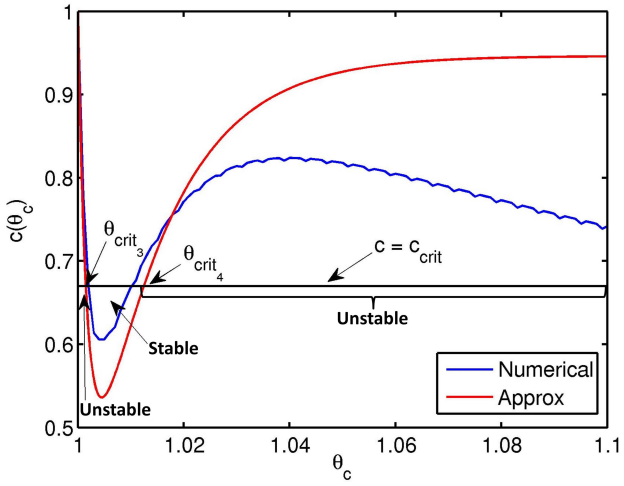

Figure 4.15: Variation of the oxygen concentration on the right-hand edge of a preserved central region with eccentricity of the edge. Numerical solution: equation (4.7) was solved using the finite difference method, with $p(\theta) = H(\theta_c - \theta)\tilde{p}(\theta)$. Approximate solution: equation (4.47). The horizontal line marks the hyperoxic threshold. The positions of the endpoints of the near-central stable region, θ_{crit_3} and θ_{crit_4}, are given by equation (4.48). Parameter values are chosen as in Table 4.3, where the parameters are scaled as described in Section 4.3 for the approximate solution.

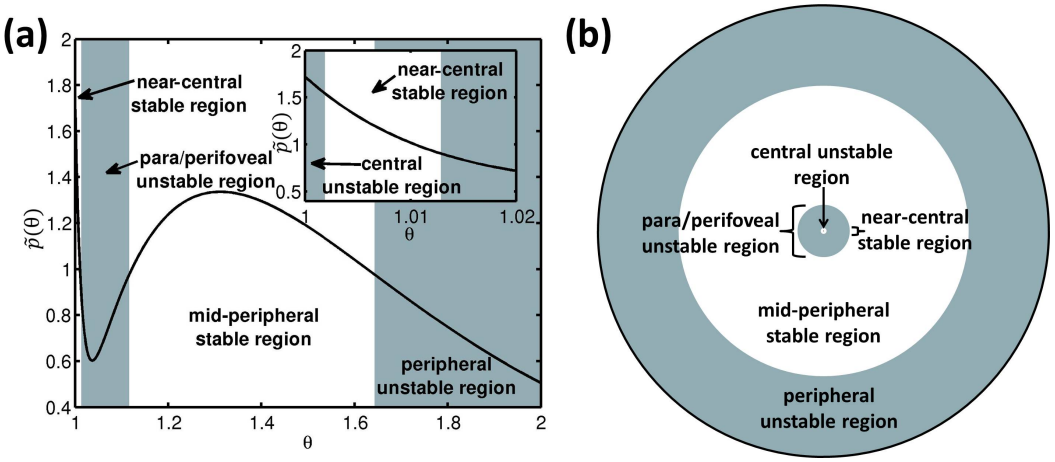

Figure 4.16: Diagrams to show the locations of the stable and unstable regions within the retina. (a) shows the relationship between the healthy photoreceptor profile and the stability regions in 1D, whilst (b) shows the locations of the stability regions in 2D. The central unstable region, which is extremely narrow, can be seen in the inset in (a).

layer. Were we to continue the plot beyond $\theta_c = 1.1$, the numerical solution would trace out a curve similar to that in Figure 4.8. We note that the numerical solution is not entirely smooth. This is because we are plotting not only a different solution, but a different point from the solution profile for each θ_c. When we plot the same point from the solution profile with varying θ_c, the resulting profile is smooth, as are the individual profiles (results not shown).

Since equation (4.47) is more involved than (4.31) it is difficult to make general statements concerning the effects of parameter changes upon the width of the near-central stable region. However, provided the other parameters remain fixed, the width of the near-central stable region will increase as Q, B_1, B_2 or c_{crit} are increased. Since terms corresponding to rod density are absent from this equation, this suggests that rod loss will have no effect upon the stability properties of the preserved central retina (see Section 4.4.3, where we confirm this numerically).

We can find an implicit equation for the boundaries of the near-central stable region, θ_{crit_3} and θ_{crit_4}, by setting $c_0(\theta_c) = c_{crit}$ in equation (4.47) to yield

$$\begin{aligned} 0 = 1 - c_{crit} &- \frac{b_1 Q B_1}{\beta - b_1^2 D}\sqrt{\frac{D}{\beta}}\left(e^{-\varepsilon^{-1}b_1(\theta_{crit_i}-\theta_L)} - e^{-\varepsilon^{-1}\sqrt{\frac{\beta}{D}}(\theta_{crit_i}-\theta_L)}\right) \\ &- \frac{Q}{2}\left[\frac{B_2}{\beta} + \frac{B_1}{\beta - b_1^2 D}\left(1 - b_1\sqrt{\frac{D}{\beta}}\right)e^{-\varepsilon^{-1}b_1(\theta_{crit_i}-\theta_L)}\right] \\ &\times\left(1 - e^{-2\varepsilon^{-1}\sqrt{\frac{\beta}{D}}(\theta_{crit_i}-\theta_L)}\right) \qquad (i = 3,4). \end{aligned} \tag{4.48}$$

As can be seen from Figure 4.15, this equation has two roots in the interval $\theta_i \in [\theta_L, \theta_L + 1]$ (the curve for the approximate solution remains level to the right of $\theta_c = 1.1$), the lower of which corresponds to θ_{crit_3} and the higher of which corresponds to θ_{crit_4}. Using the parameter values in Table 4.3 and applying the scalings described above, we find $\theta_{crit_3} = 1.002$ and $\theta_{crit_4} = 1.013$ (to four significant figures). By comparison, the numerical solution gives $\theta_{crit_{3_{numeric}}} = 1.002$ and $\theta_{crit_{4_{numeric}}} = 1.010$ (to four significant figures).

4.4 Numerical Results

We use numerical simulations to validate and extend the preceding analysis.

4.4.1 Steady-state Model

We begin by solving equation (4.7), with $p(\theta) = (H(\theta - \theta_2) + H(\theta_1 - \theta))\tilde{p}(\theta)$, for a range of values of θ_1 and θ_2, where $\theta_1 < \theta_2$, to compare the stability properties of the system with those predicted in Figures 4.9 and 4.12. Equation (4.7) was discretised in space, using second order, central difference approximations for the spatial derivatives, and the resulting system of nonlinear algebraic equations solved using the Matlab routine fsolve, employing the Trust-Region-Dogleg algorithm. (This method was also used to produce the numerical solutions in Figures 4.5–4.7, 4.10–4.11 and 4.13–4.15.)

The simulation results presented in Figure 4.17 are similar to the analytical predictions, matching more closely with Figure 4.12 than Figure 4.9. In particular, the narrow patch analysis captures the extension of region A along the line $\theta_2 = \theta_1$ well. A key difference with Figures 4.9 and 4.12 is the presence, in Figure 4.17, of a narrow region at $\theta_1 = 1.01$, passing through region D (upper-left), region B (left) and region D (lower-left). Within this narrow region, θ_1 lies within the near-central stable region revealed by the central retinal preservation analysis of Section 4.3.3 and seen in Figure 4.15 (that is $\theta_1 \in [\theta_{crit_3}, \theta_{crit_4}]$). Within this narrow region there is no leftward degeneration, but degeneration may occur to the right when θ_2 lies in an unstable region. There is also a tiny isolated region in the bottom left-hand corner of Figure 4.17, of type B. Here $\theta_2 = 1.01$, which lies in the near-central stable region, whilst $\theta_1 = 1$, and so cannot progress to the left.

The positions of the boundaries between stability regions in Figure 4.17 differ a little from the positions in Figures 4.9 and 4.12. Our analysis predicted $\theta_{crit_1} = 1.116$, whereas the numerical solutions show it to be at 1.165 for θ_1 and at 1.095 for θ_2, whilst our analysis predicted $\theta_{crit_2} = 1.643$, whereas the numerical solutions show it to be at 1.575 for θ_1 and at 1.665 for θ_2. As a result of the differences in boundary positions, a new B region (region B

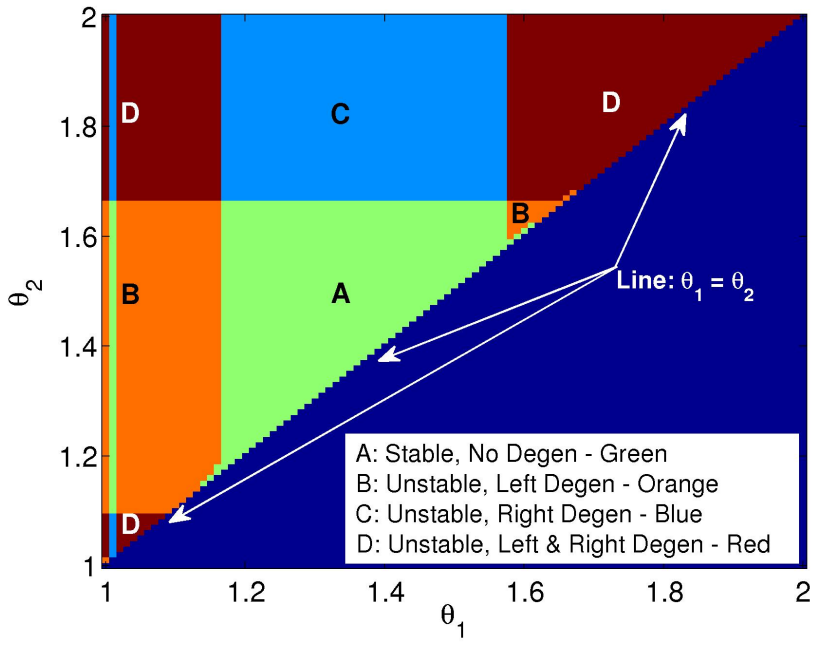

Figure 4.17: Diagram to show stable and unstable regions in (θ_1, θ_2) parameter space as revealed by numerical simulations. Equation (4.7) was solved using the finite difference method (see text for details), with 10,001 mesh points, and with $p(\theta) = (H(\theta - \theta_2) + H(\theta_1 - \theta))\tilde{p}(\theta)$ for a range of values of both θ_1 and θ_2, where $\theta_1 < \theta_2$. If $c(\theta_i) < c_{crit}$, then the boundary at θ_i is stable, and if $c(\theta_i) \geq c_{crit}$, then the boundary is unstable. Parameter values as in Table 4.3.

(right)) appears in the numerical solution, to the right of region A.

The reason for the discrepancy between boundary positions is as follows. Inspection of Figures 4.7 and 4.11 reveals that the composite solution, whilst matching closely to the numerical solution near θ_1 and θ_2, is shifted slightly to the right of the numerical solution. As a result, $c(\theta_1)$ is underestimated and $c(\theta_2)$ is overestimated, this effect being exaggerated due to the steepness of the gradient in these regions. Consequently, the boundaries of the steady region are estimated to be more widely (closely) separated in the $\theta_1(\theta_2)$-dimension.

4.4.2 Dynamic Model

We solved the time-dependent problem (equations (4.7)–(4.10)) using the method of lines, discretising in space as for the steady-state problem, and integrating in time using an explicit Runge-Kutta method (Matlab routine ode45). The quasi-steady oxygen equation (equation (4.7)) is solved at each time step using fsolve, in the same way as for the steady-state problem considered earlier. We use 4001 mesh points in all simulations, unless stated otherwise, so that the distance between mesh points corresponds to the average width of a photoreceptor. As a result, degeneration will spread only if the hyperoxic region extends by a photoreceptor width or more beyond the patch of loss, ensuring the results are biologically realistic. With the exception of Figure 4.20(b) (where the aim is simply to show that the patch is unstable), we run all simulations to time $t = 200$ (dimensionless units) or until the system reaches steady-state, whichever occurs first. We choose $t = 200$ since this corresponds to just over 60 years, the natural time span of the disease following the initial patchy loss of photoreceptors.

In Figures 4.18 and 4.19 we present simulation results for the time-dependent problem, for initial conditions selected from the seven major regions in Figure 4.17 (that is, those labelled with letters). In each case the solutions behave as predicted: the solution starting in region A remains stationary (Figure 4.18(a)), those starting in either of the B regions degenerate to the left (Figures 4.18(b) and 4.18(c)), the solution starting in region C degenerates to the right (Figure 4.18(d)) and those starting in any of the three D regions degenerate in both directions (Figures 4.19(a)–4.19(c)).

In addition to their general agreement with our analytical predictions, these simulations have two further noteworthy features. Firstly, as photoreceptor degeneration proceeds, the system may move between the regions shown in Figure 4.17. For instance, in Figure 4.18(b), the wave of leftward degeneration stalls as the system leaves region B (left) and enters region A (narrow). Similarly, in Figure 4.19(c), leftward degeneration stalls as the system leaves region D (lower-left) and enters region C (lower-narrow), followed by stalling of rightward degeneration as the system enters region A (narrow).

Secondly, the speed of the wave of degeneration varies with eccentricity. It is slower in

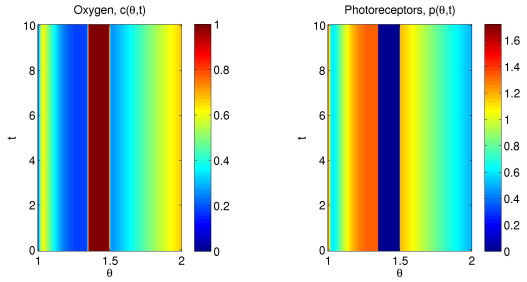

(a) Region A: $(\theta_1, \theta_2) = (1.35, 1.50)$.

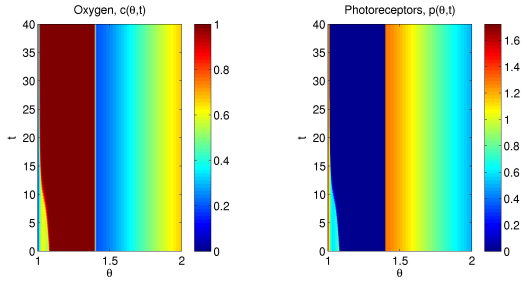

(b) Region B (left): $(\theta_1, \theta_2) = (1.08, 1.40)$.

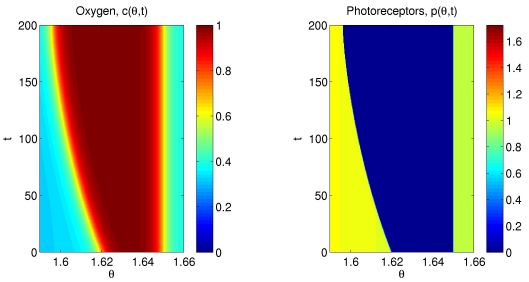

(c) Region B (right): $(\theta_1, \theta_2) = (1.62, 1.65)$.

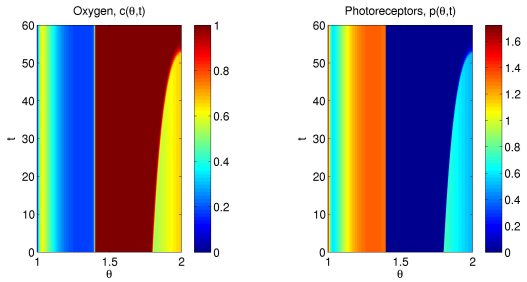

(d) Region C: $(\theta_1, \theta_2) = (1.40, 1.80)$.

Figure 4.18: Dynamic simulations of photoreceptor loss and preservation, for a range of initial degenerate patch locations (θ_1, θ_2), corresponding to (a) region A, (b) region B (left), (c) region B (right), and (d) region C. In all cases the pattern of degeneration proceeds in a manner consistent with Figure 4.17. Equations (4.7)–(4.10) were solved using the method of lines, with 4001 mesh points (see text for details). Parameter values as in Table 4.3.

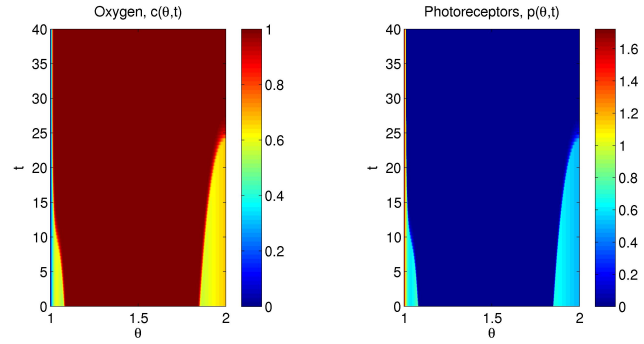

(a) Region D (upper-left): $(\theta_1, \theta_2) = (1.08, 1.85)$.

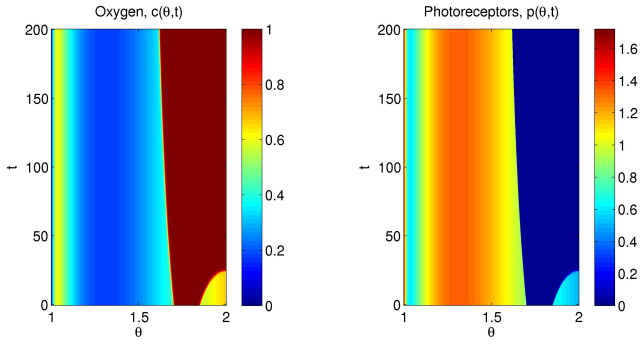

(b) Region D (upper-right): $(\theta_1, \theta_2) = (1.70, 1.85)$.

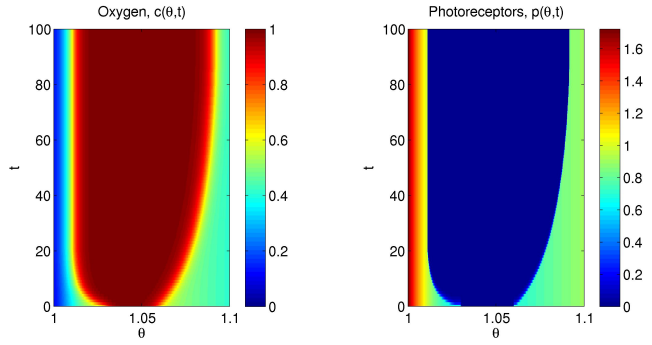

(c) Region D (lower-left): $(\theta_1, \theta_2) = (1.03, 1.06)$.

Figure 4.19: Dynamic simulations of photoreceptor loss and preservation, for a range of initial degenerate patch locations (θ_1, θ_2), corresponding to (a) region D (upper-left), (b) region D (upper-right), and (c) region D (lower-left). In all cases the pattern of degeneration proceeds in a manner consistent with Figure 4.17. Equations (4.7)–(4.10) were solved using the method of lines, with 4001 mesh points (see text for details). Parameter values as in Table 4.3.

those regions possessing a higher density of photoreceptors and faster in those regions possessing a lower density of photoreceptors. The extreme case occurs in the stable regions, where photoreceptor density is too high to permit the spread of degeneration. For example, Figure 4.19(a) demonstrates several changes in wave speed. The rightward degeneration accelerates as the wavefront approaches $\theta = 2$, corresponding to the drop in photoreceptor density toward the periphery of the retina. Meanwhile, the leftward degeneration accelerates until the wavefront reaches about $\theta = 0.04$, at which point it decelerates, corresponding to the drop in rod density followed by the sharp rise in cone density, as the wavefront approaches the centre of the fovea (see Figure 4.4).

With the exception of Figures 4.18(c) and 4.19(c), each of the above scenarios deals with a wide patch of loss. In Figure 4.20 we test our predictions for a narrow patch of loss and a preserved central patch. In Figure 4.20(a) we set $(\theta_1, \theta_2) = (1.61, 1.62)$, which lies within region A, close to the boundary $\theta_2 = \theta_1$. As predicted, the patch remains stable. In Figure 4.20(b) we decrease θ_1 by just 0.01, so that now $(\theta_1, \theta_2) = (1.60, 1.62)$, which lies in region B (right). As predicted, this is sufficient for the patch to degenerate in a leftward direction. The patch widths used here are of the same order of magnitude as those measured in the rat by Ji et al. (2012); García-Ayuso et al. (2013); Zhu et al. (2013), which lie in the (non-dimensional) range 3.8×10^{-3}–1.9×10^{-2}.

In Figure 4.20(c) we set $(\theta_1, \theta_2) = (1.01, 2.00)$, which lies within region C (upper-narrow). As predicted, the central region remains stable. In Figure 4.20(d) we decrease θ_1 to 1.001, so that now $(\theta_1, \theta_2) = (1.001, 2.00)$, which lies in region D (upper-narrow). As predicted, this is sufficient for the patch to become unstable, so that it degenerates in a leftward direction until all photoreceptors are lost. The preservation of the central region, when θ_1 lies just to the right of the near-central stable region initially, is seen in Figures 4.18(b), 4.19(a) and 4.19(c).

Having noted that the speed of degeneration depends upon the local photoreceptor density, it is of interest to explore in more detail the nature of this dependence. Figure 4.21 shows the magnitude of the distance moved by each boundary of a degenerate patch, between $t = 0$ and $t = 4$, for a range of values of initial patch boundaries, θ_1 and θ_2, where $\theta_2 > \theta_1$. Since

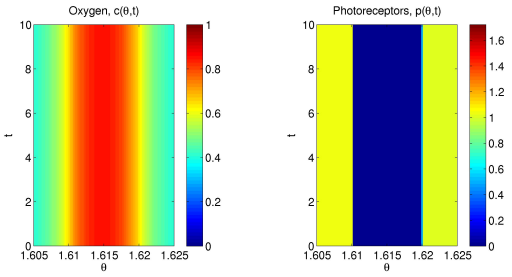

(a) Region A: $(\theta_1, \theta_2) = (1.61, 1.62)$.

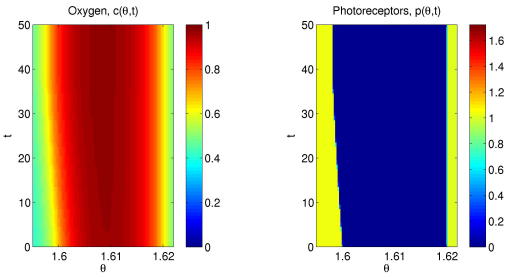

(b) Region B (right): $(\theta_1, \theta_2) = (1.60, 1.62)$.

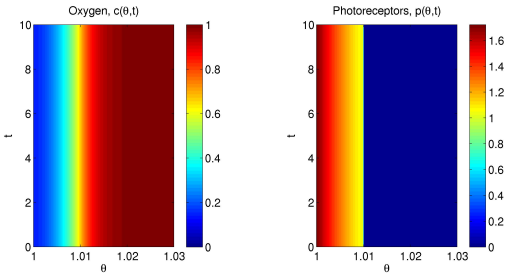

(c) Region C (upper-narrow): $(\theta_1, \theta_2) = (1.01, 2.00)$.

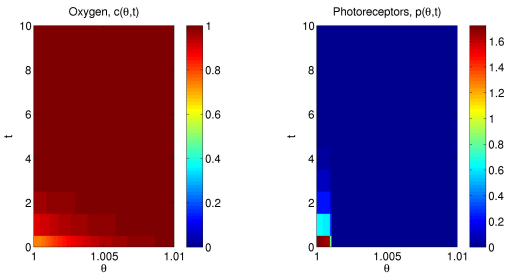

(d) Region D (upper-narrow): $(\theta_1, \theta_2) = (1.001, 2.00)$.

Figure 4.20: Dynamic simulations of photoreceptor loss and preservation, for a range of initial degenerate patch locations (θ_1, θ_2), corresponding to (a) region A, (b) region B (right), (c) region C (upper-narrow), and (d) region D (upper-narrow). In all cases the pattern of degeneration proceeds in a manner consistent with Figure 4.17. Equations (4.7)–(4.10) were solved using the method of lines, with 4001 mesh points (see text for details). Parameter values as in Table 4.3.

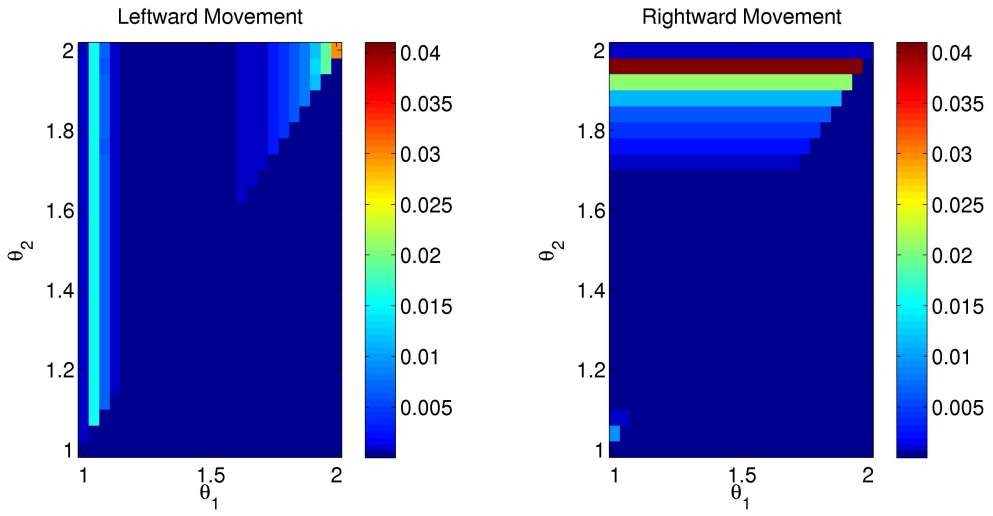

Figure 4.21: Graphs to show the distances travelled by the boundaries of degenerate patches between $t = 0$ and $t = 4$, for a range of initial patch locations. Left: distance travelled by the left-hand boundary, $\theta_1^t(0) - \theta_1^t(4)$. Right: distance travelled by the right-hand boundary, $\theta_2^t(4) - \theta_2^t(0)$. We define $\theta_1^t(t) := \inf\{\theta \in [\theta_L, 1+\theta_L] : p(\theta,t) < p_{crit}\}$ and $\theta_2^t(t) := \sup\{\theta \in [\theta_L, 1+\theta_L] : p(\theta,t) < p_{crit}\}$, where $p_{crit} = 0.1$. Equations (4.7)–(4.10) were solved using the method of lines, with 1001 mesh points (see text for details), for θ_1 and θ_2 in the range $1.0, 1.04, \ldots, 2.0$. Parameter values as in Table 4.3.

the photoreceptor density in any region with an initially positive density remains positive, we define the patch boundaries, or wavefronts, to lie at the infimum and supremum of the interval for which $p < p_{crit}$, where p_{crit} is a positive constant, denoting the critical density of photoreceptors. Therefore, the left wavefront is defined as $\theta_1^t(t) := \inf\{\theta \in [\theta_L, 1+\theta_L] : p(\theta,t) < p_{crit}\}$ and the right wavefront is defined as $\theta_2^t(t) := \sup\{\theta \in [\theta_L, 1+\theta_L] : p(\theta,t) < p_{crit}\}$, where we choose $p_{crit} = 0.1$ in our simulations. This means that the distance travelled by the left-hand boundary is $\theta_1^t(0) - \theta_1^t(4)$, whilst the distance travelled by the right-hand boundary is $\theta_2^t(4) - \theta_2^t(0)$. We use 1001 mesh points, rather than the 4001 used in previous simulations, to ensure a feasible computation time, noting that this is sufficient to reveal the regional variation in wave speed.

Examination of Figure 4.21 reveals that patch boundaries are stationary within region A, the mid-peripheral stable region. For θ_1 and θ_2 eccentric to the mid-peripheral stable region, the distance moved by the boundaries increases with increasing eccentricity (and decreasing

photoreceptor density). We note that for $\theta_2 = 1.96$, the right-hand boundary reaches $\theta = 2$ at $t < 2$, so that it can progress no further after this point. We could compensate for this effect by choosing a smaller time interval; however, this would mean that the more subtle progress near the mid-peripheral stable region would go undetected. For θ_1 and θ_2 between $\theta = 1$ and the mid-peripheral stable region, the distance moved by the boundaries increases with decreasing eccentricity (and decreasing photoreceptor density). The (θ_1, θ_2) grid is too coarse to reveal the effect of the peak in cone density. We refrained from using a finer grid size due to the prohibitively long computation times involved. We note that the distance travelled by each boundary is almost entirely independent of the initial position of the other boundary.

4.4.3 Modified Model I: Mutation-induced Rod Degeneration

In the healthy human retina, mid-peripheral rods are lost throughout adult life, whilst cone numbers, and equatorial and far-peripheral rod numbers, remain relatively stable (Curcio et al., 1993). In the RP retina, rods express mutant genes, increasing the vulnerability of rods to apoptosis across the whole retina. In this section we incorporate hyperoxia-independent, mutation-induced rod degeneration into our model, in order to examine its effects upon the spatio-temporal pattern of photoreceptor loss.

In order to incorporate this second form of rod loss, we describe the rod and cone densities independently, using the dependent variables $p_r(\theta,t)$ and $p_c(\theta,t)$ for rod and cone density respectively. Therefore, in place of equations (4.7)–(4.8), we have the following dimensionless system:

$$0 = \frac{D}{\sin(\Theta\theta)}\frac{\partial}{\partial\theta}\left(\sin(\Theta\theta)\frac{\partial c}{\partial\theta}\right) - \frac{Q(p_r+p_c)c}{\gamma+c} + \beta(1-c), \tag{4.49}$$

$$\frac{\partial p_r}{\partial t} = -(\phi_r + \lambda_2(c))p_r, \tag{4.50}$$

$$\frac{\partial p_c}{\partial t} = \mu p_c\left(1 - \frac{p_c}{\tilde{p}_c(\theta)}\right)\lambda_1(c) - p_c\lambda_2(c). \tag{4.51}$$

We do not include a logistic growth term in equation (4.50), assuming that the rods' mutant

state compromises their ability to regenerate. We also note that whilst the logistic growth term used in equation (4.51) is not strictly consistent with that used in equation (4.8), in that the sum of logistic growth terms for rods, p_r, and cones, p_c, is not the same as the logistic growth term for photoreceptors, $p = p_r + p_c$, it remains the sensible choice, since we would expect cone regrowth to obey logistic dynamics.

We have made the assumption, based on the measurements of Clarke et al. (2000), that mutation-induced rod loss is exponential, denoting its rate by ϕ_r, which we define to be constant across the domain, since RP affects all rods. In the simulations that follow we set $\phi_r = 6.6 \times 10^{-3}$, consistent with the observation of Curcio et al. (1993) that the total number of rods in the central 28.5 degrees of vision reduces by 69% between the ages of 34 and 90. We have also assumed that the contributions of mutation and hyperoxia to rod degeneration combine in an additive fashion, this being the simplest and hence most reasonable approach in the absence of further information.

We take as our initial conditions either,

$$p_r(\theta,0) = p_{r_{init}}(\theta) = \tilde{p}_r(\theta), \tag{4.52}$$

$$p_c(\theta,0) = p_{c_{init}}(\theta) = \tilde{p}_c(\theta), \tag{4.53}$$

corresponding to a healthy photoreceptor distribution, or,

$$p_r(\theta,0) = p_{r_{init}}(\theta) = (H(\theta-\theta_2)+H(\theta_1-\theta))\tilde{p}_r(\theta), \tag{4.54}$$

$$p_c(\theta,0) = p_{c_{init}}(\theta) = (H(\theta-\theta_2)+H(\theta_1-\theta))\tilde{p}_c(\theta), \tag{4.55}$$

corresponding to a single patch of loss, where

$$\tilde{p}_r(\theta) = B_3(\theta-\theta_L)e^{-b_3(\theta-\theta_L)}, \tag{4.56}$$

$$\tilde{p}_c(\theta) = B_1 e^{-b_1(\theta-\theta_L)} + B_2 e^{-b_2(\theta-\theta_L)}. \tag{4.57}$$

We close the system by imposing zero-flux boundary conditions on the oxygen concentra-

tion:

$$\frac{\partial c}{\partial \theta}(\theta_L,t) = 0 = \frac{\partial c}{\partial \theta}(1+\theta_L,t). \tag{4.58}$$

We solve this problem using the method of lines as described above, where the equations for p_r and p_c are treated in the same way as the equation for p. In this section, as with Sections 4.4.4 and 4.4.5, we use 1001 mesh points, this being sufficient to fully resolve the dynamics.

Figure 4.22 shows two examples of the patterns of degeneration that are generated when mutation-induced rod loss is incorporated into the system. In Figure 4.22(a), the steady attrition of rods causes oxygen levels to rise across the retina. This leads to the development of hyperoxia at $\theta = 1.045$ and $\theta = 2$, where photoreceptor density is lowest, resulting in waves of hyperoxia driven photoreceptor degeneration. These waves meet at $\theta = 1.287$ (corresponding to 21.8 degrees eccentricity) just to the left of the peak in photoreceptor density in the mid-periphery at $t = 135$, whilst cone density is preserved at the centre of the fovea. The fact that degeneration spreads across the domain shows that the mutation-induced loss of rods has caused the mid-peripheral stable region (region A in in Figure 4.17) to become unstable, whilst the preservation of cones at the centre of the retina demonstrates that the near-central stable region, seen in Figure 4.15, remains stable, as suggested by our analysis in Section 4.3.3.

In Section 4.3.1 we predicted that mutation-induced rod degeneration could cause a stable patch to become unstable and spread. We test this prediction in Figure 4.22(b), where we remove a patch of photoreceptors between $\theta_1 = 1.57$ and $\theta_2 = 1.66$, which lies in the upper-right corner of the (stable) region A in Figure 4.17. As rods are lost, the patch becomes unstable, degenerating to the right (at $t = 23$) and to the left (at $t = 24$).

4.4.4 Modified Model II: Mutation-induced Cone Degeneration

RP most commonly presents as a rod-cone dystrophy, in which rod loss precedes cone loss, since rods express a mutant RP gene not expressed by cones. More rarely, RP can present as a cone-rod dystrophy, in which cone loss precedes rod loss (Hamel, 2006; Hartong et al., 2006).

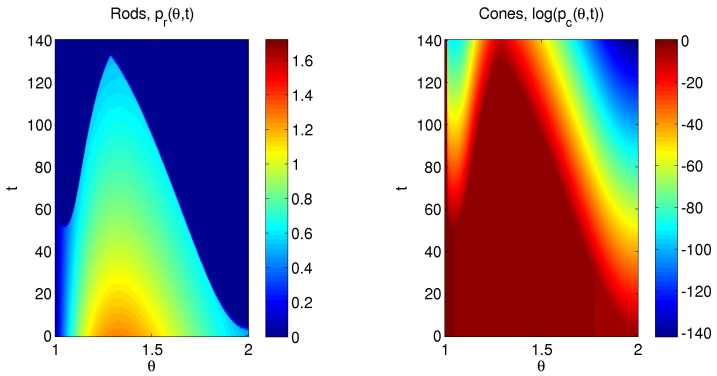

(a) No initial degenerate patch.

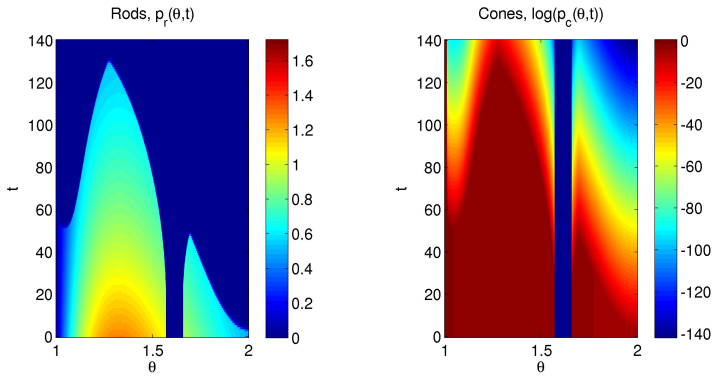

(b) Initial degenerate patch at $(\theta_1, \theta_2) = (1.57, 1.66)$.

Figure 4.22: Dynamic simulations of photoreceptor loss and preservation with mutation-induced rod loss, with, (a), and without, (b), an initial degenerate patch. Note that we plot the natural logarithm of the cone density, $\log(p_c)$, on the right. (a) and (b): hyperoxic degeneration initiates at $\theta = 1.045$ and $\theta = 2$. (b): the degenerate patch begins to spread to the right at $t = 23$ and to the left at $t = 24$. Equations (4.49)–(4.51), (4.52)–(4.53) (a), (4.54)–(4.55) (b), and (4.58) were solved using the method of lines, with 1001 mesh points (see text for details). Parameter values: $\phi_r = 6.6 \times 10^{-3}$. Remaining parameter values as in Table 4.3.

In this case, the underlying genetic mutation is more detrimental to cones than to rods. Patients with cone-rod dystrophy lose their central colour vision early in the disease (corresponding to cone loss), which is followed by loss of night vision and peripheral vision (corresponding to rod loss, Hamel, 2007).

The equations used to model cone-rod dystrophy are the same as those used to model rod-cone dystrophy in the previous section, with the exception that equations (4.50)–(4.51) become:

$$\frac{\partial p_r}{\partial t} = \mu p_r \left(1 - \frac{p_r}{\tilde{p}_r(\theta)}\right) \lambda_1(c) - \lambda_2(c) p_r, \tag{4.59}$$

$$\frac{\partial p_c}{\partial t} = -(\phi_c + \lambda_2(c)) p_c, \tag{4.60}$$

so that the hyperoxia-independent mutation-induced degeneration term is now included in the cone equation, rather than the rod equation, and only the rods, rather than the cones, are able to regenerate. As in the previous section, we set $\phi_c = 6.6 \times 10^{-3}$.

Figure 4.23 shows the results of a simulation of the above equations with no initial patch of degeneration. It can be see that hyperoxic degeneration initiates first near the centre of the retina (at $t = 71$) and later at $\theta = 2$ (at $t = 208$). This is the reverse order to that observed for mutation-induced rod degeneration. Whilst some rods will be lost near the centre of the retina for any value of $c_{crit} < 1$, only a minor increase in c_{crit} is required to prevent the hyperoxic degeneration of rods from $\theta = 2$ inwards, since the initial density of cones at $\theta = 2$ is tiny (e.g. in the simulation corresponding to Figure 4.25(b), in which c_{crit} is increased to 0.8, rod loss from $\theta = 2$ is avoided). We do not show a simulation with an initial degenerate patch since, except near the centre of the retina, where degeneration occurs even in the absence of a patch, cone density is low, such that their loss is unlikely to destabilise a patch.

We have also considered the form of RP in which both rods and cones undergo the same rate of mutation-induced degeneration ($\phi_r = \phi_c = 6.6 \times 10^{-3}$, Hartong et al., 2006). The pattern of degeneration is very similar to that in Figure 4.22 for the case of mutation-induced rod loss, the key difference being that the central island of cones is eventually lost. Two more

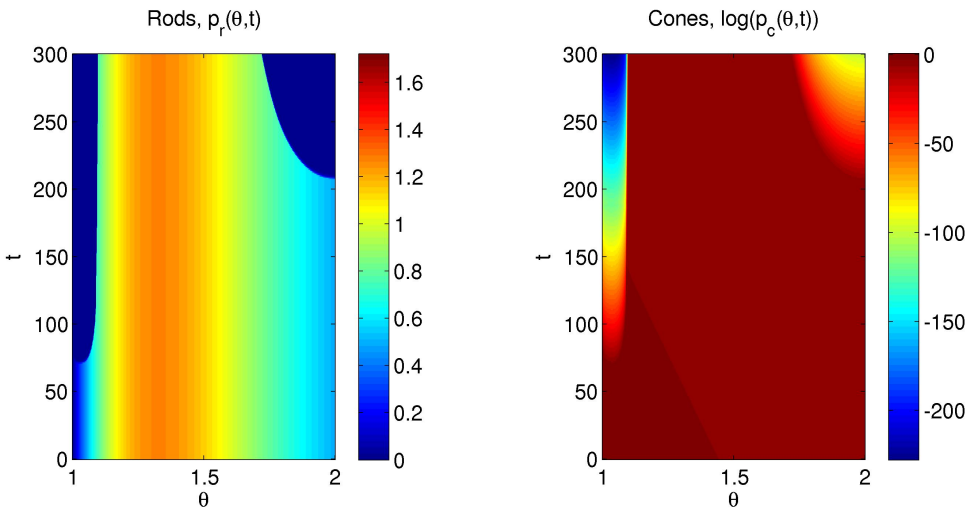

Figure 4.23: Dynamic simulation of photoreceptor loss and preservation with mutation-induced cone loss and no initial degenerate patch. Note that we plot the natural logarithm of the cone density, $\log(p_c)$, on the right. Hyperoxic degeneration initiates at $\theta = 1.03$ at $t = 71$ and later at $\theta = 2$ at $t = 208$. Equations (4.49), (4.52)–(4.53) and (4.58)–(4.60) were solved using the method of lines, with 1001 mesh points (see text for details). Parameter values: $\phi_c = 6.6 \times 10^{-3}$. Remaining parameter values as in Table 4.3.

minor differences are that the two waves of hyperoxic degeneration now meet at $\theta = 1.3$ (still a little to the left of the peak in rod density) and at the slightly earlier time of $t = 127$ (results not shown).

4.4.5 Modified Model III: Treatment with Antioxidants or Trophic Factors

Lastly, we consider the case in which treatment is applied in the form of either antioxidants or trophic factors. Antioxidants act by neutralising reactive oxygen species, whilst trophic factors increase photoreceptor resistance to apoptosis (Kohen and Nyska, 2002; Yu et al., 2004; Komeima et al., 2006, 2007). Thus, in either case, the use of these treatments will have the effect of increasing the hyperoxic threshold, c_{crit}.

In the simulations that follow, we set $c_{crit}(t) = c_{crit_1} + c_{crit_2} H(t - t_{crit})$, where c_{crit_1}, c_{crit_2} and t_{crit} are positive constants and H is a Heaviside step function, such that $c_{crit}(t) = c_{crit_1}$ for

$t < t_{crit}$ and $c_{crit}(t) = c_{crit_1} + c_{crit_2}$ for $t \geq t_{crit}$. We set $c_{crit_1} = 0.67$ in all simulations.

In Figure 4.24 we examine the effect of treatment (applied at $t_{crit} = 20$) following the spread of degeneration from an initial degenerate patch at $(\theta_1, \theta_2) = (1.03, 1.06)$. In this case mutation-induced rod and cone degeneration is excluded and so equations (4.7)–(4.10) are solved. We note that, without treatment, this problem is identical to that simulated in Figure 4.19(c). In Figure 4.24(a) we set $c_{crit_2} = 0.33$, so that c_{crit} increases from 0.67 to 1 at $t = 20$. This corresponds to a strong treatment, since photoreceptors will remain healthy for oxygen concentrations close the capillary concentration. In this case degeneration halts and the degenerate patch shrinks to its original size. In Figure 4.24(b) we set $c_{crit_2} = 0.13$, so that c_{crit} increases from 0.67 to 0.8 at $t = 20$. This corresponds to a more mild treatment. In this case degeneration halts as before, but only a minor regeneration of lost photoreceptors is achieved.

Figure 4.25(a) shows the effect of mild treatment ($c_{crit_2} = 0.13$) when mutation-induced rod degeneration is included. In this case we solve equations (4.49)–(4.51), (4.54)–(4.55) and (4.58), with $t_{crit} = 25$ and an initial degenerate patch at $(\theta_1, \theta_2) = (1.57, 1.66)$. As such, without treatment, this problem is identical to that simulated in Figure 4.22(b). It can be seen that treatment temporarily halts the progression of hyperoxic degeneration.

Lastly, Figure 4.25(b) shows the effect of mild treatment ($c_{crit_2} = 0.13$) when mutation-induced cone degeneration is included. In this case we are solving equations (4.49), (4.52)–(4.53) and (4.58)–(4.60), with $t_{crit} = 100$ and without an initial degenerate patch. As such, without treatment, this problem is identical to that simulated in Figure 4.23. It can be seen that treatment halts the progression of hyperoxic degeneration near $\theta = 1$, resulting in a minor recovery of rods. Though not visible in Figure 4.25(b), hyperoxic degeneration at $\theta = 2$ is prevented.

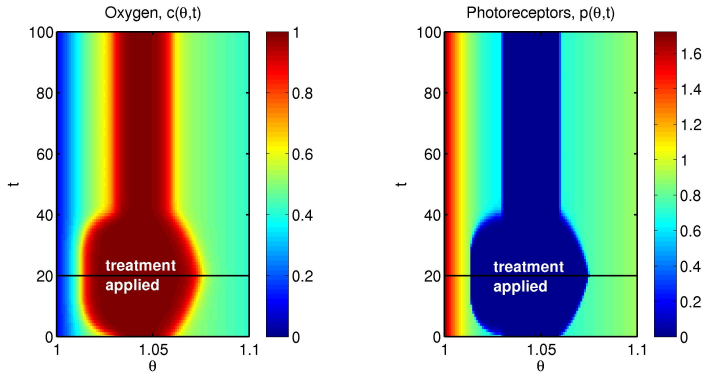

(a) Strong treatment: $c_{crit_2} = 0.33$.

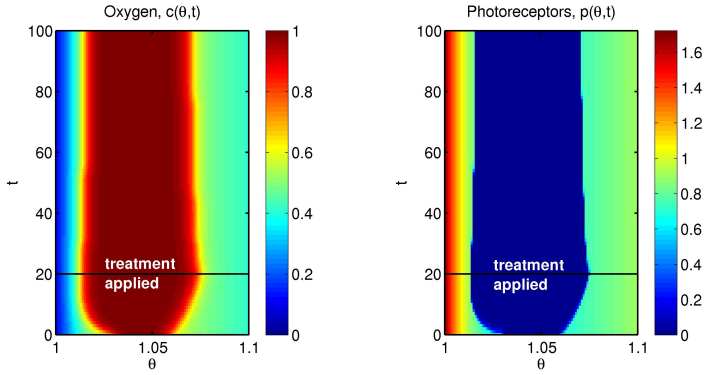

(b) Mild treatment: $c_{crit_2} = 0.13$.

Figure 4.24: Dynamic simulations showing the effect of treatment upon photoreceptor loss and preservation. Solutions show (a) full recovery and (b) minor recovery. Without treatment, the simulation would proceed as in Figure 4.19(c). Equations (4.7)–(4.10) were solved using the method of lines, with 1001 mesh points and $c_{crit}(t) = c_{crit_1} + c_{crit_2} H(t - t_{crit})$ (see text for details). Parameter values: $\theta_1 = 1.03$, $\theta_2 = 1.06$, $c_{crit_1} = 0.67$ and $t_{crit} = 20$. Remaining parameter values as in Table 4.3.

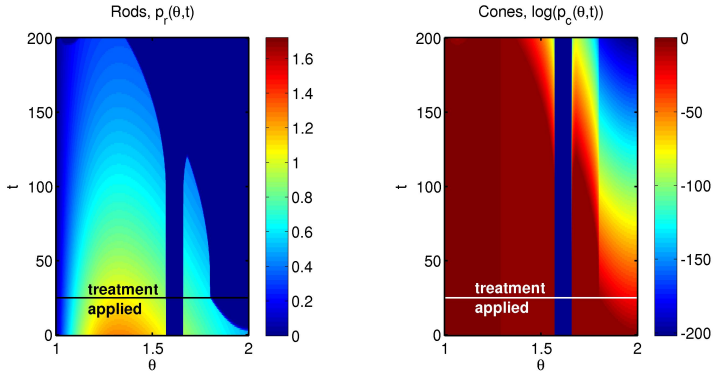

(a) Mutation-induced rod loss. Initial degenerate patch at $(\theta_1, \theta_2) = (1.57, 1.66)$. Parameter values: $\phi_r = 6.6 \times 10^{-3}$ and $t_{crit} = 25$.

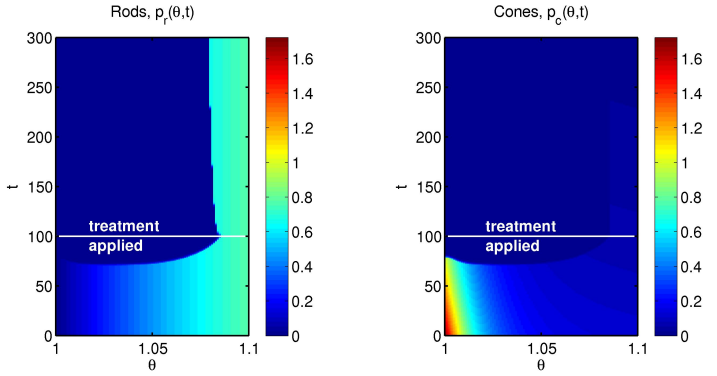

(b) Mutation-induced cone loss. No initial degenerate patch. Parameter values $\phi_c = 6.6 \times 10^{-3}$ and $t_{crit} = 100$.

Figure 4.25: Dynamic simulations showing the effect of (mild) treatment upon photoreceptor loss and preservation with mutation-induced rod (a) and cone loss (b). Note that we plot the natural logarithm of the cone density, $\log(p_c)$, on the right in (a), and p_c on the right in (b). (a) treatment temporarily stalls hyperoxic degeneration, (b) treatment results in a minor recovery of hyperoxic damage near $\theta = 1$. Without treatment, simulations (a) and (b) would proceed as in Figures 4.22(b) and 4.23 respectively. (a) equations (4.49)–(4.51), (4.54)–(4.55) and (4.58), and (b) equations (4.49), (4.52)–(4.53) and (4.58)–(4.60) were solved using the method of lines, with 1001 mesh points and $c_{crit}(t) = c_{crit_1} + c_{crit_2} H(t - t_{crit})$ (see text for details). Parameter values: $c_{crit_1} = 0.67$ and $c_{crit_2} = 0.13$. Remaining parameter values as in Table 4.3.

4.5 Discussion

We have derived a model to explore the dynamics of hyperoxia driven photoreceptor degeneration in a human retina with RP. The model demonstrates that degeneration may spread via hyperoxia and predicts specific spatio-temporal patterns of degeneration. Using this model we have determined conditions under which degeneration will spread or remain localised, and revealed the qualitative relationship between photoreceptor distribution and the wave speed of degeneration. We have also explored the effect of treatment with antioxidants and trophic factors upon the progression of photoreceptor degeneration.

In our asymptotic analysis in Section 4.3, we examined the conditions under which degeneration will spread. We considered three scenarios: a wide ($O(1)$ in width) degenerate patch, a narrow ($O(\varepsilon)$ or less in width) degenerate patch and a narrow island of preserved photoreceptors at the centre of the retina.The analysis revealed that the retina can be divided into five regions, two stable and three unstable, as shown in Figure 4.16. In order, from the centre of the retina, these regions are: the central unstable region, the near-central stable region, the para/perifoveal unstable region, the mid-peripheral stable region and the peripheral unstable region. The margins of a wide degenerate patch will remain stationary provided they are located within a stable region. If a margin lies in an unstable region it will expand outwards from the centre of the patch until it reaches either the edge of the retina or a stable region. Narrow patches remain stationary within stable regions and may also remain stationary within regions where wide patches would be unstable, provided they are sufficiently narrow.

The qualitative nature of these predictions was confirmed numerically in Section 4.4.1 (Figure 4.17), though the precise location of the stable regions differs a little from those predicted by the asymptotics.

The three scenarios described above can be viewed as different stages in the progression of RP: early in the disease, narrow patches form, which, over time, grow and coalesce to become wide patches. Later, these patches grow and coalesce until only a narrow central region, made up predominantly of cones, remains. Lastly, the central region narrows and is lost, resulting

in total blindness.

Two questions arise from this description. Firstly, what initiates the loss of a patch of photoreceptors? And secondly, in those cases where a patch of loss is stable, what causes it to expand from a narrow to a wide patch or from a wide patch to a totally degenerate retina?

The work presented in this chapter does not seek to answer the first question, treating a patch of loss as an initial condition, and focussing instead upon the subsequent hyperoxia driven expansion of the patch. Patches of loss presumably arise due to the stochastic, mutation-induced loss of photoreceptors (most commonly rods), where a cluster of degenerate photoreceptors causes the loss of neighbouring photoreceptors, perhaps due to a lack of structural support, an increase in oxygen levels, the release of toxic substances, a decrease in the production of rod trophic factor, the action of microglia, or some combination of the above.

We have explored one possible answer to the second question, namely the gradual pan retinal, mutation-induced degeneration of rods, cones, or both (see Sections 4.4.3 and 4.4.4). As photoreceptor numbers decline with age across the retina, the maximum width at which narrow patches remain stable decreases, whilst the stable regions, described in Sections 4.3.1 and 4.3.3, narrow. As a result, degenerate patches which were previously stable become unstable and start to expand, leading to the eventual loss of all photoreceptors.

Simulations predict that, in the absence of mutation-induced cone loss, a narrow island of cones will remain intact at the centre of the fovea (Sections 4.4.2 and 4.4.3). This fits with the observation that central vision is generally the last to be lost in RP, but fails to replicate the eventual loss of cones observed in many patients. It may be that, whist oxygen levels remain below the 'hyperoxic threshold', prolonged exposure to higher than normal oxygen levels proves toxic over time. Alternatively, or in addition to this, loss of structural support from neighbouring photoreceptors, the release of toxic substances by dying photoreceptors, the absence of rod trophic factor or the action of microglia could contribute to the demise of the cone island.

Our analysis and simulations suggest that the retina is most susceptible to hyperoxic damage in two regions: the peripheral unstable region and the para/perifoveal unstable region (see

Figure 4.16). Both these regions correspond to local minima in the photoreceptor density where oxygen levels are highest. It is within these regions that degenerate patches are most likely to spread and it is here that hyperoxic degeneration initiates when mutation-induced rod or cone degeneration is included in the model.

Comparison of model predictions with clinical data is instructive. Grover et al. (1998) identified three patterns of visual field loss, the first of which involves peripheral to central field loss, sometimes accompanied by parafoveal or perifoveal ring scotomas (blind spots), whilst the second two patterns originate in the mid-periphery, spreading centrally and peripherally (the differences between these two patterns cannot be captured in a 1D model, see Section 1.3.4 and Figure 1.9 for details). These same patterns of retinal degeneration and field loss were reported in a series of detailed studies described in Section 1.3.3 (Robson et al., 2003, 2004, 2006, 2008, 2011; Popović et al., 2005; Murakami et al., 2008; Lima et al., 2009, 2012; Escher et al., 2012). In our model, in the absence of mutation-induced photoreceptor degeneration, the pattern of loss is determined by the location of the initial patches of photoreceptor loss. If they initiate in the peripheral unstable region they will spread peripherally, to the ora serrata, and centrally, toward the mid-peripheral stable region, whilst if they initiate in the para/perifoveal unstable region they will spread centrally, toward the near-central stable region, and outward, toward the mid-peripheral stable region. Examination of the visual field diagrams in Grover et al. (1998) suggests that preservation of photoreceptors in a mid-peripheral stable region may be a common feature of pattern 1 visual field loss (at least in the earlier stages of the disease), though not of patterns 2 or 3 (see Figure 1.9). In order for degeneration to spread across the mid-peripheral stable region, the model must be modified in some way.

When we incorporate mutation-induced, hyperoxia-independent rod degeneration into the model, a distinctive pattern of photoreceptor loss emerges. Photoreceptor loss initiates at the ora serrata, spreading centrally and later initiates in the para/perifoveal unstable region, spreading centrally and peripherally. The mutation-induced loss of rods causes the mid-peripheral stable region to shrink and eventually to vanish, so that only a narrow island of

cones at the centre of the fovea remains at the end stage. This matches well with pattern 1 (peripheral to central) progression described in Grover et al. (1998), and in particular with the pattern 1B progression, which also includes ring scotomas surrounding the fovea (see Figure 1.9). As noted in Section 4.4.4, the model incorporating mutation-induced degeneration of both rods and cones progresses in a similar way, the key difference being that central vision is not preserved.

It appears that mutation-induced rod degeneration will always result in hyperoxic degeneration starting from the ora serrata; however, two factors could contribute to its initiating first in the para/perifoveal region. Firstly, it has been shown in the mouse that trophic factors are expressed at a higher level at the edge of the retina, protecting against hyperoxic damage (Mervin and Stone, 2002a; Stone et al., 2005). We increased the hyperoxic threshold, c_{crit}, to unity, in a rim of width 150μm around the ora serrata, as described in Mervin and Stone (2002a); Stone et al. (2005); however, it was found that hyperoxic degeneration still initiated at the ora serrata (results not shown). Secondly, since rod degeneration is confined to the mid-periphery and central retina during normal ageing (Curcio et al., 1993), it might be that rod degeneration is most severe in this region under RP.

Mutation-induced cone loss, corresponding to the cone-rod form of RP, or other cone-rod dystrophies, causes hyperoxic degeneration to initiate near the centre of the retina, spreading toward the mid-peripheral stable region where degeneration stalls. It may also cause hyperoxic degeneration to initiate at the ora serrata at a later stage, spreading centrally to the mid-peripheral stable region. This pattern of progression is similar that described by Hamel (2007), though the preservation of the mid-peripheral stable region may be unrealistic.

Although there are many studies charting the progression of visual field loss and retinal degeneration, they do not describe precisely the location (in terms of eccentricity) of the degenerate patches. Were precise measurements to be made, it would be straightforward to compare our model predictions with these clinical data.

Simulations also reveal the relationship between photoreceptor density and the wave speed of the edge of a spreading degenerate patch: the wave speed is higher for lower local photore-

ceptor densities and lower for higher local photoreceptor densities. Two factors are likely to account for this behaviour. Firstly, in those regions containing a greater density of photoreceptors it will take longer for the photoreceptors to decay beneath a given threshold (the density will never reach mathematical zero in finite time for a continuum representation, since this is impossible with an exponential decay term). Secondly, and more importantly, the width of the region exposed to hyperoxia ahead of the wavefront will be wider in those regions where the photoreceptor density is lower. More detailed longitudinal studies are required to determine whether this model prediction is correct.

Our simulations suggest that treatment with antioxidants or trophic factors may prevent the initiation of hyperoxic degeneration, that it may permanently or temporarily halt degeneration, or allow some recovery of damaged photoreceptors. Mathematically this occurs by increasing the hyperoxic threshold and hence the widths of the stable regions. Recovery is likely to be partial at best since many photoreceptors will have died or degenerated beyond recovery prior to treatment, therefore, the total recovery seen in Figure 4.24(a) is overly optimistic. Treatment would need to be maintained throughout the lifetime of the patient, otherwise degeneration would resume. Antioxidants and trophic factors could be supplied over the long-term using either encapsulated cell technology or ocular gene therapy (see, for example, Tao et al., 2002; Orosz et al., 2004; Dong et al., 2006; Tao, 2006; Musarella and MacDonald, 2011; Wen et al., 2012). If treatment could be targeted to specific regions of the retina, our results suggest that the unstable peripheral and para/perifoveal regions should be targeted, as they are most susceptible to hyperoxic damage.

Future work could include a more detailed description of the biochemistry underlying hyperoxic damage, and the action of antioxidants and trophic factors. This would require, or could proceed in tandem with, experimental work, to elucidate the relevant pathways. Another extension would be to simulate retinal degeneration in animal models (e.g. rats, mice and pigs), for which the healthy photoreceptor distribution is different to that in humans. The model could also be extended to 2D by including the radial (RPE–ILM) dimension, taking into account the layered structure of the inner and outer retina. A similar approach to that

used here, accounting for the regional variation in rod and cone density, could also be used to investigate the rod trophic factor and rod toxic substance hypotheses.

In this chapter we have shown, using a 1D model, that the oxygen toxicity hypothesis can explain some of the patterns of photoreceptor degeneration found in RP, and that the wave speed of hypoxic degeneration is negatively correlated with local photoreceptor density. We have also explored the effect of treatment with antioxidants and trophic factors. In the next chapter we extend this work in two ways: firstly, by including the degeneration of the CC and secondly, by extending the model to 2D to include the azimuthal dimension.

Chapter 5

Retinitis Pigmentosa: The Oxygen Toxicity Hypothesis (Capillary Loss and 2D)

In the previous chapter we investigated hyperoxia driven photoreceptor degeneration in 1D. In this chapter we extend this work in two ways: firstly by including degeneration of the choriocapillaris (CC) in the 1D model and secondly by extending the 1D model into 2D, to include variation in the azimuthal direction. Capillary loss is of interest, since it has the potential to counteract the hyperoxia which results from photoreceptor loss, delaying or preventing the spread of photoreceptor degeneration, whilst a 2D model allows us to explore patterns of degeneration inaccessible to the 1D model.

5.1 Introduction

Degeneration of the CC (the inner layer of the choroid) is commonly observed in human models of RP, although its immediate cause is unknown (Li et al., 1995; Milam et al., 1998; Mullins et al., 2012). The width of the submacular choroid is significantly thinner in humans with RP than in healthy controls (Dhoot et al., 2013), whilst the CC is usually absent from

areas in which photoreceptors have completely degenerated and the bone spicule pattern has formed (Li et al., 1995; Milam et al., 1998). This pattern forms following photoreceptor degeneration, when RPE cells migrate away from Bruch's membrane (BM), which divides the retina from the CC, towards the retinal capillary layers, producing black melanin granules (Li et al., 1995; Milam et al., 1998).

It is unclear whether CC degeneration is a direct result of photoreceptor loss, or of RPE loss, with photoreceptor loss as the indirect cause (Milam et al., 1998). The current evidence would seem to suggest that RPE loss is the direct cause of CC degeneration. Surgical removal of the RPE in rabbit and pig models resulted in loss of the CC (Korte et al., 1984; Del Priore et al., 1996). This led Korte et al. (1984) to suggest that the RPE produces a 'diffusible vascular modulating factor', which is required to maintain the CC in health. The RPE has been shown to produce vascular endothelial growth factor (VEGF, Maharaj et al., 2006), a protein which is known to promote the survival of capillary endothelial cells (Ferrara et al., 2003). Furthermore, Saint-Geniez et al. (2009) have shown, using a mouse model, that the CC degenerates when the RPE is prevented from producing the soluble forms of VEGF that can diffuse across BM to the CC.

Whilst this presents a compelling picture, many of the biochemical details associated with the above processes have yet to be confirmed or elucidated. In particular, it remains to be determined how photoreceptor degeneration leads to RPE degeneration or migration (see Section 1.3.3 for further discussion). Hence, in the modelling work presented below, we shall assume a simple direct dependence of the CC upon the local photoreceptor density.

The interdependence of oxygen, photoreceptors and capillaries is represented in Figure 5.1. The positive feedback loop between oxygen and photoreceptors remains the same as in Figure 4.2. The inclusion of capillaries extends the picture, with oxygen supply depending upon capillary density, which in turn depends upon photoreceptor density.

A number of different spatio-temporal patterns of photoreceptor degeneration have been observed in humans. Grover et al. (1998) identified three distinct patterns of visual field loss (see Section 1.3.4 and Figure 1.9 for more details). Pattern 1 involves the concentric loss of

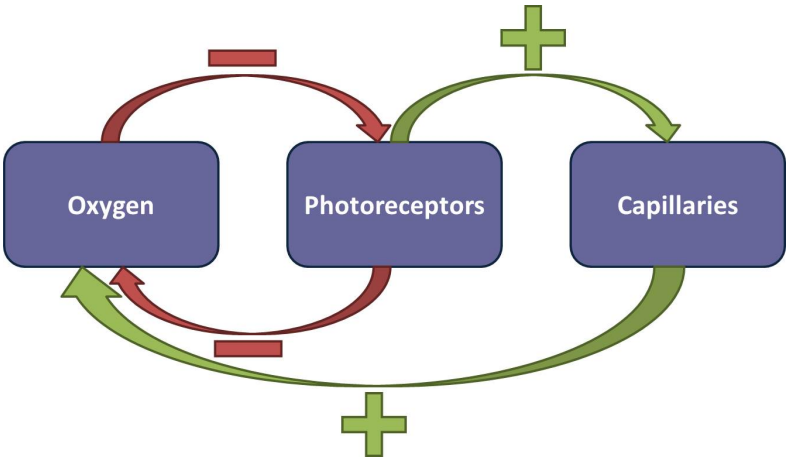

Figure 5.1: Flow chart for hyperoxia driven photoreceptor degeneration with capillary loss. Photoreceptors consume oxygen, whilst high oxygen levels damage photoreceptors. Capillaries depend upon photoreceptors for survival, whilst they themselves are necessary to maintain an oxygen supply. Key: '+' indicates a sustaining effect, whilst '-' indicates decay or consumption.

vision, starting at the far-periphery. This pattern is sometimes accompanied by a parafoveal or perifoveal ring scotoma (blind spot). Pattern 2 begins with visual field loss in the superior or nasal region, which then develops into an arcuate (shaped like a bow) scotoma. This scotoma winds either nasally or temporally through the mid-periphery, leaving central and sometimes inferior islands of vision. Lastly, pattern 3 consists of a partial or complete mid-peripheral ring scotoma, which then expands superiorly or inferiorly leaving a central island of vision, together with a 'U' or 'n' shaped peripheral visual field. The arms of the peripheral visual field then retract, extinguishing peripheral vision. In all cases the central visual field is preserved, being lost only at the end stage of the disease. Studies by Robson et al. (2003, 2004, 2006, 2008, 2011); Popović et al. (2005); Murakami et al. (2008); Lima et al. (2009, 2012); Escher et al. (2012) describe patterns of degeneration similar to patterns 1 and 3, with pattern 2 also being apparent in Escher et al. (2012).

In this chapter we seek to answer the following questions: under what conditions will capillary loss slow or prevent photoreceptor degeneration? How significant is the effect? What patterns of degeneration does our model predict in 2D? What patterns of degeneration, de-

scribed in the literature, and especially in Grover et al. (1998), cannot be reproduced by our model? What is the effect of treatment by antioxidants and trophic factors in 2D?

The remainder of this chapter is structured as follows: in Section 5.2 we develop the 1D model, incorporating capillary degeneration; in Section 5.3 we perform an asymptotic analysis of the capillary loss model, to determine conditions under which capillary loss will prevent the spread of degeneration; in Section 5.4 we solve the capillary loss model numerically; in Section 5.5 we develop the 2D model (without capillary loss); in Section 5.6 we solve the 2D problem numerically and in Section 5.7 we discuss our results and suggest directions for future research.

5.2 Model Formulation: 1D Capillary Loss

Using the same geometry and coordinate system as in Chapter 4 (see Figure 4.3), we construct equations for the retinal oxygen concentration, $c(\theta,t)$, the photoreceptor density, $p(\theta,t)$ and the capillary surface area per unit volume (CSA), $h(\theta,t)$,

$$\frac{\partial c}{\partial t} = \frac{D}{R^2\sin(\theta)}\frac{\partial}{\partial\theta}\left(\sin(\theta)\frac{\partial c}{\partial\theta}\right) - \frac{\alpha Q p c}{\gamma + c} + \beta h(c_{ch} - c), \tag{5.1}$$

$$\frac{\partial p}{\partial t} = \mu p\left(1 - \frac{p}{\tilde{p}(\theta)}\right)\lambda_1(c) - \delta p\lambda_2(c), \tag{5.2}$$

$$\frac{\partial h}{\partial t} = \eta\left(\tilde{h}\frac{p}{\tilde{p}(\theta)} - h\right), \tag{5.3}$$

where η is the rate of capillary degeneration/regeneration and equations (5.1)–(5.3) are specified on the domain $\theta \in [\theta_L, \Theta + \theta_L]$ (the remaining parameters are defined in Section 4.2). In equation (5.3), we assume that capillaries depend upon photoreceptors for survival. Since the exact manner of dependence is unknown, we choose an explicit relationship, neglecting any intermediate mechanisms. In particular, we assume that capillaries adapt to the local photoreceptor density, $p(\theta,t)$, such that they are maintained in the same proportion to $\tilde{h}$, as local photoreceptor density is to healthy photoreceptor density $\tilde{p}(\theta)$. As discussed in Section 5.1, photoreceptor loss may lead to RPE loss, halting the production of VEGF upon which the CC

may rely for survival (Saint-Geniez et al., 2009). Therefore, we are effectively assuming that RPE cells are lost in proportion to the photoreceptors upon which they rely, leading to a proportional drop in VEGF production and hence CC density. Note that we do not use a logistic term in equation (5.3), since capillary regrowth is most likely to emanate from the healthy regions of the choroid that surround the degenerate patch, rather than from within the patch itself. The constant $\tilde{h}$ represents the maximum value taken by $h(\theta,t)$. In what follows we fix $\tilde{h} = 2.01 \times 10^4$ m^{-1}, i.e. at the same value used for 'h' in Chapter 4 (where h was constant in Chapter 4).

As in Chapter 4, we define $\lambda_1(c)$ and $\lambda_2(c)$ as

$$\begin{aligned} &\lambda_1(c) = 1 - H(c - c_{crit}), \\ &\lambda_2(c) = 1 - \lambda_1(c) = H(c - c_{crit}) = \begin{cases} 0 & \text{if } c < c_{crit}, \\ 1 & \text{if } c \geq c_{crit}, \end{cases} \end{aligned} \tag{5.4}$$

and $\tilde{p}(\theta)$ as

$$\tilde{p}(\theta) = \underbrace{B_1 e^{-b_1(\theta-\theta_L)} + B_2 e^{-b_2(\theta-\theta_L)}}_{\text{Cones}} + \underbrace{B_3(\theta-\theta_L)e^{-b_3(\theta-\theta_L)}}_{\text{Rods}}. \tag{5.5}$$

We close the system by imposing initial and boundary conditions. We impose the following initial conditions

$$\begin{aligned} &c(\theta,0) = c_{init}(\theta), \qquad h(\theta,0) = h_{init}(\theta) = \tilde{h}, \\ &p(\theta,0) = p_{init}(\theta) = (H(\theta-\theta_2) + H(\theta_1-\theta))\tilde{p}(\theta), \end{aligned} \tag{5.6}$$

wherein θ_1 and θ_2 are the margins of the degenerate photoreceptor patch (where $\theta_1 < \theta_2$), and $c_{init}(\theta)$ is the steady-state oxygen concentration corresponding to the initial photoreceptor and capillary profiles (that is, the steady-state solution to equation (5.1), with $p = p_{init}(\theta)$ and $h = h_{init}(\theta)$).

Lastly, we impose zero-flux boundary conditions for oxygen on either end of the domain:

$$\frac{\partial c}{\partial \theta}(\theta_L, t) = 0 = \frac{\partial c}{\partial \theta}(\Theta + \theta_L, t). \tag{5.7}$$

See Tables 4.1 and 4.2 for dimensional parameter values. Since the rate of capillary degeneration/regeneration, η, is unknown, we compare results using a range of possible values (see Section 5.4.2).

5.2.1 Non-dimensionalisation

To simplify the subsequent analysis, we non-dimensionalise the system, scaling the independent and dependent variables, together with the initial conditions for oxygen and capillaries, as follows

$$\theta = \Theta\theta^*, \quad t = \frac{t^*}{\delta}, \quad c = c_{ch}c^*, \quad p = \tilde{p}_A p^*, \quad h = \tilde{h}h^*, \quad c_{init} = c_{ch}c^*_{init}, \quad h_{init} = \tilde{h}h^*_{init}.$$

We define the following non-dimensional parameters:

$$\begin{array}{cccc}
\theta_L^* = \frac{\theta_L}{\Theta}, & \theta_1^* = \frac{\theta_1}{\Theta}, & \theta_2^* = \frac{\theta_2}{\Theta}, & D^* = \frac{D}{R^2\Theta^2\delta}, \\
Q^* = \frac{\alpha\tilde{p}_A}{c_{ch}\delta}Q, & \gamma^* = \frac{\gamma}{c_{ch}}, & \beta^* = \frac{\tilde{h}\beta}{\delta}, & c^*_{crit} = \frac{c_{crit}}{c_{ch}}, \\
\mu^* = \frac{\mu}{\delta}, & \eta^* = \frac{\eta}{\delta} & B_1^* = \frac{B_1}{\tilde{p}_A}, & B_2^* = \frac{B_2}{\tilde{p}_A}, \\
B_3^* = \frac{\Theta B_3}{\tilde{p}_A}, & b_1^* = \Theta b_1, & b_2^* = \Theta b_2, & b_3^* = \Theta b_3,
\end{array}$$

noting that $\lambda_1^*(c^*) = \lambda_1(c)$ and $\lambda_2^*(c^*) = \lambda_2(c)$.

As in Chapter 4, we assume that the oxygen concentration is at quasi-steady-state at all

times. Therefore, dropping the stars, equations (5.1)–(5.3), (5.6) and (5.7) reduce to

$$0 = \frac{D}{\sin(\Theta\theta)}\frac{\partial}{\partial\theta}\left(\sin(\Theta\theta)\frac{\partial c}{\partial\theta}\right) - \frac{Qpc}{\gamma+c} + \beta h(1-c), \tag{5.8}$$

$$\frac{\partial p}{\partial t} = \mu p\left(1 - \frac{p}{\tilde{p}(\theta)}\right)\lambda_1(c) - p\lambda_2(c), \tag{5.9}$$

$$\frac{\partial h}{\partial t} = \eta\left(\frac{p}{\tilde{p}(\theta)} - h\right), \tag{5.10}$$

$$h(\theta,0) = h_{init}(\theta) = 1, \qquad p(\theta,0) = p_{init}(\theta) = (H(\theta-\theta_2) + H(\theta_1-\theta))\tilde{p}(\theta), \tag{5.11}$$

$$\frac{\partial c}{\partial\theta}(\theta_L,t) = 0 = \frac{\partial c}{\partial\theta}(1+\theta_L,t). \tag{5.12}$$

See Table 4.3 for non-dimensional parameter values.

5.2.2 Mutation-induced Rod Degeneration

As in Section 4.4.3, we construct a modified version of the model to account for mutation-induced rod degeneration. Denoting rod density by $p_r(\theta,t)$ and cone density by $p_c(\theta,t)$, we obtain the following dimensionless system:

$$0 = \frac{D}{\sin(\Theta\theta)}\frac{\partial}{\partial\theta}\left(\sin(\Theta\theta)\frac{\partial c}{\partial\theta}\right) - \frac{Q(p_r+p_c)c}{\gamma+c} + \beta h(1-c), \tag{5.13}$$

$$\frac{\partial p_r}{\partial t} = -(\phi_r + \lambda_2(c))p_r, \tag{5.14}$$

$$\frac{\partial p_c}{\partial t} = \mu p_c\left(1 - \frac{p_c}{\tilde{p}_c(\theta)}\right)\lambda_1(c) - p_c\lambda_2(c), \tag{5.15}$$

$$\frac{\partial h}{\partial t} = \eta\left(\frac{p_r+p_c}{\tilde{p}_r(\theta)+\tilde{p}_c(\theta)} - h\right), \tag{5.16}$$

where we take $\phi_r = 6.6\times10^{-3}$ as in Chapter 4, and $\tilde{p_r}(\theta)$ and $\tilde{p_c}(\theta)$ are defined as

$$\tilde{p}_r(\theta) = B_3(\theta-\theta_L)e^{-b_3(\theta-\theta_L)}, \tag{5.17}$$

$$\tilde{p}_c(\theta) = B_1e^{-b_1(\theta-\theta_L)} + B_2e^{-b_2(\theta-\theta_L)}. \tag{5.18}$$

We close the system by imposing initial and boundary conditions. The initial conditions are

$$p_r(\theta,0) = p_{r_{init}}(\theta) = \tilde{p}_r(\theta), \quad p_c(\theta,0) = p_{c_{init}}(\theta) = \tilde{p}_c(\theta), \quad h(\theta,0) = h_{init}(\theta) = 1, \tag{5.19}$$

whilst the zero-flux oxygen boundary conditions are given by equation (5.12).

5.2.3 Mutation-induced Cone Degeneration

Similarly, as in Section 4.4.4, we may account for mutation-induced cone degeneration by considering the dimensionless system:

$$0 = \frac{D}{\sin(\Theta\theta)}\frac{\partial}{\partial\theta}\left(\sin(\Theta\theta)\frac{\partial c}{\partial\theta}\right) - \frac{Q(p_r+p_c)c}{\gamma+c} + \beta h(1-c), \tag{5.20}$$

$$\frac{\partial p_r}{\partial t} = \mu p_r\left(1 - \frac{p_r}{\tilde{p}_r(\theta)}\right)\lambda_1(c) - \lambda_2(c)p_r, \tag{5.21}$$

$$\frac{\partial p_c}{\partial t} = -(\phi_c + \lambda_2(c))p_c, \tag{5.22}$$

$$\frac{\partial h}{\partial t} = \eta\left(\frac{p_r+p_c}{\tilde{p}_r(\theta)+\tilde{p}_c(\theta)} - h\right), \tag{5.23}$$

where $\phi_c = 6.6\times10^{-3}$ as in Chapter 4. We close the system by imposing initial and boundary conditions, given by equations (5.19) and (5.12) respectively.

5.3 Mathematical Analysis: 1D Capillary Loss

In this section we perform an asymptotic analysis, similar to those in Section 4.3, to determine the conditions under which a patch of photoreceptor loss will expand when it is also accompanied by a patch of capillary loss. For simplicity, we consider the case where the degenerate patch of photoreceptors extends from the ora serrata, at $\theta = \theta_L + 1$, to a point $\theta_p \in [\theta_L, \theta_L + 1)$ (as opposed to an isolated degenerate patch surrounded on either side by healthy photoreceptors as in Sections 4.3.1 and 4.3.2). This is a sensible choice since degeneration often initiates at the ora serrata, as seen both in clinical studies (see, for example, Grover et al., 1998; Hamel,

2006; Hartong et al., 2006) and our results in Section 4.4. Since capillary loss occurs in response to photoreceptor loss, we assume that capillary loss is confined to the region of the degenerate photoreceptor patch, such that its left-hand boundary $\theta_c \geq \theta_p$. We take the right-hand boundary of the degenerate capillary patch to lie at $\theta = \theta_L + 1$, since the degeneration of photoreceptors, and hence capillaries, is most likely to initiate here.

As in Section 4.3, a degenerate patch will spread if the oxygen concentration on the edge of the patch is greater than or equal to the hyperoxic threshold, that is if $c(\theta_p) \geq c_{crit}$. In the absence of capillary loss, this problem reduces to that of the wide degenerate patch, considered in Section 4.3.1, with $\theta_2 = \theta_L + 1$. In this case, the stability properties of the patch are as shown in Figure 4.8. Capillary loss reduces $c(\theta_p)$, and, as a result, shrinks the size of the regions in which photoreceptor degeneration will spread or remain stationary. We note that, as with the wide degenerate patch case, this analysis is not valid in a narrow region $\theta < \theta_L + 0.04$, since it does not account for the sharp peak in cone density there. A separate analysis, similar to that in Section 4.3.3, would be required to examine the effect of capillary loss on photoreceptor degeneration in this region.

As in Section 4.3, we fix $\varepsilon = O(10^{-2})$ and rescale the model parameters as follows: $D = \varepsilon^{-1}D^*$, $Q = \varepsilon^{-3}Q^*$, $\gamma = \varepsilon\gamma^*$, $\beta = \varepsilon^{-3}\beta^*$ and $b_1 = \varepsilon^{-1}b_1^*$, where D^*, Q^*, γ^*, β^* and b_1^* are all $O(1)$ constants. Under this scaling and upon dropping the stars, equation (5.8) becomes

$$0 = \varepsilon^2 D\frac{\mathrm{d}^2 c}{\mathrm{d}\theta^2} + \varepsilon^2 D\Theta\cot(\Theta\theta)\frac{\mathrm{d}c}{\mathrm{d}\theta} - \frac{Qp(\theta)c}{\varepsilon\gamma + c} + \beta h(1-c), \tag{5.24}$$

where $p(\theta) = H(\theta_p - \theta)\tilde{p}(\theta)$, $h(\theta) = H(\theta_c - \theta)$ and

$$\tilde{p}(\theta) = B_1 e^{-\varepsilon^{-1}b_1(\theta-\theta_L)} + B_2 e^{-b_2(\theta-\theta_L)} + B_3(\theta-\theta_L)e^{-b_3(\theta-\theta_L)}. \tag{5.25}$$

As before, we impose zero-flux boundary conditions so that

$$\frac{\mathrm{d}c}{\mathrm{d}\theta}(\theta_L) = 0 = \frac{\mathrm{d}c}{\mathrm{d}\theta}(1+\theta_L). \tag{5.26}$$

We form the regular perturbation expansions:

$$c(\theta) = c_0(\theta) + \varepsilon c_1(\theta) + O(\varepsilon^2), \qquad p(\theta) = p_0(\theta) + \varepsilon p_1(\theta) + O(\varepsilon^2). \tag{5.27}$$

We do not expand $h(\theta)$ since it is either 1 (for $\theta \leq \theta_c$) or 0 (for $\theta > \theta_c$).

We also note that

$$(\varepsilon\gamma + c)^{-1} = \frac{1}{c_0} - \varepsilon\frac{c_1 + \gamma}{c_0^2} + O(\varepsilon^2), \tag{5.28}$$

and $\cot(\Theta\theta) \leq O(1)$ for $\theta \in [\theta_L, 1 + \theta_L]$.

As in Section 4.3, we partition the domain into inner and outer regions. In the outer regions the oxygen concentration is either constant, or changes gradually in response to the spatial variation in photoreceptor density. In the inner regions we rescale θ, to bring the diffusion term into the dominant balance, allowing us to account for rapid variations in the oxygen concentration and so to satisfy the relevant boundary conditions. We construct the leading order solution in each interval, using the boundary conditions and asymptotic matching to determine the constants of integration (Bender and Orszag, 1999).

For reasons that will become clear as we proceed, the domain must be partitioned as shown in Figure 5.2. Equation (5.8) is discontinuous at θ_p and θ_c, due to the discontinuities in $p(\theta)$ and $h(\theta)$ respectively at these points. Therefore, we must use patching at these boundaries, imposing continuity in the concentration and flux of oxygen (Bender and Orszag, 1999).

In the left-outer region, $p(\theta) = \tilde{p}(\theta)$ and $h(\theta) = 1$, so that equation (5.25) supplies $p_0(\theta) = F(\theta)$, where $F(\theta) := B_2 e^{-b_2(\theta-\theta_L)} + B_3(\theta - \theta_L)e^{-b_3(\theta-\theta_L)}$, while equation (5.24) yields

$$c_0(\theta) = 1 - \frac{Q}{\beta}F(\theta). \tag{5.29}$$

In the right-outer region, $p(\theta) = 0$ and $h(\theta) = 0$, and the kinetic terms disappear from equation (5.24), leaving

$$0 = \frac{\mathrm{d}^2 c}{\mathrm{d}\theta^2} + \Theta\cot(\Theta\theta)\frac{\mathrm{d}c}{\mathrm{d}\theta}, \tag{5.30}$$

at leading order. Substituting $v(\theta) = \frac{\mathrm{d}c}{\mathrm{d}\theta}$ into equation (5.30) and solving using the integrating

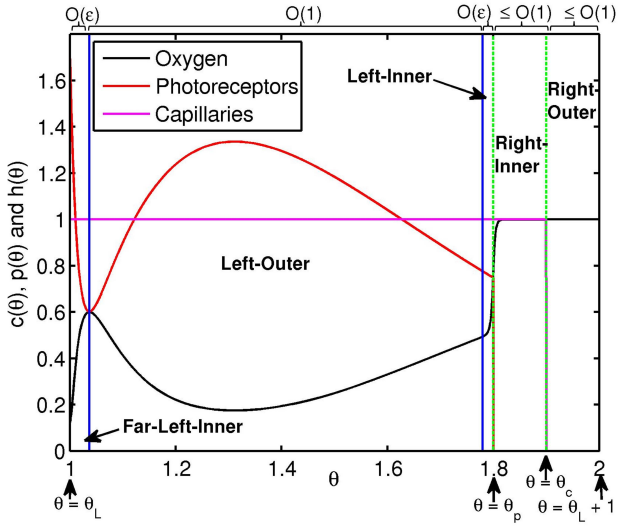

Figure 5.2: Diagram to show the locations of the outer and inner regions for the capillary loss analysis. The solid vertical lines demarcate the approximate limits of the boundary layers, whilst the dashed vertical lines mark the positions of θ_p and θ_c. Equation (5.8) was solved using the finite difference method, with $p(\theta) = H(\theta_p - \theta)\tilde{p}(\theta)$ and $h(\theta) = H(\theta_c - \theta)$. Parameter values: $\theta_p = 1.8$ and $\theta_c = 1.9$. Remaining parameter values as in Table 4.3.

factor method, we obtain $v(\theta) = K\csc(\Theta\theta)$, where K is the constant of integration. Reversing the substitution, we may use separation of variables to obtain

$$c(\theta) = A_1 \log\left(\tan\left(\frac{\Theta\theta}{2}\right)\right) + A_2, \tag{5.31}$$

where the A_is in this equation, and all equations that follow, are constants. Imposing the zero-flux boundary condition at $\theta = \theta_L + 1$, we find that $A_1 = 0$. We note that, since the outer solution satisfies this boundary condition, an inner region is not required at this boundary.

The leading order solution in the far-left-inner region is the same as in the wide and narrow degenerate patch cases in Chapter 4 (see Section 4.3.1 for the derivation), yielding

$$c_0(\theta) = 1 - \frac{QB_2}{\beta} - \frac{QB_1}{\beta - b_1^2 D}\left(e^{-\varepsilon^{-1}b_1(\theta-\theta_L)} - b_1\sqrt{\frac{D}{\beta}}e^{-\varepsilon^{-1}\sqrt{\frac{\beta}{D}}(\theta-\theta_L)}\right). \tag{5.32}$$

Similarly, the left- and right-inner solutions are the same as those in the wide (left-left-

inner and right-left-inner) and narrow (left-centre-inner and centre-centre-inner) degenerate patch cases in Chapter 4, up to the determination of the constants of integration (see Section 4.3.1 for the derivation), yielding

$$c_0(\hat{\theta}) = A_3 e^{\sqrt{\frac{\beta}{D}}\hat{\theta}} + A_4 e^{-\sqrt{\frac{\beta}{D}}\hat{\theta}} + 1 - \frac{Q}{\beta}F(\theta_p), \tag{5.33}$$

in the left-inner region, where $p_0(\hat{\theta}) = F(\theta_p)$, $h(\hat{\theta}) = 1$ and $\hat{\theta} = \varepsilon^{-1}(\theta - \theta_p)$, and

$$c_0(\hat{\theta}) = A_5 e^{\sqrt{\frac{\beta}{D}}\hat{\theta}} + A_6 e^{-\sqrt{\frac{\beta}{D}}\hat{\theta}} + 1, \tag{5.34}$$

in the right-inner region, where $p_0(\hat{\theta}) = 0$ and $h(\hat{\theta}) = 1$.

As in Section 4.3.1, we use Van Dyke's rule to match the left-outer and left-inner solutions, yielding $A_4 = 0$. This leaves us with 4 unknowns: A_2, A_3, A_5, and A_6. These are determined by imposing continuity in the concentration and flux of oxygen at $\theta = \theta_p$ and $\theta = \theta_c$. Reverting to outer variables, this yields the left-inner solution,

$$c_0(\theta) = 1 - \frac{Q}{2\beta}\left(2 - \left(1 - e^{-2\varepsilon^{-1}\sqrt{\frac{\beta}{D}}(\theta_c - \theta_p)}\right)e^{-\varepsilon^{-1}\sqrt{\frac{\beta}{D}}(\theta_p - \theta)}\right)F(\theta_p), \tag{5.35}$$

the right-inner solution,

$$c_0(\theta) = 1 - \frac{Q}{2\beta}\left(e^{-2\varepsilon^{-1}\sqrt{\frac{\beta}{D}}(\theta_c - \theta_p)}e^{\varepsilon^{-1}\sqrt{\frac{\beta}{D}}(\theta - \theta_p)} + e^{-\varepsilon^{-1}\sqrt{\frac{\beta}{D}}(\theta - \theta_p)}\right)F(\theta_p), \tag{5.36}$$

and the right-outer solution

$$c_0(\theta) = 1 - \frac{Q}{\beta}F(\theta_p)e^{-\varepsilon^{-1}\sqrt{\frac{\beta}{D}}(\theta_c - \theta_p)}. \tag{5.37}$$

The right-inner and right-outer solutions are valid across the intervals $\theta \in [\theta_p, \theta_c]$ and $\theta \in [\theta_c, \theta_L + 1]$ respectively. We construct a composite solution, using the leading order solutions in the far-left-inner, left-outer and left-inner regions, to find a solution valid across the interval

$\theta \in [\theta_L, \theta_p]$. Proceeding as in Section 4.3, this yields

$$c_0(\theta) = 1 - \frac{Q}{2\beta}\left(2F(\theta) - \left(1 - e^{-2\varepsilon^{-1}\sqrt{\frac{\beta}{D}}(\theta_c-\theta_p)}\right)e^{-\varepsilon^{-1}\sqrt{\frac{\beta}{D}}(\theta_p-\theta)}F(\theta_p)\right) - \frac{QB_1}{\beta - b_1^2 D}\left(e^{-\varepsilon^{-1}b_1(\theta-\theta_L)} - b_1\sqrt{\frac{D}{\beta}}e^{-\varepsilon^{-1}\sqrt{\frac{\beta}{D}}(\theta-\theta_L)}\right). \tag{5.38}$$

In Figure 5.3 we compare our analytical approximation with the numerical solution to (5.8) with $p(\theta) = H(\theta_p - \theta)\tilde{p}(\theta)$ and $h(\theta) = H(\theta_c - \theta)$. The numerical solution is plotted with both Michaelis-Menten ($Qpc/(\gamma + c)$) and constant (Qp) oxygen uptake terms. The analytical solution matches well with the constant uptake numerical solution in all regions, whilst it underestimates the Michaelis-Menten uptake numerical solution where the photoreceptor density is highest. The analytical solution is a good match to both numerical solutions in the neighbourhood of $\theta = \theta_p$, which is important, as we will use $c(\theta_p)$ to determine whether a degenerate patch of photoreceptors will spread.

Substituting $\theta = \theta_p$ into either of equations (5.35) or (5.36), we obtain the following expression for the concentration of oxygen on the edge of the degenerate patch of photoreceptors:

$$c_0(\theta_p) = 1 - \frac{Q}{2\beta}\left(1 + e^{-2\varepsilon^{-1}\sqrt{\frac{\beta}{D}}(\theta_c-\theta_p)}\right)F(\theta_p). \tag{5.39}$$

This expression is similar to equation (4.31), the difference being that it contains a new term which depends upon θ_c. This term is exponentially small, and hence negligible, everywhere except where $\theta_c - \theta_p = O(\varepsilon)$ (assuming $\theta_c > \theta_p$). Therefore, the degeneration of a patch of capillaries will not have a significant effect unless the inner margin of the capillary patch lies within a distance of $O(\varepsilon)$ to the inner margin of the patch of photoreceptor loss. In other words, the region of capillary loss must extend within the boundary layer at the edge of the degenerate photoreceptor patch in order to affect the oxygen concentration at the edge of this patch. If this does not occur, an outer region will emerge, in which $c_0(\theta) = 1$, between the edge of the patch of photoreceptor loss and the region of capillary loss, returning us to a scenario like that in Section 4.3.1.

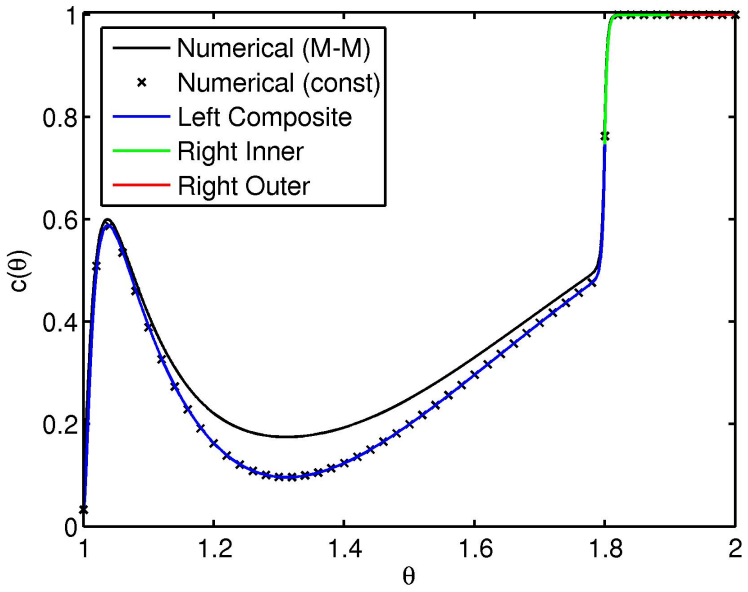

Figure 5.3: Comparison of numerical and analytical solutions for the capillary loss analysis. Numerical solutions are plotted with both Michaelis-Menten ($Qpc/(\gamma+c)$) and constant (Qp) oxygen uptake terms. The numerical solutions were obtained by solving equation (5.8) (subject to modification of the uptake term) using the finite difference method, with $p(\theta) = H(\theta_p - \theta)\tilde{p}(\theta)$ and $h(\theta) = H(\theta_c - \theta)$, whilst the analytical solutions are given by equations (5.36)–(5.38). Parameter values: $\theta_p = 1.8$ and $\theta_c = 1.9$. Remaining parameter values as in Table 4.3, where the parameters are scaled as described in Section 5.3 for the analytical solutions.

This is demonstrated in Figure 5.4(a), which shows the regions in (θ_p, θ_c) parameter space where the degenerate patch of photoreceptors is stable or unstable. This figure was obtained by evaluating equation (5.39) for a range of values of $\theta_p \leq \theta_c$ and noting whether $c(\theta_p)$ is above or below the hyperoxic threshold c_{crit}. In region I the degenerate photoreceptor patch is stable, remaining stationary. The main portion of this region coincides with regions A and C in Figure 4.9. In region II (left and right) the degenerate photoreceptor patch is unstable, expanding centrally. Region II (left) coincides with regions D (upper-left and lower-left) and B, whilst region II (right) coincides with region D (upper-right) in Figure 4.9. The correspondence between Figures 4.9 and 5.4(a) is due to the fact that θ_{crit_1} and θ_{crit_2} are preserved for $\theta_c - \theta_p > O(\varepsilon)$. Region I also extends in a narrow region along the line $\theta_p = \theta_c$, beneath the unstable regions, becoming increasingly narrow as θ_p approaches θ_L on the left, and $\theta_L + 1$ on the right. It is in this region, of width $O(\varepsilon)$ or less, that capillary loss exerts an effect on the stability of the degenerate photoreceptor patch.

In the limiting case where $\theta_c = \theta_p$, equation (5.39) reduces to equation (5.29), with $\theta = \theta_p$. Since the left-outer solution gives the oxygen concentration under healthy conditions and since $c(\theta) < c_{crit}$ under healthy conditions, $c_0(\theta_p) < c_{crit}$ when $\theta_c = \theta_p$ and we deduce that the degenerate photoreceptor patch is always stable in this case. As noted above, our analysis does not hold for $\theta_p < 0.04$; however, numerical simulations show that the degenerate photoreceptor patch is also stable in this region when $\theta_c = \theta_p$ (see Figure 5.4(b)).

Setting $c_0(\theta_p) = c_{crit}$ in equation (5.39), we obtain the following expression for the critical position of the central boundary of the degenerate capillary patch, $\theta_{c_{crit}}(\theta_p)$:

$$\theta_{c_{crit}}(\theta_p) = \theta_p + \frac{\varepsilon}{2}\sqrt{\frac{D}{\beta}}\log\left(\frac{QF(\theta_p)}{2\beta(1-c_{crit}) - QF(\theta_p)}\right). \tag{5.40}$$

For a given value of θ_p, this expression allows us to calculate how far centrally the degenerate capillary patch must extend to prevent further photoreceptor loss, in those cases where photoreceptor loss would proceed in the absence of capillary loss. For $\theta_p = 1.8$ as in Figures 5.2 and 5.3, $\theta_{c_{crit}}(\theta_p) = 1.802$ (3 d.p.), so that $\theta_{c_{crit}}(\theta_p) - \theta_p \leq O(\varepsilon)$.

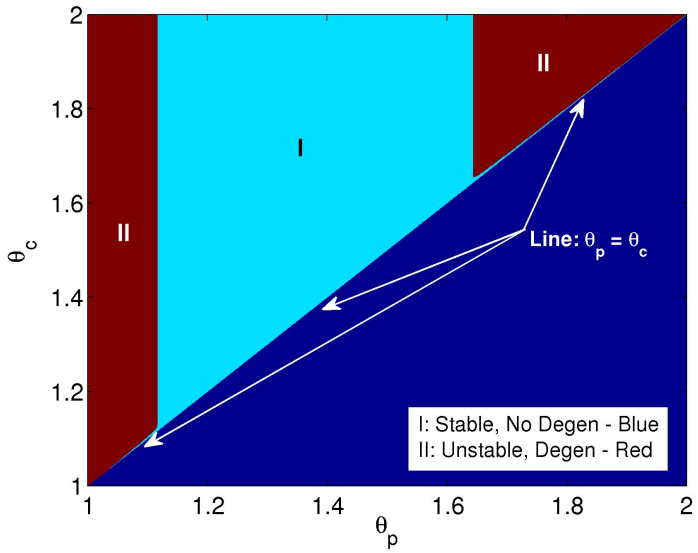

(a) Asymptotic approximation.

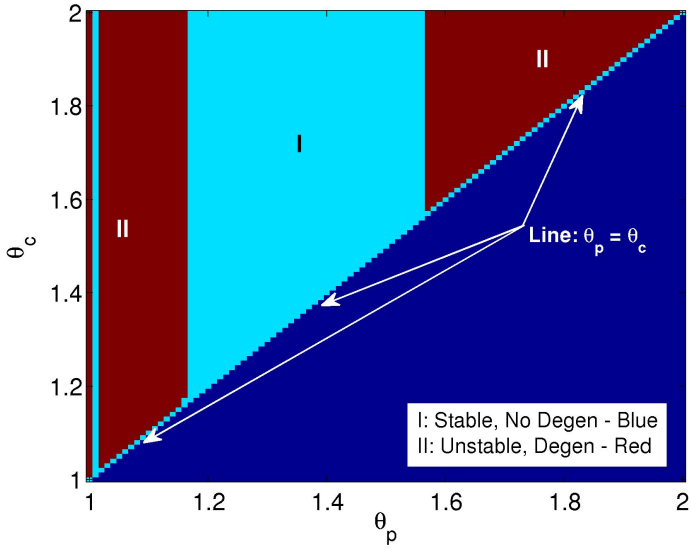

(b) Numerical solution.

Figure 5.4: Diagram to show stable and unstable regions in (θ_p, θ_c) parameter space as revealed by the asymptotic analysis and numerical solutions. (a) equation (5.39) was evaluated and (b) equation (5.8) was solved for a range of values of both θ_p and θ_c, where $\theta_p \leq \theta_c$. If $c(\theta_p) < c_{crit}$, then the boundary at θ_p is stable; if $c(\theta_p) \geq c_{crit}$, then it is unstable. The numerical solution in (b) was obtained using the finite difference method (see text for details), with 10,001 mesh points, and with $p(\theta) = H(\theta_p - \theta)\tilde{p}(\theta)$ and $h(\theta) = H(\theta_c - \theta)$. Parameter values as in Table 4.3 (using the scalings described in Section 5.3 for (a)).

5.4 Numerical Results: 1D Capillary Loss

We use numerical simulations to validate and extend the preceding analysis.

5.4.1 Steady-state Model

We begin by solving equation (5.8), with $p(\theta) = H(\theta_p - \theta)\tilde{p}(\theta)$ and $h(\theta) = H(\theta_c - \theta)$, for a range of values of θ_p and θ_c, where $\theta_p \leq \theta_c$, to compare the stability properties of the system with those predicted in Figure 5.4(a). Equation (5.8) was solved in the same way as in Section 4.4.1, discretising in space, and solving the resulting system of nonlinear algebraic equations using the Matlab routine fsolve, employing the Trust-Region-Dogleg algorithm. (This method was also used to produce the numerical solutions in Figures 5.2 and 5.3.)

The numerical solution presented in Figure 5.4(b) confirms the arrangement of stable and unstable regions predicted by the analysis. In particular, we see that capillary loss only stabilises a degenerate patch in a narrow region along the line $\theta_p = \theta_c$. Unlike in Figure 5.4(a), region II (left) is interrupted by a narrow (near-central) stable region corresponding to that in Figure 4.17. This is due to the peak in cone density, which was not included in the analysis (we assumed that θ_p and θ_c lay outside this boundary layer region). The position of the vertical boundaries between region I and region II (left and right) is also slightly different from that predicted by our analysis, for the same reasons as those discussed in Section 4.4.1.

5.4.2 Dynamic Model

In this section we simulate dynamic patch loss and mutation-induced degeneration problems (equations (5.8)–(5.23)). In all cases we assume a healthy initial capillary distribution, $h_0(\theta) = 1$, and allow capillaries to degenerate subsequent to this in response to photoreceptor loss. As in Sections 4.4.2–4.4.4, we solve the time-dependent problems using the method of lines, discretising in space as for the steady-state problem, and integrating in time using an explicit Runge-Kutta method (Matlab routine ode45). The quasi-steady oxygen equation is solved at each time step using the Matlab routine fsolve. We use 4001 spatial mesh points

in the patch loss simulations and 1001 in the mutation-induced degeneration simulations to maintain consistency with the results in Section 4.4.

Patch Loss

Figure 5.5 shows how capillary degeneration affects the progression of a degenerate patch of photoreceptors. The patch locations are the same as those in Figure 4.19, corresponding to region D (upper-left), (upper-right) and (lower-left) (reproduced in the top row of Figure 5.5). Since we do not know the *in vivo* rate of degeneration, we compare a range of values of $\eta = 0$, 10^{-2}, 10^{-1}, 1 and 10, and find that it is sufficient to demonstrate the full range of behaviours (described below). We note that when $\eta = 1$, this corresponds to a dimensional value of $\eta = \delta = 10^{-7}$ s^{-1}. In each case we have plotted the contours, $(\theta(t), t)$, on which $p(\theta, t) = 0.1$, which define the boundaries of the degenerate patches.

When $\eta = 10^{-2}$, degeneration proceeds in a manner which is almost identical to that when $\eta = 0$. For $\eta = 10^{-1}$, degeneration proceeds as with $\eta = 10^{-2}$ in Figure 5.5(a), whilst in Figure 5.5(b) degeneration proceeds as for $\eta = 10^{-2}$ on the right, whilst stalling on the left, following a minor degeneration and partial recovery. In Figure 5.5(c), significant degeneration occurs, followed by a complete recovery (not including the original degenerate patch). When $\eta = 1$, there is an initial minor photoreceptor loss, but the system soon recovers fully (again, not including the original degenerate patch). Lastly, when $\eta = 10$, the patch remains stationary, with an almost imperceptible fluctuation in photoreceptor density early on.

In summary, rapid ($\eta = 10$) capillary loss prevents the spread of degeneration, whilst gradual ($\eta = 10^{-2}$) capillary loss has little effect. Rates of capillary loss between these two extremes either behave in qualitatively the same ways as at the extremes, or exhibit degeneration, followed by partial or complete recovery. We note that, whilst full recovery may be possible mathematically; biologically, recovery may be much more limited, as many photoreceptors may degenerate past the point of recovery.

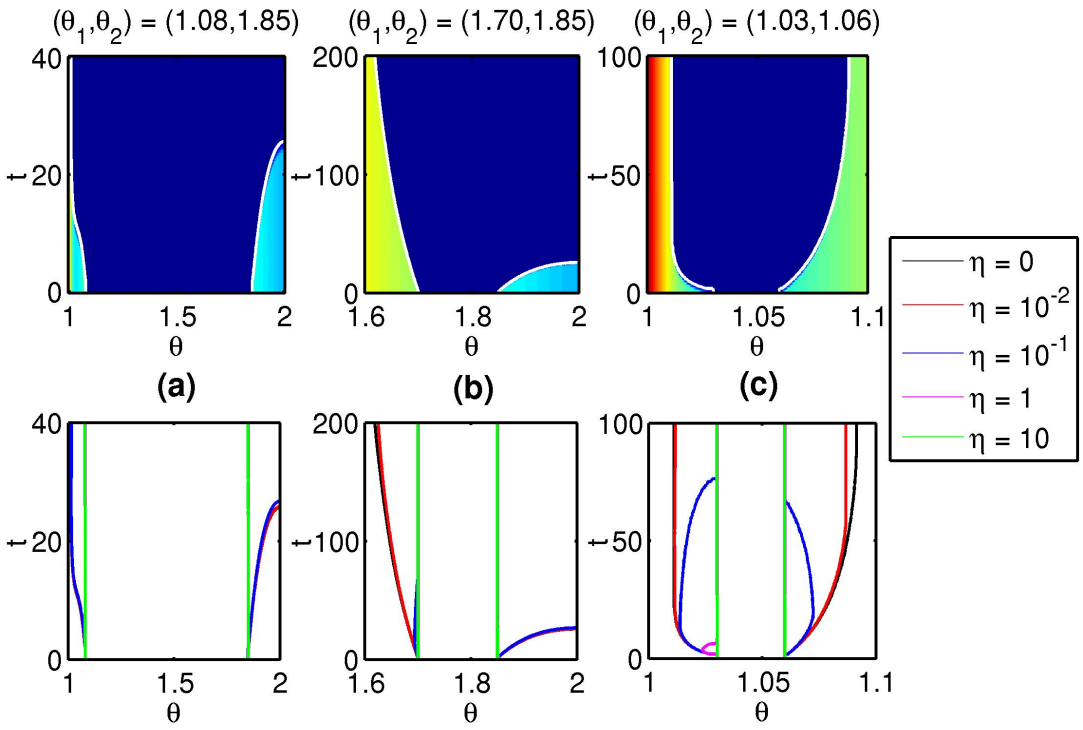

Figure 5.5: Contour plots comparing the progression of photoreceptor degeneration for a range of values of the capillary degeneration rate, η, following the removal of a patch of photoreceptors from the interval $\theta \in [\theta_1, \theta_2]$. Top row: $\eta = 0$. Bottom row: $\eta = 0, 10^{-2}, \ldots, 10$. The lines mark the contours along which $p(\theta, t) = 0.1$ and hence show the boundaries of the degenerate patches. The patch locations in graphs (a), (b) and (c) are the same as those in Figure 4.19(a), (b) and (c) respectively (reproduced in the top row), corresponding to region D (upper-left), (upper-right) and (lower-left) respectively. In all cases, the spread of photoreceptor degeneration decreases with increasing η. Equations (5.8)–(5.12) were solved using the method of lines, with 4001 mesh points (see text for details). Remaining parameter values as in Table 4.3.

Mutation-induced Rod or Cone Degeneration

Figure 5.6 shows how capillary degeneration affects the loss of rods and cones, when the retina undergoes mutation-induced rod or cone degeneration. The scenarios considered are identical to those in Figures 4.22(a) and 4.23, in which $\eta = 0$ (reproduced in the top rows of Figures 5.6(a) and (b)). In this case, we take $\eta = 0$, 10^{-4}, 10^{-3}, 10^{-2}, 10^{-1} and 1, which is sufficient to demonstrate the full range of behaviours (described below). In each case we plot the contours $(\theta(t),t)$ on which $p_r(\theta,t) = 10^{-1}$ and $p_c(\theta,t) = 10^{-2}$, taking a lower value for the cones, since their healthy density is typically much lower than that of rods, such that the pattern of degeneration is only evident for a lower threshold.

When $\eta = 10^{-3}$ and 10^{-4}, the pattern of degeneration is similar to that where $\eta = 0$, except that hyperoxic degeneration does not initiate on the right for mutation-induced cone degeneration when $\eta = 10^{-3}$. For $\eta = 10^{-2}$ and $\eta = 10^{-1}$, the wave of hyperoxic degeneration proceeds more slowly for mutation-induced rod degeneration, stalling on the right and failing to initiate on the left in the latter case, whilst it fails to initiate for mutation-induced cone degeneration. Lastly, when $\eta = 1$, hyperoxic degeneration does not initiate in either case, the contours appearing on the left and top-right of the bottom-left graph in Figure 5.6(a) being due to mutation-induced loss. The contour on the right in the bottom-right graph in Figure 5.6(b) is also due purely to the mutation-induced loss of cones.

In summary, rapid ($\eta = 1, 10^{-1}$ or 10^{-2}) capillary loss prevents or slows hyperoxic degeneration, whilst gradual ($\eta = 10^{-3}$ or 10^{-4}) capillary loss has little effect. See Section 5.7 for discussion.

5.5 Model Formulation: 2D

As with the 1D model, we model the posterior of the eye as a spherical cap, describing the geometry of the retina using spherical polar coordinates (r,θ,ϕ). We neglect variation in the radial direction, r, as before, but include variation in both the polar, θ, and azimuthal, ϕ, directions. We orient our coordinate system so that the fovea lies at $\theta = 0$, whilst the ora

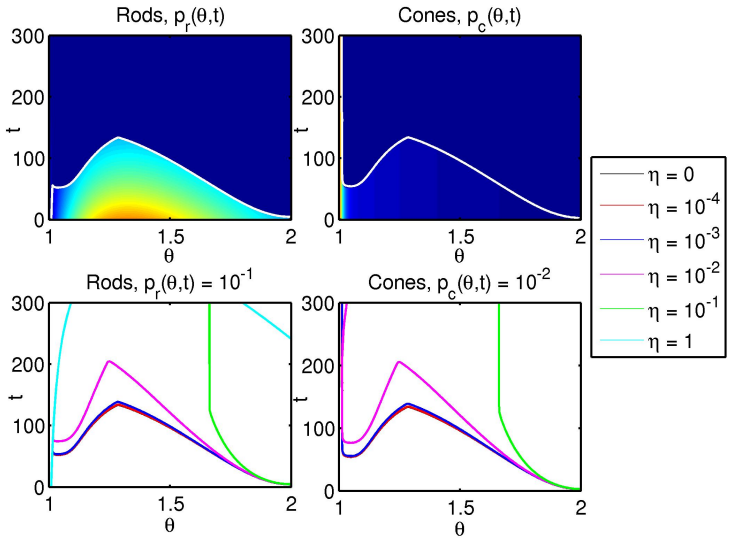

(a) Mutation-induced rod degeneration.

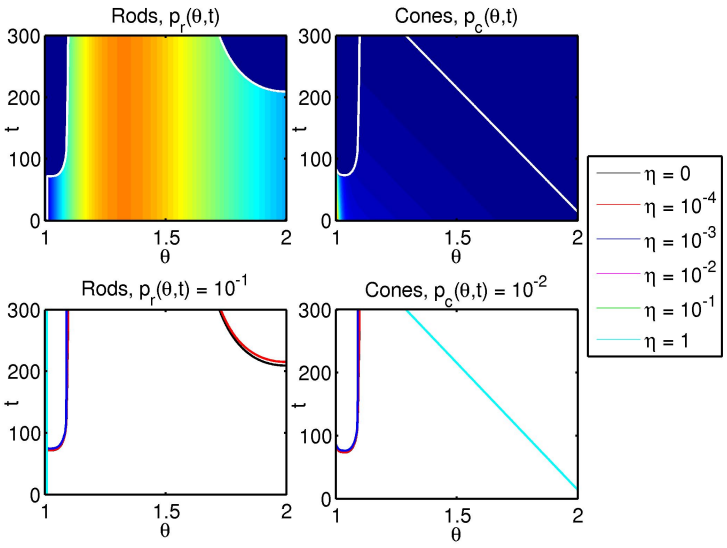

(b) Mutation-induced cone degeneration.

Figure 5.6: Contour plots comparing the progression of photoreceptor degeneration for a range of values of the capillary degeneration rate, η, where the retina undergoes mutation-induced rod (a) or cone (b) degeneration. (a) and (b) — top row: $\eta = 0$, bottom row: $\eta = 0, 10^{-4}, \ldots, 1$. The lines mark the contours along which $p_r(\theta,t) = 10^{-1}$ (for the rods) and $p_c(\theta,t) = 10^{-2}$ (for the cones). The scenarios considered in (a) and (b) are the same as in Figures 4.22(a) and 4.23, where capillary degeneration was not included (reproduced in the top rows of (a) and (b)). In all cases, the severity of photoreceptor degeneration decreases with increasing η. Equations (5.12)–(5.16) and (5.19) (a), and (5.12) and (5.19)–(5.23) (b), were solved using the method of lines, with 1001 mesh points (see text for details). Parameter values: $\phi_r = 6.6 \times 10^{-3}$ (a) and $\phi_c = 6.6 \times 10^{-3}$ (b). Remaining parameter values as in Table 4.3.

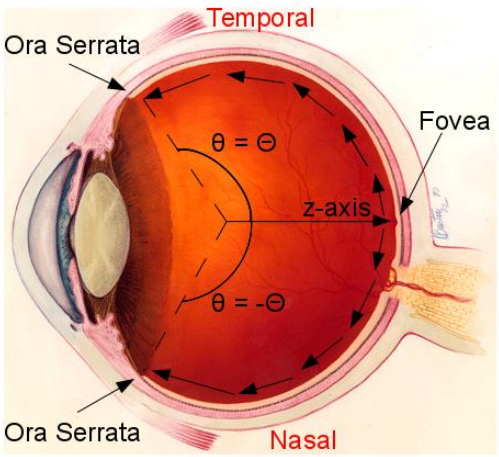

Figure 5.7: 2D Model geometry. The domain is located between the foveal centre, at $\theta = 0$, and the ora serrata, at $\theta = \Theta$, for $\phi \in [0, 2\pi]$. The eye is pictured in the transverse plane. Figure reproduced, with modifications, from `http://www.nei.nih.gov/health/coloboma/coloboma.asp`, courtesy: National Eye Institute, National Institutes of Health (NEI/NIH).

serrata lies at $\theta = \Theta$. Since the 2D model results are purely numerical and since our numerical code can cope with the coordinate singularity at $\theta = 0$, we do not rotate the coordinate system to avoid the singularity in this case. We ignore the optic disc for simplicity, noting that since it is small and is assumed neither to consume or produce oxygen, it is unlikely to have a significant effect on the behaviour of the solution. Figure 5.7 shows the model geometry.

Having defined the geometry, we construct equations for the retinal oxygen concentration, $c(\theta, \phi, t)$, and the photoreceptor density, $p(\theta, \phi, t)$, as follows

$$\frac{\partial c}{\partial t} = \frac{D}{R^2 \sin(\theta)} \left(\frac{\partial}{\partial \theta} \left(\sin(\theta) \frac{\partial c}{\partial \theta} \right) + \frac{1}{\sin(\theta)} \frac{\partial^2 c}{\partial \phi^2} \right) - \frac{\alpha Q p c}{\gamma + c} + \beta h (c_{ch} - c), \tag{5.41}$$

$$\frac{\partial p}{\partial t} = \mu p \left(1 - \frac{p}{\tilde{p}(\theta)} \right) \hat{\lambda}_1(c) - \delta p \hat{\lambda}_2(c), \tag{5.42}$$

where $\tilde{p}(\theta)$ is defined as

$$\tilde{p}(\theta) = \underbrace{B_1 e^{-b_1 \theta} + B_2 e^{-b_2 \theta}}_{\text{Cones}} + \underbrace{B_3 \theta e^{-b_3 \theta}}_{\text{Rods}}, \tag{5.43}$$

whilst $\hat{\lambda}_1(c)$ and $\hat{\lambda}_2(c)$ are defined below. Equations (5.41)–(5.42) are identical to those for the 1D case, except that the Laplacian in the oxygen equation is modified to account for variation of c in the ϕ direction, and the Heaviside functions in $\lambda_1(c)$ and $\lambda_2(c)$ are replaced by hyperbolic functions, in $\hat{\lambda}_1(c)$ and $\hat{\lambda}_2(c)$, as described below.

We impose initial and boundary conditions to close equations (5.41)–(5.42). The initial oxygen distribution and photoreceptor density are given by

$$c(\theta,\phi,0) = c_{init}(\theta,\phi), \qquad p(\theta,\phi,0) = p_{init}(\theta,\phi) = F(\theta,\phi)\tilde{p}(\theta), \tag{5.44}$$

where $0 \leq F(\theta,\phi) \leq 1$ is defined below. The initial oxygen distribution, $c_{init}(\theta,\phi)$, is the steady-state oxygen concentration corresponding to the initial photoreceptor profile (that is, the steady-state solution to (5.41), with $p = p_{init}(\theta,\phi)$).

Lastly, we impose a zero-flux boundary condition at the ora serrata:

$$\frac{\partial c}{\partial \theta}(\Theta,\phi,t) = 0. \tag{5.45}$$

See Tables 4.1 and 4.2 for parameter values (except Q and β) and Section 4.2.1 for a justification of parameter choices. We set the parameters Q and β to take a tenth of their values in Table 4.1, that is $Q = 1.26 \times 10^{-18}$ mol s^{-1} (tissue unit)$^{-1}$ and $\beta = 3.6 \times 10^{-6}$ ms^{-1}, for reasons discussed below.

5.5.1 Non-dimensionalisation

To simplify the subsequent analysis, we non-dimensionalise the system, scaling the independent and dependent variables, together with the initial condition for oxygen, as follows

$$\theta = \Theta\theta^*, \quad \phi = \phi^*, \quad t = \frac{t^*}{\delta}, \quad c = c_{ch}c^*, \quad p = \tilde{p}_A p^*, \quad c_{init} = c_{ch}c^*_{init}.$$

We define the following non-dimensional parameters:

$$D^* = \frac{D}{R^2\Theta^2\delta}, \quad Q^* = \frac{\alpha\tilde{p}_A}{c_{ch}\delta}Q, \quad \gamma^* = \frac{\gamma}{c_{ch}}, \quad \beta^* = \frac{h\beta}{\delta},$$
$$c^*_{crit} = \frac{c_{crit}}{c_{ch}}, \quad \mu^* = \frac{\mu}{\delta}, \quad B_1^* = \frac{B_1}{\tilde{p}_A}, \quad B_2^* = \frac{B_2}{\tilde{p}_A},$$
$$B_3^* = \frac{\Theta B_3}{\tilde{p}_A}, \quad b_1^* = \Theta b_1, \quad b_2^* = \Theta b_2, \quad b_3^* = \Theta b_3,$$

noting that $\hat{\lambda}_1^*(c^*) = \hat{\lambda}_1(c)$, $\hat{\lambda}_2^*(c^*) = \hat{\lambda}_2(c)$ and $F^*(\theta^*, \phi^*) = F(\theta, \phi)$.

The numerical code used to solve the 2D problem uses the fully time-dependent equations, therefore, unlike in the 1D model, we retain the time derivative in the oxygen equation, so that, dropping the stars, equations (5.41)–(5.42) reduce to:

$$\frac{\partial c}{\partial t} = \frac{D}{\sin(\Theta\theta)}\left(\frac{\partial}{\partial\theta}\left(\sin(\Theta\theta)\frac{\partial c}{\partial\theta}\right) + \frac{\Theta^2}{\sin(\Theta\theta)}\frac{\partial^2 c}{\partial\phi^2}\right) - \frac{Qpc}{\gamma + c} + \beta(1-c), \tag{5.46}$$

$$\frac{\partial p}{\partial t} = \mu p\left(1 - \frac{p}{\tilde{p}(\theta)}\right)\hat{\lambda}_1(c) - p\hat{\lambda}_2(c), \tag{5.47}$$

on the domain $\theta \in [0,1]$, $\phi \in [0, 2\pi]$, where $\hat{\lambda}_1(c)$ and $\hat{\lambda}_2(c)$ are defined as

$$\hat{\lambda}_1(c) = 1 - \frac{1}{2}(\tanh(S_c(c - c_{crit})) + 1),$$
$$\hat{\lambda}_2(c) = 1 - \hat{\lambda}_1(c) = \frac{1}{2}(\tanh(S_c(c - c_{crit})) + 1) \approx \begin{cases} 0 & \text{if } c < c_{crit}, \\ 1 & \text{if } c \geq c_{crit}, \end{cases} \tag{5.48}$$

and the parameter S_c determines the sharpness of the step, where $S_c = 10^3$ in all simulations. We use hyperbolic functions here, rather than the Heaviside functions used in the 1D work (see, for example, equation (5.4)), in order to make the governing equations smooth, improving the convergence of the numerical scheme (described in Section 5.6). This remains a biologically realistic choice for these terms.

We impose the initial conditions:

$$c(\theta, \phi, 0) = c_{init}(\theta, \phi), \qquad p(\theta, \phi, 0) = p_{init}(\theta, \phi) = F(\theta, \phi)\tilde{p}(\theta). \tag{5.49}$$

We choose $F(\theta,\phi)$ to create either an annulus or a disc of photoreceptor loss. To remove an annulus, we set $F(\theta,\phi) = \frac{1}{2}(\tanh(S(\theta_1-\theta)) + \tanh(S(\theta-\theta_2)) + 2)$, where θ_1 and θ_2 are the eccentricities of the inner and outer boundaries respectively and the parameter S determines the sharpness of the edge of the annulus. To remove a disc (or rather a spherical cap), centred at $(\theta,\phi) = (\theta_c, \hat{\phi}_c)$ and of radius ψ, we set $F(\theta,\phi) = \frac{1}{2}(\tanh(S((\theta-\theta_c)^2 + (\phi-\hat{\phi}_c)^2\sin^2(\theta) - \psi^2)) + 1)$, where the parameter S determines the sharpness of the edge of the disc. We take $S = 100$ in all simulations. The $\sin^2(\theta)$ term is required in order to preserve arc-length in the azimuthal direction. We choose hyperbolic functions, rather than step functions (as used in the 1D model), in order to smooth the transition between the healthy and degenerate retina, allowing us to use a coarser finite element mesh to resolve the initial wavefront of degeneration. The initial oxygen distribution, $c_{init}(\theta,\phi)$, is the steady-state oxygen concentration corresponding to the initial photoreceptor profile (that is, the steady-state solution to (5.46), with $p = p_{init}(\theta,\phi)$). Healthy oxygen and photoreceptor profiles are shown in Figure 5.9(a).

Lastly, we have the zero-flux boundary condition:

$$\frac{\partial c}{\partial \theta}(1,\phi,t) = 0. \tag{5.50}$$

See Table 4.3 for non-dimensional model parameter values, except for $Q = 4.89 \times 10^5$ and $\beta = 7.23 \times 10^5$.

We use reduced values for Q and β in order to increase the widths of the advancing wavefronts of degeneration, ensuring that the uptake and supply of oxygen dominate less heavily over diffusion in the fronts. This is necessary in order to avoid the need for very fine spatial meshes to resolve the details of the wavefront in the numerical solution, which would make the problem computationally infeasible given the resources available. Since the ratio of uptake to supply is preserved, the oxygen profile is not significantly affected away from the wavefront, except near $\theta = 0$, where the variation in the oxygen profile becomes less dramatic (see Figure 5.8).

Simulations in 1D show that patches of degeneration spread at approximately twice the

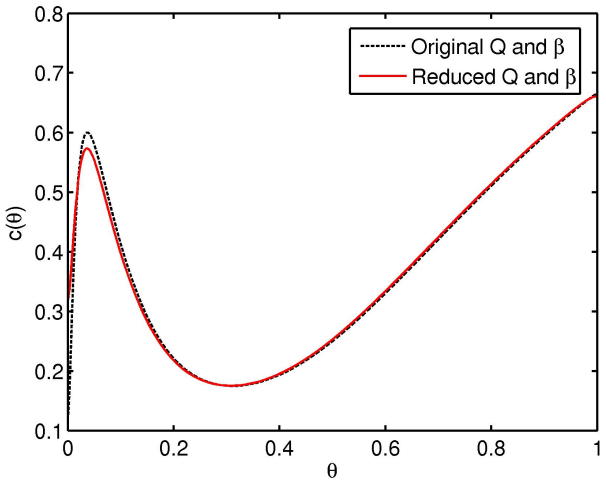

Figure 5.8: Graph to show the effect of reducing Q and β upon the healthy steady-state oxygen profile in the 1D model. Equation (4.7) was solved using the finite difference method (see Section 4.4 for details), with $p(\theta) = \tilde{p}(\theta)$, defined by (5.5) (with $\theta_L = 0$). Parameter values: original $(Q,\beta) = (4.89, 7.23) \times 10^6$ and reduced $(Q,\beta) = (4.89, 7.23) \times 10^5$. Remaining parameter values as in Table 4.3.

speed with reduced Q and β. However, since we are interested in the pattern and relative speed of degeneration, rather than the absolute speed of degeneration, the variation in the speed observed is unimportant. In addition, 2D simulations using the original values of Q and β and a finer mesh, show that degeneration spreads at the same speed as in the 1D simulations, whilst 1D simulations using the reduced values of Q and β, give rise to wave speeds matching those of the 2D simulations, validating the 2D model and the impact of reduced Q and β.

5.5.2 Mutation-induced Rod Degeneration

As in Section 4.4.3, we modify our model to account for mutation-induced rod degeneration. Denoting rod density by $p_r(\theta,\phi,t)$ and cone density by $p_c(\theta,\phi,t)$, we obtain the following

dimensionless system:

$$\frac{\partial c}{\partial t} = \frac{D}{\sin(\Theta\theta)}\left(\frac{\partial}{\partial\theta}\left(\sin(\Theta\theta)\frac{\partial c}{\partial\theta}\right) + \frac{\Theta^2}{\sin(\Theta\theta)}\frac{\partial^2 c}{\partial\phi^2}\right) - \frac{Q(p_r+p_c)c}{\gamma+c} + \beta(1-c), \quad (5.51)$$

$$\frac{\partial p_r}{\partial t} = -(\phi_r + \hat{\lambda}_2(c))p_r, \quad (5.52)$$

$$\frac{\partial p_c}{\partial t} = \mu p_c\left(1 - \frac{p_c}{\tilde{p}_c(\theta)}\right)\hat{\lambda}_1(c) - p_c\hat{\lambda}_2(c), \quad (5.53)$$

where $\phi_r = 6.6\times10^{-3}$, as in Chapter 4. We close the system by imposing zero-flux oxygen boundary conditions (given by equation (5.50)) and the following initial conditions:

$$\begin{aligned} c(\theta,\phi,0) &= c_{init}(\theta,\phi), \\ p_r(\theta,\phi,0) &= p_{r_{init}}(\theta,\phi) = F(\theta,\phi)\tilde{p}_r(\theta), \\ p_c(\theta,\phi,0) &= p_{c_{init}}(\theta,\phi) = F(\theta,\phi)\tilde{p}_c(\theta), \end{aligned} \quad (5.54)$$

where $\tilde{p}_r(\theta)$ and $\tilde{p}_c(\theta)$ are given by

$$\tilde{p}_r(\theta) = B_3\theta e^{-b_3\theta}, \quad (5.55)$$

$$\tilde{p}_c(\theta) = B_1 e^{-b_1\theta} + B_2 e^{-b_2\theta}. \quad (5.56)$$

The function $F(\theta,\phi)$ is either equal to unity, or removes a patch of photoreceptors as described above. As before, the initial oxygen concentration, $c_{init}(\theta,\phi)$, is the steady-state oxygen concentration corresponding to the initial photoreceptor profile (that is, the steady-state solution to (5.51) with $p_r = p_{r_{init}}(\theta,\phi)$ and $p_c = p_{c_{init}}(\theta,\phi)$).

5.5.3 Mutation-induced Cone Degeneration

Similarly, we may account for mutation-induced cone degeneration, as in Section 4.4.4, obtaining the dimensionless system:

$$\frac{\partial c}{\partial t} = \frac{D}{\sin(\Theta\theta)}\left(\frac{\partial}{\partial\theta}\left(\sin(\Theta\theta)\frac{\partial c}{\partial\theta}\right) + \frac{\Theta^2}{\sin(\Theta\theta)}\frac{\partial^2 c}{\partial\phi^2}\right) - \frac{Q(p_r+p_c)c}{\gamma+c} + \beta(1-c), \quad (5.57)$$

$$\frac{\partial p_r}{\partial t} = \mu p_r\left(1-\frac{p_r}{\tilde{p}_r(\theta)}\right)\hat{\lambda}_1(c) - p_r\hat{\lambda}_2(c), \quad (5.58)$$

$$\frac{\partial p_c}{\partial t} = -(\phi_c + \hat{\lambda}_2(c))p_c, \quad (5.59)$$

where $\phi_c = 1.3\times10^{-2}$. This value is twice that used in Chapter 4, in order to reduce the computation time, whilst remaining within the range of biologically realistic values for this parameter. We close the system by imposing the initial and boundary conditions given by equations (5.54) and (5.50) respectively.

5.5.4 Treatment with Antioxidants or Trophic Factors

For each of the cases above, we may apply treatment in the form of antioxidants or trophic factors. These treatments are assumed to increase the hyperoxic threshold. We set $c_{crit}(t) = c_{crit_1} + c_{crit_2}H(t-t_{crit})$, where c_{crit_1}, c_{crit_2} and t_{crit} are positive constants and H is a Heaviside step function, such that $c_{crit}(t) = c_{crit_1}$ for $t < t_{crit}$ and $c_{crit}(t) = c_{crit_1} + c_{crit_2}$ for $t \geq t_{crit}$. We set $c_{crit_1} = 0.67$ and $c_{crit_2} = 0.13$ in all simulations in this chapter (see Sections 4.2.1 and 4.4.5).

5.6 Numerical Results: 2D

We use the finite element method (FEM) to solve the above models numerically. The FEM code was written by Jonathan Whiteley. It uses the PETSc (Portable, Extensible Toolkit for Scientific Computation) libraries (which can be found at `http://www.mcs.anl.gov/petsc/` at the time of writing) and piecewise linear basis functions. The equations were solved on the

spherical polar geometry described above and then projected vertically downward onto the *xy*-plane for plotting (see Figure 5.9(b)). This preserves elemental areas near the centre and shrinks them in the polar direction towards the equator. All plots were produced and summary statistics calculated using Matlab.

The most basic finite element mesh is composed of 4 triangles, each sharing a corner at $\theta = 0$, with the remaining corners at $(\theta, \phi) = (1, 0)$, $(1, \pi/2)$, $(1, \pi)$ and $(1, 3\pi/2)$ (see the left-hand graph in Figure 5.9(c)). We refer to this as 'refinement level 1'. As we move up from one refinement level to the next, each element is split into 4 by the insertion of a new triangular element, with corners located at the mid-points of the sides of the original element (see the middle graph in Figure 5.9(c)). The new points created on the outer boundary are shifted outwards to lie on the circle described by $\theta = 1$, preserving their azimuthal angle, ϕ. Therefore, the number of elements at refinement level n is equal to 4^n. Each of the simulation results presented below are performed at one of refinement levels 6, 7, or 8; corresponding to $4^6 = 4096$, $4^7 = 16,384$ or $4^8 = 65,536$ elements respectively (see the right-hand graph in Figure 5.9(c), for the refinement level 6 mesh).

Both the number of elements and the interval between time steps vary between FEM simulations. The number of elements is chosen to be the minimum necessary to resolve wavefronts of degeneration, whilst the time intervals are the maximum that can be used whilst ensuring convergence of the numerical solution.

Simulations for mutation-induced rod degeneration require only 4096 elements, whilst simulations involving either mutation-induced cone degeneration or annular patch loss require 16,384 elements. Simulations involving a disc of photoreceptor loss are the most demanding, requiring 65,536 elements. Fewer elements are required when there is a mutation-induced loss of photoreceptors, since it is this loss, rather than the conditions at the wavefront, that drives the propagation of hyperoxic degeneration. More elements are required for mutation-induced cone loss than for mutation-induced rod loss, in order to resolve the wavefront of degeneration propagating from the narrow peak in cone density at the centre of the retina. Lastly, more elements are required for disc loss than for annular loss, in order to resolve the

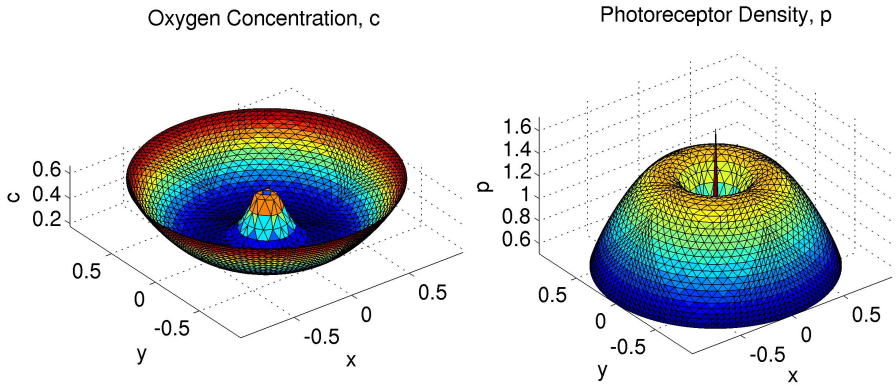

(a) Healthy oxygen and photoreceptor profiles.

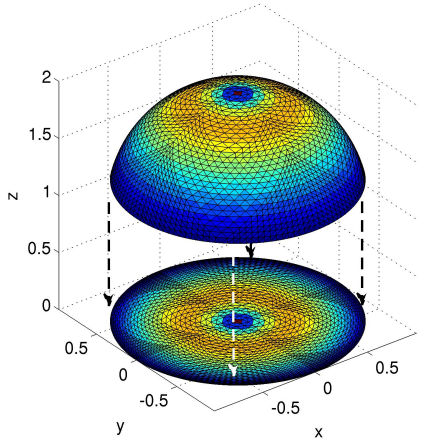

(b) The hemispherical surface is projected vertically downward onto the *xy*-plane for plotting.

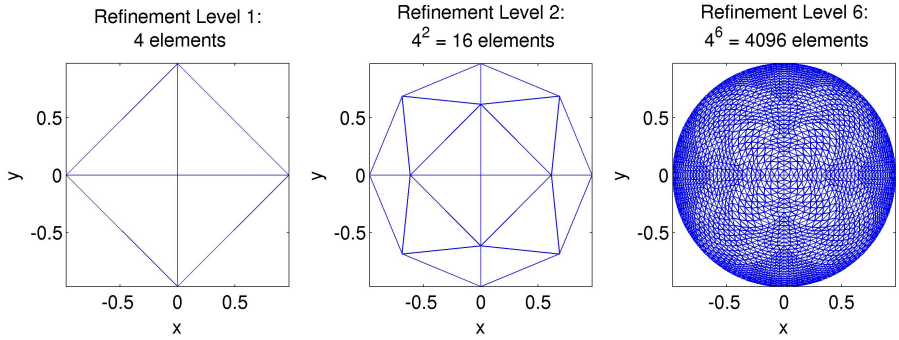

(c) Examples of the finite element mesh for different levels of refinement, projected onto the *xy*-plane.

Figure 5.9: Graphs showing details of the FEM solution. (a) 3D solution profiles, (b) projection of the solution onto the *xy*-plane, (c) finite element meshes.

more complex geometry of the resulting wavefront of degeneration.

Simulations in which rods and cones are grouped, that is where we use p and not p_r and p_c, require time intervals of $\mathrm{d}t = 0.01$, whilst those in which rods and cones are treated separately (as p_r and p_c) require time intervals of $\mathrm{d}t = 10^{-3}$ for convergence.

Patch Loss

We begin by removing patches of photoreceptors to determine the patch sizes and locations that will cause further degeneration. These patches represent the state of the system at possible stages in the disease progression. We consider two shapes: annuli and discs.

Annulus The removal of an annulus in 2D is equivalent to the removal of a patch in 1D (see simulations in Section 4.4.2). As with the 1D model, 4 distinct patterns of behaviour are observed, corresponding to regions A–D in Figure 4.17 (see also Figure 5.10). In region A degeneration stalls (Figure 5.10(a)), in region B degeneration progresses centrally, leaving a central island of cones (Figure 5.10(b)), in region C degeneration progresses outward (Figure 5.10(c)) and in region D degeneration progresses both centrally and outward, again leaving a central island of cones intact (Figure 5.10(d)). These simulations confirm that the 2D simulations agree with the 1D simulations in the previous chapter with regard to the patterns of degeneration produced. The time taken to reach steady-state is less in the 2D simulations than in 1D. This is because the widening of the wavefront, resulting from the decrease in the values of Q and β for the 2D simulations, increases the size of the region where healthy photoreceptors are exposed to hyperoxia ahead of the wavefront, thus increasing the wave speed (see discussion in Section 5.5.1). Since it is the pattern of degeneration, rather than its speed, that interests us, this difference is unimportant.

Disc Histological data from humans and rats suggest that the initial loss of photoreceptors occurs in roughly circular patches (see Cideciyan et al., 1998; Lee et al., 2011; Ji et al., 2012; García-Ayuso et al., 2013; Zhu et al., 2013). Therefore, we conducted a set of simulations

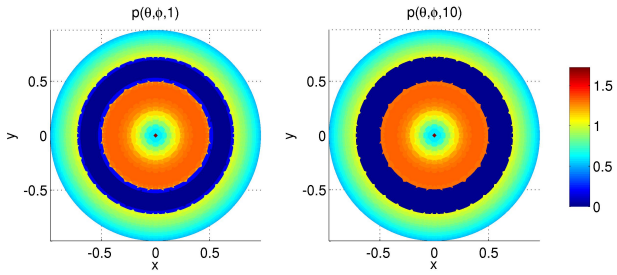

(a) Region A: $(\theta_1, \theta_2) = (0.4, 0.6)$.

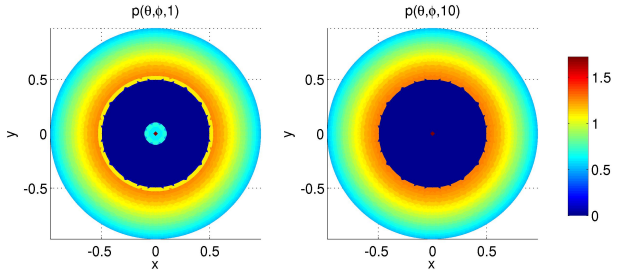

(b) Region B: $(\theta_1, \theta_2) = (0.08, 0.4)$.

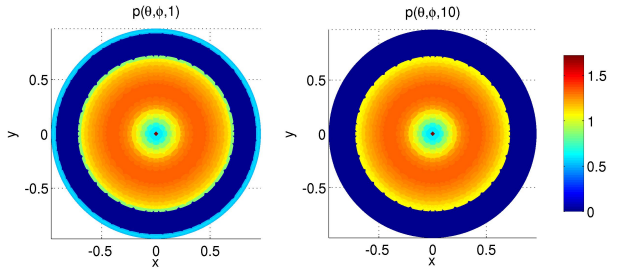

(c) Region C: $(\theta_1, \theta_2) = (0.6, 0.9)$.

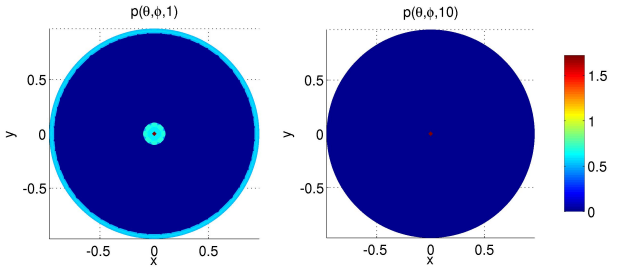

(d) Region D: $(\theta_1, \theta_2) = (0.08, 0.9)$.

Figure 5.10: Simulations of photoreceptor loss following the initial loss of an annulus of photoreceptors. Left column: $t = 1$, right column: $t = 10$. Degeneration (a) stalls, (b) spreads inwards, (c) spreads outwards and (d) spreads both inwards and outwards. Equations (5.46)–(5.47) and (5.49)–(5.50) were solved using the FEM, with 16,384 elements and time step $\mathrm{d}t = 0.01$. Parameter values: $Q = 4.89 \times 10^5$, $\beta = 7.23 \times 10^5$, $S_c = 10^3$ and $S = 100$. Remaining parameter values as in Table 4.3.

for a variety of disc eccentricities, $\theta_c = 0, 0.1, \ldots, 1.0$, and radii $\psi = 0.05, 0.025, 0.0125$, the results of which are summarised in Figure 5.11.

We kept the azimuthal position fixed at $\hat{\phi}_c = \pi$, since $\tilde{p}$ is radially symmetric, so that results at other azimuthal angles would be identical. All simulations were run to $t = 30$, which corresponds to approximately 10 years. Most simulations have reached steady-state by this time; however, a few do not.

Figure 5.11 shows how the degenerate area at t = 30 varies with θ_c and ψ. An element is termed degenerate if the photoreceptor density, p, at each of its nodes is less than or equal to $p_{crit} = 0.1$. The areas plotted correspond to a sphere of radius 1, so that the total area of the retina is approximately 4.8 (dimensionless). Recovery of the disc is possible since photoreceptors are removed through multiplication of the healthy initial conditions by smoothly varying hyperbolic functions which are nowhere zero. This also means that photoreceptor loss within the patch may be consolidated, such that the photoreceptor density decreases to zero within the patch. It can be seen from Figure 5.11 that if degeneration occurs at all for a given θ_c, it is more severe for larger ψ. We note also that the regions most prone to degeneration correspond with the unstable regions identified in Figure 4.16, whilst those in which photoreceptor loss stalls or recovers correspond with the stable regions.

Degeneration is most severe for $\theta_c \geq 0.8$ (corresponding to the peripheral unstable region in Figure 4.16). The time series for the case in which $\theta_c \geq 0.8$ and $\psi = 0.0125$ is presented in Figure 5.12, and is representative of these cases. The pattern of degeneration can be split into a number of distinct stages: firstly, the loss of photoreceptors within the patch is consolidated; secondly, the patch spreads outward, towards the periphery, until it reaches the ora serrata (top-middle, $t = 7$); thirdly, degeneration spreads around the ora serrata in two arms, one superior and the other inferior, whilst further (narrow) waves of degeneration, central to and contiguous with the two arms, proceed outwards from the patch, in the same direction as the original arms, thickening them (top-right, $t = 10$; bottom-left, $t = 18$; bottom-middle, $t = 24$); fourthly, the two arms meet at $(\theta, \phi) = (1, 0)$ (bottom-right, $t = 30$); and lastly, the secondary waves of degeneration, that were formed after the two arms, complete their circuit around the

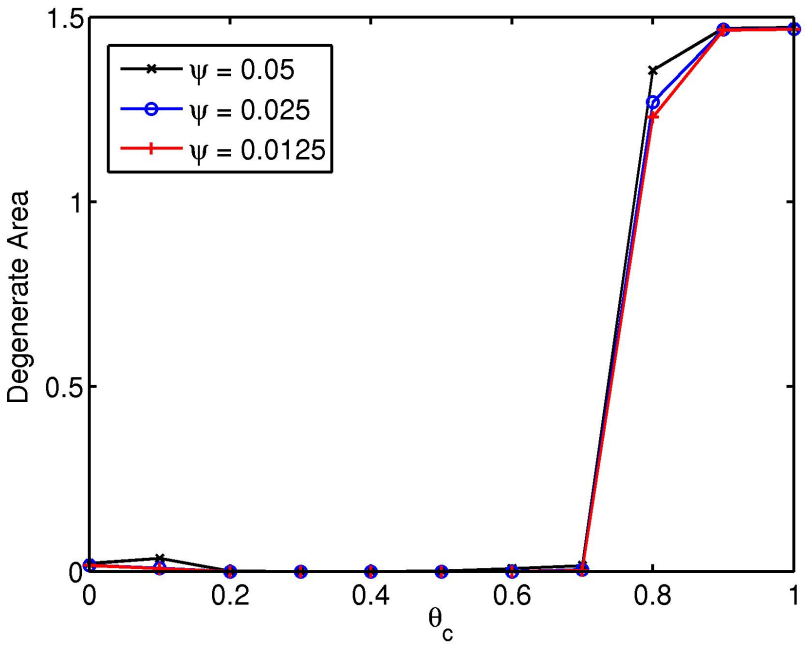

Figure 5.11: Graph to show degenerate areas at time t = 30, following the initial loss of a disc of photoreceptors. Results plotted for a range of disc eccentricities θ_c, and radii ψ. Degeneration is most severe for $\theta_c < 0.2$ and $\theta_c > 0.7$, is entirely absent for $0.3 \leq \theta_c \leq 0.4$, where photoreceptors within the disc regenerate, and is greater for larger ψ. Equations (5.46)–(5.47) and (5.49)–(5.50) were solved using the FEM, with 65,536 elements and time step $dt = 0.01$. The areas plotted are those produced on a sphere of radius 1. Parameter values: $Q = 4.89 \times 10^5$, $\beta = 7.23 \times 10^5$, $\hat{\phi}_c = \pi$, $S_c = 10^3$, $S = 100$ and $p_{crit} = 0.1$. Remaining parameter values as in Table 4.3.

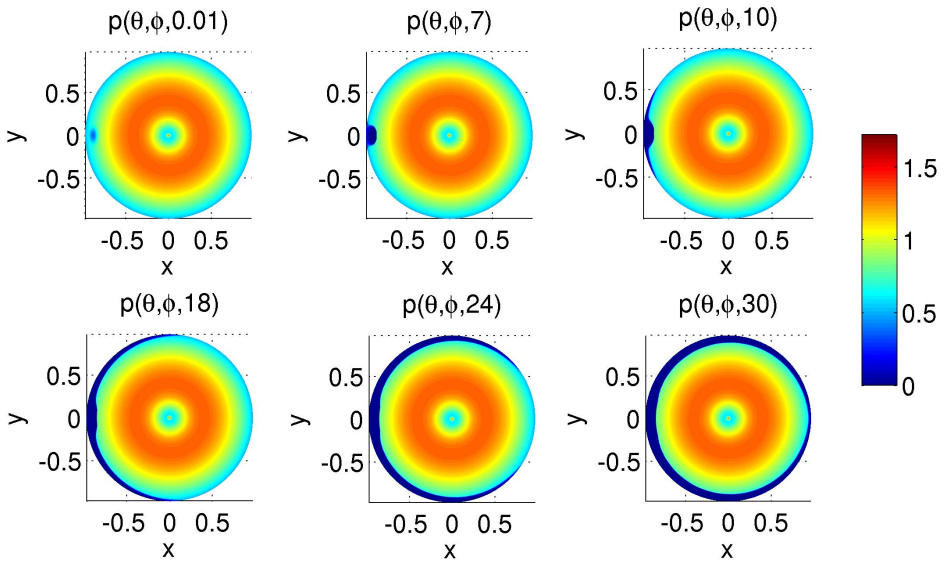

Figure 5.12: Simulation of photoreceptor loss following the initial loss of a disc of photoreceptors. The disc spreads outwards towards the periphery until it meets the ora serrata, after which degeneration spreads around the ora serrata in two arms, one superior and the other inferior, until they meet at the far side of the retina. The ring of degeneration then spreads centrally before stalling. Equations (5.46)–(5.47) and (5.49)–(5.50) were solved using the FEM, with 65,536 elements and time step $\mathrm{d}t = 0.01$. Parameter values: $Q = 4.89 \times 10^5$, $\beta = 7.23 \times 10^5$, $\theta_c = 0.8$, $\hat{\phi}_c = \pi$, $\psi = 0.0125$, $S_c = 10^3$ and $S = 100$. Remaining parameter values as in Table 4.3.

retina, leading to steady-state.

For $\theta_c = 0.7$, photoreceptor loss within the disc consolidates, but does not spread (see Figure 5.13(c)). For $\theta_c = 0.3$ and 0.4 photoreceptors completely recover (see Figure 5.13(b)), whilst for $\theta_c = 0.2$, 0.5 or 0.6 the disc either consolidates, completely recovers, or recovers in some areas whilst consolidating in others. For $\theta_c = 0$, the disc consolidates and spreads outwards a little (see Figure 5.13(a)).

For $\theta_c = 0.1$ and $\psi = 0.025$ or 0.0125, the disc consolidates; however, for $\psi = 0.05$, degeneration spreads in two arms, one superior and the other inferior, around the central cone peak, until all photoreceptors in the central retina, including those in the cone peak, are lost (see Figure 5.14).

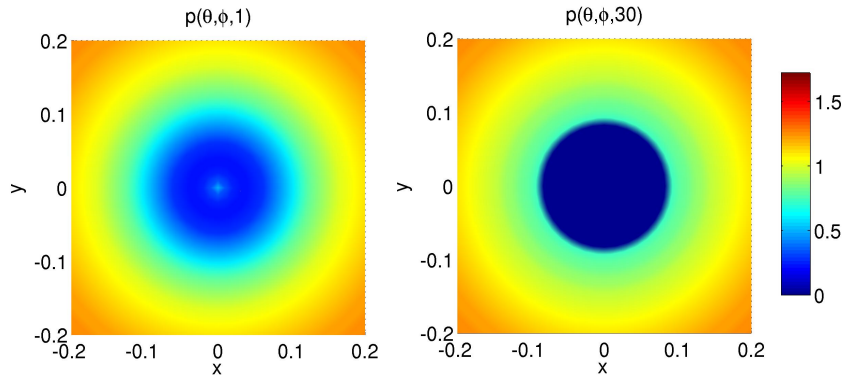

(a) Degenerate disc eccentricity: $\theta_c = 0$.

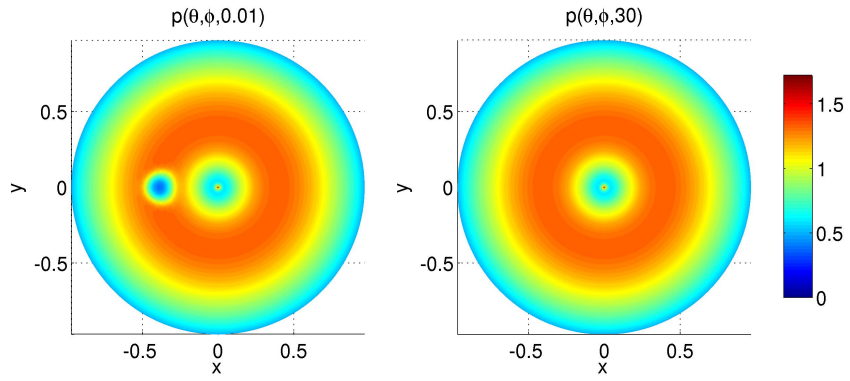

(b) Degenerate disc eccentricity: $\theta_c = 0.3$.

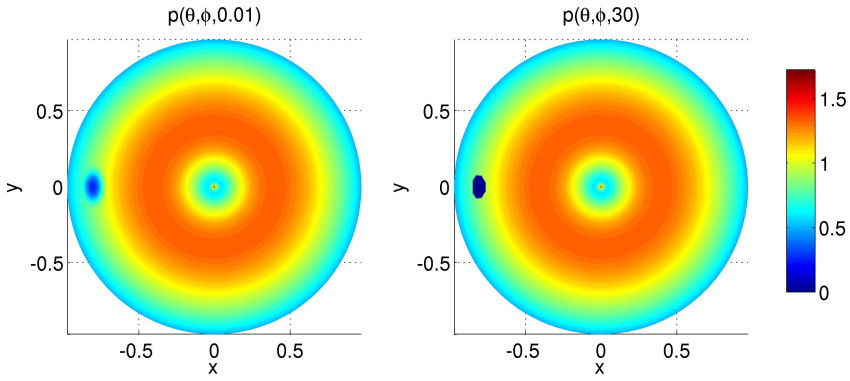

(c) Degenerate disc eccentricity: $\theta_c = 0.7$.

Figure 5.13: Simulations of photoreceptor loss and recovery following the initial loss of a disc of photoreceptors. Left column: $t = 0.01$ or 1, right column: $t = 30$. (a) the disc spreads outwards before stalling, (b) the disc recovers and (c) the disc degenerates further, but does not spread. Equations (5.46)–(5.47) and (5.49)–(5.50) were solved using the FEM, with 65,536 elements and time step $\mathrm{d}t = 0.01$. Parameter values: $Q = 4.89 \times 10^5$, $\beta = 7.23 \times 10^5$, $\hat{\phi}_c = \pi$, $\psi = 0.05$, $S_c = 10^3$ and $S = 100$. Remaining parameter values as in Table 4.3.

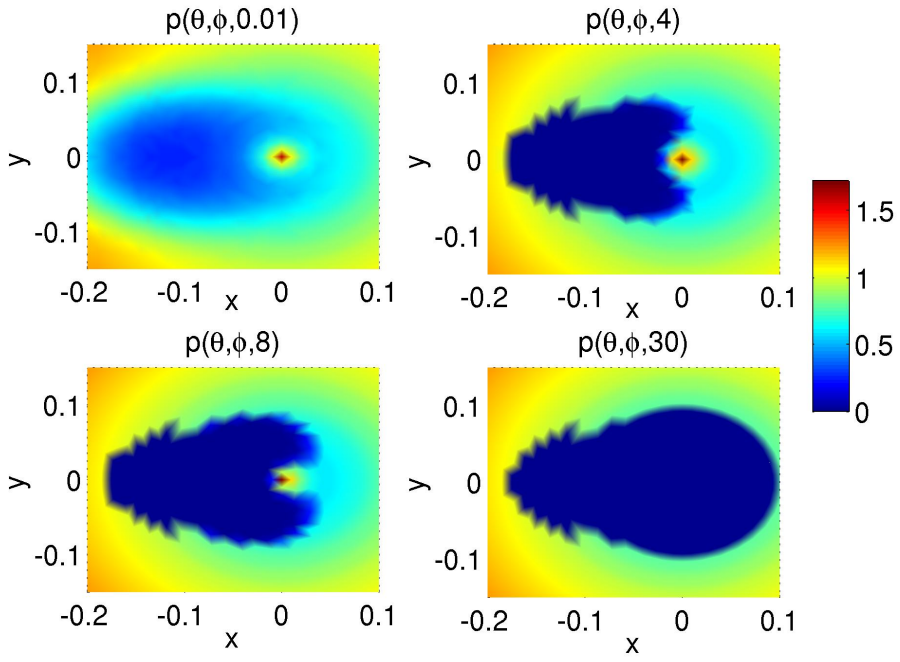

Figure 5.14: Simulation of photoreceptor loss following the initial loss of a disc of photoreceptors. The disc spreads outwards, enveloping the central retina, before stalling. Equations (5.46)–(5.47) and (5.49)–(5.50) were solved using the FEM, with 65,536 elements and time step $\mathrm{d}t = 0.01$. Parameter values: $Q = 4.89 \times 10^5$, $\beta = 7.23 \times 10^5$, $\theta_c = 0.1$, $\hat{\phi}_c = \pi$, $\psi = 0.05$, $S_c = 10^3$ and $S = 100$. Remaining parameter values as in Table 4.3.

Mutation-induced Rod Degeneration

Figure 5.15 shows a time series of rod and cone photoreceptor distributions, where photoreceptor loss is driven by mutation-induced rod degeneration. The loss of rods causes a rise in oxygen levels, leading to the initiation of two waves of hyperoxic degeneration, first at the ora serrata (top-middle, $t = 30$, Figure 5.15(a) and (b)) and later near the centre of the retina (bottom-left, $t = 90$, Figure 5.15(a) and (b)). These waves progress inwards and outwards respectively, until they meet in the mid-periphery, leaving only a central island of cones at steady-state (bottom-right, $t = 150$, Figure 5.15(a)and (b)). These results are consistent with those of the 1D model (see Figure 4.22(a)), both in spatial pattern and timescale. The timescales agree in this case, since it is the mutation-induced rod degeneration (the rate of which is the same in the 1D and 2D cases), rather than the conditions at the wavefront, that drives the propagation of hyperoxic degeneration.

Figure 5.16 shows the effect of mutation-induced rod degeneration on the stability of a disc of photoreceptor loss. In the absence of mutation-induced rod loss, the patch consolidates, but remains stable (see Figure 5.13(c)). The loss of rods causes the disc to become unstable and spread, both outwards towards the ora serrata, and in the positive and negative azimuthal directions. By $t = 11$ the patch has begun to connect with the centrally spreading annulus of degeneration (see the bottom-left graphs in Figures 5.16(a) and (b)). By $t = 30$ the disc is still discernible as a thickening of the annulus, reminiscent of the pattern of degeneration produced by the spreading of a more eccentric disc in the bottom-left graph of Figure 5.12 (see the bottom-right graphs in Figures 5.16(a) and (b)).

Mutation-induced Cone Degeneration

Figure 5.17 shows a time series of rod and cone photoreceptor distributions, where photoreceptor loss is driven by mutation-induced cone degeneration. The loss of cones causes a rise in oxygen levels, predominantly in the central retina, where the cone density is highest. This causes the complete loss of photoreceptors in the central retina. These results are consistent with those of the 1D model (see Figure 4.23) in that they both show degeneration of the central

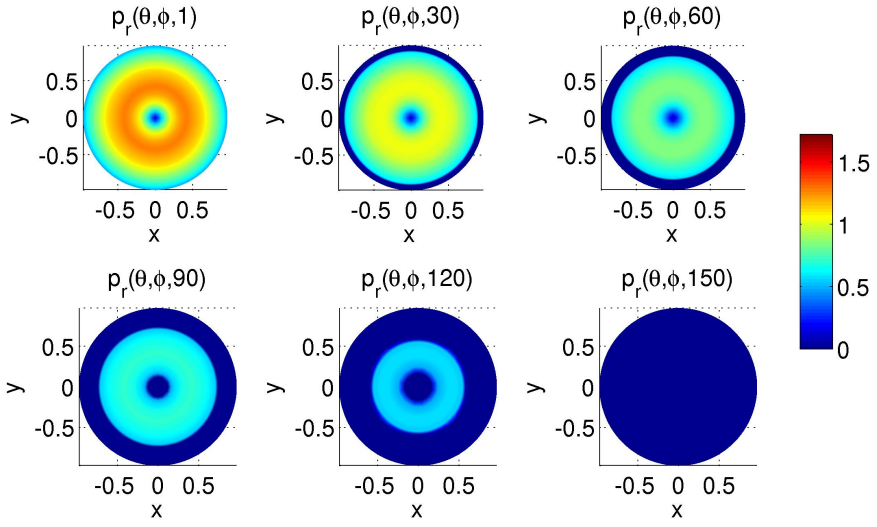

(a) Rod density, $p_r(\theta,\phi,t)$.

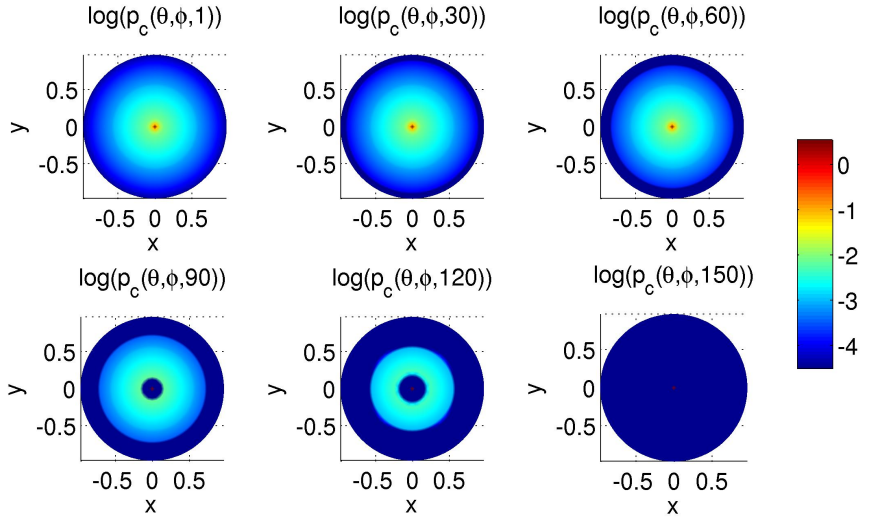

(b) Natural logarithm of cone density, $\log(p_c(\theta,\phi,t))$. The colour scale corresponds to the range of values taken by $\log(p_c)$ at $t=1$. Whilst $\log(p_c)$ drops beneath this range for $t>1$, these lower values are displayed in the same colour as the lowest value in the range at $t=1$, so that the pattern of degeneration is not obscured.

Figure 5.15: Simulation of photoreceptor loss with mutation-induced rod degeneration. (a) rod density, (b) natural logarithm of the cone density. Degeneration initially proceeds inwards from the ora serrata. A wave of degeneration then initiates near the centre of the retina, meeting the outer wave in the mid-periphery. Only a central island of cones is preserved at steady-state. Equations (5.50)–(5.54) were solved using the FEM, with 4096 elements and time step $\mathrm{d}t = 10^{-3}$. Parameter values: $Q = 4.89\times10^5$, $\beta = 7.23\times10^5$, $\phi_r = 6.6\times10^{-3}$ and $S_c = 10^3$. Remaining parameter values as in Table 4.3.

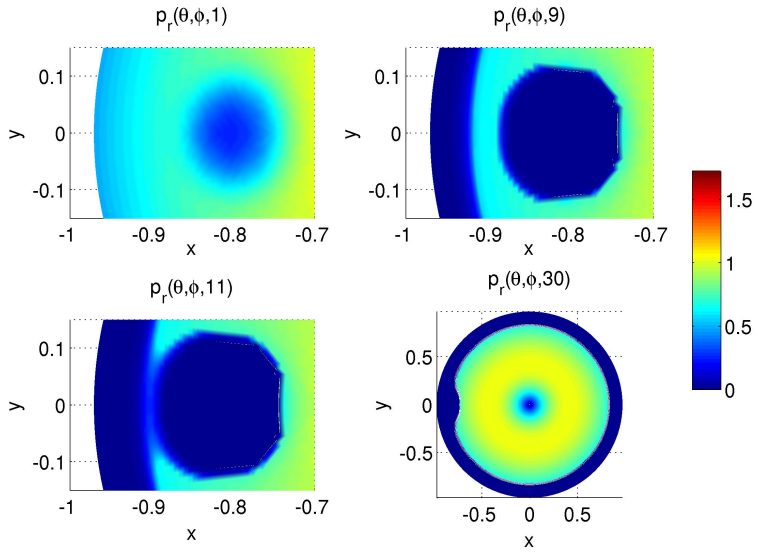

(a) Rod density, $p_r(\theta,\phi,t)$.

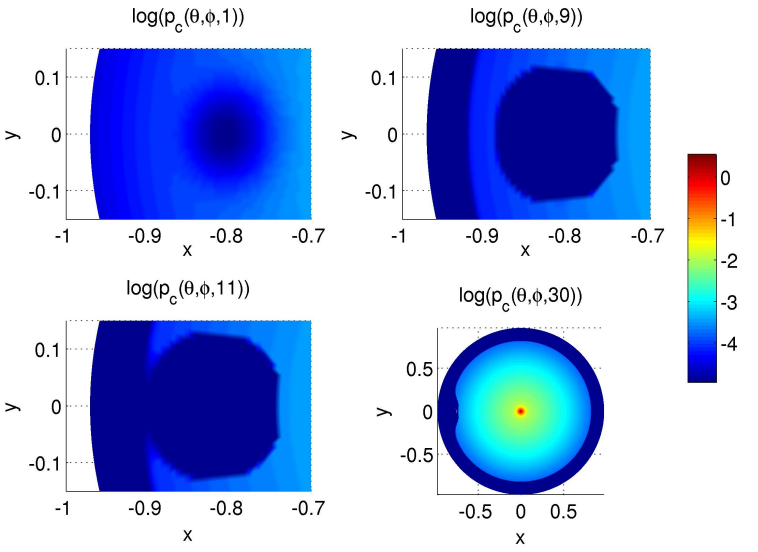

(b) Natural logarithm of cone density, $\log(p_c(\theta,\phi,t))$. The colour scale corresponds to the range of values taken by $\log(p_c)$ at $t=1$. Whilst $\log(p_c)$ drops beneath this range for $t>1$, these lower values are displayed in the same colour as the lowest value in the range at $t=1$, so that the pattern of degeneration is not obscured.

Figure 5.16: Simulation of photoreceptor loss with mutation-induced rod degeneration and an initial degenerate disc. (a) rod density, (b) natural logarithm of the cone density. The disc spreads outwards towards the ora serrata and in the positive and negative azimuthal directions. Equations (5.50)–(5.54) were solved using the FEM, with 65,536 elements and time step $dt = 10^{-3}$. Parameter values: $Q = 4.89\times10^5$, $\beta = 7.23\times10^5$, $\phi_r = 6.6\times10^{-3}$, $S_c = 10^3$, $S = 100$, $\theta_c = 0.7$, $\phi_c = \pi$ and $\psi = 0.05$. Remaining parameter values as in Table 4.3.

retina; however, the 2D model does not show the later loss of photoreceptors at the periphery, demonstrated by the 1D model. In the 1D simulation, hyperoxic degeneration begins at the ora serrata at $t = 208$, whereas in the 2D simulation it has still not begun by $t = 135$, at which point the cone density at the ora serrata has reduced by the same amount as in the 1D simulation at $t = 270$, since the value of ϕ_c in the 2D simulation is twice that in the 1D simulation. Since cone density is negligible at the ora serrata, the effects of cone loss in this region are subtle. Only a slight difference between the 1D and 2D simulations would therefore be required to give rise to this difference in results. If the reduced values of Q and β from the 2D simulations are used in the 1D simulation, hyperoxic degeneration does not initiate at the ora serrata (results not show), suggesting that this is the cause of the discrepancy. This case is extremely marginal, the sensitivity to the values of Q and β resulting from the fact that $c_{crit} = 0.67$ has been chosen to lie just above the healthy oxygen concentration at the ora serrata. For instance, increasing c_{crit} to 0.68 prevents hyperoxic degeneration from initiating at the ora serrata for either set of values of Q and β. Since the vales of Q, β and c_{crit} will differ a little between individuals, we therefore anticipate that hyperoxic degeneration will initiate at the ora serrata under mutation-driven cone degeneration in only a subset of affected individuals.

Treatment with Antioxidants or Trophic Factors

Figure 5.18 summarises the effects of treatment, portraying changes in the degenerate retinal area over time for a range of scenarios . We observe that the effectiveness of treatment depends upon the type of degeneration, the stage at which it is applied and the strength of the treatment. In each of the following simulations the treatment strength is the same, with $c_{crit_1} = 0.67$ and $c_{crit_2} = 0.13$. The areas plotted correspond to a sphere of radius 1, so that the total area of the retina is approximately 4.8 (dimensionless). As with the disc loss results presented above, an element is termed degenerate if the photoreceptor density, p, at each of its nodes is less than or equal to $p_{crit} = 0.1$.

For the cases where a patch of photoreceptors is removed, treatment either causes degeneration to stall earlier, with a lower degenerate area (Figures 5.18(a) and 5.18(c)), or results in

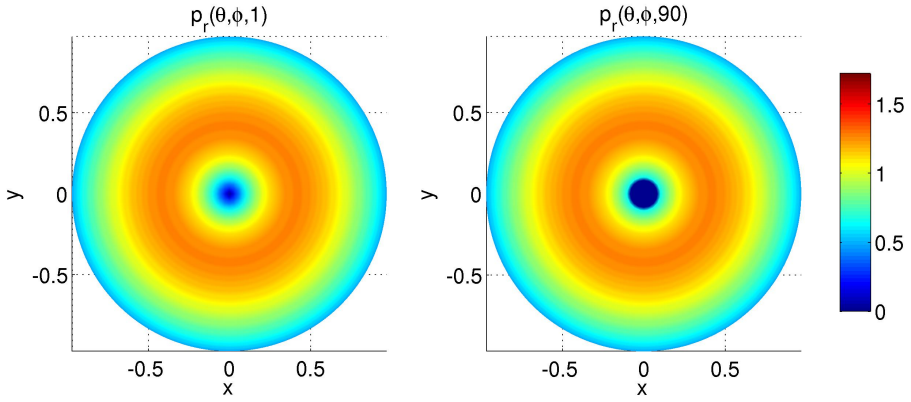

(a) Rod density, $p_r(\theta,\phi,t)$.

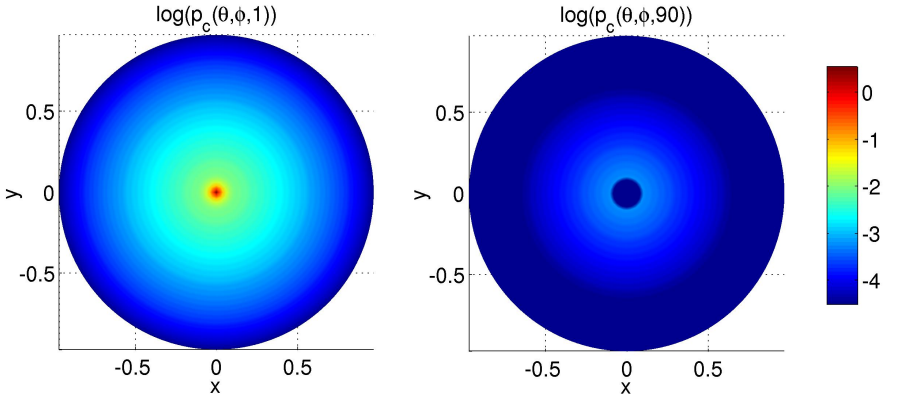

(b) Natural logarithm of cone density, $\log(p_c(\theta,\phi,t))$. The colour scale corresponds to the range of values taken by $\log(p_c)$ at $t=1$. Whilst $\log(p_c)$ drops beneath this range for $t>1$, these lower values are displayed in the same colour as the lowest value in the range at $t=1$, so that the pattern of degeneration is not obscured.

Figure 5.17: Simulation of photoreceptor loss with mutation-induced cone degeneration. (a) rod density, (b) natural logarithm of the cone density. Left column: $t=1$, right column: $t=90$. Hyperoxic degeneration initiates at the centre of the retina and then stalls after spreading a short distance. Equations (5.50), (5.54) and (5.57)–(5.59) were solved using the FEM, with 16,384 elements and time step $\mathrm{d}t=10^{-3}$. Parameter values: $Q=4.89\times10^5$, $\beta=7.23\times10^5$, $\phi_c=1.3\times10^{-2}$ and $S_c=10^3$. Remaining parameter values as in Table 4.3.

the recovery of photoreceptors (Figure 5.18(b)). We note that the extent of recovery may be exaggerated here, since photoreceptors may be unable to recover if they have been exposed to hyperoxia for a sufficient period of time. For the case involving mutation-induced rod degeneration, hyperoxic degeneration is delayed, but will eventually proceed (Figure 5.18(d)). This is because, whilst the rise in c_{crit} temporarily renders the retina normoxic, the continued loss of rods (which dominate over cones in most of the retina) eventually causes oxygen levels to rise above the new value of c_{crit}, causing hyperoxic degeneration to recommence. Degeneration also stalls when treatment is applied during mutation-induced cone degeneration (Figure 5.18(e)).

Figure 5.18(a) corresponds to the scenario in Figure 5.10(d), where treatment results in the stalling of the inward and outward progression of the degenerate annulus, preserving the edge of the peripheral retina and the central retina. Figure 5.18(b) corresponds to the scenario in Figure 5.14, where treatment results in the retraction of the arms of degeneration from around the central retina back towards the patch, preserving the central retina. Figure 5.18(c) corresponds to the scenario in Figure 5.12, where treatment results in the stalling of degeneration, shortly after the two arms of degeneration begin to form, preserving the peripheral retina. Lastly, Figures 5.18(d) and 5.18(e) correspond to the scenarios in Figures 5.15 and 5.17 respectively.

5.7 Discussion

In this chapter we have investigated the effect of capillary loss on the progression of photoreceptor degeneration in 1D and extended our work from Chapter 4 into 2D.

Asymptotic analysis of the capillary loss problem shows that capillary loss must extend to within $O(\varepsilon)$ of, and preferably be coincident with, the margins of a degenerate photoreceptor patch to prevent further photoreceptor degeneration in those cases where it would proceed in the absence of capillary loss (Section 5.3). This is because the presence of the degenerate patch of capillaries can only influence the oxygen concentration at the edge of the patch of

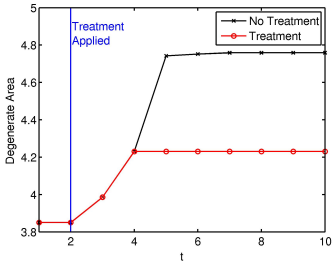

(a) Annulus, region D: $(\theta_1, \theta_2) = (0.08, 0.9)$. Equations (5.46)–(5.47) and (5.49)–(5.50) were solved using the FEM, with 16,384 elements and time step $dt = 0.01$. Parameter values: $S = 100$ and $t_{crit} = 2$.

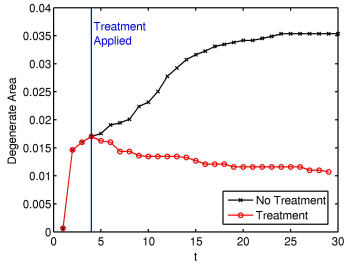

(b) Disc: $(\theta_c, \hat{\phi}_c, \psi) = (0.1, \pi, 0.05)$. Equations (5.46)–(5.47) and (5.49)–(5.50) were solved using the FEM, with 65,536 elements and time step $dt = 0.01$. Parameter values: $S = 100$ and $t_{crit} = 4$.

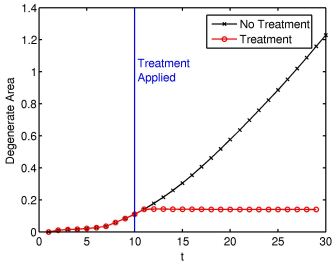

(c) Disc: $(\theta_c, \hat{\phi}_c, \psi) = (0.8, \pi, 0.0125)$. Equations (5.46)–(5.47) and (5.49)–(5.50) were solved using the FEM, with 65,536 elements and time step $dt = 0.01$. Parameter values: $S = 100$ and $t_{crit} = 10$.

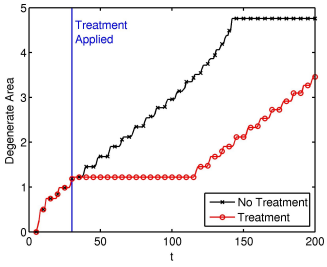

(d) Mutation-induced rod degeneration: $\phi_r = 6.6 \times 10^{-3}$. Equations (5.50)–(5.54) were solved using the FEM, with 4096 elements and time step $dt = 10^{-3}$. Parameter values: $t_{crit} = 30$.

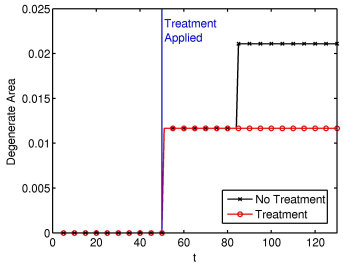

(e) Mutation-induced cone degeneration: $\phi_c = 1.3 \times 10^{-2}$. Equations (5.50), (5.54) and (5.57)–(5.59) were solved using the FEM, with 16,384 elements and time step $dt = 10^{-3}$. Parameter values: $t_{crit} = 50$.

Figure 5.18: Graphs to show the effect of treatment on the change in degenerate area over time for a range of scenarios. (a)–(c) contain initial degenerate patches, whereas (d) and (e) do not. The areas plotted are those produced on a sphere of radius 1. Parameter values: $Q = 4.89 \times 10^5$, $\beta = 7.23 \times 10^5$, $S_c = 10^3$, $c_{crit_1} = 0.67$, $c_{crit_2} = 0.13$ and $p_{crit} = 0.1$. Remaining parameter values as in Table 4.3.

photoreceptor loss if it lies within the ($O(\varepsilon)$ in width) boundary layer extending from the edge of the degenerate photoreceptor patch. This was confirmed by numerical simulations (Section 5.4.1). This model prediction could be tested experimentally, using a laser to ablate the choroid in those regions from which photoreceptors are absent. This could also be used as a treatment strategy for RP, similar to those presently used to treat macular degeneration (see, for instance, Coleman et al., 2008; Jager et al., 2008).

Dynamic simulations of the capillary loss problem reveal that capillary degeneration may prevent, reverse or retard photoreceptor degeneration, though, as noted in Section 5.4.2, recovery is likely to be limited *in vivo*. Further experimental work is needed to determine the rate of capillary degeneration and thereby to predict its effect upon photoreceptor degeneration. Experimental work is also required to elucidate the nature of the dependence of the CC upon photoreceptors and the spatio-temporal pattern of photoreceptor, RPE and CC loss. Such information would allow for a more mechanistic, as opposed to phenomenological, modelling approach.

Simulations in 2D serve to confirm and extend our 1D results, revealing several new patterns of degeneration, not accessible to the 1D model (Section 5.6).

Simulations involving an initial annulus of degenerate photoreceptors are directly comparable to those involving an initial patch of photoreceptor loss in 1D. They show the same four patterns of degeneration as in 1D, either remaining stationary, progressing inwards, progressing outwards, or progressing both inwards and outwards (Figure 5.10). In all cases a central island of cones is preserved, as in 1D. These concentric patterns of progression are similar to those described by Robson et al. (2003, 2004, 2006, 2008, 2011); Popović et al. (2005); Murakami et al. (2008); Lima et al. (2009, 2012); Escher et al. (2012) (see Section 1.3.3 for more details).

The move into a 2D geometry allows us to break the axisymmetry assumed in the 1D model. We do this by removing a disc of photoreceptors, for a range of disc radii and eccentricities. These represent the circular patches of loss observed in the early stages of RP in humans and rats (Cideciyan et al., 1998; Lee et al., 2011; Ji et al., 2012; García-Ayuso et al.,

2013; Zhu et al., 2013). Four types of behaviour were observed: recovery; recovery in some areas of the disc, with consolidation in others; consolidation across the disc; and consolidation and spreading of degeneration.

In those cases where degeneration spreads, two patterns of degeneration are noteworthy. In the first pattern, a disc near the edge of the retina expands until it meets the ora serrata, spreading around the rim of the retina in two arms which meet on the opposite side of the retina (Figure 5.12). This mode of degeneration could explain the aetiology of the later stages of the third pattern of visual field loss described by Grover et al. (1998) (see Section 1.3.4 and Figure 1.9). In this case, following the formation of a mid-peripheral ring scotoma, degeneration expands at one location, either superior of inferior, toward the ora serrata, leaving a U- or n-shaped peripheral visual field, the arms of which retract from both sides until peripheral vision is lost.

This pattern of degeneration is also similar to the second pattern of visual field loss described by Grover et al. (1998), where degeneration winds around the mid-periphery (see Figure 1.9). The key differences between our simulations and Grover et al.'s observations are that the arms of degeneration observed by Grover et al. are often located more centrally within the mid-periphery, leaving large regions near the ora serrata untouched and that one of the arms proceeds more rapidly around the retina than the other, whilst ours are perfectly symmetrical (in terms of the azimuthal angle) either side of the initial disc of loss. The second of these two discrepancies may be due to variations in the photoreceptor distribution in the azimuthal direction, or asymmetries in the initial conditions, not captured in our model. It is hard to see how the first discrepancy could be accounted for by the oxygen toxicity hypothesis, given that it predicts that waves of degeneration should stall as they move more centrally within the mid-periphery, suggesting that an additional mechanism is at work here.

In the second noteworthy pattern of degeneration produced by our disc loss simulations, a disc near the centre of the retina expands around the cone island, surrounding and eliminating it, resulting in a degenerate central retina (Figure 5.14). This pattern of degeneration is similar to the parafoveal or perifoveal ring scotomas observed in patients with pattern 1B visual field

loss (Grover et al., 1998) (see Figure 1.9). The key difference is that the central cone island is preserved in Grover et al.'s observations. Since the cone island is always preserved in our 1D patch loss simulations (see Section 4.4) it is likely that our 2D simulations would show the same behaviour, were we to use the original values of Q and β, and a much finer mesh. Since this would make the problem computationally infeasible given the resources available, we are unable to test this hypothesis; however, based upon our analysis in Section 4.3.3, it is likely to be correct.

Mutation-induced rod degeneration gives rise to the first pattern of degeneration observed by Grover et al. (1998), involving a concentric loss of the visual field, starting at the far-periphery and progressing inward (Figure 5.15, see also Figure 1.9). In particular, it corresponds to the form of pattern 1 degeneration which also involves a loss of parafoveal or perifoveal photoreceptors (see Section 4.4.3 for a similar result in 1D). It may be that, in those cases where parafoveal and perifoveal photoreceptors are preserved, mutation-induced rod loss is less severe in this region (spatial variation in the rate of rod loss has been quantitatively measured in the healthy ageing human retina, but not the RP retina, see Curcio et al., 1993). Further experimental work is required to test this hypothesis. The mutation-induced loss of rods can also give rise to the destabilisation of a degenerate patch of photoreceptors (Figure 5.16) suggesting one means by which the first small patches of loss may grow.

Mutation-induced cone degeneration leads to the complete loss of photoreceptors in the central retina (Figure 5.17). This is consistent with the disease progression in cone-rod dystrophies described by Hamel (2007).

Lastly, treatment with antioxidants or trophic factors stalled or reversed photoreceptor degeneration in patch loss simulations, delayed photoreceptor degeneration in mutation-induced rod loss simulations and stalled photoreceptor degeneration in mutation-induced cone loss simulations (Figure 5.18). Further experimental work is required to test our predictions as to the effects of these treatments upon the spatio-temporal pattern of degeneration.

The work in this chapter could be extended in a number of ways. Instead of the direct dependence of the CC upon photoreceptors assumed in this chapter, the complex interdepen-

dence of photoreceptors, RPE, CC and VEGF could be captured in the model (assuming the cellular and biochemical details could be experimentally determined). The spatio-temporal patterns of photoreceptor loss generated with photoreceptor distributions corresponding to mammals, such as mice, rats and pigs could also be explored. This may allow us to explain some of the differences in disease progression between human and animal models of RP (see Section 1.3.3). Capillary loss could be incorporated into the 2D model in the same way as with the 1D model. A more realistic photoreceptor distribution, with variation in the azimuthal direction and inclusion of the optic disc could be used in the 2D model, using data such as that in Curcio et al. (1990). The present model could also be enhanced by moving into 3D and incorporating the complex, layered structure of the retina, complete with deep and superficial retinal capillary layers and regional variations in layer widths and vasculature. The 3D model could also include constriction and atrophy of the retinal capillary layers in response to hyperoxia (which occurs earlier than the degeneration of the CC) as well as shortening of the photoreceptor OSs, bringing the oxygen-sensitive ISs closer to the CC. Lastly, models for the rod trophic factor and rod toxic substance hypotheses could be constructed, in 1D and in 2D, adapting the modelling framework developed in the present and previous chapters. The rod toxic substance hypothesis in particular has the potential to display preferential photoreceptor loss in the rod-rich region of the mid-periphery, and so to replicate patterns 2 and 3 from Grover et al. (1998), since it is here that the highest levels of toxic substance will be produced.

In conclusion, dynamic capillary loss may slow, prevent or reverse degeneration, whilst a patch of capillary loss would need to be essentially coincident with the edge of a patch of photoreceptor loss in order to prevent further photoreceptor degeneration. The 2D model is able to capture the pattern 1 degeneration observed by Grover et al. (1998), as well as elements of pattern 2 and 3 degeneration; however, it is unable to explain the preferential loss of photoreceptors in the rod-rich portion of the mid-periphery, which forms an important part of patterns 2 and 3, demonstrating that additional mechanisms must be responsible. In many ways this is the most important result of the 2D model, as it shows the limitations of the oxygen toxicity hypothesis. On the other hand, our simulations predict the preservation of the

central island of cones, a feature which is difficult to explain on either of the main alternative hypotheses: rod trophic factor and rod toxic substance (see Section 1.3.5). Lastly, treatment with antioxidants or trophic factors may halt or reverse photoreceptor loss in the patch loss case, may delay photoreceptor loss in the mutation-induced rod degeneration case and halt photoreceptor loss in the mutation-induced cone degeneration case.

In the next and final chapter we summarise and discuss the findings of this thesis, suggest directions for future research and draw conclusions.

Chapter 6

Discussion

The retina is remarkable. Conferring upon us the gift of vision, it enables us to perceive the world in a way unparalleled by any other tissue. To remain functional, it must be supplied with an appropriate level of oxygen. Too little, and it will starve. Too much, and it will be poisoned. In this thesis we have used mathematical models to explore these two scenarios. In the former, we examined the effect of the protein neuroglobin in the prevention of hypoxia, whist in the latter, we considered hyperoxia as a prospective cause behind the spread of retinal degeneration in the group of inherited retinal dystrophies, known collectively as retinitis pigmentosa.

In what follows we summarise the main results of this thesis and suggest directions for future research, before drawing final conclusions.

6.1 Summary

In Chapter 2 we investigated the role of Ngb in oxygen transport and storage using a 1D model on a domain representing a single cellular layer, supplied at one end by a capillary bed. The model was formulated as a system of four reaction-diffusion PDEs for oxygen and the three forms of Ngb. Solving these equations using the method of lines and the FEM, it was shown that Ngb may prevent or alleviate hypoxia by transporting oxygen from regions in which it

is rich to regions in which it is poor. However, Ngb's role in storage is much more doubtful, since the Ngb concentration must be high and the challenge to the retina very brief (at most a few seconds) in order for Ngb to prevent hypoxia.

Analysis of a simplified version of this model demonstrated that Ngb increases the maximum domain length that can be supported under normoxia and the minimum oxygen concentration in an otherwise normoxic retina, playing an increasingly important role as oxygen supply diminishes. Our analysis also showed that, contrary to the prevailing assumption, Ngb's oxygen affinity, far from limiting its ability to transport oxygen, is in fact near optimal for this process. At the least, this eliminates an argument against Ngb as an oxygen transporter. It also suggests that natural selection may have tuned this parameter to optimise transport.

In Chapter 3 we used an eight layer model to explore the role of Ngb in oxygen transport and storage in a physiologically human retina. The model was formulated as a system of four reaction-diffusion equations in 1D, as for the single layer model; however, in this case the domain spans four cellular layers, from the retinal pigment epithelium to the inner limiting membrane. This is the first time that a model has been constructed to include the dynamics of both oxygen and Ngb across the entire retina. The system was solved using the method of lines and the FEM.

It was found that, provided Ngb is distributed appropriately between the retinal layers and is present in sufficient quantities within those layers, Ngb could prevent either inner or outer retinal hypoxia, for average retinal concentrations within biologically realistic limits. The model also shows that, whilst the compartmentalisation of Ngb within cells limits oxygen transport, it does not prevent Ngb in one compartment from raising the oxygen concentration in other compartments.

Whilst Ngb's effect on the minimum oxygen concentration is subtle on the scale of the maximum retinal concentration, it is significant on the scale of the hypoxic threshold. Furthermore, since the Michaelis-Menten curve is steepest in the neighbourhood of this threshold, the addition of Ngb may increase the minimum rate of oxygen consumption by as much as 30–40%.

As with the single layer model, the eight layer model results indicate that Ngb is unlikely to play an important role in oxygen storage, unless the challenge to the retina was at most a few seconds long.

Asymptotic analysis of the Ngb-free version of this model demonstrated that the assumption of a piecewise constant rate of oxygen consumption is valid, provided that the oxygen concentration does not drop to hypoxic or near-hypoxic levels. This condition is satisfied for the majority of existing models. In those cases where hypoxia does occur, a quadratic approximation is still valid; however, the coefficients must be modified as described in Chapter 3. This places existing models of retinal oxygen consumption on a stronger theoretical foundation.

In Chapter 4 we explored the effects of hyperoxia driven photoreceptor degeneration as a potential mechanism behind the progression of RP. The model was formulated as a system of two or three PDEs for oxygen concentration and either photoreceptor density or rod and cone densities, defined on a 1D domain spanning the region between the foveal centre and the ora serrata. This is the first model of RP to account for the characteristic distribution of rod and cone photoreceptors in the human retina, and hence the first to be capable of explaining and predicting the spatio-temporal pattern of photoreceptor loss. It is also the first to examine the oxygen toxicity hypothesis. The conditions under which a patch of photoreceptor loss will expand were determined using an asymptotic analysis and verified numerically using a finite difference discretisation of the steady-state problem.

It was found that the retina may be divided into an alternating series of two stable and three unstable regions, between the centre of the fovea and the ora serrata. Stable regions correspond to areas with high photoreceptor density and unstable regions to areas with low photoreceptor density. The only exception is at the centre of the fovea, where there exists a narrow unstable region, despite the high cone density in this location. This region is unstable precisely because it is so narrow: the width of the region is insufficient to support normoxic conditions when the surrounding retina is dystrophic.

A degenerate patch will remain stationary provided that both boundaries lie within a stable region. If a boundary lies within an unstable region, it will propagate outwards until it reaches

either the edge of the domain or the boundary of a stable region. (In this way, regions with high photoreceptor density act as a barrier to the spread of degeneration via hyperoxia.) The exception to this rule is when the degenerate patch is very narrow. In this case the patch may remain stationary in regions where wide patches would spread, provided the patch is sufficiently narrow.

Patch loss may result in the loss of photoreceptors around the edge of the retina and in the parafoveal and perifoveal regions; however, the fovea, together with most of the mid-periphery will be spared, since they lie within stable regions. Inclusion of mutation-induced rod degeneration into the model causes waves of hyperoxic degeneration to propagate from the ora serrata and the parafoveal/perifoveal region, sparing only the fovea, whilst mutation-induced cone degeneration causes an early hyperoxic loss of photoreceptors in the fovea, which may be followed by the propagation of a wave of hyperoxic degeneration through the peripheral unstable region, initiating at the ora serrata. These patterns of degeneration correspond to some of those observed in rod-cone and cone-rod dystrophies (e.g. Grover et al. patterns 1A and 1B, see Figure 6.1 for 2D examples); however, some of the patterns observed in rod-cone dystrophies cannot be replicated, due in part to the fact that we are working in 1D (e.g. patterns 2 and 3).

It was found that the wave speed of hyperoxic degeneration is negatively correlated with local photoreceptor density: higher densities corresponding to lower speeds and lower densities to higher speeds. We suggested that this is because the width of the photoreceptor-containing hyperoxic region ahead of the wavefront is wider where the local photoreceptor density is lower.

Treatment with antioxidants or trophic factors is predicted to have the potential to prevent, halt or reverse degeneration in the case of patch loss, whilst it may delay degeneration in the cases of mutation-induced rod or cone loss. We note that *in vivo* recovery is likely to be minimal, since most photoreceptors will have degenerated past the point of recovery once the hyperoxic wavefront has passed by.

In Chapter 5 we extended the model from Chapter 4 in two ways: firstly by incorporating

degeneration of the choriocapillaris into the 1D model and secondly by expanding the original 1D model into 2D, spanning a spherical surface between the foveal centre and the ora serrata. This is the first time that a 2D model of RP has been constructed.

Asymptotic analysis of the steady-state 1D capillary loss problem showed that a patch of capillary loss must be essentially coincident with a patch of photoreceptor loss in order to prevent the spread of degeneration in those cases where degeneration would spread in the absence of capillary loss. This was confirmed by numerical solutions of the steady-state problem using a finite difference discretisation. Numerical (method of lines) solutions of the dynamic problem revealed that capillary loss may prevent, reverse or retard photoreceptor degeneration, though recovery is likely to be limited *in vivo*.

Finite element solutions of the 2D problem confirmed the results from the 1D model, whilst allowing us to observe patterns of degeneration inaccessible to the 1D model. In particular, when a disc of photoreceptors is removed, two new patterns are observed. For the first pattern, a disc is removed from near the ora serrata. Having spread toward the ora serrata, degeneration proceeds around the edge of the retina in two arms, until they meet on the far side of the retina. For the second pattern, a disc is removed near the centre of the retina. Degeneration then spreads through the parafoveal/perifoveal region around the fovea, leading to the loss of all photoreceptors in the central retina. These patterns are amongst those observed in RP (e.g. Grover et al. patterns 1 and 3, see also Figure 6.1), confirming the explanatory efficacy and sufficiency of the oxygen toxicity hypothesis for some patterns of disease progression; however, there are some distinctive patterns of degeneration that the 2D model is unable to reproduce, namely those that involve preferential loss of mid-peripheral photoreceptors (e.g. Grover et al. pattern 2 and the initial pattern of loss in pattern 3). This suggests that additional mechanisms for the spread of photoreceptor degeneration are at work, in addition to oxygen toxicity. Thus we have demonstrated the strengths and limitations of the oxygen toxicity hypothesis in explaining the spatio-temporal progression of RP, where before there was only (hand-waving) speculation.

As with the 1D model, treatment with antioxidants or trophic factors results in predictions

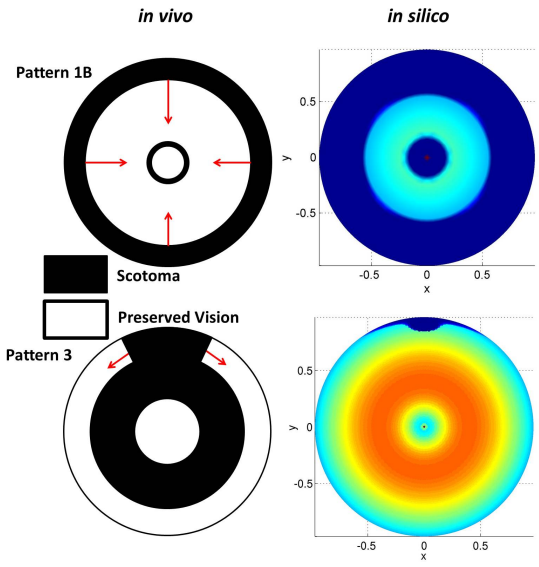

Figure 6.1: Comparison between *in vivo* patterns of photoreceptor degeneration and those predicted using our FEM simulation. Both pattern 1B and the peripheral spread of pattern 3 are replicated by the model. Left: *in vivo*. Right: FEM. Top: Pattern 1B. Bottom: Pattern 3.

of the prevention, halt, delay or reversal of degeneration.

6.2 Future Work

The work described above suggests a number of avenues for future research. These may be divided into two types: those of an experimental nature and those of a theoretical nature.

6.2.1 Experimental

In relation to our work on Ngb, detailed quantitative measurements of Ngb concentrations within each of the retinal layers, and for a range of eccentricities and azimuthal positions, would enable us to test whether Ngb is present in humans in the concentrations that we suggest would be required for Ngb to play a significant role in oxygen transport. Measurements of this type in humans and in other species would enable us to test the further hypothesis that Ngb is always most highly concentrated in those regions of the retina that are in greatest danger of

hypoxia. They would also allow us to test whether Ngb concentrations vary with eccentricity and azimuthal position, in accordance with regional variations in oxygen supply and demand within individual eyes.

It would be of great interest to test whether the oxygen affinity of Ngb varies between species in direct proportion to the square root of the average oxygen concentration at the choriocapillaris or retinal capillaries, as suggested by our analysis. It would also be of interest to determine if there exist scenarios in which the retina is challenged by an increase in oxygen demand or a decrease in supply, lasting on the order of a few seconds, in which oxygen storage by Ngb would be predicted to play an important role in the prevention of hypoxia.

Our work on RP suggests a number of avenues for experimental research. Of the greatest help in testing our predictions for the spatial spread of degeneration and in forming and testing future models would be a series of detailed longitudinal studies in humans, measuring the precise position of the boundaries of degenerate photoreceptor, retinal pigment epithelium and choriocapillaris patches at each disease stage, together with the rod and cone densities across the retina at each stage. This would also enable us to determine the rate of mutation-induced rod or cone loss (and whether this varies across the retina), together with the rate of degeneration of the choriocapillaris, as well as demonstrating the order in which photoreceptors, retinal pigment epithelium and choriocapillaries are lost. Provided measurements were made sufficiently frequently, the velocity of the wavefront of degeneration could also be calculated and the prediction that wave speed is negatively correlated with local photoreceptor density tested. These measurements could also be carried out in patients undergoing treatment with antioxidants or trophic factors, to compare the effects of treatment with those predicted by our model.

Animal models could be used to test whether ablation of the choriocapillaris is sufficient to halt or delay degeneration, as predicted by our analysis.

Lastly, examination of the detailed biochemistry behind oxidative damage as well as the action of antioxidants and trophic factors, would enable us to form more detailed mechanistic models.

6.2.2 Theoretical

In addition to the experimental work described above, there are a number of directions in which new theoretical work could proceed.

With regard to the work on Ngb, the magnitude of Ngb's histidine dissociation rate could be allowed to vary in response to the local oxygen concentration, in order to determine the extent to which this would enhance its oxygen transport and storage properties. The eight layer model could be adapted to explore the effect of Ngb at other retinal locations, or in other species. The model could also be expanded into 2D or 3D and more detailed descriptions of cell metabolism and blood flow incorporated. Cytoglobin could also be included in the model, to examine the degree to which it could augment Ngb in oxygen transport and storage.

Our modelling work on RP could also be extended in a number of ways. Capillary loss could be incorporated into the 2D model. We could also use a more detailed healthy photoreceptor distribution with variation in the azimuthal direction and examine how this affects the patterns of degeneration generated. Photoreceptor distributions corresponding to other mammals such as rats, mice and pigs could also be modelled, to determine the spatio-temporal patterns of degeneration that would result in these cases. This may allow us to explain, at least in part, the differences in the pattern of disease progression between animal and humans models of RP.

The model could be extended to 3D, accounting for the complex, layered structure of the retina, including the retinal capillary layers. In this case, a hybrid approach, such as that used by McDougall et al. (2012), could be taken, modelling the respectively lobular and branched structures of the choroidal and retinal capillaries as discrete entities (for details of this modelling approach, see the reviews by Mantzaris et al., 2004; Peirce, 2008). Details of the blood flow within the vascular network could also be included and coupled to intravascular, and hence extravascular, oxygen levels (for details of this approach, see the review by Chaplain et al., 2006). To capture the pathology of RP, the dynamic adaptation of blood vessels to hyperoxia or changes in VEGF levels via constriction and/or atrophy could also be incorporated, as could shrinkage of the photoreceptor outer segments.

Whilst the hybrid approach described above would capture the physiology of the retina in detail, it would be analytically intractable. A complementary approach that would overcome this weakness, would be to use homogenization to capture the micro level details of capillary architecture at the macro level, giving rise to a continuum description in terms of the vascular density (for examples of this approach, see Chapman et al., 2008; Shipley and Chapman, 2010).

Details of the biochemical pathways involved in oxidative damage and the action of antioxidants and trophic factors could also be included in the model, once they have been mapped out experimentally. Lastly, models could be constructed for the rod trophic factor and rod toxic substance hypotheses, using the modelling framework developed here. In particular, the rod toxic substance model has the potential to explain the loss of mid-peripheral photoreceptors, given that the toxin producing rods are most highly concentrated in his area.

6.3 Conclusion

The past few decades have seen great advances in our understanding of the physiology and biochemistry of the retina in both healthy and diseased states. However, whilst there have been innumerable experimental and clinical studies, the retina has received little attention from the mathematical modelling community. Mathematics has a clear role to play in this area, enabling us to test hypotheses and isolate mechanisms in a way that would not be possible in an experimental setting. In this thesis we have done just that, exploring the utility of Ngb in oxygen transport and storage, and isolating hyperoxia as a cause behind retinal degeneration in RP. Furthermore, these models have enabled us to make predictions that were unlikely to have been generated in the absence of modelling, and which can be tested experimentally. Thus, this thesis forms the first loop, in what has the potential to be a fruitful experimental/modelling cycle.

Appendix A

Parameter Estimates

A.1 The Width of the Retina and its Layers (L_i and $\tilde{L}$)

The total width of the retina, measured from Bruch's membrane to the ILM, varies between a maximum of 320 μm (at the foveal rim) and a minimum of 80 μm (at the ora serrata, Webvision, `http://webvision.med.utah.edu/`, see Figure A.1). Thus we choose values for the width of the retina, L, in this range, scaling the independent spatial variable x with the minimum retinal width, $\tilde{L} = 80\mu$m, upon non-dimensionalisation.

Based upon Figure A.1 we consider a retinal width of 250 μm to be typical. By inspection of a micrograph of the retina and choroid of a normal rat given in Yu et al. (1994) and reproduced in Figure A.2, we approximate the percentage width of each retinal layer and scale relative to the typical retinal width to give the absolute widths in Table A.1. Since the rat retina is anatomically very similar to that of the human retina, we expect the relative widths of the retinal layers to be similar also.

A.2 Oxygen Solubility (k)

The solubility of oxygen has not been measured in the retina (Linsenmeier and Braun, 1992). Our value for the solubility of oxygen in retinal tissue, $k = 2.4 \times 10^{-5}$ LO_2(L tissue·mmHg)$^{-1}$,

Table A.1: Percentage and absolute widths of the tissue layers in a typical section through the retina. RPE: retinal pigment epithelium. OSs: photoreceptor outer segments. ISs: photoreceptor inner segments. ONL: outer nuclear layer. OPL: outer plexiform layer. INL: inner nuclear layer. IPL: inner plexiform layer. GCL: ganglion cell layer. NFL: nerve fibre layer.

Retinal Layer	Percentage Width (%)	Width (μm)	Cumulative Width (μm)
RPE	2	5	5
OSs	9	22.5	27.5
ISs	9	22.5	50
ONL	20	50	100
OPL	5	12.5	112.5
INL	20	50	162.5
IPL	25	62.5	225
GCL and NFL	10	25	250

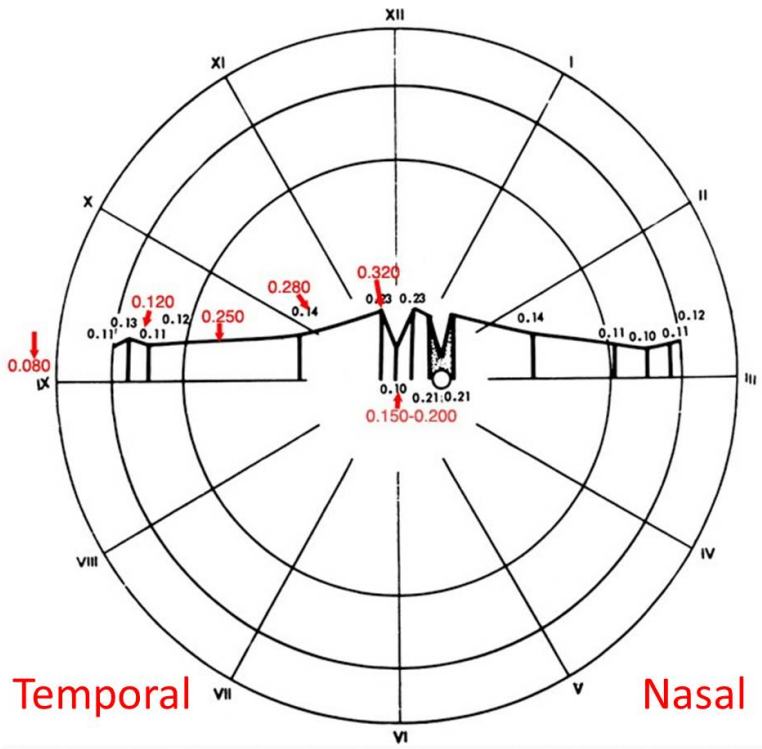

Figure A.1: Diagram to show the width of the retina across the horizontal meridian for a range of eccentricities. The retina is shown in profile. All widths given in mm. The numbers in red are more accurate. Figure reproduced, with permission and modifications, from Webvision, `http://webvision.med.utah.edu/`.

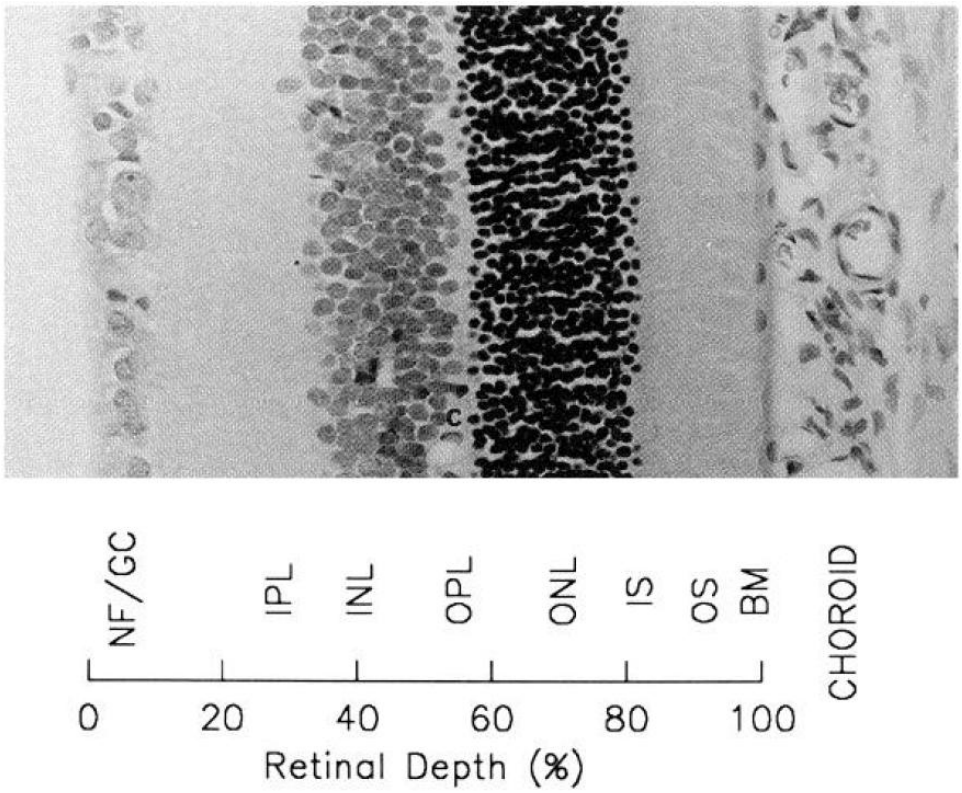

Figure A.2: Micrograph of the retina and choroid of a normal rat at a distance of two disc diameters from the optic disc. Magnification $\times$ 280. BM: Bruch's membrane. OS: photoreceptor outer segment(s). IS: photoreceptor inner segment(s). ONL: outer nuclear layer. OPL: outer plexiform layer. INL: inner nuclear layer. IPL: inner plexiform layer. GC: ganglion cell layer. NF: nerve fibre layer. Figure reproduced, with permission, from Yu et al. (1994).

is that used by Linsenmeier and Braun (1992); Braun et al. (1995) and was originally derived from the value in blood at 37 °C (Goldstick, 1973; Linsenmeier and Braun, 1992). It is similar to the values measured in the brain. For example, Ganfield et al. (1970) measured a value of $k = 1.89 \times 10^{-5}$ LO_2(L tissue·mmHg)$^{-1}$ in the cat cerebral cortex. Fago et al. (2004b) use a similar value of $k = 3.9 \times 10^{-5}$ LO_2(L tissue·mmHg)$^{-1}$. Following Braun et al. (1995), we assume that k is constant across the retina.

A.3 The ppO$_2$ at the Choriocapillaris (c_c and $\tilde{c}$)

We assume the ppO$_2$ at the edge of the RPE adjacent to the CC to be approximately $c_c = 60$ mmHg (Wangsa-Wirawan and Linsenmeier, 2003). Whilst this value has not been measured in humans, this is within the range of values measured in the macaque monkey (Birol et al., 2007), which has a retinal physiology similar to that of humans. We also use this as the reference ppO$_2$, $\tilde{c}$, with which we scale oxygen concentrations upon non-dimensionalisation.

A.4 The ppO$_2$ in the Retinal Capillaries (c_v)

The saturation of haemoglobin (Hb) under both DA and LA has been measured in human retinal arterioles and venules (Hardarson et al., 2009; Hardarson and Stefánsson, 2010). Averaging the measurements found in Hardarson et al. (2009); Hardarson and Stefánsson (2010) over arteriolar and venular saturation, DA and LA, and weighting by patient number, we obtain an average Hb saturation value of 74.32%. We can convert the Hb saturation to the corresponding partial pressure of oxygen using the Hill equation:

$$S = \frac{P^n}{P_{50}^n + P^n}, \tag{A.1}$$

where $S \in [0,1]$ is the Hb saturation, P is the partial pressure of oxygen within the retinal capillaries, P_{50} is the partial pressure of oxygen at which $S = 0.5$ and n is the Hill equation exponent. In a human under normal conditions $P_{50} = 26$ mmHg and $n = 2.7$ (Popel, 1989;

McGuire and Secomb, 2001). Inverting the Hill equation we obtain the following expression for P in terms of S,

$$P = \left(\frac{S}{1-S}\right)^{\frac{1}{n}} P_{50}. \tag{A.2}$$

Substituting in the values above, this gives us a partial pressure of 38.1 mmHg in the retinal capillaries, which we round to 40 mmHg.

A.5 The Permeability of the Retinal Capillaries ($\hat{h}_5$ and $\hat{h}_7$)

We assume that the deep and superficial retinal capillaries each form a continuous layer, whereas, in reality, capillaries are present at discrete locations. Thus the parameters $\hat{h}_5$ and $\hat{h}_7$ account for both the permeability and density of the retinal capillaries, whilst retaining the units of permeability. We choose the permeabilities such that the outer retina becomes hypoxic under DA in the absence of Ngb. Since the superficial retinal capillaries are about twice as dense as the deep retinal capillaries (Tan et al., 2012) we ensure that $\hat{h}_7 = 2\hat{h}_5$ in all simulations. Tan et al. (2012) found that the densities of the retinal capillary beds 3mm superior to the optic disc in human retinas ranges between 11.28% and 26.74%, depending upon the capillary layer (there are four capillary beds in this region). In addition, the permeability of bovine retinal capillaries to H-inulin *in vitro* has been measured to be 1.7×10^{-3} ms^{-1} (Gillies et al., 1995). Multiplying the densities by the permeability to H-inulin, this suggests that $\hat{h}_5$ and $\hat{h}_7$ should be on the order of 10^{-4} ms^{-1}.

A.6 Ngb Concentration (n_{T_i} and $\tilde{n}$)

The average concentration of Ngb across the mouse retina has been estimated to lie in the range 100–200 μM (Schmidt et al., 2003), and we assume this to be true of the human retina also. Accordingly, we choose to rescale Ngb concentrations with $\tilde{n} = 100$ μM upon non-dimensionalisation.

Ngb is not distributed uniformly across the retina, but is more highly concentrated in cer-

tain regions. For instance, in the murine retina Ngb is most highly concentrated in the photoreceptor ISs, OPL, IPL and GCL (Schmidt et al., 2003; Bentmann et al., 2005; Schmidt et al., 2005, see Figure A.3(b)), whilst our examination of confocal images of Ngb immunoreactivity in Ostojić et al. (2006) suggest that Ngb is most highly concentrated in the photoreceptor ISs of the canine retina. Only two studies have measured the Ngb distribution across the human retina. Ostojić et al. (2008) found that Ngb is present in all layers of the human retina, except the photoreceptor OSs, our examination of their Ngb immunoreactivity images suggesting that Ngb is fairly evenly distributed throughout the cytosol across these layers. However, the measurements of Rajendram and Rao (2007) suggest that Ngb is most highly concentrated in (the apical region of) the photoreceptor ISs, with lower, yet greater than average concentrations in the OPL, IPL and GCL (see Figure A.3(a)).

Assuming an average retinal Ngb concentration of 200 μM (see above), an upper bound on the mean *cytosolic* concentration of Ngb across the retina of 500μm is reasonable, given that organelles may take up more than half the intracellular space (in the macaque, mitochondrial density is 54-66% in rod and 74-85% in cone ellipsoids, which occupy the outer part of the ISs, Hoang et al., 2002).

In the case that Ngb is concentrated primarily within the photoreceptor ISs, then since the ISs (≈ 25 μm in length) represent approximately one tenth of the width of the retina (a typical width being ≈ 250 μm) and since mitochondria and other organelles may take up more than half the volume of the ISs (see above), we estimate that the Ngb concentration in the cytosol of the ISs may be as high as $200 \times 10 \times 2 = 4000$ μM. Since the cell types in all layers of the human retina other than the photoreceptor layer and the RPE are similar to those found in brain tissue, we assume that the concentration of Ngb in these layers is equal to that found in brain tissue, that is 2 μM (Schmidt et al., 2003), in this case. In the absence of further information it is also reasonable to assume that the RPE has a Ngb concentration of 2 μM. This results in a mean Ngb concentration of 362 μM across the retina.

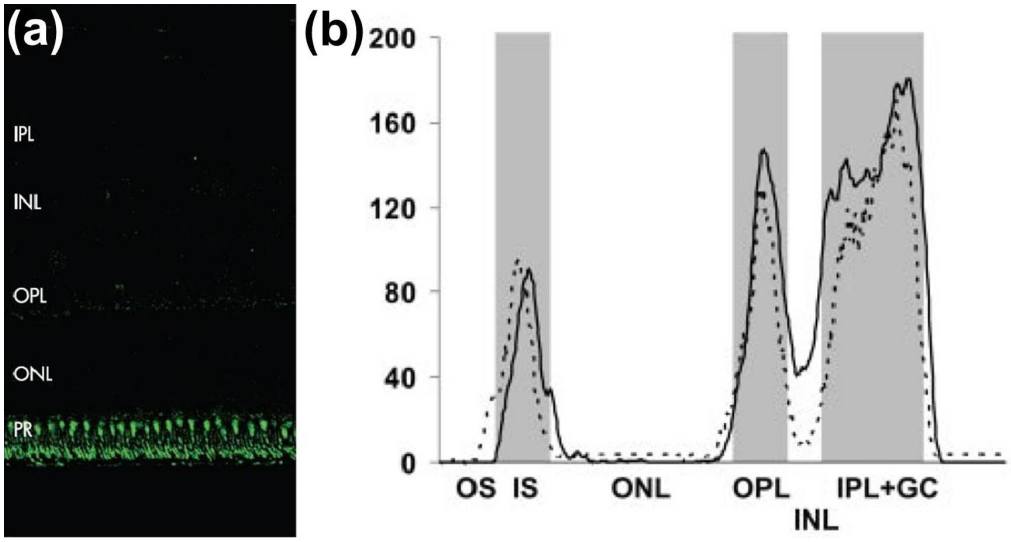

Figure A.3: Graphs showing retinal Ngb distribution. (a) Normal human retina showing immunostaining with anti-Ngb antibody (green). Staining is strongest in the photoreceptor ISs, with some staining in the ONL, OPL, INL, IPL and ganglion cell layer. Figure reproduced, with permission, from Rajendram and Rao (2007). (b) Graph to show the qualitative distribution of Ngb within the mouse retina. The solid line indicates anti-Ngb fluorescence, whilst the dotted line shows anti-cytochrome c staining, highlighting the presence of mitochondria. The shaded rectangles indicate the regions with the greatest oxygen demand. Ngb is most highly concentrated in the oxygen consuming, mitochondria rich regions of the ISs, OPL, IPL and ganglion cell layer. Figure reproduced, with permission, from Bentmann et al. (2005). PR: photoreceptor layer. OS: photoreceptor outer segment(s). IS: photoreceptor inner segment(s). ONL: outer nuclear layer. OPL: outer plexiform layer. INL: inner nuclear layer. IPL: inner plexiform layer. GC: ganglion cell layer.

A.7 The Diffusion Coefficient of Oxygen (D_o)

We take the diffusion coefficient of oxygen in retinal tissue, D_o, to be 1.97×10^{-9} m^2s^{-1}. This is the value measured by Roh et al. (1990) in the retina of a living cat, at a temperature of 37–38 °C and was found to be almost constant across the retina. This is also the value used by Braun et al. (1995) and is similar to the value of 2×10^{-9} m^2s^{-1} used by Fago et al. (2004b).

A.8 The Diffusion Coefficient of Ngb (D_n)

We were unable to find an estimate for the diffusion coefficient of Ngb in the literature; however, since Ngb and myoglobin (Mb) have a similar molecular weight ($\approx$ 17 kDa, Zaia et al., 1992; Keener and Sneyd, 1998; Schmidt et al., 2003) and structure (Burmester and Hankeln, 2009) it is reasonable to assume that their diffusion coefficients are similar. The diffusion coefficient of Mb in the rat diaphragm muscle at 22 °C is 1.17×10^{-11} m^2s^{-1} (Jürgens et al., 1994). We may find the value of the diffusion coefficient at 37 °C (the temperature of the human retina) by using the Q_{10} rule[1] with $Q_{10} = 1.3$ (Jürgens et al., 1994). This gives us a value for the Mb diffusion coefficient, and hence the Ngb diffusion coefficient, of $D_n = 1.73 \times 10^{-11}$ m^2s^{-1} (Jürgens et al., 1994; McGuire and Secomb, 2001). We note that Fago et al. (2004b) use a value of 1.7×10^{-10} m^2s^{-1}, an order of magnitude larger than our value. The source of this parameter choice is not given; however, it is likely that they are using the value measured in highly diluted aqueous Mb solutions (Jürgens et al., 1994). We assume that the diffusion coefficients of all three forms of Ngb (Ngb, Ngb-His and Ngb-O_2) are the same since the molecular weights and structures are almost identical in each case (see Keener and Sneyd, 1998, for a similar assumption concerning Mb).

[1] $Q_{10} = \left(\frac{D_2}{D_1}\right)^{\left(\frac{10}{T_2 - T_1}\right)}$, where D_1 (D_2) is the rate of diffusion at temperature T_1 (T_2).

A.9 The Rate of Oxygen Consumption (Q_i)

The rate of oxygen consumption by the RPE is assumed to be $Q_1 = 4.5$ $\text{mlO}_2 \cdot (100\text{g tissue} \cdot \text{min})^{-1}$ by analogy with epithelial cells in other parts of the body and in order to ensure that the average rate of oxygen uptake of the outer retina is correct. The photoreceptor OSs and the ONL consume negligible levels of oxygen (Cringle and Yu, 2002; Wangsa-Wirawan and Linsenmeier, 2003; Birol et al., 2007) and so we set $Q_2 = Q_4 = 0$ $\text{mlO}_2 \cdot (100\text{g tissue} \cdot \text{min})^{-1}$. The photoreceptor IS layer, which contains 55–65% of all retinal mitochondria (Medrano and Fox, 1995) is perhaps the most oxygen demanding layer of the retina. Its rate of oxygen consumption depends upon whether the eye is light adapted or dark adapted. Under DA $Q_3 =$ 15–20 $\text{mlO}_2 \cdot (100\text{g tissue} \cdot \text{min})^{-1}$ (Haugh et al., 1990; Wangsa-Wirawan and Linsenmeier, 2003; Birol et al., 2007), whilst under LA its rate of oxygen consumption has been measured to lie between 36–72% of the DA value (Medrano and Fox, 1995; Wangsa-Wirawan and Linsenmeier, 2003; Birol et al., 2007). Since the rate of oxygen consumption of the ISs of the macaque eye under LA (which are assumed to be more biochemically similar to human eyes than those of mice, rats and cats from which the other measurements were generated) is about $72 \pm 11\%$ of that under DA, we anticipate that the rate of oxygen consumption of the ISs of the human eye will not drop below $Q_3 = 10$ $\text{mlO}_2 \cdot (100\text{g tissue} \cdot \text{min})^{-1}$ under LA. Whilst the remaining layers of the retina vary in their oxygen demands, reliable data on the rate of oxygen consumption of each individual layer of the inner retina and the OPL are unavailable. However, the average rate of oxygen consumption across the inner retina is known, and so we use this value for the remaining layers, that is $Q_i = 4$ $\text{mlO}_2 \cdot (100\text{g tissue} \cdot \text{min})^{-1}$ for $i = 5,\ldots,$ 8 (Birol et al., 2007).

Table A.2 shows the relative oxygen consumption rates of each retinal layer as a percentage of the total retinal oxygen consumption for a typical 250 μm section through the retina, with layer widths as in Table 3.1 of Chapter 3, under DA and LA. Under DA the outer retina (RPE–O-OPL) accounts for 46% of the total retinal oxygen consumption, with an average oxygen consumption rate of approximately 4.7 $\text{mlO}_2 \cdot (100\text{g tissue} \cdot \text{min})^{-1}$. This agrees well with

Table A.2: Percentage oxygen consumption of each retinal layer under DA and LA. RPE: retinal pigment epithelium. OSs: photoreceptor outer segments. ISs: photoreceptor inner segments. ONL: outer nuclear layer. OPL: outer plexiform layer. INL: inner nuclear layer. IPL: inner plexiform layer. GCL: ganglion cell layer. NFL: nerve fibre layer. I-(·): inner-(·). O-(·): outer-(·).

Retinal Layer	Percentage of Retinal Oxygen Consumption (%)	
	DA	LA
1 (RPE)	2.1	2.7
2 (OSs)	0	0
3 (ISs)	42	27
4 (ONL)	0	0
5 (O-OPL)	2.3	2.9
6 (I-OPL, INL, O-IPL)	33	41
7 (I-IPL, O-GCL, O-NFL)	16	21
8 (I-GCL, I-NFL)	4.7	5.9

the value of 4.6 ± 2.3 $\text{mlO}_2 \cdot (100\text{g tissue}\cdot\text{min})^{-1}$ measured by Birol et al. (2007) in the Macaque outer retina under DA. Under LA (with $Q_3 = 10$ $\text{mlO}_2 \cdot (100\text{g tissue}\cdot\text{min})^{-1}$) the outer retina accounts for 32% of the total retinal oxygen consumption, with an average oxygen consumption rate of approximately 2.6 $\text{mlO}_2 \cdot (100\text{g tissue}\cdot\text{min})^{-1}$. The average oxygen consumption rate of the inner retina (I-OPL–NFL) is 4 $\text{mlO}_2 \cdot (100\text{g tissue}\cdot\text{min})^{-1}$ under both DA and LA, since all layers of the inner retina are assigned this oxygen consumption rate under both DA and LA.

A.10 The Michaelis Constant (γ)

Estimates for the Michaelis constant range between approximately 0.5–1 mmHg (Costa et al., 1997; Richmond et al., 1999; McGuire and Secomb, 2001; Goldman, 2008) thus a value of $\gamma = 1$ mmHg is reasonable. This is the ppO_2 at which the rate of oxygen uptake is half its maximum value, that is $Q_i/2$. Estimates for the ppO_2 at which tissue can be considered to have become hypoxic vary. Yu and Cringle (2002) suggest that retinal tissue becomes hypoxic in

the range 5–15 mmHg, citing the work of Epstein et al. (1994); Epstein (1997) on the kidney. In contrast, the work of Richmond et al. (1999) on rat skeletal muscle suggests that tissue becomes hypoxic in the range 1.2–2.9 mmHg. Lastly, McGuire and Secomb (2001) state that tissue becomes hypoxic for a ppO_2 less than 1 mmHg. It seems reasonable then, to assume that any increase in ppO_2 above 1 mmHg could be significant in preventing hypoxia in retinal tissue. We therefore take γ to be the *hypoxic threshold*, such that oxygen concentrations below this value are considered to be hypoxic, whilst those above it are normoxic.

A.11 Rate Constants of Ngb Reaction Kinetics (k_o^+, k_o^-, k_h^+ and k_h^-)

Measured values for the rate constants of human Ngb reaction kinetics show significant variation between studies. This is due in part to differences in the experimental conditions used in these studies. Table A.3 gives examples of the measured values of the rate constants, together with their associated P_{50} values. Note that only those measurements using a pH similar to that found in the retina (about pH 7) have been included. The values we have calculated for P_{50} are included in brackets and are a factor of 1.89 larger than those given in the papers cited. This discrepancy is discussed in the next section. The P_{50} of Ngb is the ppO_2 at which half the Ngb molecules in a sample will be bound to oxygen and is a measure of the binding affinity of Ngb for oxygen. Therefore, a higher P_{50} value corresponds to a lower oxygen affinity.

The temperature of the retina is equal to body temperature, that is 37°C; however, most studies measure the reaction kinetics at 25°C or below. Examination of the data in Table A.3 suggests that the P_{50} of Ngb is higher at higher temperatures. The reaction rates in the first row of Table A.3 were measured at 25°C; however, the P_{50} value was measured at 37°C (second row). The P_{50} corresponding to the kinetic terms is approximately 0.77 mmHg, using Hamdane et al.'s conversion factor (see the following section). So in this case an increase from 25 to 37°C resulted in a 30% increase in the P_{50} value, whilst the results of Fago et al. (2004a) (rows 6 and 7 of Table A.3) suggest a 50% increase.

The addition of DTT (dithiothreitol) causes the breaking (reduction) of Ngb's CD7-D5 disulphide bond. This results in an order of magnitude decrease in the histidine dissociation rate, k_h^-, and hence an increase in P_{50} (Hamdane et al., 2003). In the absence of DTT, for example in the retina, Ngb may exist in a mixture of these two forms, with and without the disulphide bond (Hamdane et al., 2003). Some of the differences in the measured values for the rate constants may be due to variations in the proportion of each form present (Hamdane et al., 2003). Hamdane et al. (2003) have suggested that the redox state of a cell may regulate this ratio, with reduction equivalents ($NADH + H^+$) accumulating under hypoxia, resulting in the reduction of Ngb disulphide bonds and a release of oxygen, counteracting hypoxia. As oxygen levels rise the disulphide bonds reform, increasing the oxygen affinity of Ngb and hence its average level of oxygen storage.

In the absence of measurements for the rate constants at 37 °C, we use values obtained by Kiger et al. (2004) since they result in the P_{50} which is in closest agreement with that measured at 37 °C. They are also similar to the values measured by Hamdane et al. (2003) under the same conditions.

A.12 Conversion between Units

In order to non-dimensionalise our models we must write the parameters involving the concentration of oxygen ($\tilde{c}$, c_c, c_v and γ), which are measured in mmHg, in the same units as the parameters involving the concentration of Ngb, that is in units of Moles (M or molL^{-1}). Multiplying the former parameters by the oxygen solubility in retinal tissue, k (see Appendix A.2), allows us to convert to units of $LO_2 \cdot (\text{L tissue})^{-1}$. We may then use the Ideal Gas Law to convert LO_2 to mol. The use of the Ideal Gas Law is valid here, since LO_2 refers to the volume that would be occupied by the oxygen dissolved in the retina when in its gaseous form (under atmospheric pressure and at body temperature).

The Ideal Gas Law relates the number of moles, n, of a substance to the corresponding

Table A.3: Measured values of human Ngb reaction rate constants and P_{50} values. Only those measurements using a pH similar to that found in the retina (about pH 7) have been included. The P_{50} values in brackets are those that we have calculated (see text).

k_o^+ ($\mu M^{-1}s^{-1}$)	k_o^- (s^{-1})	k_h^+ (s^{-1})	k_h^- (s^{-1})	P_{50} (mmHg)	Experimental Conditions	Source
250	0.8	2000	4.5	(1.5)	25 °C, pH 7.0	Dewilde et al. (2001)
—	—	—	—	1 (1.9)	37 °C, pH 7.0	Dewilde et al. (2001)
130	0.3	9800	8200	(2.7×10^{-3})	20 °C, pH 7.0	Trent and Hargrove (2002)
140	0.8	2000	7	0.9 (1.7)	25 °C, pH 7.0	Hamdane et al. (2003)
170	0.8	2000	0.6	8.4 (16.3)	25 °C, pH 7.0, DTT	Hamdane et al. (2003)
—	—	—	—	7.5 (14.2)	37 °C, pH 7.1	Fago et al. (2004a)
—	—	—	—	5 (9.5)	25 °C, pH 7.0	Fago et al. (2004a)
170	0.7	1800	0.6	6.8 (12.9)	25 °C, pH 7.0, DTT	Kiger et al. (2004)

volume, V, via the relation

$$V = \frac{nRT}{p}, \tag{A.3}$$

where $R = 8.31$ J mol^{-1}K^{-1} is the ideal gas constant, T is the temperature of the gas, which we take as body temperature, so that $T = 310.15$ K and p is the pressure of the gas, which we assume to be at atmospheric pressure, that is $p = 10^5$ Pa. Substituting these values into equation (A.3), we find that 1 mol of oxygen corresponds to a volume of 0.025 m^3 = 25 L.

The conversion factor used in Hamdane et al. (2003); Kiger et al. (2004) is different from that derived above. Where we use a conversion factor of 0.96 μM to 1 mmHg, they use a conversion factor of 1.85 μM to 1 mmHg (Hamdane et al., 2003). As a result, their estimates for P_{50} in the fourth, fifth and last rows of Table A.3 are a factor of 1.89 smaller than ours. Assuming that Dewilde et al. (2001); Fago et al. (2004a) use the same conversion factor as Hamdane et al. (2003); Kiger et al. (2004), we also show (in brackets) our estimates for the P_{50} value in rows 2, 6 and 7, multiplying the original P_{50} values by the ratio between conversion factors.

To convert Q from units of mlO_2(100g tissue·min)$^{-1}$ to Ms^{-1}, we divide by 1000 to convert from ml to L, divide by 25 to convert from L to mol, divide by 60 to convert from minutes to seconds and multiply by 10 to convert from '100g tissue' to L, assuming that the retinal tissue has roughly the density of water for which 1 L weighs approximately 1 kg.

Appendix B

Placing a Bound on the Concentration of Pentacoordinate Neuroglobin

It was found in all single and eight layer model simulations that the concentration of pentacoordinate neuroglobin, n, at any given point in space is significantly lower than that of hexacoordinate Ngb, n_h, or oxygen bound Ngb, n_o, at that point. In this appendix we derive a bound on n to explain why this is the case.

Beginning with the time-dependent equation for n, equation (2.10), we can re-write it in the form

$$\frac{\partial n}{\partial t} = D\frac{\partial^2 n}{\partial x^2} + f(x,t) - \left(\frac{1}{\kappa} + g(x,t)\right) n, \tag{B.1}$$

where $1/\kappa = k_3$, $f(x,t) = k_4 n_h + \alpha k_2 n_o \geq 0$ and $g(x,t) = \alpha k_1 c \geq 0$. Whether we are using the single or the eight layer model, this equation will be defined on a finite domain, which we can denote as $x \in [0,L]$ without loss of generality. As usual, we impose zero-flux boundary conditions at either end of the domain.

Consider the function $M = M(t)$ which satisfies

$$\frac{\mathrm{d}M}{\mathrm{d}t} = \left(\max_{x,t}(f(x,t)) + \beta\right) - \frac{1}{\kappa}M, \tag{B.2}$$

where the constant $\beta > 0$ is arbitrarily small. This can be written as

$$\frac{\mathrm{d}M}{\mathrm{d}t} = F - \frac{1}{\kappa}M, \tag{B.3}$$

where $F = (\max_{x,t}(f(x,t)) + \beta) > f(x,t) \geq 0$ is a constant. We close the system by imposing the initial condition

$$M(0) = \max_{x}(n(x,0)). \tag{B.4}$$

Solving this initial-value problem using the integrating factor method we obtain

$$M(t) = e^{-\frac{t}{\kappa}}M(0) + \kappa F(1 - e^{-\frac{t}{\kappa}}). \tag{B.5}$$

Taking the limit as t tends to infinity we find that

$$\lim_{t\to\infty} M(t) = \kappa F. \tag{B.6}$$

Let $u(x,t) := n(x,t) - M(t)$, then

$$\frac{\partial u}{\partial t} - D\frac{\partial^2 u}{\partial x^2} = (f - F) - \frac{u}{\kappa} - gn, \tag{B.7}$$

from equations (B.1) and (B.3). Since $(f - F) < 0$ and $gn \geq 0$ we have that

$$\frac{\partial u}{\partial t} - D\frac{\partial^2 u}{\partial x^2} + \frac{u}{\kappa} < 0, \tag{B.8}$$

and therefore

$$\frac{\partial}{\partial t}\left(e^{\frac{t}{\kappa}}u\right) - D\frac{\partial^2}{\partial x^2}\left(e^{\frac{t}{\kappa}}u\right) < 0. \tag{B.9}$$

Defining $v(x,t) := e^{\frac{t}{\kappa}}u(x,t)$, we have that

$$\frac{\partial v}{\partial t} - D\frac{\partial^2 v}{\partial x^2} < 0, \tag{B.10}$$

with initial condition

$$v(x,0) = n(x,0) - \max_x(n(x,0)), \tag{B.11}$$

and zero-flux boundary conditions.

By the maximum principle for parabolic PDEs we have that v must achieve its maximum on one of the boundaries $x = 0$, $x = L$ or $t = 0$ (Ockendon et al., 2003). Suppose that v takes its maximum value on $x = 0$ for some $t = t_1 > 0$. Since $n_x(0,t_1) = 0$ by the zero-flux boundary condition and since $M_x(t_1) = 0$, as M is independent of x, this implies that $u_x(0,t_1) = 0$ and so $v_x(0,t_1) = 0$. Therefore, in order for this point to be a maximum, we require both that $v_t(0,t_1) = 0$ and $v_{xx}(0,t_1) \leq 0$. This implies that $v_t(0,t_1) - Dv_{xx}(0,t_1) \geq 0$, which contradicts (B.10). Therefore, the maximum cannot lie on the boundary $x = 0$. Using a similar argument we can show that the maximum cannot lie on the boundary $x = L$. Therefore, the maximum must lie on the boundary $t = 0$. As a check we can see that if the maximum lies on the boundary $t = 0$ for some $x = x_1$, where $0 < x_1 < L$, then we must have that $v_t(x_1,0) \leq 0$, $v_x(x_1,0) = 0$ and $v_{xx}(x_1,0) \leq 0$. Thus (B.10) may be satisfied, provided $|v_t(x_1,0)| > D|v_{xx}(x_1,0)|$.

Since $v(x,t)$ takes its maximum value on $t = 0$ this means that $v(x,t) \leq \max_x(v(x,0)) = \max_x(n(x,0) - \max_x(n(x,0))) = \max_x(n(x,0)) - \max_x(n(x,0)) = 0$. Therefore $u \leq 0$, which implies that $n \leq M$. Therefore, by (B.6), we have that at steady-state $n \leq \kappa F$. Taking the limit as β tends to zero, we find $n \leq \kappa \max_{x,t}(f(x,t)) = \kappa \max_{x,t}(k_4 n_h + \alpha k_2 n_o) \leq \kappa\alpha k_2 n_T = \frac{\alpha k_2 n_T}{k_3} \approx 4n_T \times 10^{-4}$. This bound was found to be satisfied in all simulations.

Bibliography

Ach T., Best G., Rossberger S., Heintzmann R., Cremer C., Dithmar S. (2012) Autofluorescence imaging of human RPE cell granules using structured illumination microscopy. Br. J. Ophthalmol. 96(8):1141–1144

Al-Rashed M., Abu Safieh L., Alkuraya H., Aldahmesh M. A., Alzahrani J., Diya M., Hashem M., Hardcastle A. J., Al-Hazzaa S. A. F., Alkuraya F. S. (2012) RP1 and retinitis pigmentosa: report of novel mutations and insight into mutational mechanism. Br. J. Ophthalmol. 96(7):1018–1022

Alder V. A., Cringle S. J., Constable I. J. (1983) The retinal oxygen profile in cats. Invest. Ophthalmol. Vis. Sci. 24(1):30–36

Ames B. N., Shigenaga M. K., Hagen T. M. (1993) Oxidants, antioxidants, and the degenerative diseases of aging. Proc. Natl. Acad. Sci. 90(17):7915–7922

Ames B. N., Shigenaga M. K., Hagen T. M. (1995) Mitochondrial decay in aging. Biochim. Biophys. Acta. 1271(1):165–170

Anand-Apte B., Hollyfield J. G. (2009) Encyclopedia of the Eye, Academic Press, Elsevier Books, London, pp. 9–15

Anderson B. (1968) Ocular effects of changes in oxygen and carbon dioxide tension. Trans. Am. Ophthalmol. Soc. 66:423–474

Anderson B., Saltzman H. A. (1964) Retinal oxygen utilization measured by hyperbaric blackout. Arch. Ophthalmol. 72(6):792–795

Arden G. B. (2001) The absence of diabetic retinopathy in patients with retinitis pigmentosa: implications for pathophysiology and possible treatment. Br. J. Ophthalmol. 85(3):366–370

Aubert M., Chaplain M. A. J., McDougall S. R., Devlin A., Mitchell C. A. (2011) A continuum mathematical model of the developing murine retinal vasculature. Bull. Math. Biol. 73:2430–2451

Barry M. P., Dagnelie G., Argus II Study Group (2012) Use of the Argus II retinal prosthesis to improve visual guidance of fine hand movements. Invest. Ophthalmol. Vis. Sci. 53(9):5095–5101

Bender C. M., Orszag S. A. (1999) Advanced Mathematical Methods for Scientists and Engineers I: Asymptotic Methods and Perturbation Theory. Springer

Bentmann A., Schmidt M., Reuss S., Wolfrum U., Hankeln T., Burmester T. (2005) Divergent distribution in vascular and avascular mammalian retinae links neuroglobin to cellular respiration. J. Biol. Chem. 280(21):20,660–20,665

Beyer C. E., Steketee J. D., Saphier D. (1998) Antioxidant properties of melatonin — an emerging mystery. Biochem. Pharmacol. 56(10):1265–1272

Birol G., Wang S., Budzynski E., Wangsa-Wirawan N. D., Linsenmeier R. A. (2007) Oxygen distribution and consumption in the macaque retina. Am. J. Physiol. Heart Circ. Physiol. 293(3):H1696–H1704

Braun R. D., Linsenmeier R. A., Goldstick T. K. (1995) Oxygen consumption in the inner and outer retina of the cat. Invest. Ophthalmol. Vis. Sci. 36(3):542–554

Burmester T., Hankeln T. (2004) Neuroglobin: A respiratory protein of the nervous system. News Physiol. Sci. 19(3):110–113

Burmester T., Hankeln T. (2009) What is the function of neuroglobin? J. Exp. Biol. 212(10):1423–1428

Burmester T., Weich B., Reinhardt S., Hankeln T. (2000) A vertebrate globin expressed in the brain. Nature 407(6803):520–523

Burmester T., Ebner B., Weich B., Hankeln T. (2002) Cytoglobin: A novel globin type ubiquitously expressed in vertebrate tissues. Mol. Biol. Evol. 19(4):416–421

Burns J., Clarke G., Lumsden C. J. (2002) Photoreceptor death: Spatiotemporal patterns arising from one-hit death kinetics and a diffusible cell death factor. Bull. Math. Biol. 64:1117–1145

Camacho E., Rand R., Howland H. (2004) Dynamics of two van der Pol oscillators coupled via a bath. Int. J. Solids Struct. 41(8):2133–2143

Camacho E. T., Wirkus S. (2013) Tracing the progression of retinitis pigmentosa via photoreceptor interactions. J. Theor. Biol. 317(0):105–118

Camacho E. T., Colón Vélez M. A., Hernández D. J., Bernier U. R., van Laarhoven J., Wirkus S. (2010) A mathematical model for photoreceptor interactions. J. Theor. Biol. 267(4):638–646

Camacho E. T., Melara L. A., Villalobos M. C., Wirkus S. (2014) Optimal control in the treatment of retinitis pigmentosa. Bull. Math. Biol. 76(2):292–313

Campbell M., Humphries M., Kennan A., Kenna P., Humphries P., Brankin B. (2006) Aberrant retinal tight junction and adherens junction protein expression in an animal model of autosomal recessive retinitis pigmentosa: The Rho(-/-) mouse. Exp. Eye Res. 83(3):484–492

Carter-Dawson L. D., LaVail M. M., Sidman R. L. (1978) Differential effect of the rd mutation on rods and cones in the mouse retina. Invest. Ophthalmol. Vis. Sci. 17(6):489–498

Chan G., Balaratnasingam C., Yu P. K., Morgan W. H., McAllister I. L., Cringle S. J., Yu D.-Y. (2012) Quantitative morphometry of perifoveal capillary networks in the human retina. Invest. Ophthalmol. Vis. Sci. 53(9):5502–5514

Chaplain M. A. J., McDougall S. R., Anderson A. R. A. (2006) Mathematical modelling of tumour-induced angiogenesis. Annu. Rev. Biomed. Eng. 8(1):233–257

Chapman S. J., Shipley R. J., Jawad R. (2008) Multiscale modeling of fluid transport in tumors. Bull. Math. Biol. 70(8):2334–2357

Choi M. Y., Yu Y. S., Kim S. K., Kim Y. J., Seo J. S. (2001) The effect of oxygen on retinal degeneration in wild-type and hsp70.1 knockout neonatal retinal degeneration mice. Korean J. Ophthalmol. 15(1):1–7

Chrysostomou V., Stone J., Stowe S., Barnett N. L., Valter K. (2008) The status of cones in the rhodopsin mutant P23H-3 retina: Light-regulated damage and repair in parallel with rods. Invest. Ophthalmol. Vis. Sci. 49(3):1116–1125

Cideciyan A. V., Hood D. C., Huang Y., Banin E., Li Z.-Y., Stone E. M., Milam A. H., Jacobson S. G. (1998) Disease sequence from mutant rhodopsin allele to rod and cone photoreceptor degeneration in man. Proc. Natl. Acad. Sci. 95(12):7103–7108

Cingolani C., Rogers B., Lu L., Kachi S., Shen J., Campochiaro P. A. (2006) Retinal degeneration from oxidative damage. Free Radic. Biol. Med. 40(4):660–669

Clarke G., Lumsden C. J. (2005a) Heterogeneous cellular environments modulate one-hit neuronal death kinetics. Brain Res. Bull. 65(1):59–67

Clarke G., Lumsden C. J. (2005b) Scale-free neurodegeneration: cellular heterogeneity and the stretched exponential kinetics of cell death. J. Theor. Biol. 233(4):515–525

Clarke G., Collins R. A., Leavitt B. R., Andrews D. F., Hayden M. R., Lumsden C. J., McInnes R. R. (2000) A one-hit model of cell death in inherited neuronal degenerations. Nature 406:195–199

Clarke G., Lumsden C. J., McInnes R. R. (2001) Inherited neurodegenerative diseases: the one-hit model of neurodegeneration. Hum. Mol. Genet. 10(20):2269–2275

Coleman H. R., Chan C. C., Ferris III F. L., Chew E. Y. (2008) Age-related macular degeneration. Lancet 372(9652):1835–1845

Colón Vélez M. A., Hernández D. J., Bernier U. R., van Laarhoven J., Camacho E. T. (2003) Mathematical models for photoreceptor interactions. Tech. rep., Cornell University, Department of Biological Statistics and Computational Biology

Costa L. E., Mendez G., Boveris A. (1997) Oxygen dependence of mitochondrial function measured by high-resolution respirometry in long-term hypoxic rats. Am. J. Physiol. 273(3):C852–C858

Cringle S. J., Yu D. Y. (2002) A multi-layer model of retinal oxygen supply and consumption helps explain the muted rise in inner retinal PO(2) during systemic hyperoxia. Comp. Biochem. Physiol. 132(1):61–66

Curcio C. A., Sloan K. R., Kalina R. E., Hendrickson A. E. (1990) Human photoreceptor topography. J. Comp. Neurol. 292(4):497–523

Curcio C. A., Millican C. L., Allen K. A., Kalina R. E. (1993) Aging of the human photoreceptor mosaic: evidence for selective vulnerability of rods in central retina. Invest. Ophthalmol. Vis. Sci. 34(12):3278–3296

Daiger S. P., Bowne S. J., Sullivan L. S. (2007) Perspective on genes and mutations causing retinitis pigmentosa. Arch. Ophthalmol. 125(2):151–158

Del Priore L. V., Kaplan H. J., Hornbeck R., Jones Z., Swinn M. (1996) Retinal pigment epithelial debridement as a model for the pathogenesis and treatment of macular degeneration. Am. J. Ophthalmol. 122(5):629–643

Dewilde S., Kiger L., Burmester T., Hankeln T., Baudin-Creuza V., Aerts T., Marden M. C., Caubergs R., Moens L. (2001) Biochemical characterization and ligand binding properties of neuroglobin, a novel member of the globin family. J. Biol. Chem. 276(42):38,949–38,955

Dhoot D. S., Huo S., Yuan A., Xu D., Srivistava S., Ehlers J. P., Traboulsi E., Kaiser P. K. (2013) Evaluation of choroidal thickness in retinitis pigmentosa using enhanced depth imaging optical coherence tomography. Br. J. Ophthalmol. 97(1):66–69

Dollery C. T., Bulpitt C. J., Kohner E. M. (1969) Oxygen supply to the retina from the retinal and choroidal circulations at normal and increased arterial oxygen tensions. Invest. Ophthalmol. Vis. Sci. 8(6):588–594

Dong A., Shen J., Krause M., Akiyama H., Hackett S. F., Lai H., Campochiaro P. A. (2006) Superoxide dismutase 1 protects retinal cells from oxidative damage. J. Cell Physiol. 208(3):516–526

Dorey C. K., Wu G., Ebenstein D., Garsd A., Weiter J. J. (1989) Cell loss in the aging retina - relationship to lipofuscin accumulation and macular degeneration. Invest. Ophthalmol. Vis. Sci. 30(8):1691–1699

Eglen S. J. (2006) Development of regular cellular spacing in the retina: theoretical models. Math. Med. Biol. 23(2):79–99

Epstein F. H. (1997) Oxygen and renal metabolism. Kidney Int. 51(2):381–385

Epstein F. H., Agmon Y., Brezis M. (1994) Physiology of renal hypoxia. Ann. NY Acad. Sci. 718(1):72–82

Escher P., Tran H. V., Vaclavik V., Borruat F. X., Schorderet D. F., Munier F. L. (2012) Double concentric autofluorescence ring in NR2E3-p.G56R-linked autosomal dominant retinitis pigmentosa. Invest. Ophthalmol. Vis. Sci. 53(8):4754–4764

Fago A., Hundahl C., Dewilde S., Gilany K., Moens L., Weber R. E. (2004a) Allosteric regulation and temperature dependence of oxygen binding in human neuroglobin and cytoglobin. J. Biol. Chem. 279(43):44,417–44,426

Fago A., Hundahl C., Malte H., Weber R. E. (2004b) Functional properties of neuroglobin and cytoglobin. insights into the ancestral physiological roles of globins. IUBMB Life 56(11-12):689–696

Ferrara N., Gerber H. P., LeCouter J. (2003) The biology of VEGF and its receptors. Nat. Med. 9(6):669–676

Fintz A. C., Audo I., Hicks D., Mohand-Saïd S., Léveillard T., Sahel J. (2003) Partial characterization of retina-derived cone neuroprotection in two culture models of photoreceptor degeneration. Invest. Ophthalmol. Vis. Sci. 44(2):818–825

Friedland A. B. (1978) A mathematical model of transmural transport of oxygen to the retina. Bull. Math. Biol. 40(6):823–837

Ganesan P., He S., Xu H. (2010a) Analysis of retinal circulation using an image-based network model of retinal vasculature. Microvasc. Res. 80(1):99–109

Ganesan P., He S., Xu H. (2010b) Development of an image-based network model of retinal vasculature. Ann. Biomed. Eng. 38:1566–1585

Ganfield R. A., Nair P., Whalen W. J. (1970) Mass transfer, storage, and utilization of O_2 in cat cerebral cortex. Am. J. Physiol. 219(3):814–821

García-Ayuso D., Ortín-Martínez A., Jiménez-López M., Galindo-Romero C., Cuenca N., Pinilla I., Vidal-Sanz M., Agudo-Barriuso M., Villegas-Pérez M. P. (2013) Changes in the photoreceptor mosaic of P23H-1 rats during retinal degeneration: Implications for rod-cone dependent survival. Invest. Ophthalmol. Vis. Sci. 54(8):5888–5900

García-Fernández J. M., Jimenez A. J., Foster R. G. (1995) The persistence of cone photoreceptors within the dorsal retina of aged retinally degenerate mice (rdrd): implications for circadian organization. Neurosci. Lett. 187(1):33–36

Gillies M. C., Su T., Naidoo D. (1995) Electrical resistance and macromolecular permeability of retinal capillary endothelial cells in vitro. Curr. Eye Res. 14(6):435–442

Goldman D. (2008) Theoretical models of microvascular oxygen transport to tissue. Microcirculation 15(8):795–811

Goldstick T. K. (1973) Engineering Principles in Physiology, vol 2, Academic Press, New York, chap Oxygen transport, pp. 257–282

Grover S., Fishman G. A., Brown Jr J. (1998) Patterns of visual field progression in patients with retinitis pigmentosa. Ophthalmology 105(6):1069–1075

Gupta N., Brown K. E., Milam A. H. (2003) Activated microglia in human retinitis pigmentosa, late-onset retinal degeneration, and age-related macular degeneration. Exp. Eye Res. 76(4):463–471

Hamdane D., Kiger L., Dewilde S., Green B. N., Pesce A., Uzan J., Burmester T., Hankeln T., Bolognesi M., Moens L., Marden M. C. (2003) The redox state of the cell regulates the ligand binding affinity of human neuroglobin and cytoglobin. J. Biol. Chem. 278(51):51,713–51,721

Hamel C. (2006) Retinitis pigmentosa. Orphanet. J. Rare Dis. 1(1):40

Hamel C. (2007) Cone rod dystrophies. Orphanet. J. Rare Dis. 2(1):7

Hardarson S. H., Stefánsson E. (2010) Oxygen saturation in central retinal vein occlusion. Am. J. Ophthalmol. 150(6):871–875

Hardarson S. H., Basit S., Jonsdottir T. E., Eysteinsson T., Halldorsson G. H., Karlsson R. A., Beach J. M., Benediktsson J. A., Stefansson E. (2009) Oxygen saturation in human retinal vessels is higher in dark than in light. Invest. Ophthalmol. Vis. Sci. 50(5):2308–2311

Hart Jr. W. (ed) (1992) Adler's Physiology of the Eye, 9th edn. Mosby-Year Book, Inc.

Hartong D. T., Berson E. L., Dryja T. P. (2006) Retinitis pigmentosa. Lancet 368(9549):1795–1809

Haugh L., Linsenmeier R., Goldstick T. (1990) Mathematical models of the spatial distribution of retinal oxygen tension and consumption, including changes upon illumination. Ann. Biomed. Eng. 18:19–36

Hoang Q. V., Linsenmeier R. A., Chung C. K., Curcio C. A. (2002) Photoreceptor inner segments in monkey and human retina: Mitochondrial density, optics, and regional variation. Vis. Neurosci. 19(4):395–407

Huang W. C., Wright A. F., Roman A. J., Cideciyan A. V., Manson F. D., Gewaily D. Y., Schwartz S. B., Sadigh S., Limberis M. P., Bell P., Wilson J. M., Swaroop A., Jacobson S. G. (2012) RPGR-associated retinal degeneration in human X-linked RP and a murine model. Invest. Ophthalmol. Vis. Sci. 53(9):5594–5608

Iwasaki M., Inomata H. (1986) Relation between superficial capillaries and foveal structures in the human retina. Invest. Ophthalmol. Vis. Sci. 27(12):1698–1705

Jager R. D., Mieler W. F., Miller J. W. (2008) Age-related macular degeneration. N. Engl. J. Med. 358(24):2606–2617

Ji Y., Zhu C. L., Grzywacz N. M., Lee E. J. (2012) Rearrangement of the cone mosaic in the retina of the rat model of retinitis pigmentosa. J. Comp. Neurol. 520(4):874–888

Jürgens K. D., Peters T., Gros G. (1994) Diffusivity of myoglobin in intact skeletal muscle cells. Proc. Natl. Acad. Sci. 91(9):3829–3833

Kaplan H. J., Fernandez de Castro J. P. (2012) Retinal regeneration and stem cell therapy in retinitis pigmentosa. Taiwan J. Ophthalmol. 2(2):41–44

Keener J., Sneyd J. (1998) Mathematical Physiology. Springer

Kennedy C. J., Rakoczy P. E., Constable I. J. (1995) Lipofuscin of the retinal pigment epithelium: A review. Eye 9(6):763–771

Kiger L., Uzan J., Dewilde S., Burmester T., Hankeln T., Moens L., Hamdane D., Baudin-Creuza V., Marden M. C. (2004) Neuroglobin ligand binding kinetics. IUBMB Life 56(11-12):709–719

Kohen R., Nyska A. (2002) Invited review: Oxidation of biological systems: Oxidative stress phenomena, antioxidants, redox reactions, and methods for their quantification. Toxicol. Pathol. 30(6):620–650

Komeima K., Rogers B., Lu L., Campochiaro P. (2006) Antioxidants reduce cone cell death in a model of retinitis pigmentosa. Proc. Natl. Acad. Sci. 103(30):11,300–11,305

Komeima K., Rogers B. S., Campochiaro P. A. (2007) Antioxidants slow photoreceptor cell death in mouse models of retinitis pigmentosa. J. Cell Physiol. 213(3):809–815

Korte G. E., Reppucci V., Henkind P. (1984) RPE destruction causes choriocapillary atrophy. Invest. Ophthalmol. Vis. Sci. 25(10):1135–1145

Kranz K., Paquet-Durand F., Weiler R., Janssen-Bienhold U., Dedek K. (2013) Testing for a gap junction-mediated bystander effect in retinitis pigmentosa: Secondary cone death is not altered by deletion of connexin36 from cones. PLoS One 8(2):e57,163

Kur J., Newman E. A., Chan-Ling T. (2012) Cellular and physiological mechanisms underlying blood flow regulation in the retina and choroid in health and disease. Prog. Retin. Eye. Res. 31(5):377–406

Kusnyerik A., Greppmaier U., Wilke R., Gekeler F., Wilhelm B., Sachs H. G., Bartz-Schmidt K. U., Klose U., Stingl K., Resch M. D., Hekmat A., Bruckmann A., Karacs K., Nemeth J., Suveges I., Zrenner E. (2012) Positioning of electronic subretinal implants in blind retinitis pigmentosa patients through multimodal assessment of retinal structures. Invest. Ophthalmol. Vis. Sci. 53(7):3748–3755

Lee D. C., Vazquez-Chona F. R., Ferrell W. D., Tam B. M., Jones B. W., Marc R. E., Moritz O. L. (2012) Dysmorphic photoreceptors in a P23H mutant rhodopsin model of retinitis

pigmentosa are metabolically active and capable of regenerating to reverse retinal degeneration. J. Neurosci. 32(6):2121–2128

Lee E. J., Ji Y., Zhu C. L., Grzywacz N. M. (2011) Role of Müller cells in cone mosaic rearrangement in a rat model of retinitis pigmentosa. Glia 59(7):1107–1117

Léveillard T., Mohand-Saïd S., Lorentz O., Hicks D., Fintz A. C., Clérin E., Simonutti M., Forster V., Cavusoglu N., Chalmel F., Dollé P., Poch O., Lambrou G., Sahel J. A. (2004) Identification and characterization of rod-derived cone viability factor. Nat. Genet. 36(7):755–759

Li G., De La Garza B., Shih Y.-Y. I., Muir E. R., Duong T. Q. (2012) Layer-specific blood-flow MRI of retinitis pigmentosa in RCS rats. Exp. Eye Res. 101(0):90–96

Li Z. Y., Possin D. E., Milam A. H. (1995) Histopathology of bone spicule pigmentation in retinitis pigmentosa. Ophthalmology 102(5):805–816

Li Z. Y., Wong F., Chang J. H., Possin D. E., Hao Y., Petters R. M., Milam A. H. (1998) Rhodopsin transgenic pigs as a model for human retinitis pigmentosa. Invest. Ophthalmol. Vis. Sci. 39(5):808–819

Lima L. H., Cella W., Greenstein V. C., Wang N. K., Busuioc M., Smith R. T., Yannuzzi L. A., Tsang S. H. (2009) Structural assessment of hyperautofluorescent ring in patients with retinitis pigmentosa. Retina 29(7):1025–1031

Lima L. H., Burke T., Greenstein V. C., Chou C. L., Cella W., Yannuzzi L. A., Tsang S. H. (2012) Progressive constriction of the hyperautofluorescent ring in retinitis pigmentosa. Am. J. Ophthalmol. 153(4):718–727

Linsenmeier R. A. (1986) Effects of light and darkness on oxygen distribution and consumption in the cat retina. J. Gen. Physiol. 88(4):521–542

Linsenmeier R. A., Braun R. D. (1992) Oxygen distribution and consumption in the cat retina during normoxia and hypoxemia. J. Gen. Physiol. 99(2):177–197

Linsenmeier R. A., Padnick-Silver L. (2000) Metabolic dependence of photoreceptors on the choroid in the normal and detached retina. Invest. Ophthalmol. Vis. Sci. 41(10):3117–3123

Linsenmeier R. A., Yancey C. M. (1989) Effects of hyperoxia on the oxygen distribution in the intact cat retina. Invest. Ophthalmol. Vis. Sci. 30(4):612–618

Liu D., Wood N. B., Witt N., Hughes A. D., Thom S. A., Xu X. Y. (2009) Computational analysis of oxygen transport in the retinal arterial network. Curr. Eye Res. 34(11):945–956

Lomasko T., Lumsden C. J. (2009) One-hit stochastic decline in a mechanochemical model of cytoskeleton-induced neuron death III: Diffusion pulse death zones. J. Theor. Biol. 256(1):104–116

Lomasko T., Clarke G., Lumsden C. J. (2007a) One-hit stochastic decline in a mechanochemical model of cytoskeleton-induced neuron death I: Cell-fate arrival times. J. Theor. Biol. 249(1):1–17

Lomasko T., Clarke G., Lumsden C. J. (2007b) One-hit stochastic decline in a mechanochemical model of cytoskeleton-induced neuron death II: Transition state metastability. J. Theor. Biol. 249(1):18–28

Ma Y., Kawasaki R., Dobson L. P., Ruddle J. B., Kearns L. S., Wong T. Y., Mackey D. A. (2012) Quantitative analysis of retinal vessel attenuation in eyes with retinitis pigmentosa. Invest. Ophthalmol. Vis. Sci. 53(7):4306–4314

Maggelakis S. A., Savakis A. E. (1996) A mathematical model of growth factor induced capillary growth in the retina. Mathl. Comput. Modelling 24(7):33–41

Maggelakis S. A., Savakis A. E. (1999) A mathematical model of retinal neovascularization. Mathl. Comput. Modelling 29(2):91–97

Maharaj A. S. R., Saint-Geniez M., Maldonado A. E., D'Amore P. A. (2006) Vascular endothelial growth factor localization in the adult. Am. J. Pathol. 168(2):639–648

Mantzaris N. V., Webb S., Othmer H. G. (2004) Mathematical modeling of tumor-induced angiogenesis. J. Math. Biol. 49(2):111–187

Maslim J., Valter K., Egensperger R., Holländer H., Stone J. (1997) Tissue oxygen during a critical developmental period controls the death and survival of photoreceptors. Invest. Ophthalmol. Vis. Sci. 38(9):1667–1677

McDougall S. R., Watson M. G., Devlin A. H., Mitchell C. A., Chaplain M. A. J. (2012) A hybrid discrete-continuum mathematical model of pattern prediction in the developing retinal vasculature. Bull. Math. Biol. 74:2272–2314

McGuire B. J., Secomb T. W. (2001) A theoretical model for oxygen transport in skeletal muscle under conditions of high oxygen demand. J. Appl. Physiol. 91(5):2255–2265

Medrano C. J., Fox D. A. (1995) Oxygen consumption in the rat outer and inner retina: Light- and pharmacologically-induced inhibition. Exp. Eye Res. 61(3):273–284

Mervin K., Stone J. (2002a) Developmental death of photoreceptors in the C57BL/6J mouse: Association with retinal function and self-protection. Exp. Eye Res. 75(6):703–713

Mervin K., Stone J. (2002b) Regulation by oxygen of photoreceptor death in the developing and adult C57BL/6J mouse. Exp. Eye Res. 75(6):715–722

Milam A. H., Zong Y. L., Fariss R. N. (1998) Histopathology of the human retina in retinitis pigmentosa. Prog. Retin. Eye Res. 17(2):175–205

Mohand-Saïd S., Hicks D., Simonutti M., Tran-Minh D., Deudon-Combe A., Dreyfus H., Silverman M. S., Ogilvie J. M., Tenkova T., Sahel J. (1997) Photoreceptor transplants increase host cone survival in the retinal degeneration (rd) mouse. Ophthalmic Res. 29:290–297

Mohand-Saïd S., Deudon-Combe A., Hicks D., Simonutti M., Forster V., Fintz A. C., Léveillard T., Dreyfus H., Sahel J. A. (1998) Normal retina releases a diffusible factor stimulating cone survival in the retinal degeneration mouse. Proc. Natl. Acad. Sci. 95(14):8357–8362

Mohand-Saïd S., Hicks D., Dreyfus H., Sahel J. A. (2000) Selective transplantation of rods delays cone loss in a retinitis pigmentosa model. Arch. Ophthalmol. 118(6):807–811

Mullins R. F., Kuehn M. H., Radu R. A., Enriquez G. S., East J. S., Schindler E. I., Travis G. H., Stone E. M. (2012) Autosomal recessive retinitis pigmentosa due to ABCA4 mutations: Clinical, pathologic, and molecular characterization. Invest. Ophthalmol. Vis. Sci. 53(4):1883–1894

Murakami T., Akimoto M., Ooto S., Suzuki T., Ikeda H., Kawagoe N., Takahashi M., Yoshimura N. (2008) Association between abnormal autofluorescence and photoreceptor disorganization in retinitis pigmentosa. Am. J. Ophthalmol. 145(4):687–694

Musarella M. A., MacDonald I. M. (2011) Current concepts in the treatment of retinitis pigmentosa. J. Ophthalmol. 2011:753,547

Ockendon J., Howison S., Lacey A., Movchan A. (2003) Applied Partial Differential Equations, revised edn. Oxford University Press

Okoye G., Zimmer J., Sung J., Gehlbach P., Deering T., Nambu H., Hackett S., Melia M., Esumi N., Zack D. J., Campochiaro P. A. (2003) Increased expression of brain-derived neurotrophic factor preserves retinal function and slows cell death from rhodopsin mutation or oxidative damage. J. Neurosci. 23(10):4164–4172

Orosz K. E., Gupta S., Hassink M., Abdel-Rahman M., Moldovan L., Davidorf F. H., Moldovan N. I. (2004) Delivery of antiangiogenic and antioxidant drugs of ophthalmic interest through a nanoporous inorganic filter. Mol. Vis. 10:555–565

Østerberg G. (1935) Topography of the Layer of Rods and Cones in the Human Retina. Acta ophthalmologica: Supplementum, Levin & Munksgaard

Ostojić J., Sakaguchi D. S., de Lathouder Y., Hargrove M. S., Trent J. T., Kwon Y. H., Kardon R. H., Kuehn M. H., Betts D. M., Grozdanić S. (2006) Neuroglobin and cytoglobin: Oxygen-binding proteins in retinal neurons. Invest. Ophthalmol. Vis. Sci. 47(3):1016–1023

Ostojić J., Grozdanić S. D., Syed N. A., Hargrove M. S., Trent J. T., Kuehn M. H., Kwon Y. H., Kardon R. H., Sakaguchi D. S. (2008) Patterns of distribution of oxygen-binding globins, neuroglobin and cytoglobin in human retina. Arch. Ophthalmol. 126(11):1530–1536

Oyster C. W. (1999) The Human Eye: Structure and Function. Sinauer Associates Inc.

Padnick-Silver L., Linsenmeier R. A. (2003) Effect of acute hyperglycemia on oxygen and oxidative metabolism in the intact cat retina. Invest. Ophthalmol. Vis. Sci. 44(2):745–750

Padnick-Silver L., Derwent J. J. K., Giuliano E., Narfström K., Linsenmeier R. A. (2006) Retinal oxygenation and oxygen metabolism in abyssinian cats with a hereditary retinal degeneration. Invest. Ophthalmol. Vis. Sci. 47(8):3683–3689

Panorgias A., Zawadzki R. J., Capps A. G., Hunter A. A., Morse L. S., Werner J. S. (2013) Multimodal assessment of microscopic morphology and retinal function in patients with geographic atrophy. Invest. Ophthalmol. Vis. Sci. 54(6):4372–4384

Pearlman J. T. (1979) Mathematical models of retinitis pigmentosa: a study of the rate of progress in the different genetic forms. Trans. Am. Ophthalmol. Soc. 77:643–656

Peirce S. M. (2008) Computational and mathematical modeling of angiogenesis. Microcirculation 15(8):739–751

Pennesi M. E., Michaels K. V., Magee S. S., Maricle A., Davin S. P., Garg A. K., Gale M. J., Tu D. C., Wen Y., Erker L. R., Francis P. J. (2012) Long-term characterization of retinal degeneration in rd1 and rd10 mice using spectral domain optical coherence tomography. Invest. Ophthalmol. Vis. Sci. 53(8):4644–4656

Petters R. M., Alexander C. A., Wells K. D., Collins E. B., Sommer J. R., Blanton M. R., Rojas G., Hao Y., Flowers W. L., Banin E., Cideciyan A. V., Jacobson S. G., Wong F. (1997) Genetically engineered large animal model for studying cone photoreceptor survival and degeneration in retinitis pigmentosa. Nat. Biotech. 15(10):965–970

Popel A. S. (1989) Theory of oxygen transport to tissue. Crit. Rev. Biomed. Eng. 17:257–321

Popović P., Jarc-Vidmar M., Hawlina M. (2005) Abnormal fundus autofluorescence in relation to retinal function in patients with retinitis pigmentosa. Graefes Arch. Clin. Exp. Ophthalmol. 243:1018–1027

Pournaras C. J., Rungger-Brändle E., Riva C. E., Hardarson S. H., Stefansson E. (2008) Regulation of retinal blood flow in health and disease. Prog. Retin. Eye. Res. 27(3):284–330

Rajendram R., Rao N. A. (2007) Neuroglobin in normal retina and retina from eyes with advanced glaucoma. Br. J. Ophthalmol. 91(5):663–666

Richmond K. N., Shonat R. D., Lynch R. M., Johnson P. C. (1999) Critical PO(2) of skeletal muscle in vivo. Am. J. Physiol. Heart Circ. Physiol. 277(5):H1831–H1840

Ripps H. (2002) Cell death in retinitis pigmentosa: Gap junctions and the 'bystander' effect. Exp. Eye Res. 74(3):327–336

Robson A. G., El-Amir A., Bailey C., Egan C. A., Fitzke F. W., Webster A. R., Bird A. C., Holder G. E. (2003) Pattern ERG correlates of abnormal fundus autofluorescence in patients with retinitis pigmentosa and normal visual acuity. Invest. Ophthalmol. Vis. Sci. 44(8):3544–3550

Robson A. G., Egan C. A., Luong V. A., Bird A. C., Holder G. E., Fitzke F. W. (2004) Comparison of fundus autofluorescence with photopic and scotopic fine-matrix mapping in patients with retinitis pigmentosa and normal visual acuity. Invest. Ophthalmol. Vis. Sci. 45(11):4119–4125

Robson A. G., Saihan Z., Jenkins S. A., Fitzke F. W., Bird A. C., Webster A. R., Holder G. E. (2006) Functional characterisation and serial imaging of abnormal fundus autofluorescence in patients with retinitis pigmentosa and normal visual acuity. Br. J. Ophthalmol. 90(4):472–479

Robson A. G., Michaelides M., Saihan Z., Bird A. C., Webster A. R., Moore A. T., Fitzke F. W., Holder G. E. (2008) Functional characteristics of patients with retinal dystrophy that

manifest abnormal parafoveal annuli of high density fundus autofluorescence; a review and update. Doc. Ophthalmol. 116(2):79–89

Robson A. G., Tufail A., Fitzke F., Bird A. C., Moore A. T., Holder G. E., Webster A. R. (2011) Serial imaging and structure-function correlates of high-density rings of fundus autofluorescence in retinitis pigmentosa. Retina 10(10):1–10

Roh H. D., Goldstick T. K., Linsenmeier R. A. (1990) Spatial variation of the local tissue oxygen diffusion coefficient measured in situ in the cat retina and cornea. Adv. Exp. Med. Biol. 277:127–136

Ross J. W., Fernandez de Castro J. P., Zhao J., Samuel M., Walters E., Rios C., Bray-Ward P., Jones B. W., Marc R. E., Wang W., Zhou L., Noel J. M., McCall M. A., DeMarco P. J., Prather R. S., Kaplan H. J. (2012) Generation of an inbred miniature pig model of retinitis pigmentosa. Invest. Ophthalmol. Vis. Sci. 53(1):501–507

von Rückmann A., Fitzke F. W., Bird A. C. (1995) Distribution of fundus autofluorescence with a scanning laser ophthalmoscope. Br. J. Ophthalmol. 79(5):407–412

von Rückmann A., Fitzke F. W., Bird A. C. (1999) Distribution of pigment epithelium autofluorescence in retinal disease state recorded in vivo and its change over time. Graefes Arch. Clin. Exp. Ophthalmol. 237:1–9

Sahaboglu A., Paquet-Durand O., Dietter J., Dengler K., Bernhard-Kurz S., Ekstrom P. A. R., Hitzmann B., Ueffing M., Paquet-Durand F. (2013) Retinitis pigmentosa: rapid neurodegeneration is governed by slow cell death mechanisms. Cell Death. Dis. 4:e488

Saint-Geniez M., Kurihara T., Sekiyama E., Maldonado A. E., D'Amore P. A. (2009) An essential role for RPE-derived soluble VEGF in the maintenance of the choriocapillaris. Proc. Natl. Acad. Sci. 106:18,751–18,756

Samardzija M., Wariwoda H., Imsand C., Huber P., Heynen S. R., Gubler A., Grimm C.

(2012) Activation of survival pathways in the degenerating retina of rd10 mice. Exp. Eye Res. 99(0):17–26

Sanz M. M., Johnson L. E., Ahuja S., Ekström P. A. R., Romero J., van Veen T. (2007) Significant photoreceptor rescue by treatment with a combination of antioxidants in an animal model for retinal degeneration. Neuroscience 145(3):1120–1129

Schmidt M., Giessl A., Laufs T., Hankeln T., Wolfrum U., Burmester T. (2003) How does the eye breathe? J. Biol. Chem. 278(3):1932–1935

Schmidt M., Laufs T., Reuss S., Hankeln T., Burmester T. (2005) Divergent distribution of cytoglobin and neuroglobin in the murine eye. Neurosci. Lett. 374(3):207–211

Seth D. (2012) An analytical solution for diffusion and nonlinear uptake of oxygen in the retina. IJM2C 2(3):181–188

Shen J., Yang X., Dong A., Petters R. M., Peng Y. W., Wong F., Campochiaro P. A. (2005) Oxidative damage is a potential cause of cone cell death in retinitis pigmentosa. J. Cell Physiol. 203(3):457–464

Shintani K., Shechtman D. L., Gurwood A. S. (2009) Review and update: Current treatment trends for patients with retinitis pigmentosa. Optometry 80(7):384–401

Shipley R. J., Chapman S. J. (2010) Multiscale modelling of fluid and drug transport invascular tumours. Bull. Math. Biol. 72(6):1464–1491

Sneyd J., Tranchina D. (1989) Phototransduction in cones: An inverse problem in enzyme kinetics. Bull. Math. Biol. 51(6):749–784

Snodderly D. M., Weinhaus R. S., Choi J. C. (1992) Neural-vascular relationships in central retina of macaque monkeys (Macaca fascicularis). J. Neurosci. 12(4):1169–1193

Sparrow J. R., Boulton M. (2005) RPE lipofuscin and its role in retinal pathobiology. Exp. Eye Res. 80(5):595–606

Stefánsson E. (1988) Retinal oxygen tension is higher in light than dark. Pediatr. Res. 23:5–8

Stone J., Maslim J., Valter-Kocsi K., Mervin K., Bowers F., Chu Y., Barnett N., Provis J., Lewis G., Fisher S. K., Bistid S., Gargini C., Cervetto L., Merin S., Pe'er J. (1999) Mechanisms of photoreceptor death and survival in mammalian retina. Prog. Retin. Eye Res. 18(6):689–735

Stone J., Mervin K., Walsh N., Valter K., Provis J. M., Penfold P. L. (2005) Photoreceptor stability and degeneration in mammalian retina: Lessons from the edge. In: Penfold P. L., Provis J. M. (eds) Macular Degeneration, Springer Berlin Heidelberg, pp. 149–165

Sun Y., Jin K., Mao X. O., Zhu Y., Greenberg D. A. (2001) Neuroglobin is up-regulated by and protects neurons from hypoxic-ischemic injury. Proc. Nalt. Acad. Sci. 98(26):15,306–15,311

Sun Y., Jin K., Peel A., Mao X. O., Xie L., Greenberg D. A. (2003) Neuroglobin protects the brain from experimental stroke in vivo. Proc. Nalt. Acad. Sci. 100(6):3497–3500

Swaroop A., Kim D., Forrest D. (2010) Transcriptional regulation of photoreceptor development and homeostasis in the mammalian retina. Nat. Rev. Neurosci. 11:563–576

Tan P. E. Z., Yu P. K., Balaratnasingam C., Cringle S. J., Morgan W. H., McAllister I. L., Yu D.-Y. (2012) Quantitative confocal imaging of the retinal microvasculature in the human retina. Invest. Ophthalmol. Vis. Sci. 53(9):5728–5736

Tao W. (2006) Application of encapsulated cell technology for retinal degenerative diseases. Expert Opin. Biol. Ther. 6(7):717–726

Tao W., Wen R., Goddard M. B., Sherman S. D., O'Rourke P. J., Stabila P. F., Bell W. J., Dean B. J., Kauper K. A., Budz V. A., Tsiaras W. G., Acland G. M., Pearce-Kelling S., Laties A. M., Aguirre G. D. (2002) Encapsulated cell-based delivery of CNTF reduces photoreceptor degeneration in animal models of retinitis pigmentosa. Invest. Ophthalmol. Vis. Sci. 43(10):3292–3298

Tayyab M., Usson Y., Leveillard T., Demongeot J. (2009) Imaging and modelling of a degenerative disease of retina. In: In: International Conference on Advanced Information Networking and Applications Workshops, 2009. WAINA '09, pp. 936 –941

Till S. J., Till J., Milsom P. K., Rowlands G. (2003) A new model for laser-induced thermal damage in the retina. Bull. Math. Biol. 65(4):731–746

Törnquist P., Alm A., Bill A. (1990) Permeability of ocular vessels and transport across the blood-retinal-barrier. Eye 4(2):303–309

Tranchina D., Sneyd J., Cadenas I. D. (1991) Light adaptation in turtle cones. testing and analysis of a model for phototransduction. Biophys. J. 60(1):217–237

Travis G. H., Sutcliffe J. G., Bok D. (1991) The retinal degeneration slow (rds) gene product is a photoreceptor disc membrane-associated glycoprotein. Neuron 6(1):61–70

Trent J. T., Hargrove M. S. (2002) A ubiquitously expressed human hexacoordinate hemoglobin. J. Biol. Chem. 277(22):19,538–19,545

Tso M. O. M., Li W. W. Y., Zhang C., Lam T. T., Hao Y., Petters R. M., Wong F. (1997) A pathologic study of degeneration of the rod and cone populations of the rhodopsin Pro347Leu transgenic pigs. Trans. Am. Ophthalmol. Soc. 95:467–483

Tsuruma K., Nishimura Y., Kishi S., Shimazawa M., Tanaka T., Hara H. (2012) SEMA4A mutations lead to susceptibility to light irradiation, oxidative stress, and ER stress in retinal pigment epithelial cells. Invest. Ophthalmol. Vis. Sci. 53(10):6729–6737

Valter K., Mervin K., Maslim J., Stone J. (1997) The influence of oxygen on the survival and death of photoreceptors. In: LaVail M. M., Hollyfield J. G., Anderson R. E. (eds) Degenerative Retinal Diseases, Springer US, pp. 353–367

Valter K., Maslim J., Bowers F., Stone J. (1998) Photoreceptor dystrophy in the RCS rat: roles of oxygen, debris, and bFGF. Invest. Ophthalmol. Vis. Sci. 39(12):2427–2442

Van Soest S., Westerveld A., De Jong P. T. V. M., Bleeker-Wagemakers E. M., Bergen A. A. B. (1999) Retinitis pigmentosa: Defined from a molecular point of view. Surv. Ophthalmol. 43(4):321–334

Vingolo E. M., Pelaia P., Forte R., Rocco M., Giusti C., Rispoli E. (1999) Does hyperbaric oxygen (HBO) delivery rescue retinal photoreceptors in retinitis pigmentosa? Doc. Ophthalmol. 97(1):33–39

Vingolo E. M., Rocco M., Grenga P. L., Salvatore S., Pelaia P. (2008) Slowing the degenerative process, long lasting effect of hyperbaric oxygen therapy in retinitis pigmentosa. Graefes Arch. Clin. Exp. Ophthalmol. 246(1):93–98

Wang R., Jiang C., Ma J., Young M. J. (2012) Monitoring morphological changes in the retina of rhodopsin -/- mice with spectral domain optical coherence tomography. Invest. Ophthalmol. Vis. Sci. 53(7):3967–3972

Wang X., Ryter S. W., Dai C., Tang Z. L., Watkins S. C., Yin X. M., Song R., Choi A. M. K. (2003) Necrotic cell death in response to oxidant stress involves the activation of the apoptogenic Caspase-8/Bid pathway. J. Biol. Chem. 278(31):29,184–29,191

Wangsa-Wirawan N. D., Linsenmeier R. A. (2003) Retinal oxygen: Fundamental and clinical aspects. Arch. Ophthalmol. 121(4):547–557

Watson M. G., McDougall S. R., Chaplain M. A. J., Devlin A. H., Mitchell C. A. (2012) Dynamics of angiogenesis during murine retinal development: a coupled in vivo and in silico study. J. R. Soc. Interface

Wellard J., Lee D., Valter K., Stone J. (2005) Photoreceptors in the rat retina are specifically vulnerable to both hypoxia and hyperoxia. Vis. Neurosci. 22(4):501–507

Wen R., Tao W., Li Y., Sieving P. A. (2012) CNTF and retina. Prog. Retin. Eye Res. 31(2):136–151

Whiteley J. P., Gavaghan D. J., Hahn C. E. W. (2002) Mathematical modelling of oxygen transport to tissue. J. Math. Biol. 44:503–522

Wilson D. F., Rumsey W. L., Green T. J., Vanderkooi J. M. (1988) The oxygen dependence of mitochondrial oxidative phosphorylation measured by a new optical method for measuring oxygen concentration. J. Biol. Chem. 263(6):2712–2718

Wright A. F., Jacobson S. G., Cideciyan A. V., Roman A. J., Shu X., Vlachantoni D., McInnes R. R., Riemersma R. A. (2004) Lifespan and mitochondrial control of neurodegeneration. Nat. Genet. 36(11):1153–1158

Wright A. F., Chakarova C. F., Abd El-Aziz M. M., Bhattacharya S. S. (2010) Photoreceptor degeneration: genetic and mechanistic dissection of a complex trait. Nat. Rev. Genet. 11(4):273–284

Wyman J. (1966) Facilitated diffusion and the possible role of myoglobin as a transport mechanism. J. Biol. Chem. 241(1):115–121

Yamada H., Yamada E., Hackett S. F., Ozaki H., Okamoto N., Campochiaro P. A. (1999) Hyperoxia causes decreased expression of vascular endothelial growth factor and endothelial cell apoptosis in adult retina. J. Cell Physiol. 179(2):149–156

Yamada H., Yamada E., Ando A., Esumi N., Bora N., Saikia J., Sung C.-H., Zack D. J., Campochiaro P. A. (2001) Fibroblast growth factor-2 decreases hyperoxia-induced photoreceptor cell death in mice. Am. J. Pathol. 159(3):1113–1120

Yin Z. Q., Li S. Y. (2012) Cell therapy for retinitis pigmentosa: From rats to pigs. Taiwan J. Ophthalmol. 2(2):45–50

Young R. W. (1967) The renewal of photoreceptor cell outer segments. J. Cell Biol. 33(1):61–72

Young R. W. (1971) The renewal of rod and cone outer segments in the rhesus monkey. J. Cell Biol. 49:303–318

Young R. W. (1978) The daily rhythm of shedding and degradation of rod and cone outer segment membranes in the chick retina. Invest. Ophthalmol. Vis. Sci. 17(2):105–16

Young R. W., Bok D. (1969) Participation of the retinal pigment epithelium in the rod outer segment renewal process. J. Cell Biol. 42:392–403

Yu D. Y., Cringle S. J. (2001) Oxygen distribution and consumption within the retina in vascularised and avascular retinas and in animal models of retinal disease. Prog. Retin. Eye Res. 20(2):175–208

Yu D. Y., Cringle S. J. (2002) Outer retinal anoxia during dark adaptation is not a general property of mammalian retinas. Comp. Biochem. Physiol. 132(1):47–52

Yu D. Y., Cringle S. J. (2005) Retinal degeneration and local oxygen metabolism. Exp. Eye Res. 80(6):745–751

Yu D. Y., Cringle S. J., Alder V. A., Su E. N. (1994) Intraretinal oxygen distribution in rats as a function of systemic blood pressure. Am. J. Physiol. Heart. Circ. Physiol. 267(6):H2498–H2507

Yu D. Y., Cringle S. J., Alder V., Su E. N. (1999) Intraretinal oxygen distribution in the rat with graded systemic hyperoxia and hypercapnia. Invest. Ophthalmol. Vis. Sci. 40(9):2082–2087

Yu D. Y., Cringle S. J., Su E. N., Yu P. K. (2000) Intraretinal oxygen levels before and after photoreceptor loss in the RCS rat. Invest. Ophthalmol. Vis. Sci. 41(12):3999–4006

Yu D. Y., Cringle S., Valter K., Walsh N., Lee D., Stone J. (2004) Photoreceptor death, trophic factor expression, retinal oxygen status, and photoreceptor function in the P23H rat. Invest. Ophthalmol. Vis. Sci. 45(6):2013–2019

Zaia J., Annan R. S., Biemann K. (1992) The correct molecular weight of myoglobin, a common calibrant for mass spectrometry. Rapid Commun. Mass Spectrom. 6(1):32–36

Zhou J., Jang Y. P., Kim S. R., Sparrow J. R. (2006) Complement activation by photooxidation products of A2E, a lipofuscin constituent of the retinal pigment epithelium. Proc. Natl. Acad. Sci. 103(44):16,182–16,187

Zhu C. L., Ji Y., Lee E.-J., Grzywacz N. M. (2013) Spatiotemporal pattern of rod degeneration in the S334ter-line-3 rat model of retinitis pigmentosa. Cell Tissue Res. 351(1):29–40